UNIVERSITY OF OKLAHOMA

GRADUATE COLLEGE

THREE-DIMENSIONAL FULLY COUPLED THERMOPOROMECHANICAL MODELLING OF FRACTURED RESERVOIR ROCK

A DISSERTATION

SUBMITTED TO THE GRADUATE FACULTY

in partial fulfillment of the requirements for the

Degree of

DOCTOR OF PHILOSOPHY

By

QIAN GAO
Norman, Oklahoma
2019

THREE-DIMENSIONAL FULLY COUPLED THERMOPOROMECHANICAL MODELLING OF FRACTURED RESERVOIR ROCK

A DISSERTATION APPROVED FOR THE
MEWBOURNE SCHOOL OF PETROLEUM AND GEOLOGICAL ENGINEERING

BY

Dr. Ahmad Ghassemi, Chair

Dr. Matthew J. Pranter

Dr. Mashhad Fahes

Dr. Deepak Devegowda

Dr. Jean-Claude Roegiers

Dedication

To my parents, brothers, and sisters,

Acknowledgements

I would like to express my sincerest and deepest gratitude to my advisor, Dr. Ahmad Ghassemi, for his guidance, encouragement, and patience throughout my Ph.D. work over the last six years. Dr. Ghassemi's dedication to research has been and will always be the excellent model for me to follow.

I would like to thank for my dissertation committee: Dr. Jean-Claude Roegiers, Dr. Matthew J. Pranter, Dr. Deepak Devegowda, Dr. Mashhad Fahes, Dr. Ahmad Jamili for their help.

I have been fortunate to have an opportunity to study with and learn from a group of excellent colleagues in the Reservoir Geomechanics & Seismicity Research Group. Many thanks go to Dr. Xiaonan Wang, Dr. Varahanaresh Sesetty, Lianbo Hu, Dr. Dharmendra Kumar, Dr. Yawei Li, Dr. Kai Huang, Dr. Zhi Ye, Dr. Qinglu Cheng, Jianrong Lu, Jiman Liu, and many others. I want to thank all my friends for sharing the joyful and wonderful life during my Ph.D. study.

I would like to thank my parents, brothers and sisters for their endless love and support.

Table of Contents

List of Tables

List of Figures

Abstract

The coupled behaviors of fluid flow, heat transport and geomechanics in fractured porous media are studied. Emphasis is placed on the coupled hydro-mechanical processes involved in hydraulic fracture propagation, thermal circulation in pre-existing fractures, and reactivation of joints due to fluid injection.

A 3D fully coupled hydro-mechanical model is developed to simulate hydraulic fracturing. The model is built on a parallel computation framework. Finite element method is utilized to discretize the governing equations. Hydraulic fracture propagation and fluid flow in the created hydraulic fracture are modeled through a special zero-thickness interface element which is developed based on the cohesive zone model (CZM). The 3D model is verified by considering a penny-shaped hydraulic fracture and a KGD hydraulic fracture (in 3D domain) propagating in both the viscosity- and toughness-dominated regimes. Good agreements have been achieved between numerical results and asymptotic analytical solutions with respect to fluid pressure, fracture height, length and width distributions. The effects of some key CZM parameters and the size of interface element on modeling of hydraulic fracturing are investigated.

Using the hydro-mechanical model, height growth of hydraulic fractures in layered formations is simulated. First, the model is validated through a laboratory hydraulic fracturing experiment in the presence of stress contrast. Through explicit modeling of the injection wellbore, the compressibility effects of the wellbore are demonstrated. Comparing the numerical results to those obtained in the laboratory experiment, good agreements in the distribution of fracture aperture, injection pressure and fracture footprint are achieved. Then, numerical analyses are performed to investigate the impacts of in-situ stress contrast, modulus contrast and formation ductility on hydraulic fracture height growth.

The interaction between hydraulic fractures and discontinuities is analyzed. The nonlinear mechanical behavior of frictional sliding along interface surfaces is considered. Typical loading paths demonstrated through numerical examples exhibit the capability of the model to simulate different working conditions. Since discontinuities are explicitly simulated through the use of interface element, detailed descriptions of the deformation processes are revealed. For example, information related to aperture opening/sliding and stress distribution along the discontinuities is obtained in the simulations. Numerical simulations of height growth in a layered rock with the existence of a formation interface are performed. The model is first evaluated through the commonly used Renshaw and Pollard's criterion. Then laboratory experiments on fracture-discontinuity interaction under triaxial-stress conditions are studied. Numerical results match well with those predicted through theoretical formulations and with those observed in laboratory. Typical processes associated with fracture-discontinuity interaction are reveled. With the existence of a horizontal interface, the influence of modulus contrast and stress contrast on hydraulic fracture height growth is analyzed. It is found that the combined effects of material properties of rock, mechanical properties of interfaces, and in-situ stress distribution could effectively inhibit the height growth of hydraulic fractures.

Based on the theory of thermo-poroelasticity, together with the equations describing fluid flow and heat transport in fractures, and the equation for fluid flow in wellbore, the coupled processes of fluid flow, heat transport and geomechanics are studied. The thermo-hydro-mechanical behaviors of a fracture/matrix system are modeled through a special zero-thickness interface element. The constitutive law of the interface element is built based on the cohesive zone model (CZM), which is suitable for simulating both tensile and shear failures. Fracture flow is formulated through the commonly used "cubic law". The fluid flux exchange between the

fractures and the surrounding permeable rock matrix is determined by a fluid transfer coefficient. A convective heat transfer coefficient is introduced in the equation governing heat transport in the fractures. Numerical analyses are performed to verify the model, to illustrate some fundamental phenomena, and to provide some applications to laboratory injection and circulation experiments to further validate the model. Numerical simulations reveal the role of mechanical, hydraulic and thermal properties and the coupled processes in the experiments.

In addition, the stress and pore pressure distributions during hydraulic stimulation in a heterogeneous poroelastic rock are studied. Results indicate that the stress- and pore pressure distributions are more complex in a heterogeneous reservoir than in a homogeneous one. The spatial extent of stress reorientation during hydraulic stimulations is a function of time and is continuously changing due to the diffusion of pore pressure in the heterogeneous system. In contrast to the stress distributions in homogeneous media, irregular distributions of stresses and pore pressure are observed. Due to the change of material properties, shear stresses and non-uniform deformations are generated. The induced shear stresses in heterogeneous rock cause the initial horizontal principal stresses to rotate out of horizontal planes.

At last, an on-site hydraulic stimulation at the Phase I Fenton Hill geothermal reservoir is studied. Four scenarios are proposed to analyze the mechanisms involved in repeated injection-venting experiments. It is found that the stiffness of joint, a key parameter used in aperture calculation, controls the flow-back volume and trapped fluid pressure during venting operations. Considering the size dependent characteristic of joint stiffness and hysteresis behaviors observed during injection and venting, a parameter related to stiffness is gradually changed after each injection-venting treatment. In this way, the numerical simulations yield results close to those observed in the field test.

1 Introduction

1.1 Motivation

Underground resources, such as geothermal energy and hydrocarbons are essential for the development of our society. To effectively and efficiently recovery the energy stored in the reservoirs, the physical mechanisms involved in production should be understood for operation design and forecasting. Fluid flow and the associated rock deformation are always associated with the transportation or migration of energy in underground reservoirs. The storage and transport of fluids in fractured porous rock can give rise to significant coupling processes between fluid flow, rock deformation, and heat transfer. In the development of geothermal reservoirs and unconventional shale reservoirs, newly created fractures or pre-existing natural fractures are extremely important for economical production.

Due to the deficiency of either water or permeability, or both (the so-called hot dry rock), vast geothermal resources have yet to be utilized (Ghassemi 2012). To reduce the high cost and (or) risks in reservoir creation (including drilling), the development technology should be carefully executed based on rock mechanics/geomechanics principles, since the geothermal reservoirs are stimulated mainly based on fluid injection and the effectivity of hydraulic stimulation is largely determined by in-situ stress, the characteristics of discontinuities and rock properties. After the creation of geothermal reservoirs, circulation paths covering a large portion of the reservoirs and having high conductivity are necessary for economic production. The mechanical, hydraulic, thermal and chemical processes that arise from fluid circulation control the conductivity of induced and natural fractures.

Hydraulic fracturing as an effective reservoir stimulation technique is widely used in creating fresh fractures and in reactivating pre-existing natural fractures. Following the pursuit

for green and clean geothermal energy and also the demands for hydrocarbon resource, especially with the development of unconventional reservoirs since the mid-2000s, researches on the subject of hydraulic fracturing have increased dramatically. In addition to theoretical and numerical analyses, lab-scale experiments are also widely performed to investigate the mechanisms involved in hydraulic fracturing (Jeffrey and Bunger 2009; Hu and Ghassemi 2017).

1.2 Literature review

The main focus of this study is about hydraulic stimulation and the coupled mechanical, hydraulic, and thermal processes. In the following, the literature review related to these aspects is presented.

1.2.1 Hydraulic fracturing in reservoirs

As the most widely used reservoir stimulation technique, hydraulic fracturing has attracted numerous research efforts. The pioneering works in hydraulic fracturing attribute to the KGD model (Khristianovic and Zheltov 1955; Geertsma and De Klerk 1969) and the PKN model (Perkins and Kern 1961; Nordgren 1972) developed in the 1960s – 1970s.

The PKN model assumes a fixed height when the fracture propagates away from the wellbore. The vertical cross section is elliptic and is filled by fluid with a constant pressure. The pressure drop along the propagation direction is determined by the flow resistance of fluid in a narrow elliptically shaped channel. The width of the cross sections perpendicular to the direction of fracture propagation is determined by the width formula for a plain strain crack. This treatment makes each cross section "mechanical independent" with other. The PKN model is suitable in estimating long fractures with limited height.

The KGD model assumes constant width at cross sections perpendicular to the propagation direction. The fractures in KGD model also have a fixed height. The plain strain

condition prevails in the plane perpendicular to the cross sections of fractures. This makes the cross section be rectangular. The fluid pressure in each cross section is constant. The pressure drop in the fracture propagation direction is determined by the flow resistance of fluid in a rectangular slit. The KGD model utilizes a concept proposed by Barenblatt (1962). It states that the faces of a hydraulic fracture close smoothly at the edge when it is in mobile equilibrium in a homogeneous brittle solid (Geertsma and De Klerk 1969; Geertsma and Haafkens 1979). This essentially indicates the stress intensity factor is zero at the fracture tips, since the stress component perpendicular to the fracture surfaces at the tip of the fracture is finite and equal to the tensile strength of the rock.

The self-similar solutions for plain strain hydraulic fracture considering the fracture toughness was derived by Spence and Sharp (1985). Later the solutions were used to analyze the magma-driven propagation of cracks (Spence and Turcotte 1985). Two limiting cases (small fracture toughness and high fracture toughness) were studied. When small fracture toughness was used, the obtained fracture tip is a cusp; when large fracture toughness was used, the fracture was elliptical and the pressure in fractures has a uniform value. The near tip processes in hydraulic fractures were studied by the SCR Geomechanics Group (1993) and Desroches et al. (1994) in view of the works of Spence and Sharp (1985). The problem was treated in more detail and the competition processes (viscous/toughness dominated, storage/leak-off dominated) in hydraulic fracturing were studied by Garagash and Detournay (1999), Adachi and Detournay (2002), Savitski and Detournay (2002) and Adachi and Detournay (2008). The competition processes make the fracture tips exhibit multi-scale behaviors. The initiation of hydraulic fractures is in the toughness-dominated regime; the propagation of hydraulic fractures with typical properties for reservoir rock generally is in the viscosity-dominated regime and stays in

this regime for a long time (i.e., at least one order of magnitude longer than the stimulation time) before it reaches back to the toughness-dominated regime. The derived asymptotic analytical solutions assume the rock is isotropic and homogeneous and only elastic deformation is considered.

To simulate problems with complex geometry or sophisticate stress configuration and material property distribution, numerical simulations must be adopted. There are several coupled processes involved in the hydraulic fracturing modelling: (a) mechanical deformation of rock matrix generated by the fluid pressure on the fracture surfaces; (b) fluid and heat flow in the fracture and leak-off of fluid from the fracture to the surrounding rock; (c) fracture propagation. These complex processes could be modelled through a fully coupled numerical scheme. Compared to sequential coupling schemes, fully coupled method is accurate but computation heavy.

Boundary element method (BEM), which uses integral equation representations of the governing partial differential equations to solve problems of interest (Ghassemi et al. 2013), has been widely used in modeling fracture behaviors. Displacement discontinuity method (DD), as a branch of BEM, is an effective method for solving problems involving discontinuities and fractures in rock. Vandamme and Curran (1989) proposed a 3D numerical simulator based on DD to model the propagation of non-planar hydraulic fractures. A 2D coupled DD model was used by Sesetty and Ghassemi (2015) to simulate facture propagation in simultaneous and sequential hydraulic fracture operations. Simulations were performed for both single well and multiple parallel wells. It was found that facture spacing as well as the boundary conditions of the previous created fractures affects the fracture geometry. Kumar and Ghassemi (2016) studied the 3D hydraulic fracturing in conventional zipper manner and in modified zipper manner based

on DD. The conventional zipper manner tended to generate relatively straight fractures. More complex fractures could be produced through the modified zipper manner. The effects of in-situ stress, rock and fluid properties, and "stress shadowing" were demonstrated. Numerical simulations of multistage hydraulic fracturing in a permeable porous medium were performed by Kumar and Ghassemi (2018). The results indicated that the mechanical interactions between fractures strongly influence the created fracture network geometries; the poroeleastic effects cause the increase of the net fracture pressure and the decrease of the fracture volume.

In BEM, only the boundaries and discontinuities, which could be treated as interior boundaries, are discretized. The computation time could be tremendously less than that required by domain mesh-based methods, since the generated matrix in BEM is much smaller than those generated by discretizing the whole domain of interest. However, BEM is mostly limited to homogeneous reservoirs so that for complex geology the finite element method (FEM) is a strong alternative since it can handle complex geometry, nonlinear deformation, and multiphysics coupling, albeit at the cost of larger of computation efforts and complexities in simulation of facture propagation.

As we know, hydraulic fracture propagation involves moving boundaries. When FEM is used to discretize both the fracture and the surrounding rock, a large number of elements are utilized. How to incorporate the moving fracture front into FEM mesh, especially in 3D, is a major challenge when the FEM is used. Different approaches are adopted to handle the mesh for fracture propagation. A commonly used one is to pre-define the propagation path by using symmetric initial and boundary conditions. As an effective way to simulate fracture initiation and propagation, cohesive zone model (CZM) is also utilized to simulate hydraulic fracturing. CZM assumes the existence of a fracture process zone (where the rock has yielded or experienced

micro-cracking) in front of the crack tip. The mechanical behaviors of CZM are governed by a traction-separation law. Boone and Ingraffea (1990) proposed a numerical procedure based on CZM to model a 2D hydraulic fracturing in a poroelastic medium. Finite difference method was utilized to discretize the equation for fluid flow in fractures. The mechanical deformation for the porous medium and the fluid flow in the hydraulic fracture were solved in a sequential manner. Papanastasiou (1999a) and Papanastasiou (1999b) studied the influence of plastic deformation on hydraulic fracturing based on CZM. The high net injection pressure that is often encountered in field operations was explained through the non-linear deformation of rock. Chen et al. (2009) simulated the toughness-dominated hydraulic fracture propagation by using a pore pressure cohesive finite element. The effects of cohesive material parameters and fluid viscosity on the behaviors of hydraulic fractures were analyzed. Utilizing CZM, Chen (2012) modeled the propagation of hydraulic fractures in the viscosity-dominated regime. Hydraulic fracturing in a poroelastic medium was studied by Carrier and Granet (2012) based on CZM. Toughness/viscosity- and leak-off/storage- dominated regimes were simulated.

For hydraulic fractures under mixed model loading and curving in arbitrary directions, adaptive re-meshing technique is usually needed. Paluszny and Zimmerman (2011) studied the curved fractures through the re-mesh technique. As an alternative way to model fracturing curving, the extended finite element method (XFEM) is developed to minimize the requirement of re-mesh. Paul et al. (2018) developed a 3D coupled hydro-mechanical XFEM model. Non-planar hydraulic fracture propagation was simulated. The interference between multiple hydraulic fractures was demonstrated. In addition to mesh-related operations, constitutive models are also developed to simulate the failure processes during fracture propagation using traditional finite element types, such as 4-node tetrahedron, 8-node hexahedron elements. Min et al. (2010)

studied the usage of virtual multidimensional internal bonds (VMIB) to analyze multiple fracture propagation in heterogeneous rock. Huang et al. (2013) modeled 3D hydraulic fracture propagating using the method of VMIB.

When performing hydraulic fracturing, the geometry of hydraulic fractures (e.g. fracture height and length) is largely determined by in-situ geological conditions, which often exhibit complex rock properties and in-situ stress. Simplified geological conditions are often assumed partly due to the complexity of the coupled hydro-mechanical processes if heterogeneous distributions of rock properties and in-situ stress are all considered. In many studies, the layered formation properties are not modeled explicitly in hydraulic fracturing. Instead, an average value (e.g. thickness weighted average) is usually adopted for each layered property (e.g. Young's modulus). As pointed out by Smith et al. (2001), the thickness weighted average (effective modulus) is purely a mathematical treatment and does not consider the mechanical effects. In reservoir formations with layered in-situ stress, the in-situ stress contrast could be the most important factor that directly controls the height growth of hydraulic fractures. To simplify analyses, static step-wise pressurization is often used in approximately calculating fracture height. A constant pressure is applied on the whole fracture surface and is adjusted through trial-and-error to satisfy a critical equilibrium state. The so-called equilibrium height model was first proposed by Simonson et al. (1978). The variation of fracture width and fluid pressure within hydraulic fractures are not considered in this kind of static model.

1.2.2 Coupled analysis of fluid flow, heat transport and geomechanics

Fluid flow in geothermal reservoirs usually is dominated by high permeable discontinuities (such as natural fractures, joints and faults). One of the main purposes of hydraulic stimulation is to create new fractures with high fluid conductivity or to enhance the

fluid conductivity of pre-existing fractures. The opening, closing, sliding of fractures and the associated fracture conductivity evolution are related to the coupling of mechanical, hydraulic, and/or chemical processes. They are also heavily influenced by heat transport processes in geothermal reservoirs. The coupled thermo-hydro-mechanical behaviors of fractured rock are studied extensively in both laboratory experiments and field applications.

Experimental study on hydro-mechanical behaviors is usually conducted through uniaxial normal compression tests, biaxial compression/shear tests. Many tests were performed to investigate the relationships among hydraulic aperture, mechanical aperture and effective normal stress (Rutqvist and Stephansson 2003). The size effect on fracture normal closure was observed in experiments (Yoshinaka et al. 1991). It was shown that the maximum closure increases with sample size. Based on laboratory experiments, validation of the commonly used "cubic law" (Witherspoon et al. 1980) for fluid flow in fractures was performed (Boitnott 1991). It was found the cubic law works for a wide variety of fractures.

The in-situ tests on hydro-mechanical behaviors of fractured rock were performed in lots of projects and by lots of researchers. Jung (1989) conducted in-situ experiments to study turbulent friction losses in the vicinity of an injection and a production borehole and to investigate the hydro-mechanical behaviors of a fracture. The friction pressure losses in the fracture were recorded under different injection rates. The theory of laminar and turbulent flow was utilized to explain the observed relationship between friction pressure losses and flow rates. The behaviors of hydraulic aperture and mechanical aperture were recorded and analyzed. During the development of Fenton Hill HDR geothermal reservoir, a number of in-situ experiments were conducted and recorded (Brown et al. 2012). In the beginning of this project, fluid injection was intended for creating fresh hydraulic fractures which would be penny-shaped

and vertical. After a few years of development, it was gradually realized that hydraulic fracturing at Fenton Hill was not actually breaking open intact crystalline rock; instead, pre-existing, sealed joints were being opened.

There are mainly two kinds of numerical approaches to handle the coupled thermo-hydro-mechanical processes in fractured porous rock. One is based on boundary element method (BEM), which uses integral equation representations of the governing partial differential equations to solve problems of interest (Ghassemi et al. 2013). The second type of numerical approach is domain mesh-based, such as finite element method, finite volume method and discrete element method. The entire spatial domain of interest needs to be discretized when these methods are adopted.

1.3 Research objectives

Through literature review, it is found that CZM is widely used in simulating fracture propagation, especially for mix mode fractures. However, most of studies utilizing CZM to simulate hydraulic fracturing are in 2D. A 3D fully coupled hydro-mechanical model is rarely found to be verified through asymptotic analytical solutions for hydraulic fracturing. At the same time, the coupled mechanical, hydraulic and thermal processes associated with fluid flow and heat transport through fractures are of vital importance in analyzing the behaviors of fractured rock. The impacts of transportation of fluid and heat from fractures to the surrounding rock matrix in a fracture/rock system are not fully understood.

The main purpose of this dissertation is to study the thermo-hydro-mechanical behaviors due to fluid injection into fractured porous media. Emphasis is focused on the coupled hydro-mechanical processes involved in hydraulic fracture propagation, thermal circulation in pre-existing fractures, and reactivation of joints due to fluid injection.

Specifically, the main objectives include:

(1) Develop a parallel computation framework which is suitable for simulating coupled thermo-hydro-mechanical problems;

(2) Develop a 3D fully coupled thermo-hydro-mechanical model for simulating fractured reservoir rock;

(3) Develop thermo-hydro-mechanical interface element that is capable to model the behaviors of discontinuities, such as fresh created fractures, pre-existing fractures, and joints;

(4) Analyze the pore pressure and stress distribution around hydraulic fractures during fluid injection in homogeneous and heterogeneous porous media;

(5) Simulate and analyze the hydro-mechanical responses of a joint during hydraulic stimulation in Fenton Hill HDR geothermal reservoir.

1.4 Dissertation outline

Chapter 1 states the motivation and research objectives of this dissertation. Literature review is performed.

Chapter 2 develops and analyzes a hydro-mechanical interface element, which is built based on cohesive zone model (CZM). The model is verified through the penny-shaped hydraulic fracture and the KGD hydraulic fracture (in 3D domain) propagating in both viscosity- and toughness-dominated regimes. Impacts of some key CZM parameters and the size of cohesive interface elements on hydraulic fracturing are analyzed.

Chapter 3 studies the height growth of hydraulic fractures in layered formations. The model presented in Chapter 2 is validated through a laboratory experiment. The influence of Young's module contrast, stress contrast and formation ductility on height growth are analyzed.

Chapter 4 analyzes the interaction between hydraulic fractures and discontinuities. The numerical model is evaluated through a commonly used crossing/arrest criterion. Laboratory tests on fracture-discontinuity interaction are also modeled. The combined effects of material properties, in-situ stress and the existence of discontinuities are investigated.

Chapter 5 describes a 3D fully coupled thermo-hydro-mechanical (THM) model. The finite element formulations are presented. Hydraulic fracture initiation and propagation are studied. Some typical coupled THM processes are analyzed. A lab-scale geothermal system is model.

Chapter 6 studies pore pressure and stress distributions around a hydraulic fracture in both homogeneous and heterogeneous porous rock. The reasons for nonuniform distribution of stresses in heterogeneous rock are investigated.

Chapter 7 simulates the reactivation of a joint during hydraulic stimulation in Fenton Hill HDR geothermal reservoir. The effects of joint stiffness on fluid flow back after injection are studied.

In the last chapter, Chapter 8, a summary of this dissertation is conducted; some recommendations are given for future research.

References

Adachi, J. I. and Detournay, E. 2002. Self-similar solution of a plane-strain fracture driven by a power-law fluid. *International Journal for Numerical and Analytical Methods in Geomechanics* **26** (6): 579-604. http://dx.doi.org/10.1002/nag.213.

Adachi, J. I. and Detournay, E. 2008. Plane strain propagation of a hydraulic fracture in a permeable rock. *Engineering Fracture Mechanics* **75** (16): 4666-4694. http://dx.doi.org/10.1016/j.engfracmech.2008.04.006.

Barenblatt, G. I. 1962. The Mathematical Theory of Equilibrium Cracks in Brittle Fracture. In *Advances in applied mechanics*, ed. Th von Kármán G. Kuerti F. H. van den Dungen H.L. Dryden and L. Howarth, 55-129. Elsevier.

Boitnott, G. 1991. Mechanical and transport properties of joints PhD Thesis, Columbia University, New York.

Boone, T. J. and Ingraffea, A. R. 1990. A numerical procedure for simulation of hydraulically-driven fracture propagation in poroelastic media. *International Journal for Numerical and Analytical Methods in Geomechanics* **14** (1): 27-47. http://dx.doi.org/10.1002/nag.1610140103.

Brown, D. W., Duchane, D. V., Heiken, G. et al. 2012. *Mining the earth's heat: hot dry rock geothermal energy*. Heidelberg: Springer Science & Business Media.

Carrier, B. and Granet, S. 2012. Numerical modeling of hydraulic fracture problem in permeable medium using cohesive zone model. *Engineering Fracture Mechanics* **79**: 312-328. http://dx.doi.org/10.1016/j.engfracmech.2011.11.012.

Chen, Z. 2012. Finite element modelling of viscosity-dominated hydraulic fractures. *Journal of Petroleum Science and Engineering* **88–89**: 136-144. http://dx.doi.org/10.1016/j.petrol.2011.12.021.

Chen, Z., Bunger, A. P., Zhang, X. et al. 2009. Cohesive zone finite element-based modeling of hydraulic fractures. *Acta Mechanica Solida Sinica* **22** (5): 443-452. http://dx.doi.org/10.1016/S0894-9166(09)60295-0.

Garagash, D. and Detournay, E. 1999. The tip region of a fluid-driven fracture in an elastic medium. *Journal of applied mechanics* **67** (1): 183-192. http://dx.doi.org/10.1115/1.321162.

Desroches, J., Detournay, E., Lenoach, B. et al. 1994. The Crack Tip Region in Hydraulic Fracturing. *Proceedings: Mathematical and Physical Sciences* **447** (1929): 39-48. http://dx.doi.org/10.2307/52430.

Geertsma, J. and De Klerk, F. 1969. A Rapid Method of Predicting Width and Extent of Hydraulically Induced Fractures. *Journal of Petroleum Technology* **21** (12): 1571-1581. http://dx.doi.org/10.2118/2458-pa.

Geertsma, J. and Haafkens, R. 1979. A Comparison of the Theories for Predicting Width and Extent of Vertical Hydraulically Induced Fractures. *Journal of energy resources technology* **101** (1): 8-19. http://dx.doi.org/10.1115/1.3446866.

Ghassemi, A. 2012. A Review of Some Rock Mechanics Issues in Geothermal Reservoir Development. *Geotechnical and Geological Engineering* **30** (3): 647-664. http://dx.doi.org/10.1007/s10706-012-9508-3.

Ghassemi, A., Zhou, X. X. and Rawal, C. 2013. A three-dimensional poroelastic analysis of rock failure around a hydraulic fracture. *Journal of Petroleum Science and Engineering* **108**: 118-127. http://dx.doi.org/10.1016/j.petrol.2013.06.005.

Hu, L. and Ghassemi, A. 2017. Experimental Investigation of Hydraulically Induced Fracture Properties in Enhanced Geothermal Reservoir Stimulation. Paper presented at the 42nd Workshop on Geothermal Reservoir Engineering, Stanford, California, 13-15 February 2017.

Huang, K., Zhang, Z. and Ghassemi, A. 2013. Modeling three-dimensional hydraulic fracture propagation using virtual multidimensional internal bonds. *International Journal for Numerical and Analytical Methods in Geomechanics* **37** (13): 2021-2038. http://dx.doi.org/10.1002/nag.2119.

Jeffrey, R. G. and Bunger, A. 2009. A Detailed Comparison of Experimental and Numerical Data on Hydraulic Fracture Height Growth Through Stress Contrasts. *SPE Journal* **14** (03): 413-422. http://dx.doi.org/10.2118/106030-pa.

Jung, R. 1989. Hydraulic in situ investigations of an artificial fracture in the Falkenberg granite. *International Journal of Rock Mechanics and Mining Sciences & Geomechanics Abstracts* **26** (3): 301-308. http://dx.doi.org/10.1016/0148-9062(89)91978-5.

Khristianovic, S. A. and Zheltov, Y. P. 1955. Formation of Vertical Fractures by Means of Highly Viscous Liquid. Paper presented at the 4th World Petroleum Congress, Rome, Italy, 1955/1/1/.

Kumar, D. and Ghassemi, A. 2016. A three-dimensional analysis of simultaneous and sequential fracturing of horizontal wells. *Journal of Petroleum Science and Engineering* **146** (Supplement C): 1006-1025. http://dx.doi.org/10.1016/j.petrol.2016.07.001.

Kumar, D. and Ghassemi, A. 2018. Three-Dimensional Poroelastic Modeling of Multiple Hydraulic Fracture Propagation from Horizontal Wells. *International Journal of Rock Mechanics and Mining Sciences* **105**: 192-209. http://dx.doi.org/10.1016/j.ijrmms.2018.01.010.

Min, K. S., Z.Zhang and A.Ghassemi. 2010. Numerical Analysis of Multiple Fracture Propagation In Heterogeneous Rock. Paper ARMA-10-363 presented at the, 27-30 June 2010.

Nordgren, R. P. 1972. Propagation of a Vertical Hydraulic Fracture. *SPE Journal* **12** (04): 306-314. http://dx.doi.org/10.2118/3009-pa.

Paluszny, A. and Zimmerman, R. W. 2011. Numerical simulation of multiple 3D fracture propagation using arbitrary meshes. *Computer methods in applied mechanics and engineering* **200** (9): 953-966. http://dx.doi.org/10.1016/j.cma.2010.11.013.

Papanastasiou, P. 1999a. The Effective Fracture Toughness in Hydraulic Fracturing. *International journal of fracture* **96** (2): 127. http://dx.doi.org/10.1023/a:1018676212444.

Papanastasiou, P. 1999b. An efficient algorithm for propagating fluid-driven fractures. *Computational Mechanics* **24** (4): 258-267. http://dx.doi.org/10.1007/s004660050514.

Paul, B., Faivre, M., Massin, P. et al. 2018. 3D coupled HM–XFEM modeling with cohesive zone model and applications to non planar hydraulic fracture propagation and multiple hydraulic fractures interference. *Computer methods in applied mechanics and engineering* **342**: 321-353. http://dx.doi.org/10.1016/j.cma.2018.08.009.

Rutqvist, J. and Stephansson, O. 2003. The role of hydromechanical coupling in fractured rock engineering. *Hydrogeology Journal* **11** (1): 7-40. http://dx.doi.org/10.1007/s10040-002-0241-5.

Savitski, A. A. and Detournay, E. 2002. Propagation of a penny-shaped fluid-driven fracture in an impermeable rock: asymptotic solutions. *International Journal of Solids and Structures* **39** (26): 6311-6337. http://dx.doi.org/10.1016/S0020-7683(02)00492-4.

Sesetty, V. and Ghassemi, A. 2015. A numerical study of sequential and simultaneous hydraulic fracturing in single and multi-lateral horizontal wells. *Journal of Petroleum Science and Engineering* **132**: 65-76. http://dx.doi.org/10.1016/j.petrol.2015.04.020.

Simonson, E. R., Abou-Sayed, A. S. and Clifton, R. J. 1978. Containment of Massive Hydraulic Fractures. *SPE Journal*: 27-32. http://dx.doi.org/10.2118/6089-pa.

Smith, M. B., Bale, A. B., Britt, L. K. et al. 2001. Layered Modulus Effects on Fracture Propagation, Proppant Placement, and Fracture Modeling. Paper presented at the SPE Annual Technical Conference and Exhibition, New Orleans, Louisiana, 2001/1/1/. http://dx.doi.org/10.2118/71654-ms.

Spence, D. A. and Sharp, P. 1985. Self-Similar Solutions for Elastohydrodynamic Cavity Flow. *Proceedings of the Royal Society of London. A. Mathematical and Physical Sciences* **400** (1819): 289.

Spence, D. A. and Turcotte, D. L. 1985. Magma-driven propagation of cracks. *Journal of Geophysical Research: Solid Earth* **90** (B1): 575-580. http://dx.doi.org/10.1029/JB090iB01p00575.

The, S. C. R. G. G. 1993. On the modelling of near tip processes in hydraulic fractures. *International Journal of Rock Mechanics and Mining Sciences & Geomechanics Abstracts* **30** (7): 1127-1134. http://dx.doi.org/10.1016/0148-9062(93)90082-O.

Vandamme, L. and Curran, J. H. 1989. A three-dimensional hydraulic fracturing simulator. *International Journal for Numerical Methods in Engineering* **28** (4): 909-927. http://dx.doi.org/10.1002/nme.1620280413.

Witherspoon, P. A., Wang, J. S. Y., Iwai, K. et al. 1980. Validity of Cubic Law for fluid flow in a deformable rock fracture. *Water Resources Research* **16** (6): 1016-1024. http://dx.doi.org/10.1029/WR016i006p01016.

Wu, R., Bunger, A. P., Jeffrey, R. G. et al. 2008. A comparison of numerical and experimental results of hydraulic fracture growth into a zone of lower confining stress. Paper presented at the The 42nd U.S. Rock Mechanics Symposium (USRMS), San Francisco, California, June 29 - July 2.

Yoshinaka, R., Yoshida, J., Shimizu, T. et al. 1991. Scale Effect In Shear Strength And Deformability of Rock Joints. Paper presented at the 7th ISRM Congress, Aachen, Germany, 1991/1/1/.

2 3D planar hydraulic fracture propagation in an elastic medium: formulation and verification

Abstract

In this study, we develop and use a 3D fully coupled hydro-mechanical model to simulate hydraulic fracturing. The hydraulic fracturing simulator is developed based on the finite element method utilizing a parallel computation framework. A special zero-thickness interface element based on the cohesive zone model (CZM) is developed for modeling fracture propagation and fluid flow in the created hydraulic fracture. A standard local traction-separation law with strain-softening is used to capture the main characteristics of tensile cracking. The commonly used cubic law is adopted to describe the fluid flow in fractures. In this study we verify the 3D model by considering a penny-shaped hydraulic fracture and a KGD hydraulic fracture (in 3D domain) propagating in both the viscosity- and the toughness-dominated regimes. Good agreement between numerical results and asymptotic analytical solutions has been achieved with respect to fluid pressure, fracture height, length and width distributions. The model is then used to investigate the influence of rock and fluid properties on hydraulic fracturing via sensitivity analyses. Lower stiffness cohesive elements tend to yield a larger elastic deformation around the fracture tips before the tensile strength is reached. It generates a larger fracture length and lower fluid pressure in fracture when compared with those using higher stiffness. It is also found that the energy release rate has almost no influence on hydraulic fracturing in the viscosity-dominated regime since the energy spent on creating new fractures is too small when compared to the total input energy. For the toughness-dominated regime, the released energy during fracturing should be accurately captured. It requires smaller elements when compared with those used in the viscosity-dominated regime. To obtain stable and accurate results from a cohesive

zone model, certain number of elements should be contained within the cohesive zone ahead of the crack tips which is a function of the energy release rate and the tensile strength. According to our numerical experience, it is recommended that at least 5 interface elements should be contained within the cohesive zone in order to get stable and accurate numerical results.

2.1 Introduction

Hydraulic fracturing is a technique used to enhance reservoir production in the petroleum industry and/or in the development of a geothermal reservoir. For ultralow-permeability shale reservoirs now being regularly exploited, hydraulic treatment is essential to obtain an economic level of production. Hydraulic fracturing involves complex processes and has been the subject of significant research efforts. During the last few decades, both analytical and numerical methods have been proposed to solve problems in hydraulic fracturing. The well-known 2D plane strain PKN and KGD models, and the axisymmetric penny-shaped model were developed in the 1960s (Khristianovich and Zheltov 1955; Perkins and Kern 1961; Geertsma and De Klerk 1969). Due to the geometric limitations of the analytical models, numerical models are developed and applied to simulate the propagation of hydraulic fractures in more complex and realistic geometries. Although significant progress has been achieved in developing 2D and 3D numerical hydraulic fracture models, it is still a challenging task to solve the strongly coupled hydro-mechanical problems particularly in unconventional reservoirs (Huang et al. 2013; Sesetty and Ghassemi 2015; Kumar and Ghassemi 2016).

When considering failure of rock, it is often observed that most rocks are not perfectly brittle in the Griffith sense, but exhibit some ductility during the post-peak deformation (de Borst 2003; Huang and Ghassemi 2017). This behavior has led to the concept of cohesive zone and cohesive zone models for fracture propagation. The cohesive zone model was introduced by

Barenblatt (1962) and Dugdale (1960) for analyzing elastic-plastic fracture in ductile metals, and by Hillerborg et al. (1976) for simulating fracture and fragmentation processes in quasi-brittle materials, such as concrete, rock, ceramics. Instead of using the classic linear elastic fracture mechanics (LEFM) to deal with an elastic crack tip region where stress singularity exists, the cohesive zone model assumes the existence of a fracture process zone (where the rock has yielded or experienced micro-cracking) in front of the material crack tip (Figure 1), which is governed by a traction-separation law. The stress singularity at the crack tip is avoided in cohesive zone models through this constitutive law. In this way, the cohesive zone model provides an alternative approach to explicitly simulate fracture processes near the tip, and is often applied in modeling hydraulic fracturing. Chen et al. (2009) and Chen (2012) applied a cohesive zone based finite element method (2D) to study a toughness dominated penny-shaped hydraulic fracture and the propagation of hydraulic fractures in a viscosity-dominated regime. Based on a 2D plane strain finite element framework, Carrier and Granet (2012) simulated the four limiting propagation regimes (toughness-fracture storage, toughness-leak-off, viscosity-fracture storage, and viscosity-leak-off dominated) utilizing a cohesive zone model. The influence of cohesive process zone on hydraulic fracturing was investigated by Sarris and Papanastasiou (2011), they found that higher interface stiffness generates lower injection pressure; the exact shape of the post-peak softening stage on the traction-separation curve has almost no influences on results.

In this study, a 3D fully coupled interface element utilizing cohesive zone model is developed to analyze hydro-mechanical processes involved in hydraulic fracturing. We first give the governing equations and their corresponding finite element discretization. Then, the proposed model is verified through numerical examples. Sensitivity analyses are performed to investigate

the influence of input parameters on hydraulic fracturing. The influence of interface element size on the behaviors of the numerical model is also analyzed.

2.2 Governing equations

The basic equations governing a hydraulic fracturing model are (1) the rock constitutive equations; (2) the fracture fluid flow equation; (3) the fracture propagation condition and (4) the fluid leak-off from the fracture into the reservoir rock. The fracture initiation and propagation in reservoir rocks are natural outcomes of a cohesive zone model. In this work, the cohesive damage zone is permeable and filled with the fracturing fluid with zero lag. We do not consider the leak-off and poroelastic effects (e.g., Kumar and Ghassemi 2018; Gao and Ghassemi 2017; Cheng 2016, Safari and Ghassemi, 2016) considering the very low permeability of unconventional petroleum and geothermal reservoirs.

2.2.1 The cohesive law

There are numerous researches on using the cohesive zone model to simulate fracture propagation. The technique has attracted considerable attention due to its efficient and powerful algorithms to describe the behaviors of both fracture initiation and propagation (Boone et al. 1986). Interface damage initiates when the traction (normal, shear or combined normal and shear) on a pair of cohesive surfaces reaches the strength of the interface. Once a fracture has initiated, it propagates when the energy release rate reaches a critical value G_{IC}, which is related to fracture toughness for the case of small-scale yielding (Irwin 1957). The cohesive zone ahead of the crack tip is characterized by micro-cracking along the crack path. Conceptually, when the micro-cracks have coalesced with each other, a main fracture is formed. In the CZM concept, there are several ‘crack tips’ (Shet and Chandra 2002), as illustrated in Figure 2.1. The mathematical crack tip refers to a point which is yet to separate. The cohesive crack tip

corresponds to a point where the separation stress has reached the cohesive strength. The material crack tip is where complete failure has occurred and the cohesive traction decreases to zero. It is assumed that the rock deformation in the cohesive zone ahead of material crack tip has of an elastic part and an inelastic softening part. This behavior is similar to the softening stress-displacement relation that exhibits by various quasi-brittle materials, such as rock.

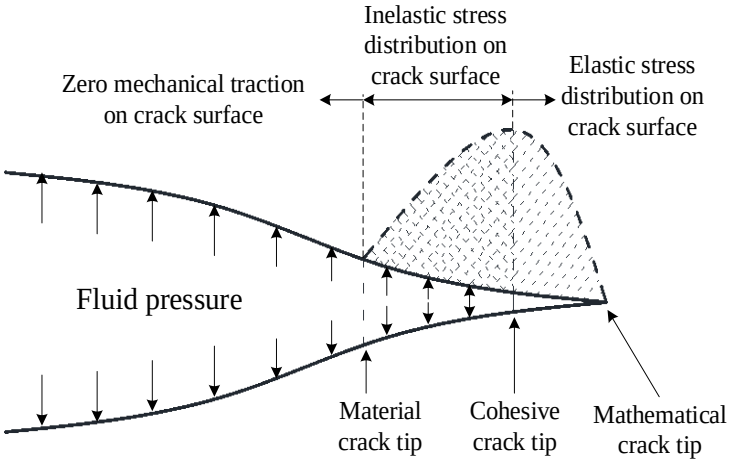

Figure 2.1 Cohesive process zone and fluid pressure distribution in a cohesive zone model.

Since the cohesive zone is filled with liquid at pressure p_f, similarly to the theory of poroelasticity, the effective stress ($\boldsymbol{T}'$) is introduced and is related to the total stress ($\boldsymbol{T}$) and fluid pressure (p_f) through the following equation (tension is considered positive):

$$\boldsymbol{T} = \boldsymbol{T}' - p_f \boldsymbol{n} \tag{2.1}$$

where $\boldsymbol{n}$ is the normal of the cohesive zone interface. When the cohesive zone is completely damaged, the cohesive traction ($\boldsymbol{T}'$) is zero and the fluid pressure (p_f) is acting as traction on the open fracture surfaces.

The stress singularity in linear elastic fracture mechanics is eliminated in the cohesive zone model by considering a nonlinear fracture process zone in front of the crack tip. The relationship between the traction ($\boldsymbol{T}'$) and the displacement jump ($\boldsymbol{\Delta}$) across a cohesive interface is defined by a cohesive law, which is defined through a potential function ($\boldsymbol{\psi}$):

$$\boldsymbol{T}' = \frac{\partial \psi}{\partial \boldsymbol{\Delta}} \tag{2.2}$$

The "PPR" potential-based traction-separation law (Park and Paulino 2012; Spring and Paulino 2014) is adopted in this study, which is shown in Figure 2.2. Four deformation stages exist in the cohesive crack propagation. They are elastic deformation, crack initiation, softening deformation and complete failure. Before reaching the maximum cohesive strength (T_{max}), the law exhibits reversible elastic behaviors. After the peak strength, the traction gradually reduces to zero (Park and Paulino 2012). The area under the pure normal traction-separation curve represents the fracture energy G_{IC} in the normal direction:

$$G_{IC} = \int_0^{\delta_n} T_n(\Delta_n) d\Delta_n \tag{2.3}$$

where δ_n is the final normal opening width between two fracture surfaces. The fracture energy G_{IC} is an independent input parameter to the model. When the size of cohesive zone is much smaller than the fracture length, the cohesive energy (G_{IC}) can be related to the fracture toughness in mode-I (K_{IC}) in LEFM through Irwin's formula (Irwin 1957):

$$G_{IC} = \frac{K_{IC}^2}{E}\left(1-\upsilon^2\right) \tag{2.4}$$

where E is Young's modulus and υ the Poisson's ratio.

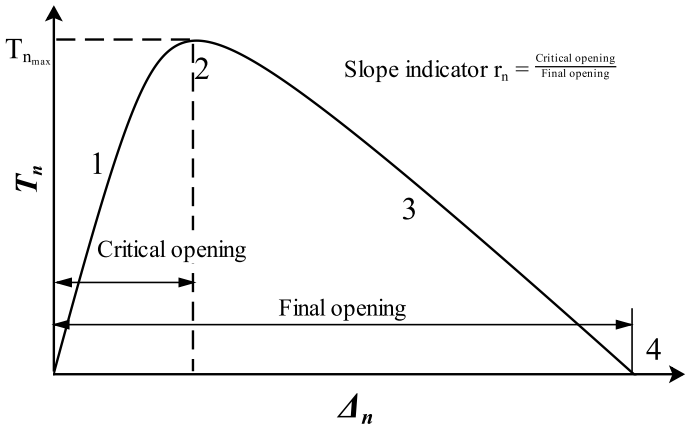

Figure 2.2 Normalized traction-separation law for the cohesive elements: 1 elastic deformation; 2 crack initiation; 3 softening deformation; 4 complete failure.

2.2.2 Fluid flow in hydraulic fracture

The fracturing fluid is assumed to be incompressible, linear (Newtonian) viscous fluid. From mass conservation in the fracture, the fluid mass balance equation is formulated as:

$$\frac{\partial w}{\partial t} + \nabla \cdot \boldsymbol{q} = Q(t) \tag{2.5}$$

where w is the local fracture width, which is equal to the displacement jump (Δ_n) in the normal direction of a fracture surface, $\boldsymbol{q}$ is the fluid flux of the longitudinal flow, and $Q(t)$ is the injection rate.

The longitudinal flow within the fracture is derived from conservation of momentum. For fluid flow between parallel plates, the lubrication equation is written

$$\boldsymbol{q} = \boldsymbol{v}w = -\frac{w^3}{12\mu}\nabla p_f \tag{2.6}$$

where $\boldsymbol{v}$ is the average fluid velocity, μ is the viscosity of the Newtonian fluid. The above equation is commonly called cubic law (Witherspoon et al. 1980).

Combining equation (2.5) and (2.6), it is obtained:

$$\frac{\partial w}{\partial t} - \nabla \cdot \frac{w^3}{12\mu} \nabla p_f = Q(t) \tag{2.7}$$

The boundary conditions at the fracture tips are given as

$$\begin{aligned} w(x,t)\big|_{x=R} &= 0 \\ q(x,t)\big|_{x=R} &= 0 \end{aligned} \tag{2.8}$$

At the injection point, we have

$$q(x,t)\big|_{x=0} = Q(t) \tag{2.9}$$

2.3 Numerical implementation

The finite element method is adopted to implement the hydro-mechanical interface element. Spatial and temporal discretizations are performed separately using the standard Galerkin method and the finite difference method (θ method). The predicted hydraulic fracture path is represented by the cohesive interface elements, while the reservoir matrix is meshed through the traditional hexahedron elements.

2.3.1 Hydro-mechanical interface element

A triple-node interface element with zero thickness (Figure 2.3), on which the cohesive zone model is built, is developed to simulate the coupled hydro-mechanical behaviors. The hydro-mechanical interface element is isoparametric and quadrangular. As illustrated in Figure 2.3, it is composed of three layers of quadrilateral elements. Initially the three layers have zero thickness and are overlapped with each other. The top and bottom surfaces (1-2-3-4 and 5-6-7-8) represent the surfaces of a hydraulic fracture. Fluid filled in the hydraulic fracture flows along the center plane (9-10-11-12) and is governed by the lubrication equation (Eq. (2.7)). Each of nodes 1 ~ 8 has three degrees of freedom for displacements (u_x, u_y, u_z); each of nodes 9 ~ 12 has one degree of freedom for fluid pressure (p_f) in the hydraulic fracture. We assume the pore

pressure on fracture surfaces equals to the fluid pressure in hydraulic fracture with aperture Δ_n. This assumption could be made for freshly created hydraulic fractures on which no mud cake has been built yet. To summarize, the mechanical and hydraulic degrees of freedom are written in vectors at each node as

$$\begin{aligned} \boldsymbol{u} &= \left[u_x, u_y, u_z \right] \text{ for nodes 1~8} \\ \boldsymbol{p_f} &= \left[p_f \right] \text{ for nodes 9~12} \end{aligned} \tag{2.10}$$

Propagation of hydraulic fracture generates two fracture surfaces (1-2-3-4 and 5-6-7-8), the propagation of which is governed by the cohesive law (Eq. (2.2)). The opening between the two surfaces is filled with injected fluid. Lubrication equation (Eq. (2.7)) is used to describe the fluid flow within the hydraulic fracture and is discretized on the center plane (9-10-11-12). As an example, Figure 2.4 shows the deformation of hydro-mechanical interface elements after fluid injection. The interface elements are linked to and bounded by conventional elastic continuum elements.

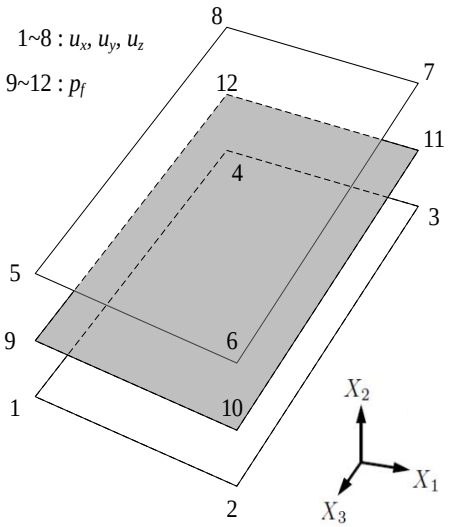

Figure 2.3 12-node hydro-mechanical interface element. Nodes 1 ~ 8 have degrees of freedom for displacement; nodes 9 ~ 12 have degrees of freedom for fluid pressure in hydraulic fractures. Initially the three layers have zero thickness and are overlapped with each other in numerical models. Here they are separated for visualization purpose.

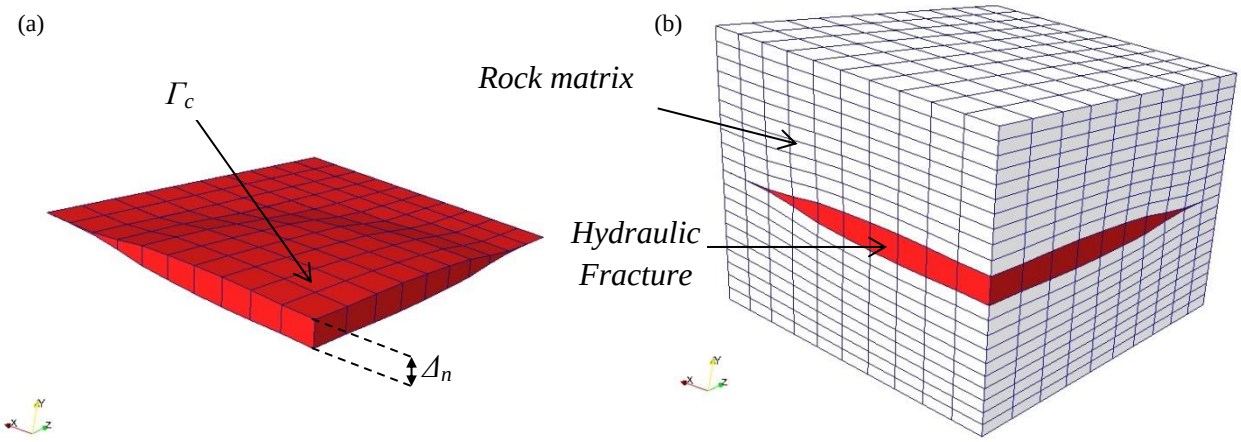

Figure 2.4 (a) Deformation of 12-node hydro-mechanical interface elements after fluid injection; (b) The hydro-mechanical interface elements are linked to and bounded by conventional elastic elements.

2.3.2 Finite element formulation

Based on the principle of virtual work, the weak form of the governing equations is obtained (Carrier and Granet 2012):

$$\int_{\Omega} \delta\boldsymbol{\varepsilon} : \boldsymbol{\sigma} \mathrm{d}\Omega + \int_{\Gamma} \delta\boldsymbol{\Delta} \cdot \left(\boldsymbol{T_C}' - p_f \boldsymbol{n} \right) \mathrm{d}\Gamma = \int_{\partial\Omega} \delta\boldsymbol{u} \cdot \boldsymbol{T_{ext}} \mathrm{d}\Gamma \tag{2.11}$$

$$\int_{\Gamma} \delta p_f \frac{\partial w}{\partial t} \mathrm{d}\Gamma - \int_{\Gamma} \delta p_f \nabla \cdot \frac{w^3}{12\mu} \nabla p_f \mathrm{d}\Gamma = \int_{\Gamma} \delta p_f Q(t) \mathrm{d}\Gamma \tag{2.12}$$

A standard Galerkin finite element discretization procedure is used to discretize the above variational equations.

The displacement u_i, and fluid pressure in hydraulic fractures pf are discretized through spatial interpolation functions (trial functions) in the domain of interest and expressed as:

$$u_i^h = \boldsymbol{N}^u \boldsymbol{u_i}, \quad p_f^h = \boldsymbol{N}^{p_f} \boldsymbol{p_f} \tag{2.13}$$

where $\boldsymbol{N}^u$ and $\boldsymbol{N}^{pf}$ are displacement and fluid pressure shape functions, and $\boldsymbol{u_i}$ and $\boldsymbol{p_f}$ are corresponding unknown nodal values. The test functions are written in a similar manner:

$$\omega_{u_i}{}^h = \boldsymbol{N}^u \boldsymbol{\omega}_{\boldsymbol{u_i}}, \quad \omega_{p_f}{}^h = \boldsymbol{N}^{p_f} \boldsymbol{\omega}_{\boldsymbol{p_f}} \tag{2.14}$$

Using Eq. (2.13), the gradient and divergence of the unknown variables could be obtained and represented in the following format:

$$\begin{aligned} &\nabla \boldsymbol{u}^h = \nabla \boldsymbol{N}^u \boldsymbol{u} = \boldsymbol{B}^u \boldsymbol{u} \\ &\nabla \cdot \boldsymbol{u}^h = I^T \boldsymbol{B}^u \boldsymbol{u} \\ &\nabla\, p_f{}^h = \nabla \boldsymbol{N}^{p_f} \boldsymbol{p_f} = \boldsymbol{B}^{p_f} \boldsymbol{p_f} \\ &I = \begin{bmatrix} 1 & 1 & 1 & 0 & 0 & 0 \end{bmatrix}^T \\ &I_d = \begin{bmatrix} 1 & 0 & 0 \end{bmatrix}^T \end{aligned} \tag{2.15}$$

The local opening of hydraulic fracture surfaces (Δ_n) is related to the global nodal displacements (u_i) on the fracture surfaces and is given as

$$\Delta_n = I_d{}^T \boldsymbol{B}^c \boldsymbol{u} \tag{2.16}$$

Substituting the trial and test functions into Eqs. (2.11) and (2.12), invoking the arbitrariness of the test functions, we obtain the following residual equations:

$$\begin{aligned} R_U{}^{n+1} = &\int_{\Omega} \left(\boldsymbol{B}^u\right)^T \left(\boldsymbol{D}\boldsymbol{B}^u \boldsymbol{u}\right)^{n+1} \mathrm{d}\Omega + \int_{\Gamma_{tc}} \left(\boldsymbol{B}^c\right)^T \left(T'_n\right)^{n+1} \mathrm{d}\Gamma_{tc} - \int_{\Gamma_{tc}} \left(\boldsymbol{B}^c\right)^T I_d \boldsymbol{N}^p \left(\boldsymbol{p_f}\right)^{n+1} \mathrm{d}\Gamma_{tc} \\ &- \int_{\Omega} \left(\boldsymbol{N}^u\right)^T \boldsymbol{F}^{n+1} \mathrm{d}\Omega - \int_{\Gamma_t} \left(\boldsymbol{N}^u\right)^T \bar{\boldsymbol{t}}^{n+1} \mathrm{d}\Gamma_t = 0 \end{aligned} \tag{2.17}$$

$$\begin{aligned} R_{p_f}{}^{n+1} = &\int_{\Gamma_{tc}} \left(\boldsymbol{N}^{p_f}\right)^T \left(\frac{\left(\Delta_n\right)^{n+1} - \left(\Delta_n\right)^n}{\Delta t} \right) \mathrm{d}\Gamma_{tc} + \int_{\Gamma_{tc}} \left(\boldsymbol{B}^{p_f}\right)^T \frac{\left(\Delta_n\right)^3_{n+\theta}}{12\mu} \left(\boldsymbol{B}^{p_f} \boldsymbol{p_f}\right)^{n+\theta} \mathrm{d}\Gamma_{tc} \\ &- \int_{\Gamma_{tc}} \left(\boldsymbol{N}^{p_f}\right)^T Q(t)^{n+\theta} \mathrm{d}\Gamma_{tc} - \int_s \left(\boldsymbol{N}^{p_f}\right)^T \bar{q}_f{}^{n+\theta} \mathrm{d}s = 0 \end{aligned} \tag{2.18}$$

where $\theta = 0$, giving the "explicit" method; $\theta = 1/2$, giving the "Crank-Nicolson" method; $\theta = 1$, giving the "fully implicit" method.

The incremental solution at the k+1 iteration is determined as

$$\begin{bmatrix} \dfrac{\partial R_U}{\partial \boldsymbol{u}} & \dfrac{\partial R_U}{\partial \boldsymbol{p_f}} \\ \dfrac{\partial R_{p_f}}{\partial \boldsymbol{u}} & \dfrac{\partial R_{p_f}}{\partial \boldsymbol{p_f}} \end{bmatrix}_k \begin{pmatrix} \Delta U \\ \Delta p_f \end{pmatrix}_{k+1} = -\begin{pmatrix} R_U \\ R_{p_f} \end{pmatrix}_k \tag{2.19}$$

$$U_{n+1} = U_n + \Delta U$$

$$p_{f\,n+1} = p_{f\,n} + \Delta p_f$$

The above generated stiffness matrix is a function of fracture opening (Δ_n) which is an unknown variable and is updated using the value obtained in the previous iteration. Newton-Raphson iterative method is adopted to solve the nonlinear system equations for each time step. The unknowns for rock deformation (U) and fluid pressure (p_f) are solved simultaneously at each time step.

2.4 Parallel computing environment

Numerical simulations in petroleum or geothermal reservoir development usually involve models with very large degrees of freedom (DOFs). Millions of DOFs could easily be reached when we try to obtain accurate results. For 3D multi-physics and multi-scale problems at reservoir scale, e.g. 3D fracture propagation in elastic or poroelastic rocks, it is common to have multi-million DOFs in a model. To efficiently simulate problems at large scale, a 3D fully coupled thermo-hydro-mechanical simulator is developed using the finite element method through a parallel computation framework. The parallelism is implemented through MPI (Message Passing Interface). It is designed to run on distributed memory systems, like commodity clusters.

Domain decomposition is performed to split a whole finite element mesh into pieces (sub-domains) that have almost equal number of elements. They are then distributed to each processor. The stiffness matrix assembly and internal force calculation are performed at each

processor. The sub-domain contributions are assembled through the PETSc library (Balay et al. 2018) to form a system of equations for the whole domain of the original problem. Figure 2.5 illustrates the running procedures in a serial manner on each processor.

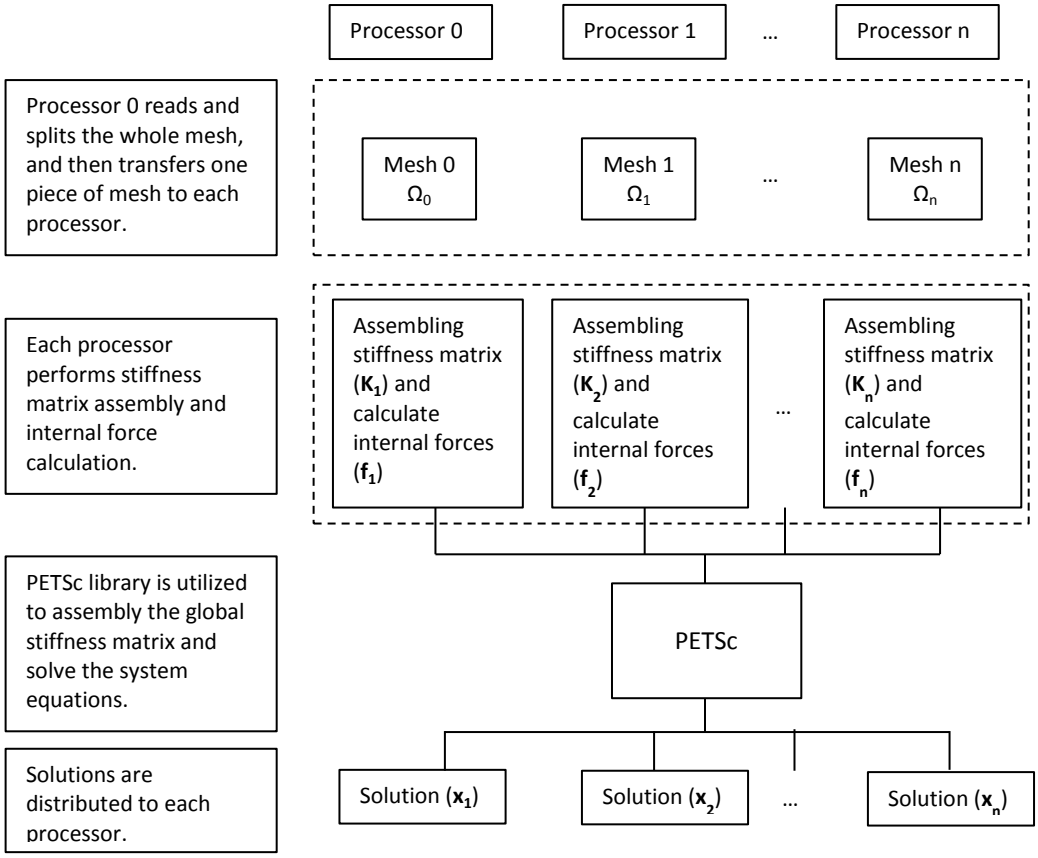

Figure 2.5 Running procedures on each processor in a serial manner.

The model in this work is developed to be flexible as possible. A series of element types are developed particularly for modeling coupled fluid flow and geomechanical problems. Each element type is encapsulated in a relatively independent class. They are mechanical element type (without DOFs for pore pressure and temperature), hydro-mechanical element type, thermo-hydro-mechanical element type, and interface element type. The interface elements can be used to simulate fluid flow and thermal transport in discontinuities. All of them are implemented in 3D. Currently we focus on hexahedron and brick interface elements though other types of

elements can be implemented into the simulator in a similar manner. Figure 2.6 shows all the element types available in the simulator. The material types are given in Figure 2.7. The code is designed to allow element types to be used solely or in a mix form. For example, we use 8-node mechanical hexahedron elements together with 12-node hydro-mechanical interface elements in this study.

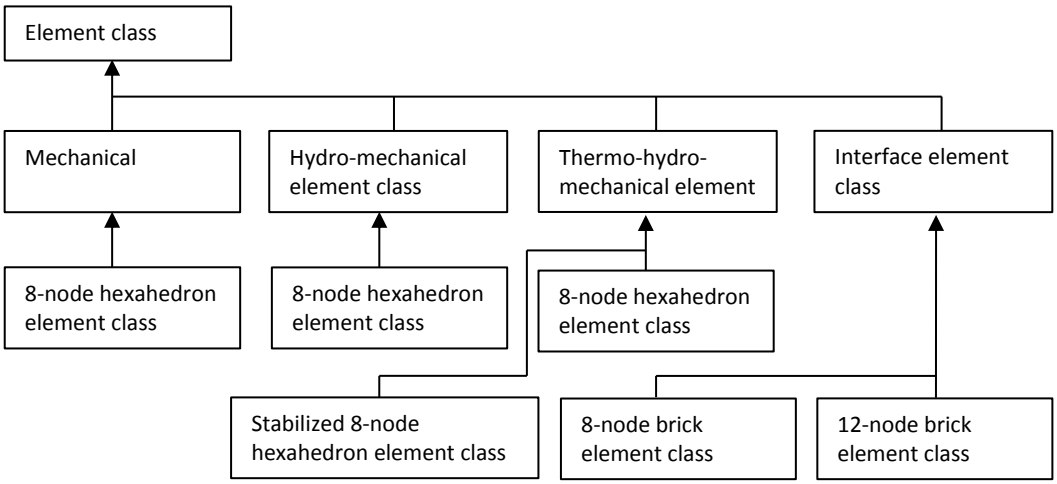

Figure 2.6 Diagram for element type class.

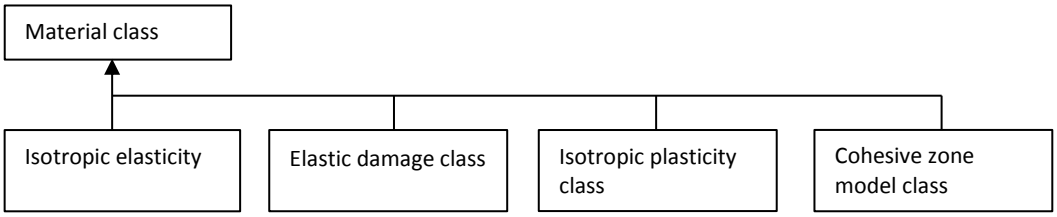

Figure 2.7 Diagram for material type class.

2.5 Model verification

2.5.1 Mode I test

In order to verify the mechanical behavior of the implemented cohesive zone model, the uniaxial tensile test (mode I test) is simulated. The geometry and mesh are shown in Figure 2.8. The mesh has one cohesive zone element and one 8-node hexahedron element. The cohesive

element has zero thickness. A thickness is added in Figure 2.8 for illustration purpose. The bottom surface of the cohesive element is fixed in vertical direction. Incremental displacements are applied on the top surface of the hexahedron element.

For the 8-node hexahedron element, the Young's modulus is 32 GPa, and the Poisson's ratio is 0.2. The fracture parameters for the cohesive zone element are: normal fracture energy (G_{IC}) = 100 N/m, normal cohesive strength (σ_{max}) = 30 MPa.

As shown in Figure 2.9, the force in the vertical direction (*z* direction) gradually increases up to the normal cohesive strength (30 MPa), and then it decreases close to zero during the softening stage.

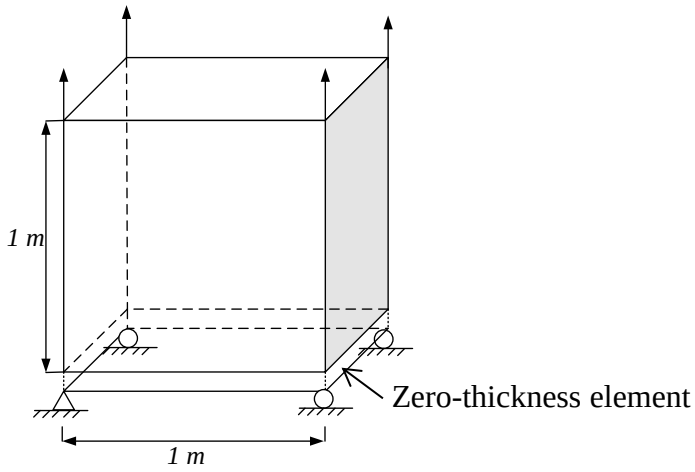

Figure 2.8 The mesh and boundary conditions used in the mode I test. The top element is 8-node hexahedron; the bottom one is zero-thickness cohesive element, a thickness is added to it for demonstration purpose.

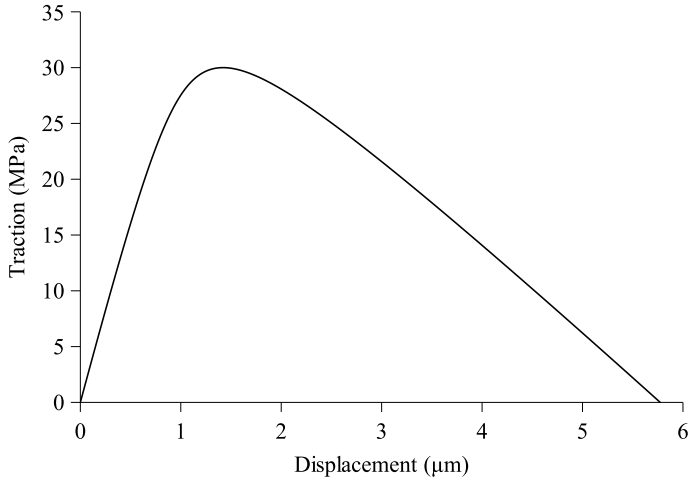

Figure 2.9 Traction-displacement curve for the mode I test.

2.5.2 Penny-shaped hydraulic fracture

The proposed 3D fully coupled hydro-mechanical cohesive model is utilized to simulate the viscosity-dominated hydraulic fracture propagation. Numerical results are compared with the asymptotic analytical solutions for a penny-shaped hydraulic fracture (Savitski and Detournay 2002). Both viscosity- and toughness-dominated propagation are considered. The assumed material parameters are given in Table 2.1. Fixed displacement boundaries are adopted. Figure 2.10 illustrates one quarter of the 3D model due to the symmetry of the boundaries with respect to the injection point. The model is discretized into 106×16×106 8-node hexahedral elements and 106×1×106 12-node hydro-mechanical cohesive interface elements. Hexahedron elements are used to discretize the bulk volume of rock matrix. For hydro-mechanical cohesive elements, a uniform element size, 0.06 m, is adopted for the region of interest; element sizes of 5 m and 10 m are used to discretize far field regions. We assume the rock matrix is impermeable. The cohesive elements are on a horizontal plane, as indicated by the blue color in Figure 2.10. The injection point is located at the corner of the horizontal plane which is discretized into interface elements.

(1) Viscosity-dominated regime

The dimensionless toughness, κ, in the viscosity scaling is usually considered as a parameter to distinguish the fracture propagation in a viscosity-dominated regime ($\kappa \leq 1$) from toughness-dominated regime ($\kappa \geq 3.5$) (Savitski and Detournay 2002), which is expressed as:

$$\kappa = K'\left(\frac{t^2}{\mu'^5 Q_0^3 E'^{13}}\right)^{1/18}$$
$$E' = \frac{E}{1-\nu^2}, K' = \left(\frac{32}{\pi}\right)^{1/2} K_{IC}, \mu' = 12\mu \tag{2.20}$$

As shown in Figure 2.11, κ is plotted as a function of time. In this verification case, κ is less than 1.1 during injection, which indicates that the fracture propagates in a viscosity-dominated regime and can be approximated through the zero-toughness asymptotic solutions.

Table 2.1 Rock and fluid properties used for penny-shaped hydraulic fracture.

	Viscosity-dominated	Toughness-dominated
Poisson's ratio, ν	0.15	0.15
Young's modulus, E	3.88×10^{10} Pa	3.88×10^{10} Pa
Fracture toughness, K_{IC}	1.13×10^{6} Pa.m$^{1/2}$	8.91×10^{6} Pa.m$^{1/2}$
Tensile strength, T_n	1.5×10^{6} Pa	14.0×10^{6} Pa
Energy release rate, G_{IC}	32.0 N/m	2000.0 N/m
Slop indicator, r_n	0.01	0.005
Fluid viscosity, μ	1.0 cp	0.5 cp
Injection rate, Q_0:	0.001 m^3/s	0.004 m^3/s

Note: Fracture toughness K_{IC} is not an input parameter for CZM, it is calculated using Eq. (2.4) for reader's convenient.

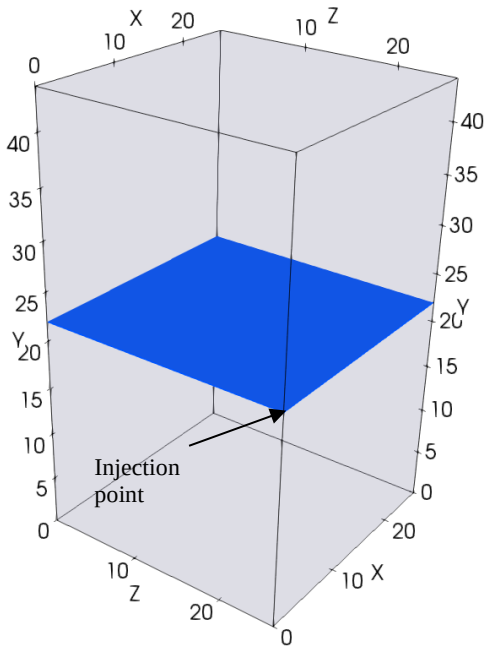

Figure 2.10 Geometry of one quarter of the 3D model. The center plane shown in blue color is discretized into 12-node interface elements; the matrix indicated by the light gray color is discretized into 8-node hexahedral elements. The injection point is located in the corner of the center blue plane. (Unit: m).

In Figure 2.12, the fracture aperture and fluid pressure are plotted separately as functions of the created fracture radius at different injection time. The dimensionless aperture and pressure are also plotted as functions of the normalized fracture radius and shown in Figure 2.13 (a) and (b), respectively. In addition, the aperture and pressure at injection point are shown in Figure 2.14 (a) and (b). Figure 2.14 (c) gives the facture radius as a function of time. As shown, our numerical results match well with the asymptotic analytical solutions. This suggests that the 3D coupled hydro-mechanical cohesive model can produce satisfactory results with respect to fluid pressure, fracture aperture and fracture radius in a viscosity-dominated regime.

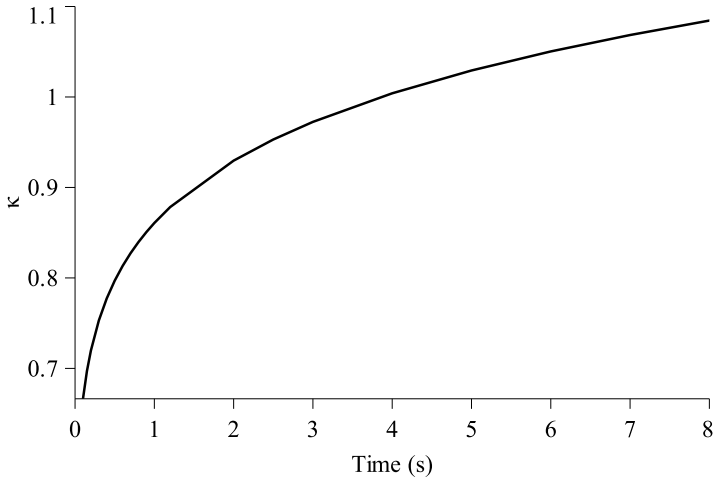

Figure 2.11 κ plotted as a function of time for viscosity-dominated regime.

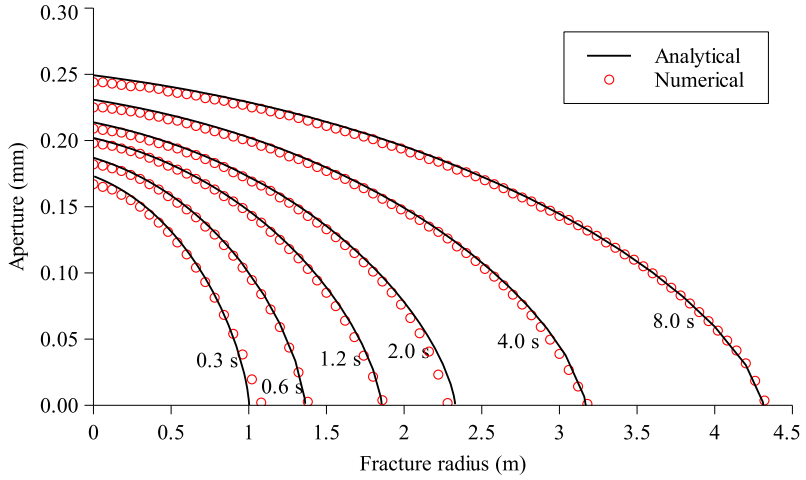

(a)

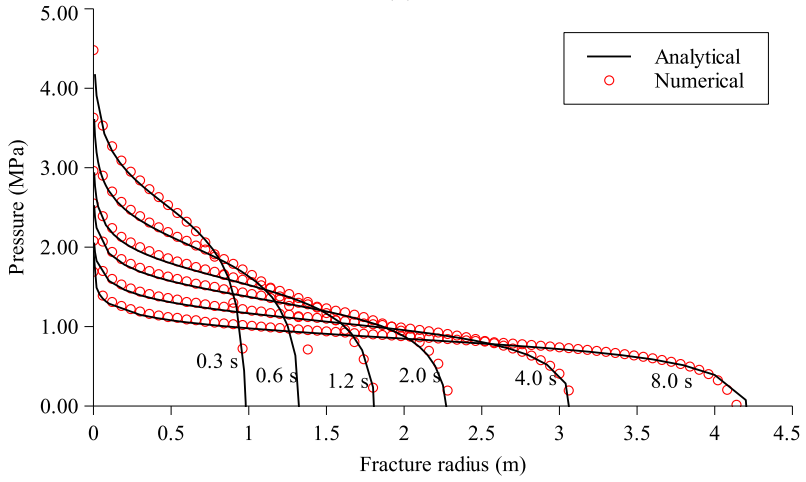

(b)

Figure 2.12 Fracture aperture (a) and pressure (b) plotted as a function of fracture radius at different injection time for penny-shaped hydraulic fracture in viscosity-dominated regime.

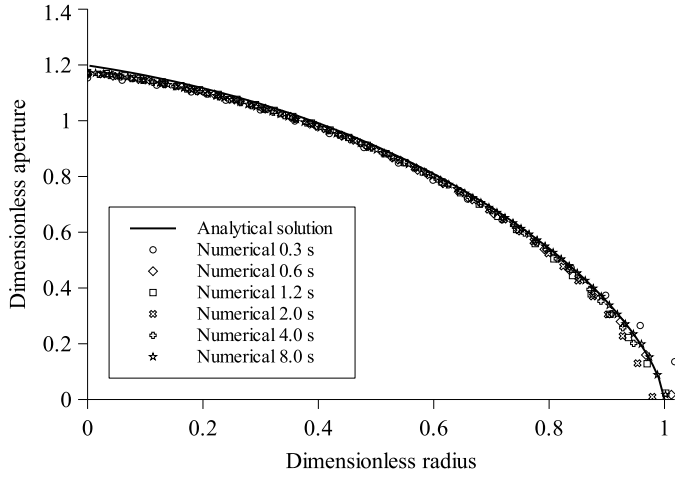

(a)

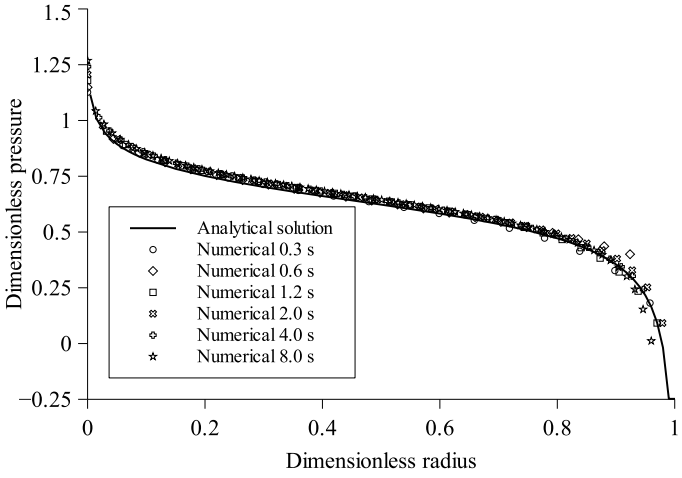

(b)

Figure 2.13 Dimensionless aperture (a) and pressure (b) plotted as a function of normalized fracture radius at different injection time.

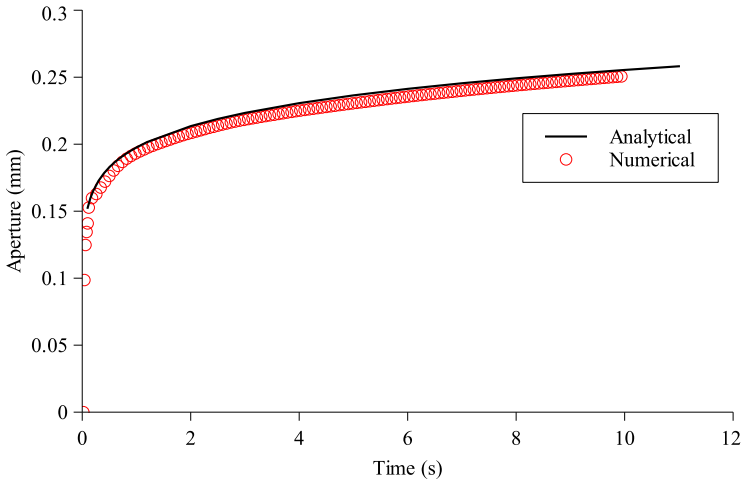

(a)

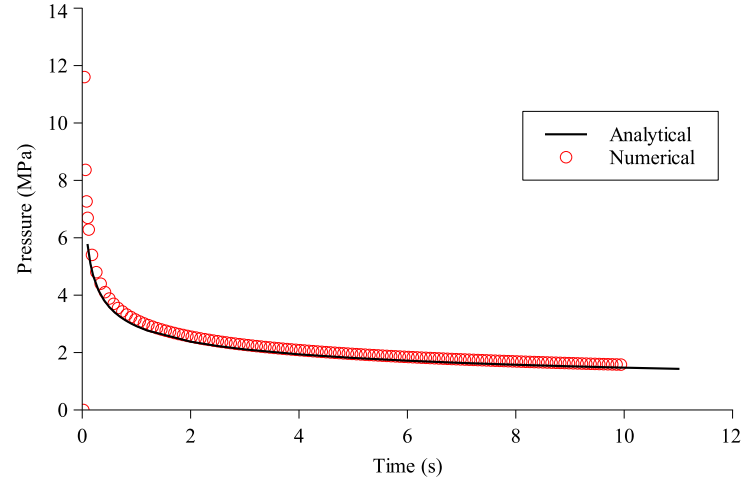

(b)

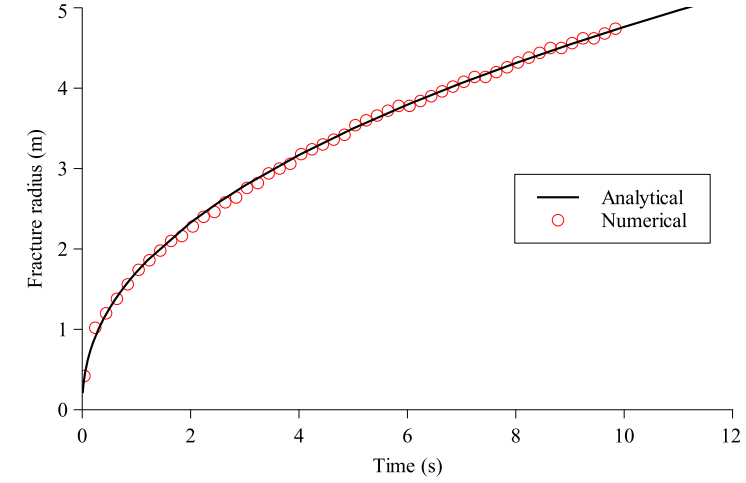

(c)

Figure 2.14 Aperture, pressure and fracture radius plotted as a function of injection time: (a) aperture at the injection point; (b) pressure at the injection point; (c) fracture radius.

The verification case is also used to demonstrate the performance of the parallel simulator. OU's newest supercomputer – Schooner, which has over 10,000 CPU cores, 23TB of RAM and 450TB of usable hard disk space, is utilized to run all the simulations in this study. The same model is run using different number of processors. There are 179,776 8-node hexahedral elements and 11,236 12-node interface elements. The direct solver MUMPS is chosen to solve the assembled system of equations. Figure 2.15 shows the total execution time plotted as a function of the number of processors for one time step. Total execution time, relative speedup and efficiency for cases with different processors in one time step are summarized in Table 2.2. For problems of this size, a good performance is obtained when 100 processors are used. The efficiency reaches more than 80%. The results also indicate that the simulator can be used to handle large scale problems on large number of processors with good speedup performance.

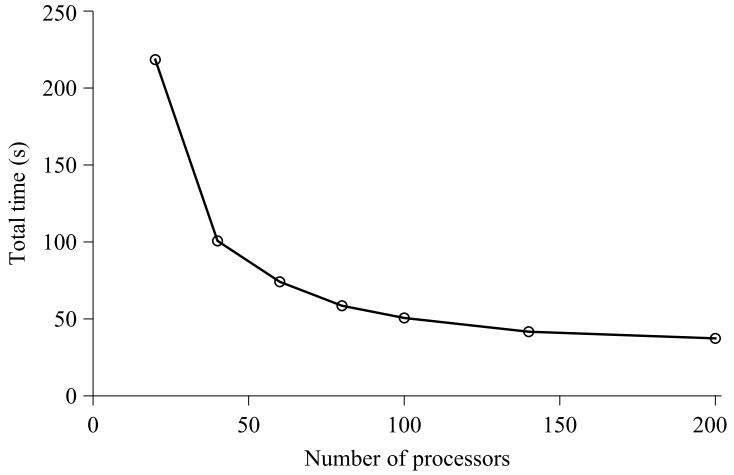

Figure 2.15 Total execution time in one time step versus the number of processors used.

Table 2.2 Total execution time, relative speedup and efficiency for the verification case in one time step. The mesh is composed by 106×16×106 8-node hexahedral and 106×1×106 12-node hydro-mechanical interface elements.

# Processors	Total time (s)	Relative speedup	Efficiency
20	218.45	-	-
60	74.12	2.95	0.98
80	58.54	3.73	0.93
100	50.62	4.32	0.86
140	41.68	5.24	0.75
200	37.35	5.85	0.58
300	34.57	6.32	0.42

(2) Toughness-dominated regime

The asymptotic analytical solutions are derived based on LEFM. Fracture toughness (K_{IC}) is one of the parameters used in analytical solutions. However, in CZM, energy release rate (G_{IC}) is used instead of fracture toughness. To verify fracture propagation in toughness-dominated regime, released energy needs to be accurately captured and Eq. (2.4) should be satisfied. Usually element size should be smaller than the length of fracture process zone in order to accurately obtain the released energy. In 3D models, this requires tremendous number of elements if remesh technology is not available. To reduce the computational cost, the same mesh as that used for viscosity-dominated regime is utilized.

Using the parameters given in Table 2.1, κ is plotted as a function of time in Figure 2.16. As can be seen, κ ranges from 3.90 to 8.13. The fracture propagates in the toughness-dominated regime ($\kappa \geq 3.5$) for this verification case. Figure 2.17 (a) shows the aperture profile in the radial direction at different injection time. The numerical results do not match the asymptotic solutions exactly at the fracture tips. As mentioned before, analytical solutions are derived based on LEFM; stress singularity exists at the tips. CZM allows ductile deformation at the tips. Figure 2.18 (a) and (b) illustrate the dimensionless aperture and pressure distributions, separately. We can observe that the pressure in hydraulic fracture is almost uniform and matches the asymptotic

analytical solution very well (Figure 2.17 (b) and Figure 2.18 (b)). The aperture and pressure are separately plotted as a function of time in Figure 2.19. They have a good match with the asymptotic analytical solutions. The fracture radius is also shown in Figure 2.19. It is slightly larger than the asymptotic analytical solutions but do not match them exactly since different assumptions are implied.

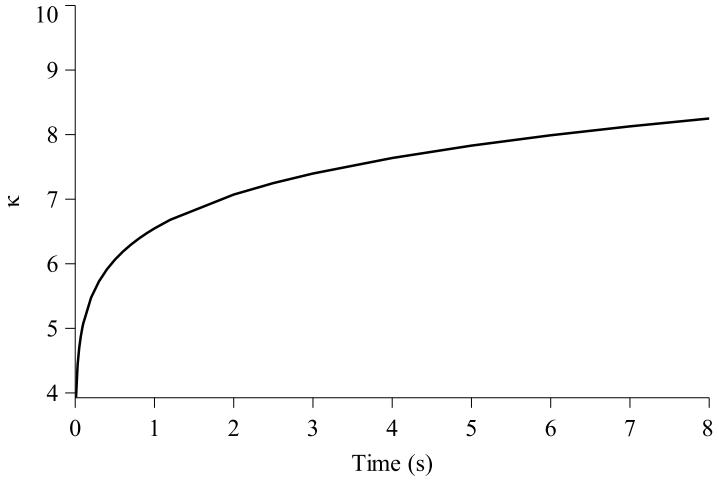

Figure 2.16 κ plotted as a function of time for toughness-dominated regime.

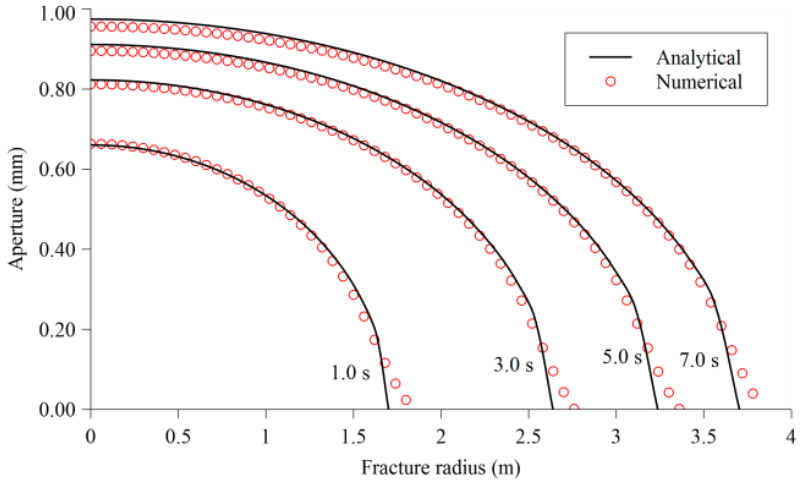

(a)

Figure 2.17 Fracture aperture (a) and pressure (b) plotted as a function of fracture radius at different injection time for penny-shaped hydraulic fracture in toughness-dominated regime. (continued)

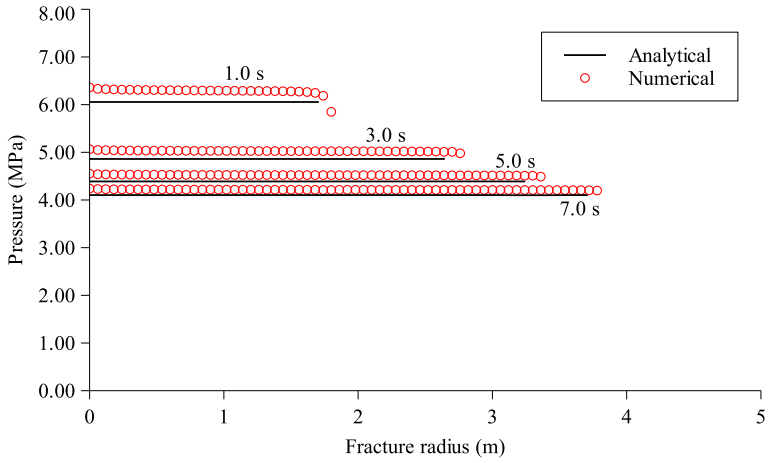

(b)

Figure 2.17 (continued). (Caption shown on previous page.)

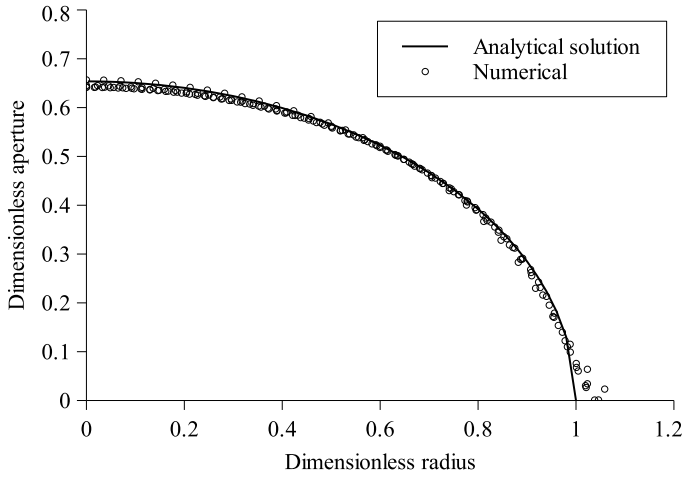

(a)

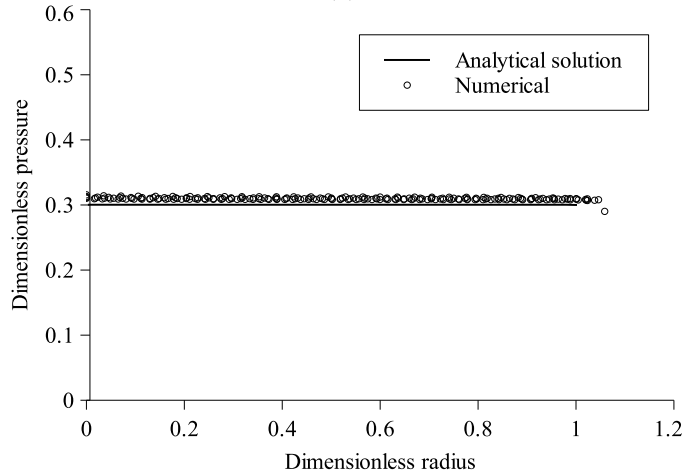

(b)

Figure 2.18 Dimensionless aperture (a) and pressure (b) plotted as a function of normalized fracture radius at different injection time.

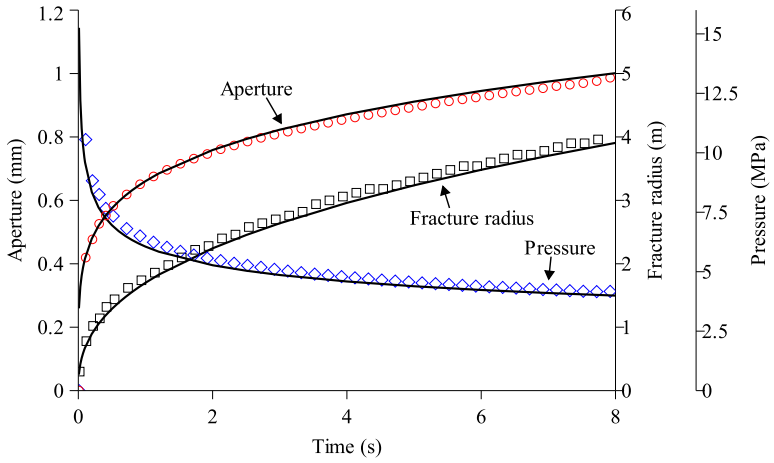

Figure 2.19 Aperture, pressure and fracture radius plotted as a function of injection time for penny-shaped hydraulic fracture in toughness-dominated regime. Solid lines are for asymptotic analytical solutions; data markers are for numerical solutions.

2.5.3 KGD hydraulic fracture in 3D domain

The KGD hydraulic fracture in 3D domain is also analyzed. As shown in Figure 2.20, injection rates are the same along the *z* direction to make the variables along the z direction distributed uniformly. The two boundaries perpendicular to the *z* axis are fixed in the *z* direction. With this configuration, the *xy* plane is under plane strain condition. The size of hydro-mechanical interface element is 0.0015 m. The input parameters for fracture propagation in viscosity- and toughness-dominated regimes are given in Table 2.3. The dimensionless toughness, κ, is calculated using the following expression (Detournay 2004):

$$\kappa = \frac{K'}{\left(E'^3 \mu' Q_0\right)^{1/4}} \tag{2.21}$$

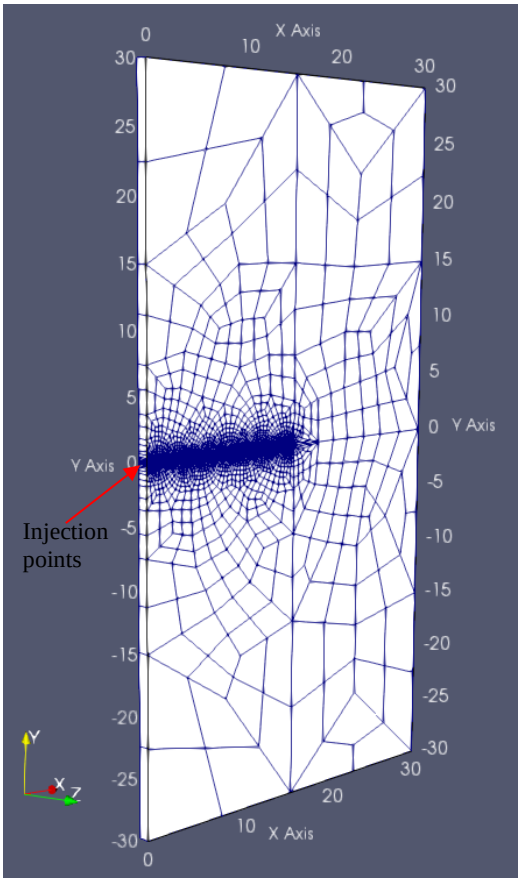

Figure 2.20 Geometry of the KGD model in 3D. (Unit: m)

Table 2.3 Rock and fluid properties used for penny-shaped hydraulic fracture.

	Viscosity-dominated	Toughness-dominated
Poisson's ratio, v	0.15	0.15
Young's modulus, E	3.88×10^{10} Pa	3.88×10^{10} Pa
Fracture toughness, K_{IC}	0.63×10^{6} Pa.m$^{1/2}$	8.91×10^{6} Pa.m$^{1/2}$
Tensile strength, T_n	1.0×10^{6} Pa	10.0×10^{6} Pa
Energy release rate, G_{IC}	10.0 N/m	2000.0 N/m
Slop indicator, r_n	0.1	0.005
Fluid viscosity, μ	10.0 cp	0.5 cp
Injection rate, Q_0:	0.001 m^2/s	0.001 m^2/s
Dimensionless toughness, κ	0.216	6.461

Note: Fracture toughness K_{IC} is not an input parameter for CZM, it is calculated using Eq. (2.4) for reader's convenient.

(1) Viscosity-dominated regime

As shown in Table 2.3, the dimensionless toughness (κ = 0.216) is less than 1, which indicates the hydraulic fracture propagates in viscosity-dominated regime and can be approximated through the zero-toughness solution as provided by Adachi (2001) and Detournay (2004). Figure 2.21 (a) and (b) illustrate the fracture aperture and fluid pressure plotted separately as a function of fracture length at different injection time. The dimensionless aperture and pressure distributions are shown in Figure 2.22 (a) and (b). Also the aperture and pressure at the injection point are plotted as a function of time and shown in Figure 2.23 (a) and (b). Figure 2.23 (c) gives the fracture length at different injection time. As can be seen from these figures, the 3D KGD model also produces results that match well with the asymptotic analytical solutions (plane strain solutions) in terms of injection aperture, injection pressure, fracture length, aperture and pressure profiles. There is some mismatch in dimensionless pressure near close vicinity of the fracture tip (Figure 2.22 (b)). Asymptotic analytical solutions predict pressure singularity (infinite negative pressure) close to the fracture tip. Numerical models can only produce finite values and could experience oscillations when singularity exists. In addition, the existence of the cohesive process zone ahead of the fracture tip may contribute to the discrepancy in fluid pressure.

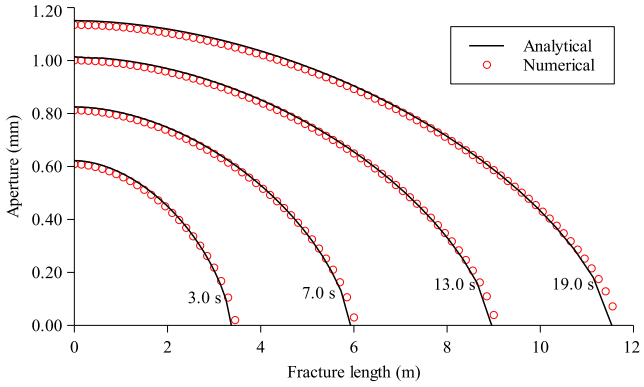

(a)

Figure 2.21 Fracture aperture (a) and pressure (b) plotted as a function of fracture length at different injection time for 3D KGD hydraulic fracture in viscosity-dominated regime. (continued)

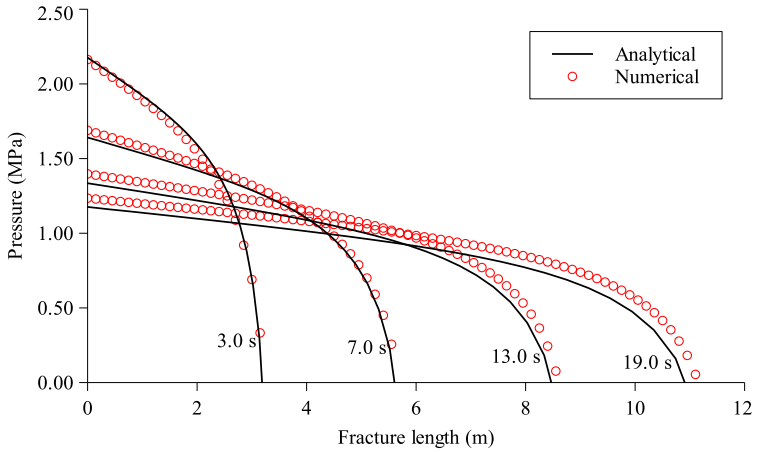

(b)

Figure 2.21 (continued). (Caption shown on previous page.)

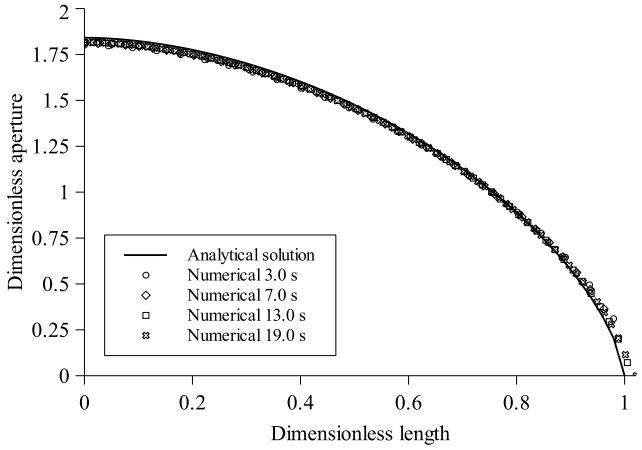

(a)

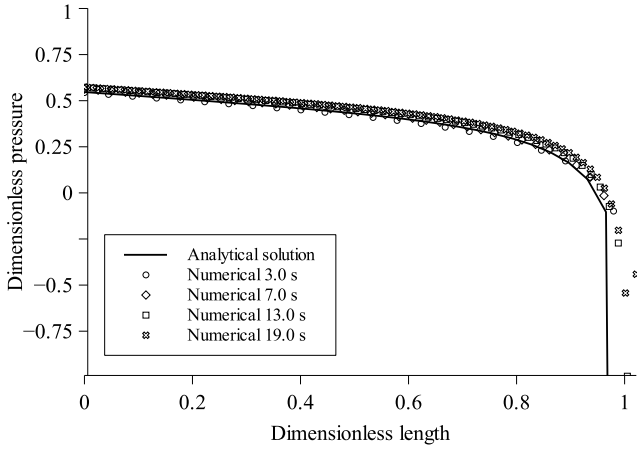

(b)

Figure 2.22 Dimensionless aperture (a) and pressure (b) plotted as a function of normalized fracture length at different injection time. The asymptotic analytical solution predicts negative infinite pressure in the vicinity of fracture tip; numerical simulations yield finite values close to the tip as shown by the discrete dots near the tip in (b).

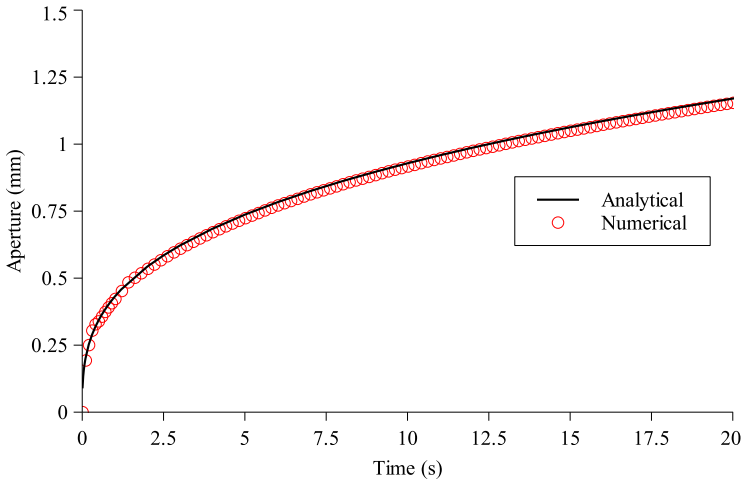

(a)

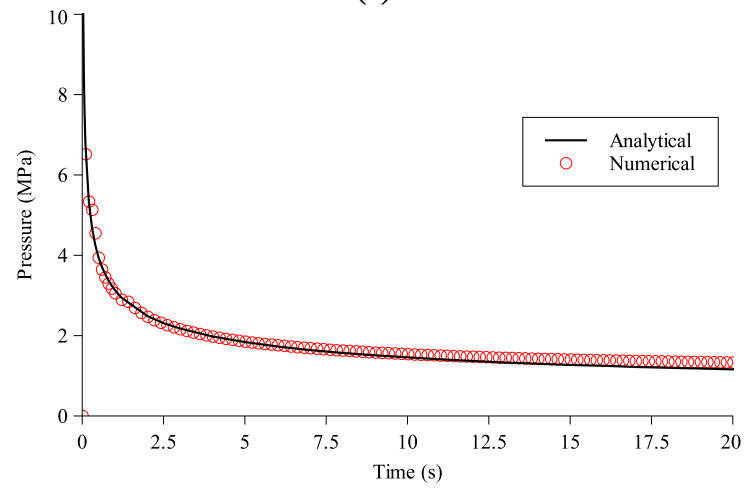

(b)

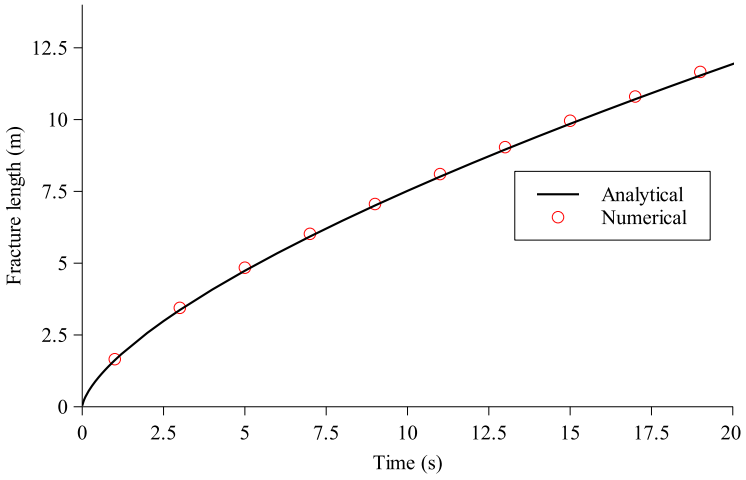

(c)

Figure 2.23 Dimensionless aperture (a) and pressure (b) plotted as a function of normalized fracture length at different injection time. The asymptotic analytical solution predicts negative infinite pressure in the vicinity of fracture tip; numerical simulations yield finite values close to the tip as shown by the discrete dots near the tip in (b).

(2) Toughness-dominated regime

The parameters given in Table 2.3 produce dimensionless toughness κ = 6.461 for simulations in this section. Figure 2.24 (a) and (b) present the aperture and pressure at the injection point plotted as a function of fracture length at different injection time. The numerical results have a good match with the asymptotic solutions even for areas near fracture tips. It should be noted that the element size for KGD verification (0.0015 m) is much smaller than that (0.06 m) used in the verification of the penny-shaped hydraulic fracture. Figure 2.25 (a) and (b) illustrate the dimensionless aperture and pressure distributions. They all have a good match with the asymptotic analytical solutions. The aperture and pressure at injection point are shown in Figure 2.26. Figure 2.26 also shows the fracture length as a function of time. It can be seen that the KGD model in 3D domain produces results matching well with the asymptotic analytical solutions.

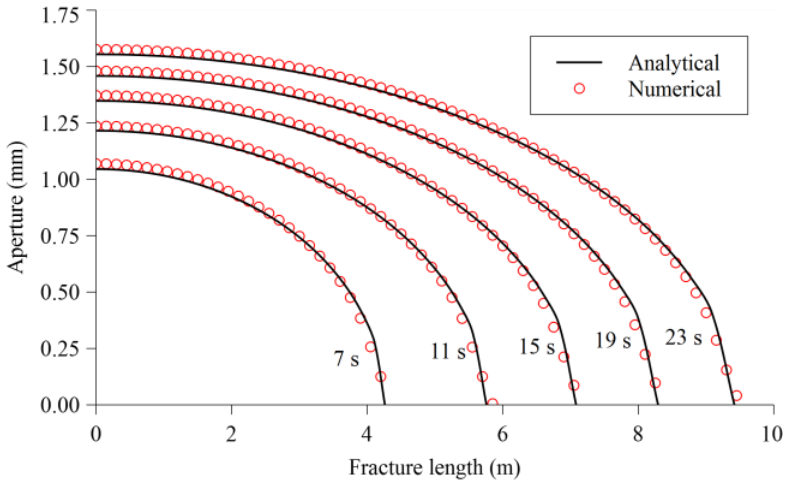

(a)

Figure 2.24 Fracture aperture (a) and injection pressure (b) plotted as a function of fracture length at different injection time for KGD hydraulic fracture in 3D domain in toughness-dominated regime. (continued)

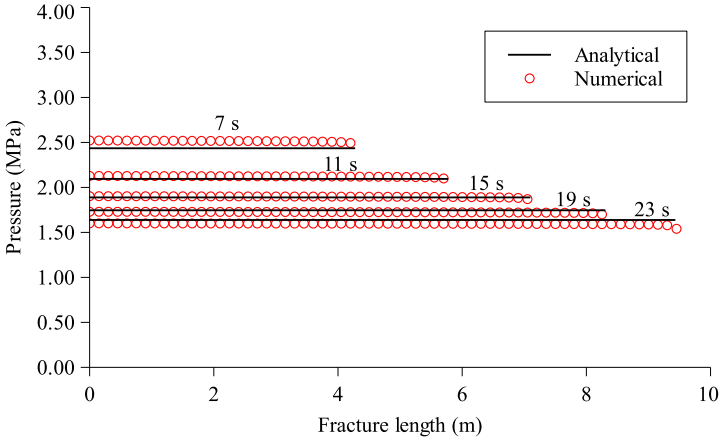

(b)

Figure 2.24 (continued). (Caption shown on previous page.)

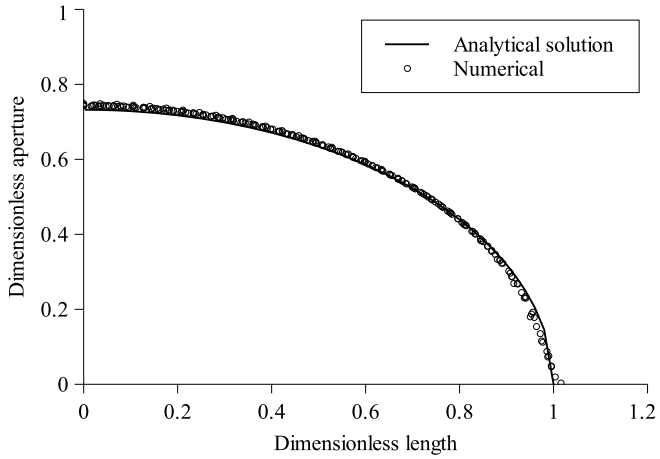

(a)

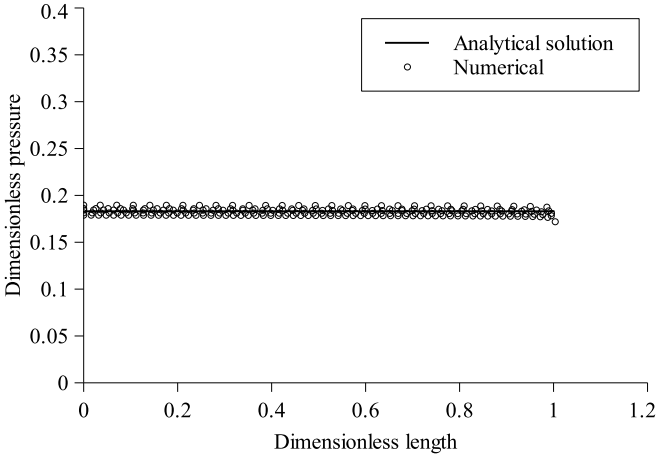

(b)

Figure 2.25 Dimensionless aperture and pressure plotted as a function of normalized fracture length at different injection time: (a) dimensionless aperture; (b) dimensionless pressure.

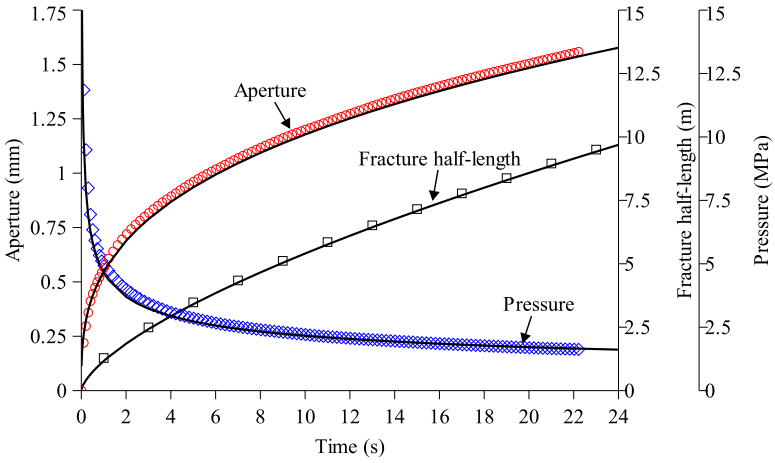

Figure 2.26 Aperture, pressure and fracture half-length plotted as a function of injection time for KGD hydraulic fracture in toughness-dominated regime. Solid lines are for asymptotic analytical solutions; dots are for numerical solutions.

2.6 Numerical analyses: CZM parameters and element size

When using CZM to simulate fracture propagation, a set of parameters is required, including tensile strength, energy release rate and parameters to control the stiffness of a cohesive interface element. Only purely tensile failure and its corresponding CZM parameters are considered in this study. The behaviors of a cohesive interface element are defined through these parameters. To obtain a successful (or accurate) simulation, the size of interface elements must by smaller than the cohesive zone length, which is also called as fracture process zone ahead of fracture tips and is an inherent property for quasi-brittle materials. This condition limits the application of CZM for large scale applications due to the fact that the fracture process zone is usually much smaller when compared with the size of a model for field applications. For quasi-brittle materials, such as rock and concrete, the process zone is usually at scale of centimeter or millimeter (Otsuka and Date 2000; Turon et al. 2007). In this section, the influences of cohesive zone parameters and element size on hydraulic fracture propagation are analyzed. The parameters are chosen to make fracture propagate in the viscosity-dominated

regime, which is commonly encountered in reservoir stimulation and when the hydraulic fractures propagate in a cluster manner (Sesetty and Ghassemi 2017).

2.6.1 Sensitivity analyses of CZM parameters

The distance from the physical crack tip to the point where the maximum tensile strength is reached (mathematical crack tip) is usually called the cohesive zone length (Figure 2.1). The cohesive zone length is a function of energy release rate (G_{IC}), tensile strength, Young's modulus and other material properties. Different models are proposed to estimate the cohesive zone length l_{cz} in the literature. They share the formulation

$$l_{cz} = M \frac{E}{\left(1-\nu^2\right)} \frac{G_{IC}}{T_{\max}^2} \tag{2.22}$$

where M is a constant that is determined by each cohesive zone model. The models proposed by Irwin (1957), Barenblatt (1962), Hillerborg et al. (1976), Rice (1979) and Hui et al. (2003), have M equal to $1/\pi$, $\pi/8$, 1.0, $9\pi/32$ and $2/3\pi$, respectively. A brief literature review about the formulations can be found in Turon et al. (2007).

As we can see, the main parameters for cohesive elements that influence the cohesive zone length are the critical energy release rate G_{IC}, and the tensile strength T_{max}. Either increase of the critical energy release rate G_{IC} or decrease of the tensile strength T_{max} could make the cohesive zone length larger. When using relatively coarse mesh, a larger cohesive zone length is preferred in order to accurately capture the released energy in cohesive elements. There are no strict rules to determine the number of elements that should be confined within the cohesive zone. A minimum of 5 to 10 elements is usually suggested.

In the sensitivity analyses, influences of tensile strength, critical energy release rate, and stiffness of cohesive elements on hydraulic fracture propagation are studied. The mesh is the same as that used for verifying the penny-shaped hydraulic fracture.

(1) Stiffness of cohesive elements

The stiffness of a cohesive element is indicated by the slope of the elastic deformation part (before tensile strength is reached) on a traction-separation curve. For a fixed energy release rate, the slope, and thus the stiffness, is characterized through the ratio of the critical crack opening width to the final crack opening width (Park and Paulino 2012), as shown in Figure 2.2. The slope indicator r_n is used to represent the ratio in this study. The critical crack opening is the opening at which the tensile strength is reached and softening deformation starts; the final crack opening is the opening at the complete failure of a cohesive element. Through the variation of slop indicator r_n, the influence of cohesive element stiffness on fracture propagation is analyzed. Figure 2.27 illustrates the traction-separation curves corresponding to slop indicators of 0.01, 0.05 and 0.1 with the critical energy release rate of 32 N/m. As shown, the smaller the slop indicator, the steeper the slopes of the elastic deformation portion of the curve, which makes the cohesive element stiffer. It should be remembered that the area under the three curves are the same and equal to the critical energy release rate. Except for the slope indicator, all the other parameters are the same as those given in Table 2.1 for the viscosity-dominated regime.

Figure 2.28 (a) and (b) illustrate aperture and pressure profiles plotted along the radius of the penny-shaped fracture, respectively. Since the slop indicator is related to the elastic deformation before the tensile strength is reached, a larger slop indicator implies relatively larger fracture opening is needed to reach the tensile strength and to enter into softening deformation. As shown in Figure 2.28, this property makes the material around fracture tips more ductile when larger slop indicator is used. The fluid pressure and the fracture aperture are smaller but the fracture length is larger when fracture tips experience larger ductile deformation. The aperture

and fluid pressure at the injection point are shown in Figure 2.29 (a) and (b). They both match well with the asymptotic analytical solutions.

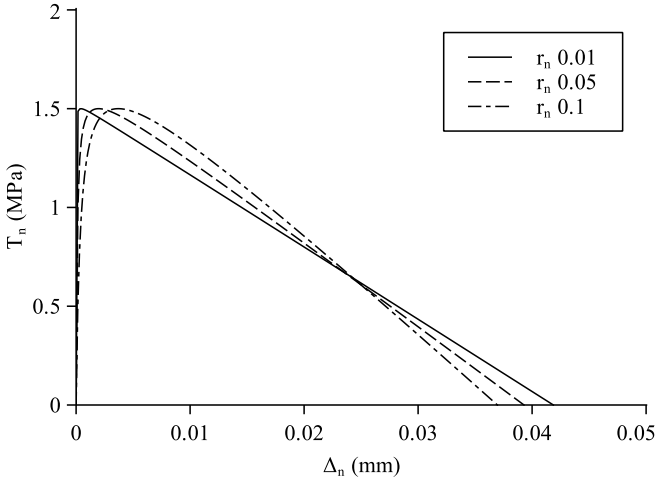

Figure 2.27 Relationship between normal cohesive traction (T_n) and normal separation (Δ_n) for cohesive elements with r_n of 0.01, 0.05 and 0.1, respectively.

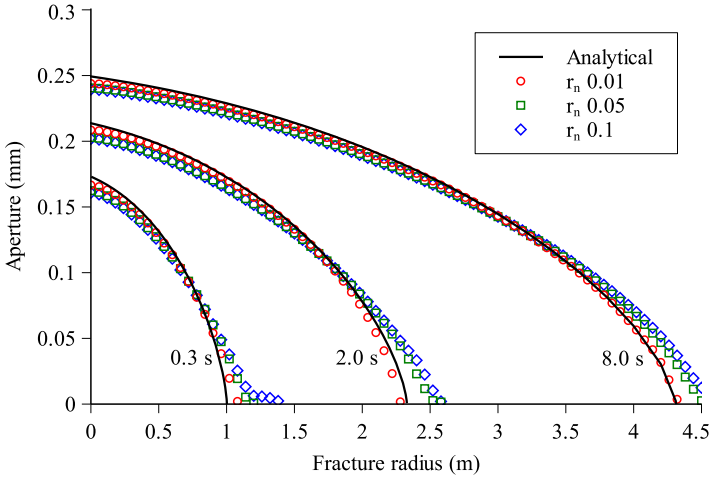

(a)

Figure 2.28 Fracture aperture (a) and pressure (b) plotted as a function of fracture radius at different injection time for r_n being 0.01, 0.05 and 0.1, respectively. Larger slope indicator (r_n) makes the material ahead of fracture tips more ductile, thus experiencing larger deformation. (continued)

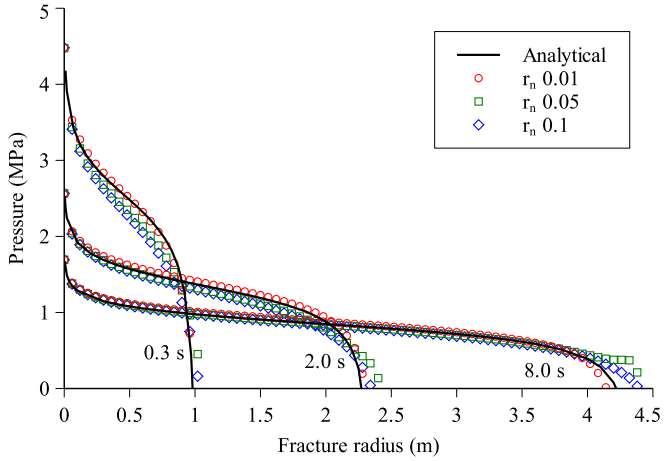

(b)

Figure 2.28 (continued). (Caption shown on previous page.)

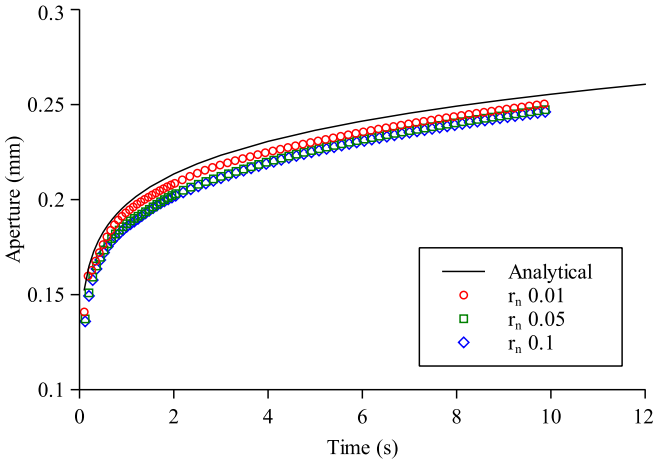

(a)

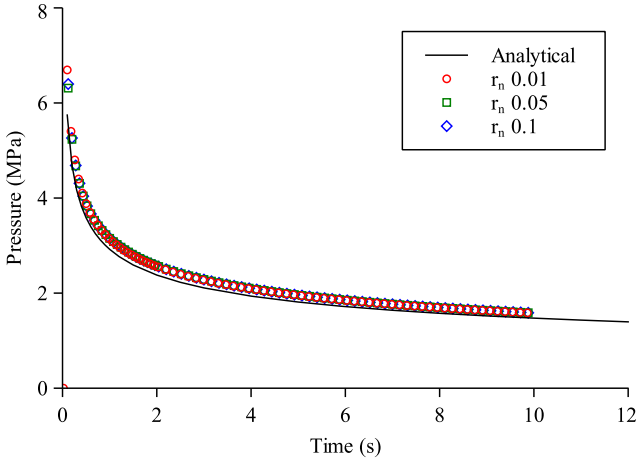

(b)

Figure 2.29 Fracture aperture (a) and pressure (b) at injection point versus injection time for r_n being 0.01, 0.05 and 0.1, respectively.

(2) Tensile strength

Three scenarios are considered. The tensile strength for each scenario is 0.5 MPa, 1.5 MPa, and 5.0 MPa. Except for tensile strength, all the other rock and fluid properties are the same as those provided in Table 2.1.

Figure 2.30 (a) and (b) illustrate the profiles of fracture aperture and fluid pressure respectively at different injection times. As illustrated, the change of tensile strength from 0.5 MPa to 1.5 MPa has a slight influence on the distributions of aperture and pressure for a large portion of the profiles. Relatively larger aperture and fluid pressure and smaller fracture length are generated when the tensile strength equals 5.0 MPa. Large tensile strength produces more resistance for fracture propagation in the CZM. The aperture and pressure at the injection point are almost the same for the three scenarios, as shown in Figure 2.31 (a) and (b). There are discrepancies in the aperture and pressure near the tips when compared with asymptotic analytical solutions. A higher tensile strength generates a smaller aperture and pressure in the close vicinity of fracture tips. This is likely due to the basic differences in the assumptions involved in the CZM and the LEFM from which the asymptotic solutions are derived. Tensile strength is an input parameter for CZM and is related to the stiffness of cohesive interface element; it is not needed in LEFM when deriving the asymptotic solutions.

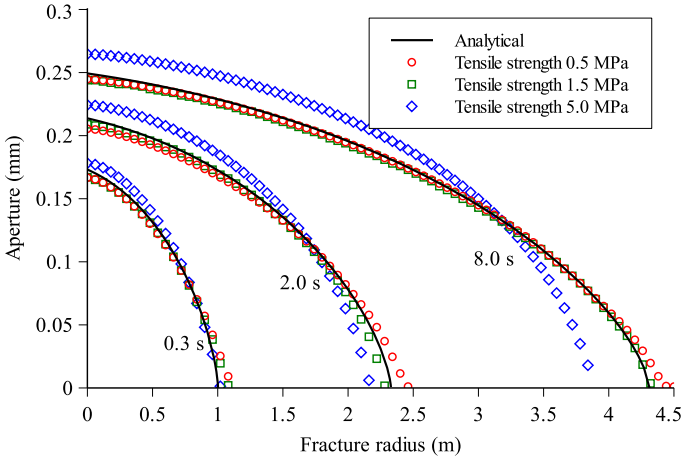

(a)

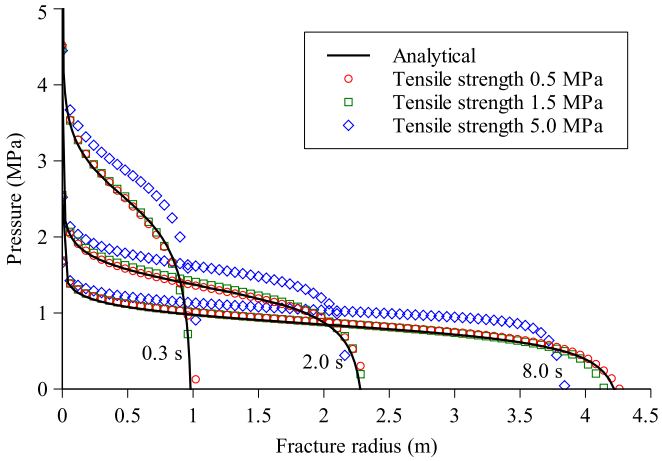

(b)

Figure 2.30 Fracture aperture (a) and pressure (b) plotted as a function of fracture radius at different injection time for tensile strength being 0.5 MPa, 1.5 MPa and 5.0 MPa. Larger tensile strength generates smaller aperture in the vicinity of fracture tip.

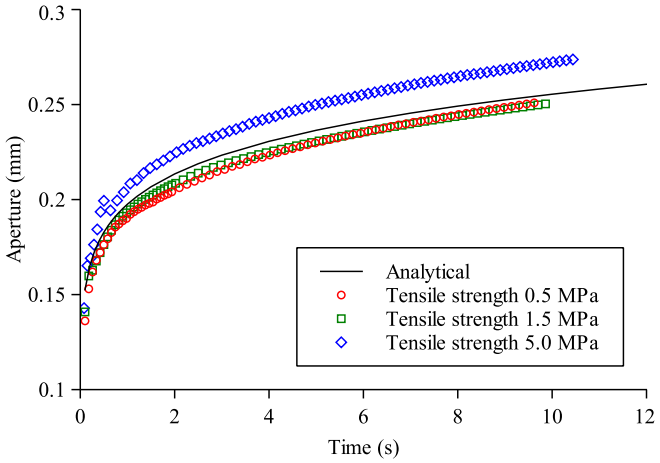

(a)

Figure 2.31 Fracture aperture (a) and pressure (b) at injection point versus injection time for tensile strength being 0.5 MPa, 1.5 MPa and 5.0 MPa. (continued)

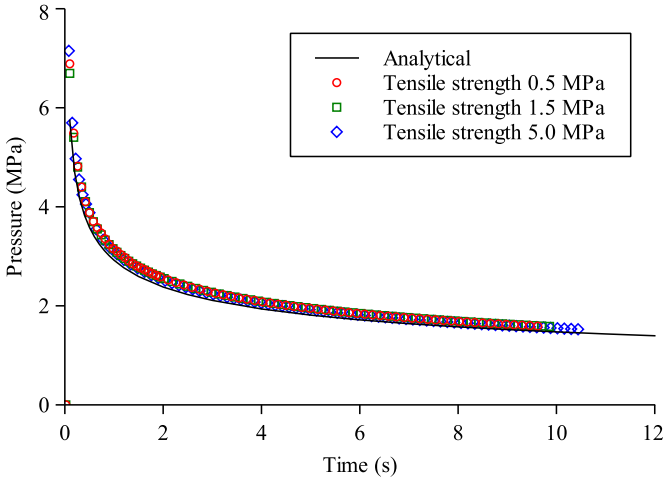

(b)

Figure 2.31 (continued). (Caption shown on previous page.)

In Figure 2.32, the normal cohesive traction (T_n) is plotted as a function of normal separation (Δ_n) for cohesive elements with tensile strength of 0.5 MPa, 1.5 MPa and 5.0 MPa, respectively. Since the critical energy release rate (the area under the traction-separation curve) has a fixed prescribed value, the larger the tensile strength, the steeper the curve's slope for both the elastic deformation part and the inelastic deformation part on the traction-separation profile, though the elastic deformation is too small to be seen on Figure 2.32. A steeper slope of the elastic deformation part represents a higher stiffness. The fracture aperture would be smaller for cohesive elements with higher stiffness during fluid pressurization at tips where traction is not zero. This is manifested in numerical results. Numerical results indicate that cohesive elements with higher stiffness yields smaller fracture aperture and fluid pressure at the fracture tips, as shown in Figure 2.30 (a) and (b). The solutions at fracture tips influence the aperture and pressure distributions for the whole domain of interest. It should be mentioned that smaller tensile strength yields a larger cohesive zone length, within which more cohesive elements are contained. Larger cohesive zone length benefits numerical stability. When the stiffness of cohesive elements is too high and makes the corresponding cohesive zone length too small to contain enough cohesive elements, it then often causes loss of computation stability and crash.

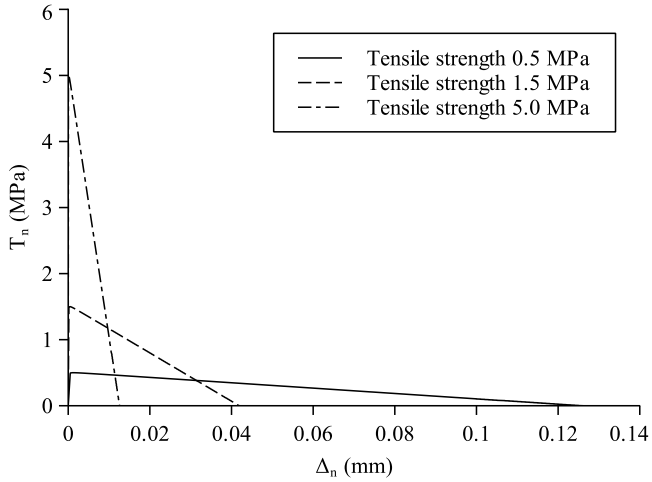

Figure 2.32 Relationship between normal cohesive traction (T_n) and normal separation (Δ_n) for cohesive elements with tensile strength of 0.5 MPa, 1.5 MPa and 5.0 MPa, respectively.

(3) Critical energy release rate

The influence of the critical energy release rate (G_{IC}) on fracture propagation is analyzed through its variation. Three scenarios with critical energy release rates equal to 5 N/m, 12 N/m and 32 N/m are considered. The tensile strength is set to 0.5 MPa. The rest of the parameters are the same as those provided in Table 2.1.

The fracture aperture and fluid pressure are plotted as a function of fracture radius, and are shown in Figure 2.33 (a) and (b). The aperture and pressure at injection point are also given in Figure 2.34 (a) and (b). As can be seen, the numerical results match well with the asymptotic solutions even when the critical energy release rate changes from 5 N/m to 32 N/m. Figure 2.35 shows the κ as a function of injection time. All the three scenarios have κ less than 1.2, which indicates all examples are in the viscosity-dominated regime. Converting the critical energy release rate of 5 N/m, 12 N/m and 32 N/m to fracture toughness through Eq. (2.4), the corresponding fracture toughness values are 0.45 MPa/m$^{1/2}$, 0.69 MPa/m$^{1/2}$ and 1.13 MPa/m$^{1/2}$. According to these numerical simulations, it is considered that the hydraulic fracture propagation is not sensitive to the critical energy release rate or fracture toughness given that the propagation is within the viscosity-dominated regime. This numerical characteristic would facilitate the

selection of CZM parameters since the critical energy release rates within a large range produce almost identical results in the viscosity-dominated regime.

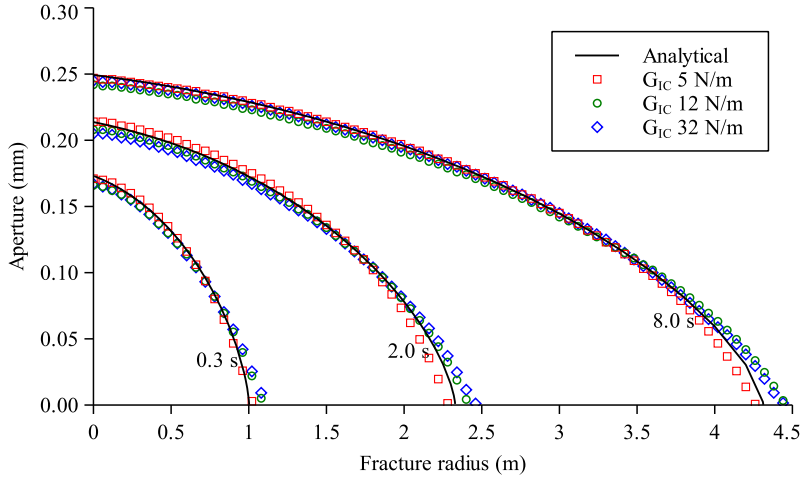

(a)

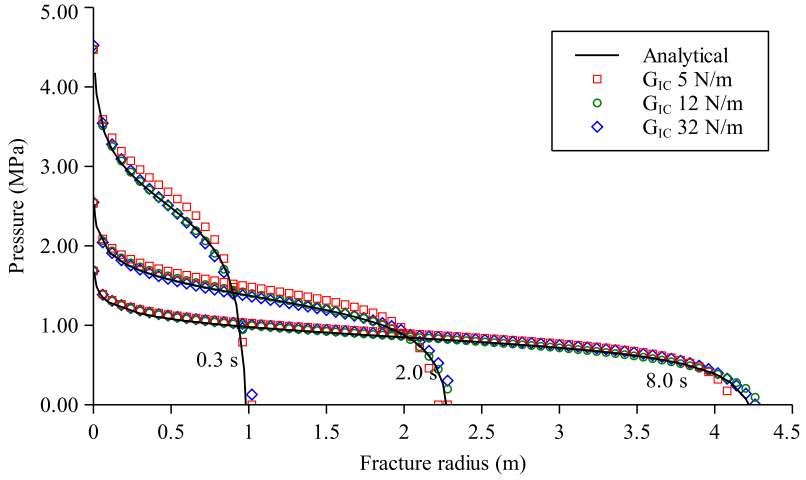

(b)

Figure 2.33 Fracture aperture (a) and pressure (b) plotted as a function of fracture radius at different injection time for energy release rate (G_{IC}) being 5.0 N/m, 12.0 N/m and 32.0 N/m.

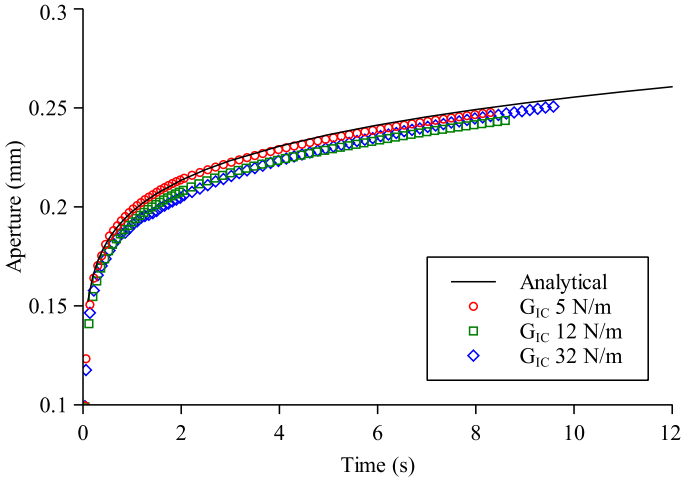

(a)

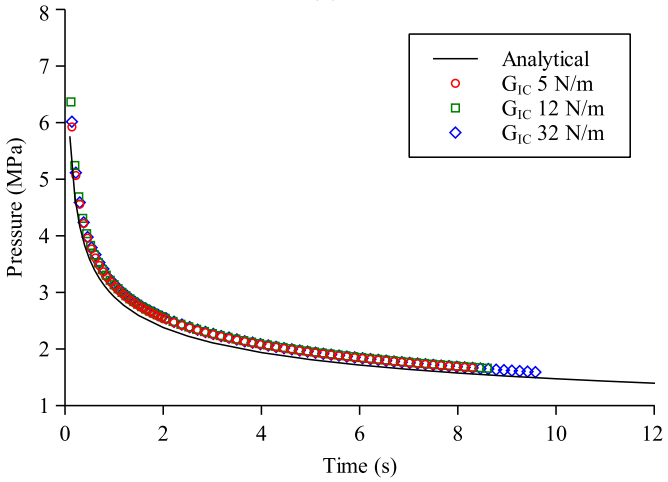

(b)

Figure 2.34 Fracture aperture (a) and pressure (b) at injection point versus injection time for energy release rate (G_{IC}) being 5.0 N/m, 12.0 N/m and 32.0 N/m.

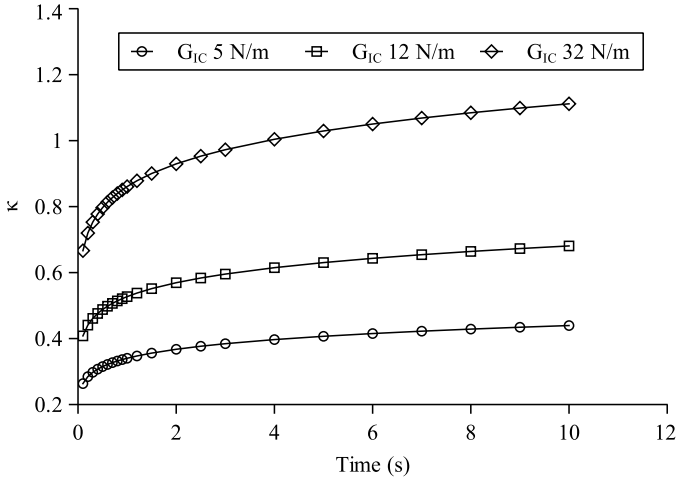

Figure 2.35 κ plotted as a function of injection time.

The traction-separation curves for critical energy release rates of 5 N/m, 12 N/m and 32 N/m are shown in Figure 2.36. A higher value of critical energy release rate corresponds to a larger area under the curves and to a larger ultimate failure separation (zero cohesive traction exists) when a fixed tensile strength is used here. It also makes the cohesive elements more ductile. Higher critical energy release rate also indicates a larger cohesive zone length according to Eq. (2.22). Provided that fracture propagation is within the viscosity-dominated regime, a higher value of critical energy release rate benefits numerical simulations and produces the same results as those obtained using smaller critical energy release rate.

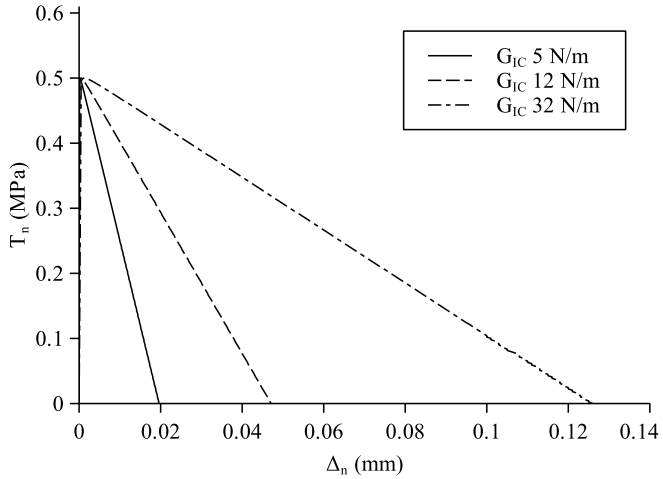

Figure 2.36 Relationship between normal cohesive traction (T_n) and normal separation (Δ_n) for cohesive elements with energy release rate of 5 N/m, 12 N/m and 32 N/m, respectively. Larger G_{IC} corresponds to more ductile deformation.

2.6.2 Influence of the interface element size on hydraulic fracturing

Interface elements are used to represent 2D planar surfaces in 3D space (Figure 2.3 and Figure 2.4). The sizes of interface elements are the same in the two spatial directions for the 2D planar surfaces for all the simulations in this study. As stated before, to accurately capture the traction distribution and the energy released ahead of the crack tips, a sufficient number of interface elements should be placed within the cohesive zone. The size of the interface element

becomes critical when we try to obtain accurate results. Here we study the influence of element size on fracture propagation.

Three different element sizes are considered. They are 0.12 m, 0.4 m and 0.8 m. The material and fluid properties are given in Table 2.4. In order to use a relatively large element size, the tensile strength is chosen as 0.5 MPa. Although simulations using larger critical energy release rate (e.g. G_{IC} = 22 N/m, G_{IC} = 32 N/m) are performed, only the results for G_{IC} = 12 N/m are presented for the sake of brevity.

Table 2.4 Rock and fluid properties used for penny-shaped hydraulic fracture.

Poisson's Ratio, v:	0.15
Young's Modulus, E:	3.88×10^{10} Pa
Tensile strength, T_{nc}:	0.5×10^{6} Pa
Energy release rate, G_{IC}	12.0 N/m
Slop indicator, r_n	0.1
Fluid Viscosity, μ:	1.0 cp
Injection rate, Q_0:	0.001 m^3/s

Fracture aperture and fluid pressure are plotted as a function of fracture radius and are shown in Figure 2.37 (a) and (b), respectively. As shown, compared with the asymptotic analytical solutions, the aperture distributions from numerical results are smaller around the injection point and larger around the fracture tip. The relative error is about 5% at the injection point. For pressure profiles along the radial direction, numerical results match well with the asymptotic ones, even when the element size is as large as 0.8 m. The aperture and pressure at the injection point are separately plotted as a function of time in Figure 2.38 (a) and (b). The pressure has a good match with asymptotic solution. For element size equal to 0.8 m, the aperture at the injection point experiences oscillations, especially in the beginning of injection. Apparently, the oscillation is caused by the relatively large element size. Even when larger element sizes (e.g. 0.12 m, 0.4 m in this study) are used, numerical results are still close to asymptotic solutions though there are discrepancies.

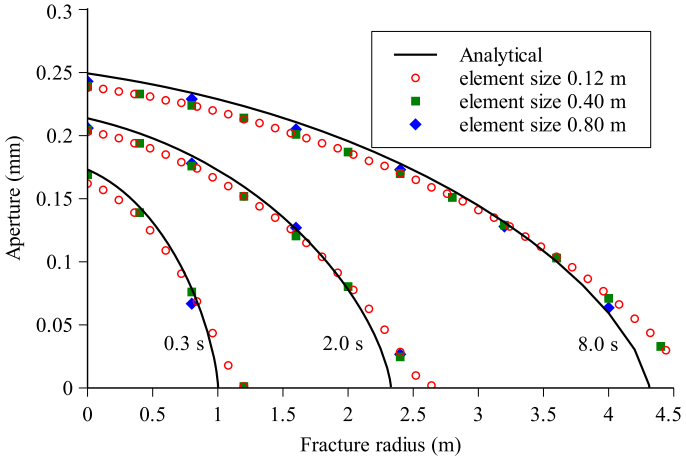

(a)

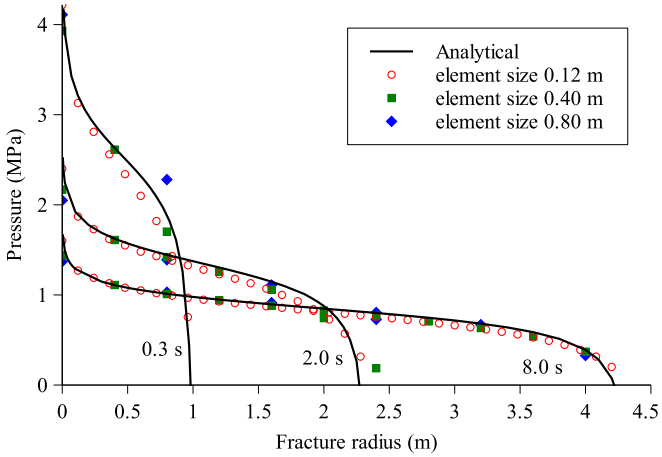

(b)

Figure 2.37 Fracture aperture (a) and pressure (b) plotted as a function of fracture radius at different injection time for element size being 0.12 m, 0.40 m and 0.80 m.

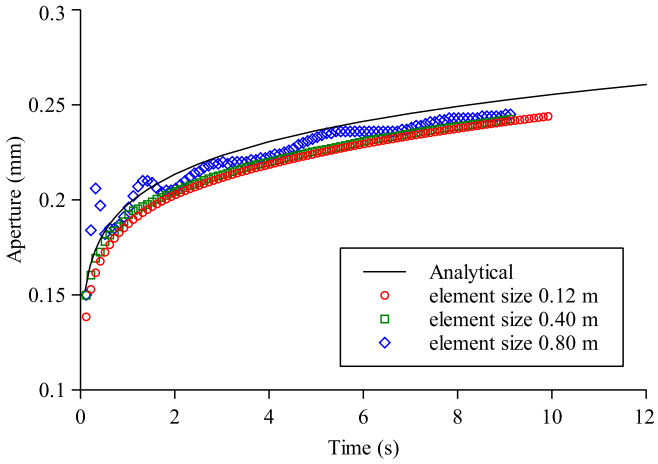

(a)

Figure 2.38 Fracture aperture (a) and pressure (b) at injection point versus injection time for element size being 0.12 m, 0.40 m and 0.80 m. (continued)

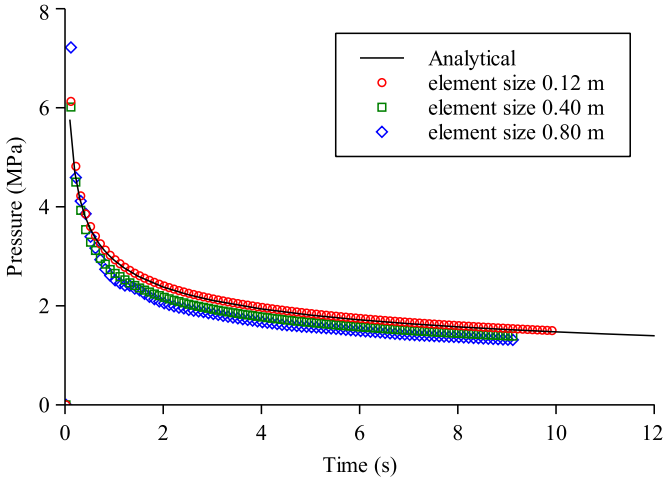

(b)

Figure 2.38 (continued). (Caption shown on previous page.)

2.6.3 Discussion

The fundamental difference between CZM and models based on LEFM is that there are inelastic deformations around the fracture tips in CZM. To accurately capture the behaviors of CZM, certain number of elements should be contained in cohesive zone. Table 2.5 summarizes different combinations of parameters and their corresponding number of elements in cohesive zone. Through numerical experiments, it is found that most of the combinations yield results very close to the asymptotic solutions. The number of elements in the cohesive zone not only influences the accuracy of results but also affects the stability of the model. For the case with G_{IC} = 5N/m, T_{max} = 2 MPa and element size = 0.06 m, the corresponding number of elements in the cohesive zone is less than 1 (0.7) and the simulation fails. Another factor related to the stability of the model is the stiffness indicator r_n. When r_n is too low (e.g. r_n = 0.0001), the stiffness of cohesive element will be large and the simulation may also fail. From numerical experiments, it is observed that simulations with the number of elements in cohesive zone larger than 5, and r_n close to 0.01 usually run smoothly without failure and could yield results close to the asymptotic solution. It should be emphasized that the discussions are focused on viscosity-dominated propagation regime.

Table 2.5 Different combinations of CZM parameters and their corresponding number of elements in cohesive zone.

Energy release rate, G_{IC} (N/m)	Tensile strength, T_{max} (Pa)	Cohesive zone length, l_{cz} (m)	Element size (m)	Number of elements
5	0.5	0.70	0.06	11.7
12	0.5	1.68	0.06	28.1
32	0.5	4.49	0.06	74.8
5	1.5	0.08	0.06	1.3
12	1.5	0.19	0.06	3.1
32	1.5	0.50	0.06	8.3
5	2	0.04	0.06	0.7
12	2	0.11	0.06	1.8
32	2	0.28	0.06	4.7
12	0.5	1.68	0.12	14.0
12	0.5	1.68	0.4	4.2
12	0.5	1.68	0.8	2.1

For the propagation of hydraulic fractures in toughness-dominated regime, the solutions of aperture, pressure and fracture radius/length are functions of fracture toughness. To generate a toughness-dominated propagation regime, the fracture toughness K_{IC} (and the corresponding energy release rate G_{IC}) should be much larger than the common values for reservoir rock (around 1 ~ 2 MPa.m$^{1/2}$) while other parameters are within ranges for engineering applications (i.e. fluid viscosity around 1 cp). It is intuitive to consider that materials having large fracture toughness should have high tensile strength. The impact of tensile strength on the penny-shaped hydraulic fracturing in toughness-dominated regime is analyzed. Except tensile strength, other parameters are the same as those used in the verification section (Table 2.1). As shown in Figure 2.39, tensile strength equal to 14 MPa and even 20 MPa produce results matching well with the asymptotic analytical solutions. However, when tensile strength = 8 MPa (and 2 MPa, 5 MP, corresponding results are not given for the sake of brevity), the aperture and pressure profiles cannot match well with the asymptotic analytical solutions. It yields relatively smaller aperture size and injection fluid pressure. It is suggested that when large energy release rate is chosen for

hydraulic fracturing in toughness-dominated regime, the corresponding tensile strength for the cohesive interface element should also be high. As illustrated, a wide range of tensile strength (i.e. 14 MPa – 20 MPa in this study) would yield almost the same results that match well with the asymptotic solutions.

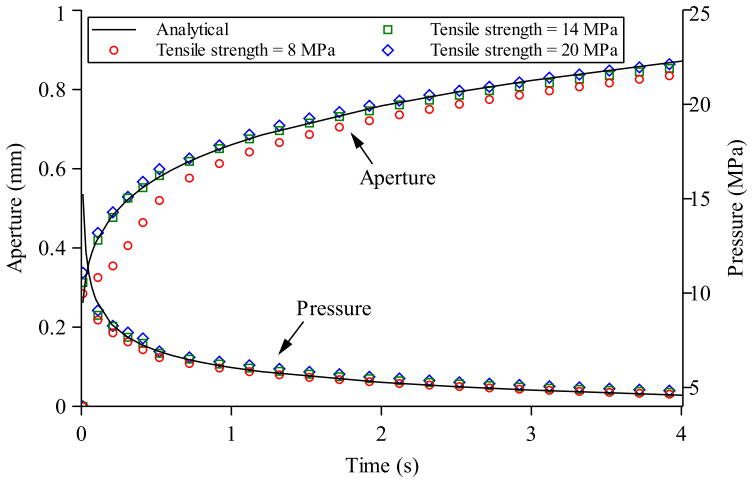

Figure 2.39 Fracture aperture and pressure at injection point versus injection time for the penny-shaped hydraulic fracture propagating in toughness-dominated regime with tensile strength equal to 8 MPa, 14 MPa, and 20 MPa. Other parameters are the same as those provided in Table 2.1. The solid lines are for asymptotic analytical solutions, the data markers are for numerical results.

As we know there are several input parameters for CZM. Given that the input parameters are corresponding to a viscosity-dominated propagation regime, variation of CZM parameters within a certain range could yield the almost same results. As shown previously, using either r_n = 0.01 or r_n = 0.1, the results are close to asymptotic solutions. The same is true for the variations of energy release rate G_{IC} and maximum tensile strength T_{max}. This flexible property benefits the choice of input parameters for CZM though it has more parameters than traditional models based on LEFM. Of course, all the chosen CZM parameters should make sense within ranges of engineering applications. Another advantage of this property is that we could reduce the tensile strength to get a relatively large length of cohesive zone, so as to incorporate more elements in the cohesive zone even when relatively large elements are used. This feature is attractive in field applications at reservoir scale. As shown in analyses about element size, when element size is as

large as 0.8 m, we can still capture the pressure and aperture distributions quite well though there are oscillations in the beginning of injection. The same point is also suggested by Bažant and Oh (1983) and Turon et al. (2007) for engineering applications of CZM.

The relationship between the total work done during injection and the energy dissipated in creating new hydraulic fracture surfaces are analyzed below. Integrating the product of injection pressure and fluid flow rate with respect to time, the total work done can be calculated as:

$$W_{in} = \frac{3}{2} QE' p\left(0, P(t)\right)\left(\frac{\mu'}{E'}\right)^{1/3} t^{2/3} \text{ for viscosity-dominated regime}$$
$$W_{in} = \frac{5}{4} QE' p\left(0, P(t)\right)\left(\frac{K'^6}{E'^6 Q}\right)^{1/5} t^{4/5} \text{ for toughness-dominated regime} \quad (2.23)$$

where Q is the injection rate, $p(\rho, P(t))$ is the dimensionless pressure which is a function the scaled radius ρ and the dimensionless evolution parameter $P(t)$ (Savitski and Detournay 2002). At the injection point, $\rho = 0$.

The total work done during injection and the energy spent on fracture creation for the previous sensitivity analyses (viscosity-dominated regime) with respect to G_{IC} are shown in Figure 2.40. As can be seen, the energy dissipated in creating new fracture surface is much less than the total input energy. Small alteration of G_{IC} has almost no influence on the overall response of the model from the energy point of view. In contrast, the situation is different for hydraulic fracture propagates in toughness-dominated regime. Figure 2.41 illustrates the total work done during injection and the energy dissipated by creating new fractures for the verification of penny-shaped hydraulic fracture in toughness-dominated regime. As shown, the energy spent on fracture creation takes the majority portion of the total input energy. To get accurate results, the dissipated energy should be captured accurately. This usually requires a

small element size. Given that the size of elements is small enough, as shown in the verification for KGD hydraulic fracture in 3D, we indeed capture the toughness- (and viscosity-) dominated propagation accurately.

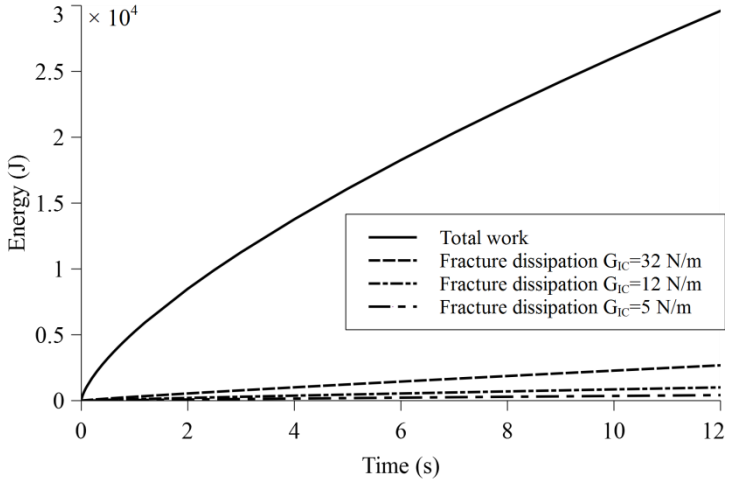

Figure 2.40 Total work done during injection and the energy spent on fracture creation with different G_{IC} for hydraulic fracture propagating in the viscosity-dominated regime.

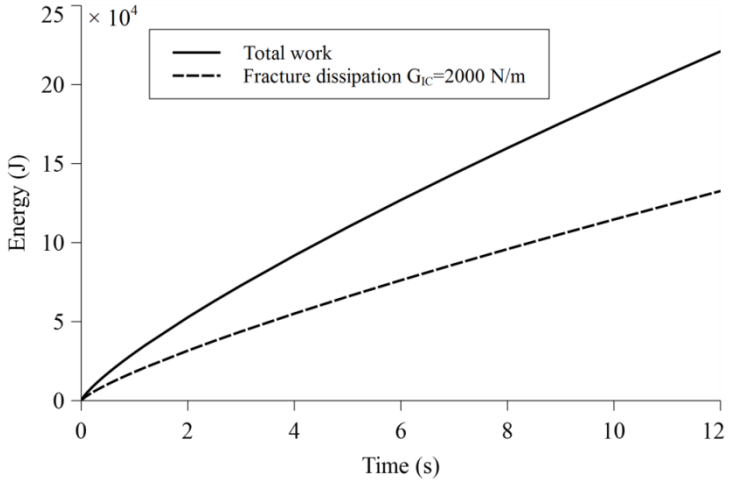

Figure 2.41 Total work done during injection and the energy spent on fracture creation with G_{IC} = 2000 N/m for hydraulic fracture propagating in the toughness-dominated regime.

There are two nonlinear processes involved in the coupled processes of hydraulic fracturing. The first one is the nonlinear lubrication equation Eq. (2.7). The second one is the moving boundary condition about the fracture tip (or fluid front). The Newton-Raphson method can handle the nonlinear lubrication equation quite well. The moving boundary condition usually needs iterations to update the tip position. In the CZM, no special treatments of the fracture tip

are needed. In other words, the moving boundary is automatically satisfied. This feature may be due to the fact that the cohesive element is a special continuous element that can simulate discontinuous behaviors. For 3D FEM simulations at reservoir scale, the computational cost is usually heavy so that when the iterations for the moving boundary are not needed, tremendous time savings could be made.

Cohesive zone model is an effective way to deal with fracture propagation problems based on FEM, and it becomes popular in hydraulic fracturing. When we use it, different strategies should be adopted. It should also be kept in mind that the CZM should be accurate at least on qualitative level when we pursue efficiency. One limitation of the proposed interface element is that it can only be aligned with the surfaces of the continuum element used for the main problem domain (e.g., 8-node hexahedron element). This limits the ability of interface element to propagate in arbitrary directions. Many efforts are still needed to improve the proposed model.

2.7 Conclusions

In this work, a 3D fully coupled hydro-mechanical interface element is developed. Governing equations and corresponding finite element discretization are given. The hydro-mechanical interface element is implemented based on the cohesive zone model. Numerical examples are provided to verify the proposed model. The first one illustrates the mechanical behaviors of the cohesive zone model. The second and third examples study separately the penny-shaped hydraulic fracture and the KGD hydraulic fracture (in 3D domain) in both viscosity- and toughness-dominated regimes. Comparison our numerical results with asymptotic analytical solutions indicates that good agreement has been achieved.

Sensitivity analyses are performed to investigate the influence of input parameters of CZM on hydraulic fracturing. Smaller stiffness of cohesive elements tends to have larger ductile deformation around fracture tips. The tensile strength influences the number of elements within the cohesive zone. The energy release rate has almost no influence on hydraulic fracturing in viscosity-dominated regime since the energy consumed on fracture creation is too small when compared with the total input energy. The property simplifies the selection of input parameters because small variation of energy release rate would yield almost the same results. On the contrary, for hydraulic fracturing in toughness-dominated regime, the energy spent on fracture creation takes a majority portion of the total input energy; to obtain correct numerical results, the energy spent on creating new fractures should be accurately captured. The size of interface element is directly related to the stability and accuracy of numerical simulations. From our numerical experience, it is recommended that at least 5 interface elements should be contained within the cohesive zone.

References

Adachi, J. 2001. Fluid-Driven Fracture in Permeable Rock. Ph.D. Dissertation, University of Minnesota, Minneapolis.

Balay, S., Abhyankar, S., Adams, M. F. et al. PETSc Web page, http://www.mcs.anl.gov/petsc.

Barenblatt, G. I. 1962. The Mathematical Theory of Equilibrium Cracks in Brittle Fracture. In *Advances in applied mechanics*, ed. Th von Kármán G. Kuerti F. H. van den Dungen H.L. Dryden and L. Howarth, 55-129. Elsevier.

Bažant, Z. P. and Oh, B. H. 1983. Crack band theory for fracture of concrete. *Matériaux et construction* **16** (3): 155-177.

Boone, T. J., Wawrzynek, P. A. and Ingraffea, A. R. 1986. Simulation of the fracture process in rock with application to hydrofracturing. *International Journal of Rock Mechanics and*

Mining Sciences & Geomechanics Abstracts **23** (3): 255-265. http://dx.doi.org/10.1016/0148-9062(86)90971-X.

Carrier, B. and Granet, S. 2012. Numerical modeling of hydraulic fracture problem in permeable medium using cohesive zone model. *Engineering Fracture Mechanics* **79**: 312-328. http://dx.doi.org/10.1016/j.engfracmech.2011.11.012.

Chen, Z. 2012. Finite element modelling of viscosity-dominated hydraulic fractures. *Journal of Petroleum Science and Engineering* **88–89**: 136-144. http://dx.doi.org/10.1016/j.petrol.2011.12.021.

Chen, Z., Bunger, A. P., Zhang, X. et al. 2009. Cohesive zone finite element-based modeling of hydraulic fractures. *Acta Mechanica Solida Sinica* **22** (5): 443-452. http://dx.doi.org/10.1016/S0894-9166(09)60295-0.

Cheng, A. H.-D. 2016. Poroelasticity. Switzerland: Springer International Publishing.

de Borst, R. 2003. Numerical aspects of cohesive-zone models. *Engineering Fracture Mechanics* **70** (14): 1743-1757. http://dx.doi.org/10.1016/S0013-7944(03)00122-X.

Detournay, E. 2004. Propagation Regimes of Fluid-Driven Fractures in Impermeable Rocks. *Int. J. Geomech.* **4** (1): 35-45. https://doi.org/10.1061/(ASCE)1532-3641(2004)4:1(35).

Donea, J. and Huerta, A. 2003. Finite element methods for flow problems. Chichester: John Wiley & Sons.

Dugdale, D. S. 1960. Yielding of steel sheets containing slits. *Journal of the Mechanics and Physics of Solids* **8** (2): 100-104. http://dx.doi.org/10.1016/0022-5096(60)90013-2.

Gao, Q. and Ghassemi, A. 2017. Pore Pressure and Stress Distributions Around a Hydraulic Fracture in Heterogeneous Rock. Rock Mechanics and Rock Engineering 50 (12): 3157-3173. https://doi.org/10.1007/s00603-017-1280-5.

Geertsma, J. and De Klerk, F. 1969. A Rapid Method of Predicting Width and Extent of Hydraulically Induced Fractures. Journal of Petroleum Technology. http://dx.doi.org/10.2118/2458-pa.

Gu, H. and Siebrits, E. 2008. Effect of Formation Modulus Contrast on Hydraulic Fracture Height Containment. *SPE Production & Operations* **23** (02): 170-176. https://doi.org/10.2118/103822-PA.

Hillerborg, A., Modéer, M. and Petersson, P.-E. 1976. Analysis of crack formation and crack growth in concrete by means of fracture mechanics and finite elements. *Cement and concrete research* **6** (6): 773-781.

Huang, K., Zhang, Z. and Ghassemi, A. 2013. Modeling three-dimensional hydraulic fracture propagation using virtual multidimensional internal bonds. *International Journal for Numerical and Analytical Methods in Geomechanics* 37 (13): 2021-2038. https://dx.doi.org/10.1002/nag.2119.

Huang, J. and Ghassemi, A. 2017. Poro-viscoelastic modeling of production from shale gas reservoir: An adaptive dual permeability model. *Journal of Petroleum Science and Engineering* **158** (Supplement C): 336-350. https://doi.org/10.1016/j.petrol.2017.08.046.

Hui, C. Y., A, J., Bennison, S. J. et al. 2003. Crack blunting and the strength of soft elastic solids. *Proceedings of the Royal Society of London. Series A: Mathematical, Physical and Engineering Sciences* **459** (2034): 1489.

Irwin, G. R. 1957. Analysis of stresses and strains near the end of crack traversing a plate. *Journal of applied mechanics* **24**: 361-364.

Khristianovich, S.A. and Zheltov, Y.P. (1955) "Hydraulic Fracture of on Oil-Bearing Reservoir," Izv. Akad. Nauk SSSR, ONT: No. 5, 3-41.

Kumar, D. and Ghassemi, A. 2016. A three-dimensional analysis of simultaneous and sequential fracturing of horizontal wells. *Journal of Petroleum Science and Engineering 146* (Supplement C): 1006-1025. https://doi.org/10.1016/j.petrol.2016.07.001.

Kumar, D. and Ghassemi, A. 2018. Three-Dimensional Poroelastic Modeling of Multiple Hydraulic Fracture Propagation from Horizontal Wells. International Journal of Rock Mechanics and Mining Sciences 105: 192-209. https://doi.org/10.1016/j.ijrmms.2018.01.010.

Otsuka, K. and Date, H. 2000. Fracture process zone in concrete tension specimen. *Engineering Fracture Mechanics* **65** (2): 111-131. https://doi.org/10.1016/S0013-7944(99)00111-3.

Park, K. and Paulino, G. H. 2012. Computational implementation of the PPR potential-based cohesive model in ABAQUS: Educational perspective. *Engineering Fracture Mechanics* **93** (0): 239-262. http://dx.doi.org/10.1016/j.engfracmech.2012.02.007.

Perkins, T. K. and Kern, L. R. 1961. Widths of Hydraulic Fractures. *Journal of Petroleum Technology*. https://doi.org/10.2118/89-pa.

Rice, J. 1979. *The mechanics of earthquake rupture*: Division of Engineering, Brown University.

Sarris, E. and Papanastasiou, P. 2011. The influence of the cohesive process zone in hydraulic fracturing modelling. *International journal of fracture* **167** (1): 33-45. https://doi.org/10.1007/s10704-010-9515-4.

Savitski, A. A. and Detournay, E. 2002. Propagation of a penny-shaped fluid-driven fracture in an impermeable rock: asymptotic solutions. *International Journal of Solids and Structures* **39** (26): 6311-6337. http://dx.doi.org/10.1016/S0020-7683(02)00492-4.

Sesetty, V. and Ghassemi, A. 2015. A numerical study of sequential and simultaneous hydraulic fracturing in single and multi-lateral horizontal wells. *Journal of Petroleum Science and Engineering* 132: 65-76. https://dx.doi.org/10.1016/j.petrol.2015.04.020.

Sesetty, V. and Ghassemi, A. 2017. Complex Fracture Network Model for Stimulation of Unconventional Reservoirs. Paper presented at the 51st U.S. Rock Mechanics/Geomechanics Symposium, San Francisco, California, USA

Shet, C. and Chandra, N. 2002. Analysis of Energy Balance When Using Cohesive Zone Models to Simulate Fracture Processes. *Journal of Engineering Materials and Technology* **124** (4): 440-450. https://doi.org/10.1115/1.1494093.

Smith, M. B., Bale, A. B., Britt, L. K. et al. 2001. Layered Modulus Effects on Fracture Propagation, Proppant Placement, and Fracture Modeling. Paper presented at the SPE Annual Technical Conference and Exhibition, New Orleans, Louisiana, https://doi.org/2001/1/1/. 10.2118/71654-ms.

Sneddon, I. N. 1946. The Distribution of Stress in the Neighbourhood of a Crack in an Elastic Solid. *Proceedings of the Royal Society of London Series a-Mathematical and Physical Sciences* **187** (1009): 229-260. https://doi.org/10.1098/rspa.1946.0077.

Spring, D. W. and Paulino, G. H. 2014. A growing library of three-dimensional cohesive elements for use in ABAQUS. *Engineering Fracture Mechanics* **126** (0): 190-216. http://dx.doi.org/10.1016/j.engfracmech.2014.04.004.

Turon, A., Dávila, C. G., Camanho, P. P. et al. 2007. An engineering solution for mesh size effects in the simulation of delamination using cohesive zone models. *Engineering Fracture Mechanics* **74** (10): 1665-1682. http://dx.doi.org/10.1016/j.engfracmech.2006.08.025.

Witherspoon, P. A., Wang, J. S. Y., Iwai, K. et al. 1980. Validity of Cubic Law for fluid flow in a deformable rock fracture. *Water Resources Research* **16** (6): 1016-1024. https://doi.org/10.1029/WR016i006p01016.

3 3D planar hydraulic fracture propagation in an elastic medium: height growth in layered formations

Abstract

There are many challenges associated with hydraulic fracturing, such as the lithological layering, the heterogeneity of rock and the in-situ stress. In the previous chapter, a fully coupled model using hydro-mechanical interface elements was developed and verified along with additional analyses to characterize the influence of the cohesive zone model parameters on hydraulic fracturing simulations. In this chapter we treat the important problem of hydraulic fracturing in the presence of elastic modulus contrast and stress contrast in layered rock systems encountered in petroleum resources development. First, the model is validated by simulating a laboratory hydraulic fracturing experiment dealing with the influence of stress contrast. The compressibility effects of the wellbore are considered through explicitly modeling the wellbore. Good agreements in the distribution of fracture aperture, injection pressure and fracture footprint have been achieved. Then, numerical analyses are performed to investigate the influence of in-situ stress and formation layer properties, such as Young's modulus and fracture energy release rate, on the height growth and containment of hydraulic fractures. Comparing the results of simulations using conventional thickness-weighted Young's modulus to those from explicit modeling of layers' Young's moduli, it is found that, given the same amount of injection volume, the thickness-weighted modulus generates a higher injection pressure than the layered modulus. Explicit modeling of the layers (with higher or lower modulus than the target layer) influences the hydraulic fracture aperture distribution in the pay zone as well as in the surrounding layers. When modulus contrast is considered, a relatively large fracture aperture is observed in the layer with lower Young's modulus. Also, the hydraulic fracture tends to propagates mainly in the

lower Young's modulus layers which could facilitate containment of the hydraulic fracture by limiting height growth. When considering the influence of stress contrast on height growth, the conventional equilibrium height model produces a relatively large aperture and overestimates the fracture height, since it applies a uniform pressure and does not consider the pressure drop along fracture height. Under the assumed injection rate, fluid viscosity, and in-situ stress, the numerical simulations based on the fully coupled model show stress contrast larger than a certain value, for example 30% of the in-situ minimum horizontal stress, could effectively inhibit the height growth of hydraulic fractures. When the payzone is bounded by ductile top and bottom layers, the injection pressure is higher and the corresponding aperture at the injection point is larger than those obtained from using uniform material properties.

3.1 Introduction

Layered formations with different material properties and in-situ stress are widely encountered during petroleum resource extraction. When performing hydraulic fracturing, the geometry of hydraulic fractures (e.g. fracture height and length) is largely determined by in-situ geological conditions. One of the main problems in stimulation designs is to accurately predict the fracture height growth. In hydraulic fracturing treatments, height growth is needed to achieve good pay zone coverage and height confinement is desirable to generate long fractures and to minimize environmental impact. Field experiments have shown the height growth of many hydraulic fractures is much less than their lateral growth (Warpinski et al. 1998). Due to the importance of fracture height prediction, many studies have been conducted to understand the mechanisms involved in. The formation Young's modulus, in-situ stress, fracture toughness and interface slippage are considered as the main factors that affect the height growth and are the focus of analyses in the literature.

According to the principles of linear elastic fracture mechanics (LEFM), when the stress intensity factor (depending on stress state and fracture geometry) at the fracture tips is larger than the fracture toughness (material property), fractures will propagate. It is thus natural to consider the use of the stress intensity factor to analyze fracture height containment. When a hydraulic fracture is confined between different formation layers, it usually has a much larger lengths than height. To generate a suitable aperture size for proppant placement, while at the same time preventing the fracture growth in the vertical direction, the required fracture toughness at the upper and lower edges of the fractures would need to be an order of magnitude larger than the typical value for rocks (van Eekelen 1982). It was suggested that fracture toughness alone would not be sufficient to stop the height growth in order to confine the hydraulic fractures within the target zone.

Often when simulating hydraulic fracture growth, layered modulus is not considered as an important factor that directly controls height growth. However, elastic modulus influences the fracture width, the shape of the fracture, and hence the fluid pressure distribution and the transportability of proppant inside the fracture (van Eekelen 1982; Smith et al. 2001; Gu and Siebrits 2008). Both laboratory experiments (Daneshy 1978) and field tests (Warpinski et al. 1998) have indicated that modulus contrast, by itself, is insufficient to act as a barrier to prevent fracture propagation. Formulations have been developed to estimate the width and the propagation rates of fractures that have crossed the interface between two layers having different modulus (van Eekelen 1982). It has been shown the fracture width is narrow when it propagates in the high-modulus layer. The smaller width reduces the flow of viscous fluid in the facture, and thus decreases the height growth rate. Simulations based on finite element method were utilized

to investigate the width distribution in layered formations (Smith et al. 2001) and to illustrate the shortcomings of using average modulus to approximate layered modulus.

In-situ stress difference is generally suggested to have the dominant effect on controlling fracture height. Decades of hydraulic fracturing in conventional reservoirs have supported this view. Laboratory experiments have demonstrated the containment of hydraulic fracture due to the existence of a stress contrast. Warpinski, Clark, et al. (1982) and Teufel and Warpinski (1983) performed laboratory experiments to investigate the impacts of material properties and stress contrasts on the confinement of hydraulic fracture propagation. Their experiments have shown that 2 to 4 MPa stress contrast across the rock interface is sufficient to restrict the height growth of hydraulic fractures under the designed experimental conditions. A laboratory experiment that created step-like stress changes on the contact surface of two transparent Polymethyl methacrylate (PMMA) block was carried out by Jeffrey and Bunger (2007). The fracture height and length evolution in the lower-stress region, which was bounded by two symmetric higher-stress regions, were recorded. A hydraulic fracture with the ratio of overall height to half-length equal to 1.7 to 3 was generated. The height growth was effectively restricted by the created stress barriers. Wu et al. (2008) also studied the propagation of a hydraulic fracture using the transparent PMMA blocks. Three distinct stress layers on the contact surface between two PMMA blocks were generated. The experiment clearly showed that the propagation of the hydraulic fracture was impeded when the layer with higher confining stress was encountered, and was favored when the layer with lower confining stress was met. A simple static model to estimate the fracture height in a layered-stress medium was proposed by Simonson et al. (1978). The model assumes a uniform fluid pressure in the hydraulic fracture and no variations of material properties. This is commonly called the “equilibrium-height model”.

The assumptions, especially the uniform internal pressure of hydraulic fracture, are overly simplified. Both the reduction of aperture size towards fracture tips and the fluid viscosity can restrict flow, and induce a pressure drop along the fracture height during injection, and thereby make the fracture height growth lower than that obtained by assuming a uniform fluid pressure.

In addition to modulus contrast and stress contrast, interface slippage should also be considered in analyses of fracture height containment. Laboratory experiments conducted by Daneshy (1978) showed that shear sliding on interfaces between layers caused fracture arrest. Warpinski et al. (1998) considered many factors in an attempt to explain the mechanisms involved in fracture height containment in field tests. The observed height growth from microseismic imaging was considerably less than that predicted from most fracture models. Neither stress contrast nor different fracture toughness in bounding layers could be used to reasonably explain the field observations. It was suggested that enhanced toughness, interface slip and stress and energy dissipation in the rock layers were combined to contribute to the fracture containment. Many studies have also suggested that slippage along pre-existing planes may cause of arrest in fracture propagation (Huang et al. 2018; Ye et al. 2018), and thus the fracture height growth. A review of the interaction between a hydraulic fracture and an interface can be found in Ghassemi (2017) and Mendelsohn (1984). There are many other factors that contribute to the fracture height containment. In this study, we focus on the impacts of Young's modulus, in-situ stress and formation ductility. Details of the numerical method and its verification can be found in the previous paper.

3.2 Problem description

From theoretical work, experimental and field observations (Simonson et al. 1978; Warpinski et al. 1998; Wu et al. 2008), it is well-known that both material properties and in-situ

stress influence the hydraulic fracture propagation. However, the variation of material properties (e.g., Young's modulus) in multi-layered formations has often been ignored in modeling, partly due to the complexity of the coupled problem. In this work, we utilize the 3D finite element method (FEM) presented in the previous chapter, to treat the problem involving multi-layered formations. We use 8-node hexahedron elements exclusively in this study.

van Eekelen (1982) proposed an approximate formulation to estimate fracture height growth in layers with modulus contrasts. In the vertical section of hydraulic fractures, the fluid pressure was assumed as a constant. Smith et al. (2001) discussed the layered modulus effects on fracture height growth and proppant placement. Constant fluid pressure within fractures was also assumed. This assumption simplifies calculations and the derivation of approximate formulations and is appropriate when fractures propagate in a toughness-dominated regime. However, when the fractures propagates in a viscosity-dominated regime, the distribution of fluid pressure from the injection point to the fracture tip would not be constant. The input energy is mainly spent on fluid flow and deformation of matrix, rather than the creation of new fracture surfaces. In this paper, we investigate hydraulic fracture propagation under various configurations of modulus contrast and compare with results obtained using a uniform modulus.

When assuming perfectly bonded (without any interface slippage) interfaces in a layered-stress rock system, the in-situ stress contrast could be the most important factor that directly controls the height growth of hydraulic fractures. To simplify analyses, static step-wise pressurization is often used in approximately calculating fracture height in a layered rock system with stress contrast. A constant pressure is applied on the whole fracture surface and is adjusted through trial-and-error to satisfy a critical equilibrium state. The so-called equilibrium height model was first proposed by Simonson et al. (1978). Thereafter, more complex situations have

been considered based on Simonson's work. As pointed by van Eekelen (1982) thirty years ago, the static model of fracture propagation does not consider the variation of fracture width and hence the variation of fluid pressure within the fracture; it also does not consider the competition between horizontal and vertical growth of hydraulic fractures. In the following sections, hydraulic fracture propagation in a layered environment with stress contrast is investigated through the fully coupled hydro-mechanical model and is compared with results obtained from static step-wise pressurization.

3.3 Validation of the numerical model

A laboratory experiment (Wu et al. 2008) on the influence of in-situ stress on hydraulic fracture height growth is studied and used as to validate our numerical model. Step-like confining stresses were generated when a machined PMMA block with a designed profile was pressed against another block with a flat surface (Wu et al. 2008). Three zones with distinctive confining stresses were created. The injection zone had intermediate confining stress. It was bounded on one side by a barrier zone with higher confining stress, and on the other side by a zone with smaller confining stress. Figure 3.1 illustrates the geometry and stress profile of the laboratory test. The material properties and fluid injection parameters are presented in Table 3.1.

Since the PMMA is impermeable, there was no leak-off into the block sample. In the laboratory experiment, a constant injection rate (2.3×10^{-9} m^3/s) was used. After considering the compressibility effects of the experimental system, the injection rate was adjusted into a step-like manner as given in Table 3.1 (Wu et al. 2008). Fluid flow in the wellbore and its corresponding compressibility effects are characterized in our numerical model through a partial differential equation. A brief description of the equation and the corresponding FEM formulation are given in the Appendix of this paper. We simulate the experiment first using the adjusted injection rate

without explicitly using wellbore elements. Then, numerical simulations are performed by considering the compressibility effects of wellbore through wellbore elements. Constant injection rate at the inlet of wellbore elements is used in the latter cases.

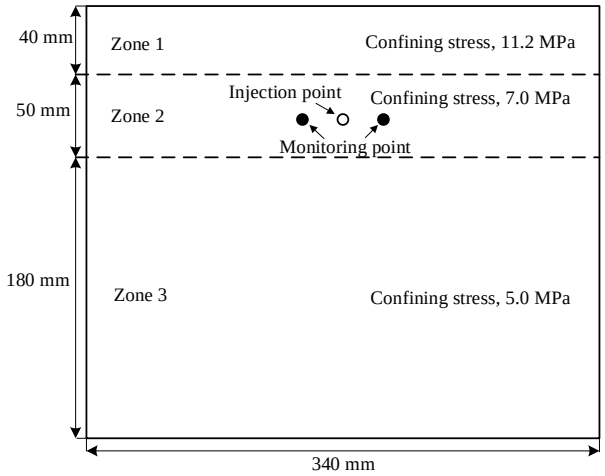

Figure 3.1 Geometry and stress configuration of the laboratory test.

Table 3.1 Material properties and injection parameters used in the laboratory test.

Poisson's Ratio, v:	0.4
Young's Modulus, E:	3.3×10^9 Pa
Fluid Viscosity, μ:	30 Pa.s
Injection rate, Q_0:	0.9×10^{-9} m^3/s ($0 < t \leq 31$ s)
	6.5×10^{-9} m^3/s ($31 < t \leq 151$ s)
	2.3×10^{-9} m^3/s ($151 < t \leq 665$ s)
Initial fracture radius, a:	5 mm

3.3.1 Simulation results for the step-like injection rate without wellbore elements

The numerical model described in Part I of this paper is utilized to simulate the laboratory experiment. The CZM parameters for the simulation are $r_n = 0.05$, tensile strength = 1 MPa, G_{IC} = 15 N/m (corresponding K_{IC} = 0.24 MPa.m$^{1/2}$). In the laboratory, the interface on which the hydraulic fracture propagates is the contact surface between two unbonded transparent PMMA blocks. Therefore, the created interface has zero tensile strength and zero energy release rate. However, finite values for CZM parameters are needed in the numerical simulation. Three

layers are built, each of which has the confining stress as shown in Figure 3.1. Figure 3.2 gives the injection pressure obtained from both the experimental records and the numerical simulation. Since the fluid is injected through a point source in the numerical model, an initially high pressure is obtained, but it rapidly drops close to the pressure observed in the laboratory test. The sudden increase of the pressure at t = 31 s corresponds to the increase of injection rate. The drop of pressure at t = 151 s is caused by the sudden decrease in the injection rate used in the simulation. The trends of the injection pressure profiles from the laboratory test and the numerical simulations have a good overall match though there is approximately 1 MPa difference. The difference is further analyzed in the following section. The fracture width, recorded at two monitoring pints at a distance of 30 mm from the injection point on the line parallel to the layered-stress interface (see Figure 3.1), is compared in Figure 3.3. The numerical results are symmetric to the injection point, and match well with those from the laboratory experiment. The fracture fronts at distinct times obtained from the laboratory observation and the numerical simulation are compared in Figure 3.4. The aperture profiles from the numerical simulation at t = 144 s and at t = 665 s are illustrated in Figure 3.5, within which the corresponding fracture fronts from the laboratory test are also given. The fracture initially propagates in Zone 2, which has the intermediate confining stress. After it reaches the boundary separating layers with different confining stress, it stops propagating towards the layer with the higher confining stress and starts growing into the layer with the lower confining stress. As shown, a very good match between the laboratory records and the numerical results is achieved. Both the laboratory experiment and the numerical simulation clearly show that the propagation of hydraulic fracture is inhibited by relatively a larger stress barrier, and is favored when a relatively smaller stress barrier is encountered.

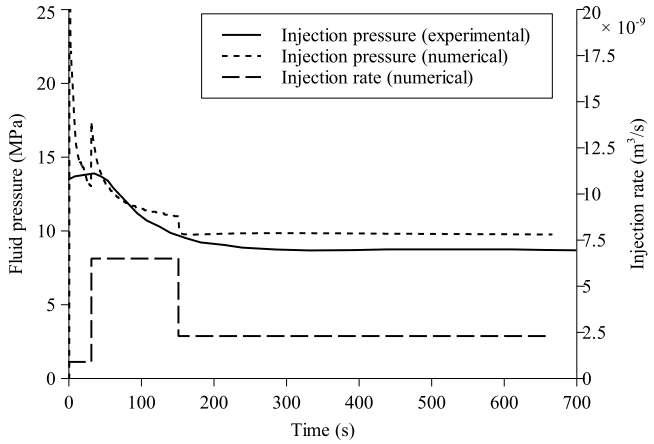

Figure 3.2 Injection pressure plotted as a function of time for the experimental observation and the numerical simulation. The jump of pressure at t = 31 s is caused by the increase in the injection rate; the drop of pressure at t = 151 s is due to the decrease in the injection rate in the simulation.

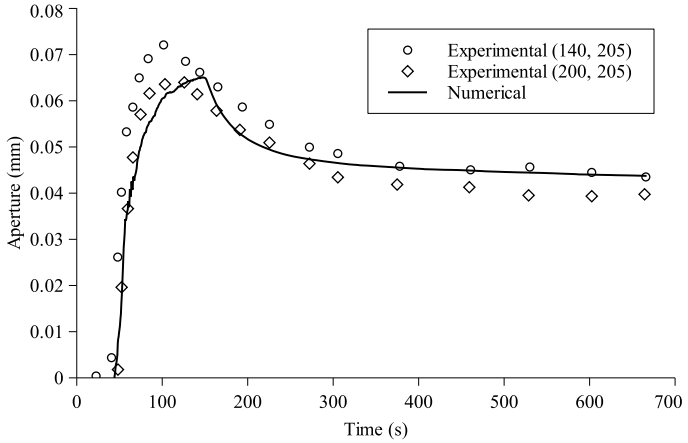

Figure 3.3 Aperture plotted as a function of time at two monitoring points for the laboratory observation and the numerical simulation. Since the two observation points are symmetric to the injection point, numerical results are identical at these locations.

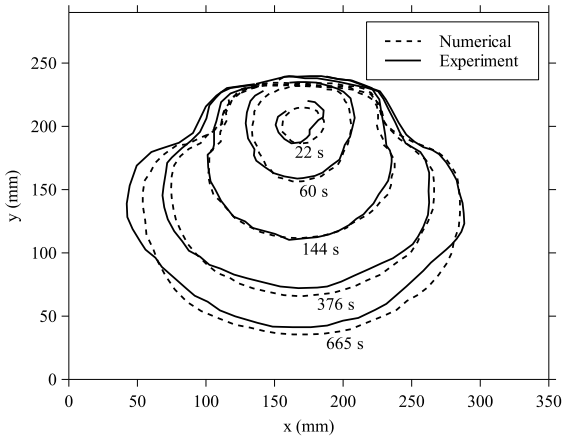

Figure 3.4 Fracture front at distinctive time from the laboratory experiment and the numerical simulation.

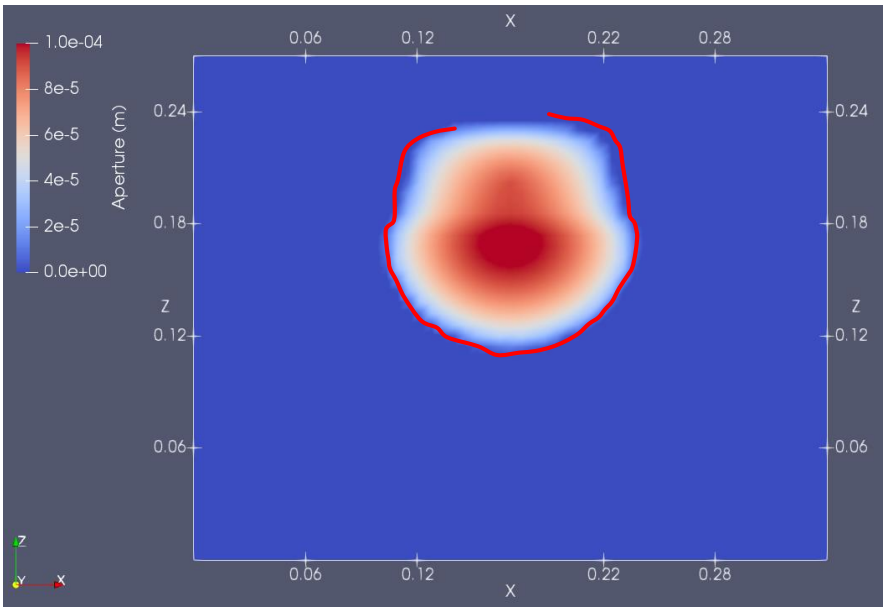

(a)

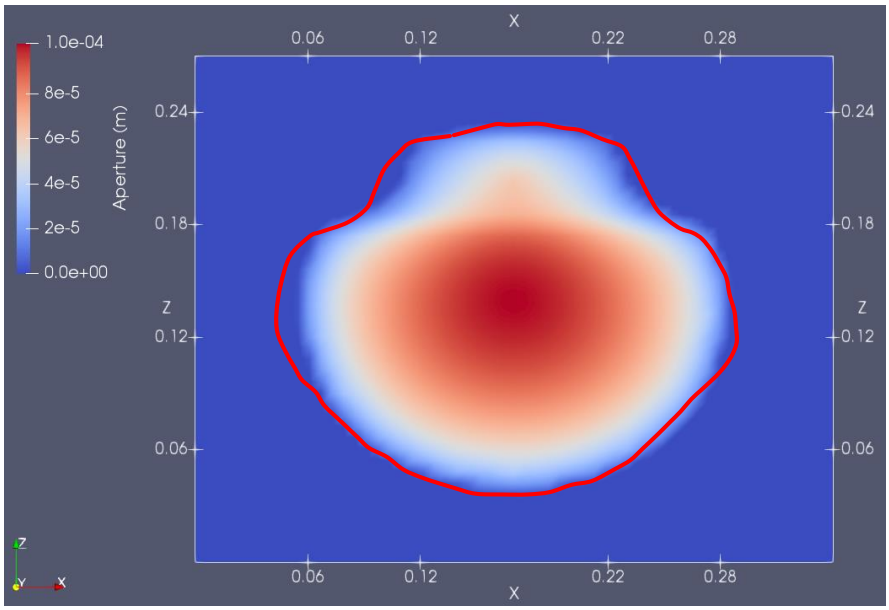

(b)

Figure 3.5 Aperture distribution from the numerical simulation at injection time of 144 s (a), and 665 s (b). The red line shows the fracture front obtained from the laboratory experiment. (Unit: m)

3.3.2 Simulation results for the constant injection rate with wellbore elements

The injection point, shown in Figure 3.1, is connected to 1D elements representing the wellbore. The compressibility effects of the wellbore (and the whole injection system) are considered through a compressibility parameter c (see the following chapter). A linear pressurization stage before the propagation of the hydraulic fracture can be observed on the pressure vs. time record from the laboratory experiment. The compressibility parameter c is calculated as 8.72×10^{-9} based on the pressure vs. time record. The geometry of the wellbore used in the simulation (length = 0.2 m; diameter = 0.01 m) is created based on the information provided by Wu et al. (2008).

As analyzed in the previous chapter, there are several CZM parameters that impact the simulation. Through comparison of the laboratory record, the influences of CZM parameters on pressure and aperture distributions are demonstrated. Three cases are considered by adjusting the slope indicator r_n and the tensile strength in numerical simulations:

- Case 1 $r_n = 0.05$ Tensile strength = 1 MPa
- Case 2 $r_n = 0.05$ Tensile strength = 2 MPa
- Case 3 $r_n = 0.2$ Tensile strength = 2 MPa

The energy release rate (G_{IC}) is 15 N/m for all the simulations. Figure 3.6 illustrates the injection pressure plotted as a function of time. The trend of numerical simulations matches well with the pressure records from the laboratory experiment. Before fracture propagation, there is a linear pressurization stage. A perfect match is obtained. After break down, the difference in injection pressure between the numerical simulations and the laboratory experiment is approximately 0.8 MPa. We use 1D wellbore elements in the numerical model to represent the 3D borehole. The fluid is injected through one node in the numerical model rather than a 3D

circular notch as used in the laboratory. These factors cause the small differences in the injection pressure. The aperture variation vs. time at the two monitoring points is shown in Figure 3.7. Results from Case 1 and Case 3 match well with the experimental records. Case 2 generates a slightly larger aperture size at the monitoring points. A relatively larger pressure and aperture are obtained in Case 2. Case 2 has a larger tensile strength compared to Case 1. It has a smaller slop indicator r_n (thus larger element stiffness) than Case 3. These observations are consistent with those sensitivity analyses performed in the previous chapter. The fracture footprints from the three cases also have a good match with those obtained from the laboratory experiment. They are not presented for the sake of brevity.

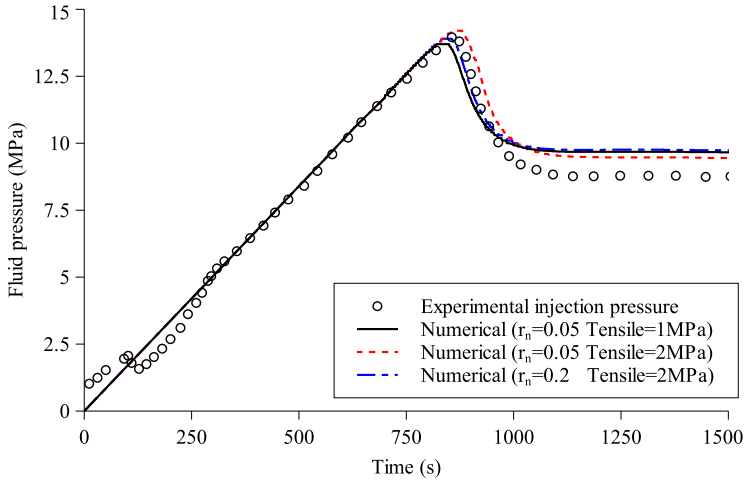

Figure 3.6 Injection pressure plotted as a function of time for the experimental observation and the numerical simulation.

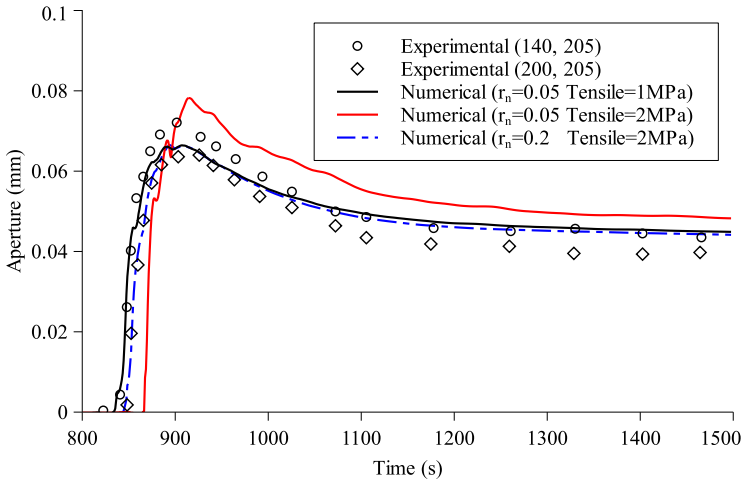

Figure 3.7 Aperture plotted as a function of time at two monitoring points for the laboratory observation and the numerical simulation.

3.4 Numerical analyses of hydraulic fracturing in layered formations

As an application of the proposed model, the influence of layered modulus on hydraulic fracturing is studied first. Thickness-weighted modulus and explicitly modeled layered modulus are used in simulations. Then, the effects of in-situ stress contrasts on hydraulic fracture propagation, especially on height growth, are investigated. Both static pressurization and quasi-static hydraulic fracture propagation are considered.

3.4.1 Effects of layered Young's modulus

Review of the literature regarding the influence of layered Young's modulus (e.g., layered formations with different modulus in each layer) suggests, compared to stress contrast, modulus contrast is probably not an important parameter that directly controls the fracture height growth. It mainly influences the fracture width and conductivity. However, hydraulic fracturing involves strongly coupled processes and the variation of fracture width caused by modulus contrast, affects the pressure distribution in the fracture, influencing fracture propagation or height growth. Since it is a common practice to calculate an average modulus from the layered modulus based on well logs, we first analyze the case of the averaging operation (or

homogenization). After obtaining the average modulus, fracture propagation is simulated using both the average modulus and the layered modulus, and the results are compared.

(1) Pressurization of a stationary fracture in a multi-layer rock system

A commonly used approach to analysis of a hydraulic fracture in a multi-layer rock system is to use an effective equivalent modulus calculated from the layers' moduli via thickness weighted averaging or homogenization. As pointed out by Smith et al. (2001), the thickness weighted average (effective modulus) is purely a mathematical treatment and does not consider the mechanical effects. In other words, it is assumed the average modulus should yield the same average width calculated based on a rigorous, layered modulus solution when the fracture is pressurized. To consider the mechanical effects in the process of assessing the impacts of the homogenization approach, a numerical experiment on fluid injection is proposed. The purpose is to evaluate whether, for the same fracture size and injection volume, the injection pressure at the end of the injection time obtained from using the average modulus approach yields the same value as that obtained based on the layered modulus. Here we evaluate at the resulting injection pressure rather than the average width, since the injection pressure is directly measurable during operations.

To simplify the analytical solution which relates the injection volume and the injection pressure to the Young's modulus, a stationary penny-shaped is considered. Based on Sneddon's solution for a penny-shaped fracture under constant internal pressure (Sneddon 1946), the volume of the fracture is a function of loading pressure, fracture radius, Young's modulus and Poisson's ratio. Through integration of Sneddon's equation for aperture profile, the volume of fracture is obtained as:

$$V = \frac{16}{3} \frac{P_{net}\left(1-\nu^2\right)a^3}{E} \tag{3.1}$$

where P_{net} is the net pressure at the end of injection, E is Young's modulus, ν is Poisson's ratio, and a is the radius of the penny-shaped fracture. To obtain a uniform distribution of the net pressure in the fracture, a small value of viscosity is assumed. Through numerical experiments utilizing layered modulus, an equivalent average Young's modulus E can be calculated using the above equation. It should be emphasized that the assumption of fixed fracture size is just for calculating the average Young's modulus. In addition, since there is a linear relationship between the injection volume and the net pressure, different injection volumes and their corresponding net pressures will yield the same Young's modulus when the same material parameters are used.

The proposed model is verified through an injection test. Figure 3.8 shows the geometry and the penny-shaped fracture. The penny-shaped fracture is discretized using zero-thickness hydro-mechanical interface elements. The inputs are given in Table 3.2.

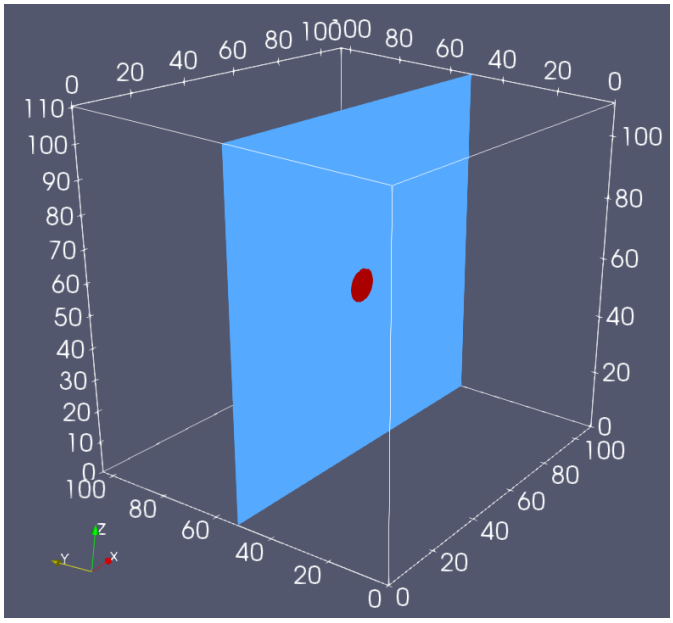

Figure 3.8 Aperture plotted as a function of time at two monitoring points for the laboratory observation and the numerical simulation.

Table 3.2 Fracture radius, rock and fluid properties used for the verification test.

Poisson's Ratio, v:	0.15
Young's Modulus, E:	3.88×10^{10} Pa
Fluid Viscosity, μ:	1.0×10^{-5} Pa.s
Injection rate, Q_0:	0.001 m^3/s
Injection time, t:	8 s
Fracture radius, a:	5 m

At the end of injection, the uniformly distributed net pressure, P_{net} is found to be 4.4×10^5 Pa. Using the net pressure and Eq. (3.1), the injected volume is calculated as 7.43×10^{-3} m^3. The relative error is around -7% when comparing the fracture volume obtained from the numerical model (0.008 m^3) to that from Eq. (3.1). Figure 3.9 illustrates the fracture half width profile. The induced stress distributions along the line perpendicular to the center point of the fracture are shown in Figure 3.10. Figure 3.11 shows the induced stresses along a line parallel to the fracture surface. The distance from the line to the fracture surface is 0.4a (2 m). As shown in the aperture and stress distributions, good agreement between numerical results and analytical solutions (Sneddon 1946) has been achieved.

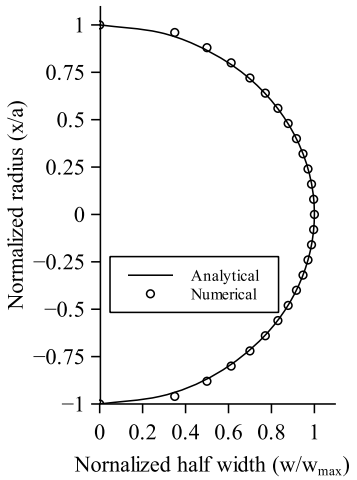

Figure 3.9 Normalized fracture half width plotted as a function of normalized fracture radius.

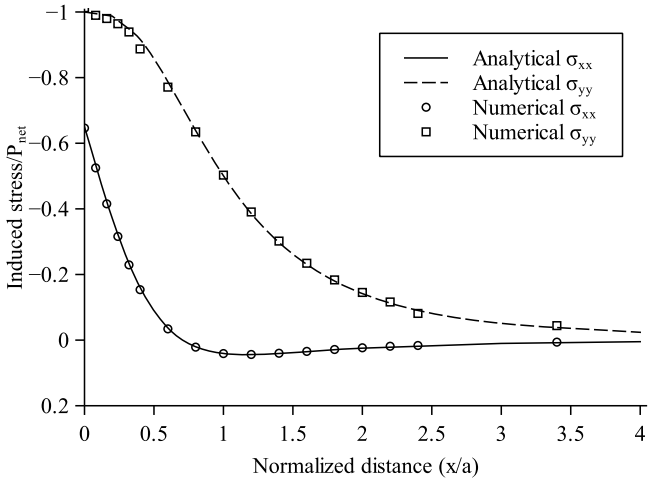

Figure 3.10 Normalized stress distributions along the line perpendicular to the center point of the fracture.

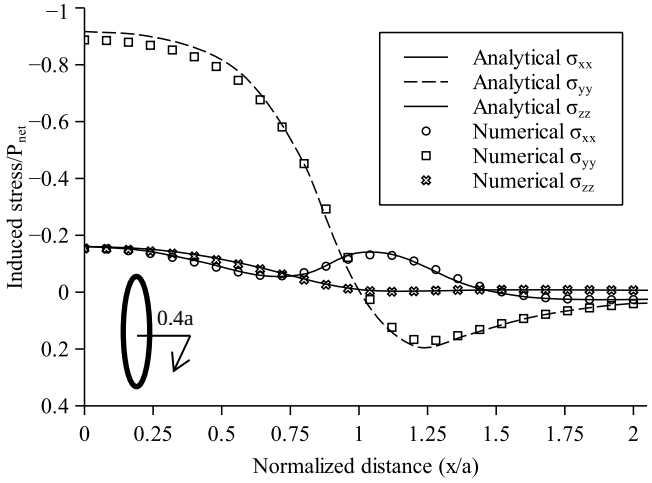

Figure 3.11 Normalized stress distributions along the line parallel to the fracture surface (the line with an arrow). The distance from the line to the fracture surface is 0.4a (0.58 m).

As an example, well log data for Woodford shale (Figure 3.12(a)) is utilized to analyze the approach of calculating an "average modulus" from layered modulus through thickness-weighted method. The thickness-weighted modulus is obtained as 16.3 GPa. Simulations are performed separately to compare the differences due to the use of layered modulus and the thickness-weighted modulus. Other parameters needed in the injection test are Poisson's ratio ν = 0.21, fracture radius a = 5.93 m, and injection volume V = 0.5 m^3. When the thickness-weighted Young's modulus is used, the numerical simulation yields an injection pressure of 7.65 MPa. Using layered modulus, the injection pressure is 7.62 MPa. A slightly higher injection pressure is

obtained when thickness-weighted Young's modulus is used. Figure 3.13(a) gives the aperture profiles generated from the analytical solution and the numerical simulations. As shown, the aperture profile is symmetric to the injection point when the thickness-weighted modulus is used. Using layered modulus, the aperture distribution is not symmetric to the injection point and relatively larger aperture size exists in the region having lower Young's modulus.

Two additional examples are investigated by adding synthetic layers into the well log. Figure 3.12(b) and Figure 3.12(c) illustrate respectively the well logs with the added synthetic layers having higher and lower Young's modulus. The average Young's moduli calculated through thickness-weighted method are 22.8 GPa and 14.4 GPa for the two cases. Figure 3.13(b) and Figure 3.13(c) plot the aperture profiles along fracture radius in vertical direction. As expected, aperture experiences variation when layers' Young's modulus is used. When thickness-weighted Young's modulus is used, the injection pressure is higher than that obtained from simulations using the layers' moduli, regardless of whether the synthetic neighboring or bounding layers have relatively higher or lower Young's moduli. Table 3.3 summarizes the injection pressures for different simulation scenarios. When four synthetic layers having relatively higher or lower Young's moduli than the surrounding rock are used, the injection pressure is approximately 9% higher than that obtained from simulations using layered moduli. The results are not listed for the sake of brevity.

Table 3.3 Injection pressures when using layered modulus and thickness-weighted modulus (average modulus) for three different scenarios.

	Woodford shale	Synthetic layers (having higher modulus)	Synthetic layers (having lower modulus)
Using layered modulus	7.62×10^6 Pa	1.00×10^7 Pa	6.25×10^6 Pa
Using average modulus	7.65×10^6 Pa	1.04×10^7 Pa	6.81×10^6 Pa

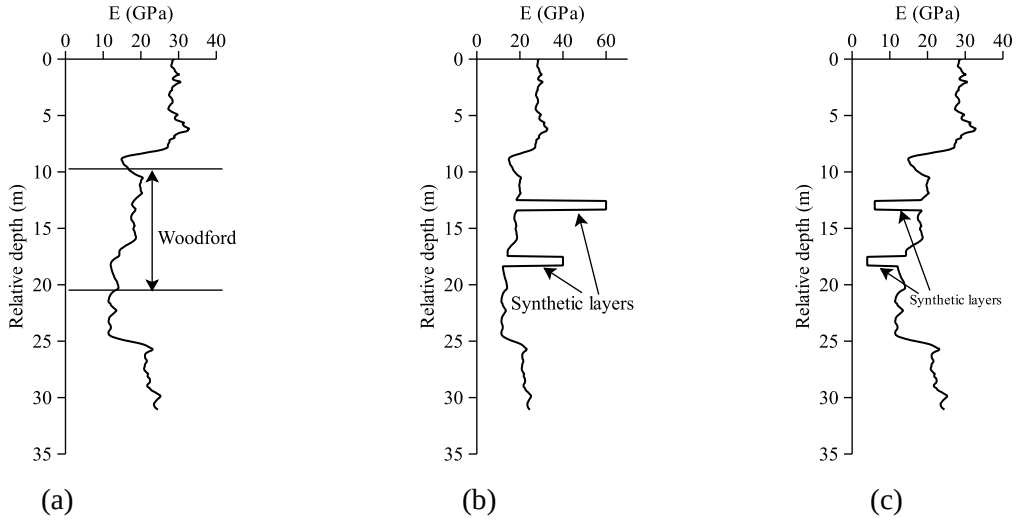

Figure 3.12 Distribution of layered Young's modulus in vertical direction: (a) Well log for Woodford shale; (b) Well log with two synthetic layers above and below the payzone having higher Young's modulus; (c) Well log with the two synthetic layers having lower Young's modulus.

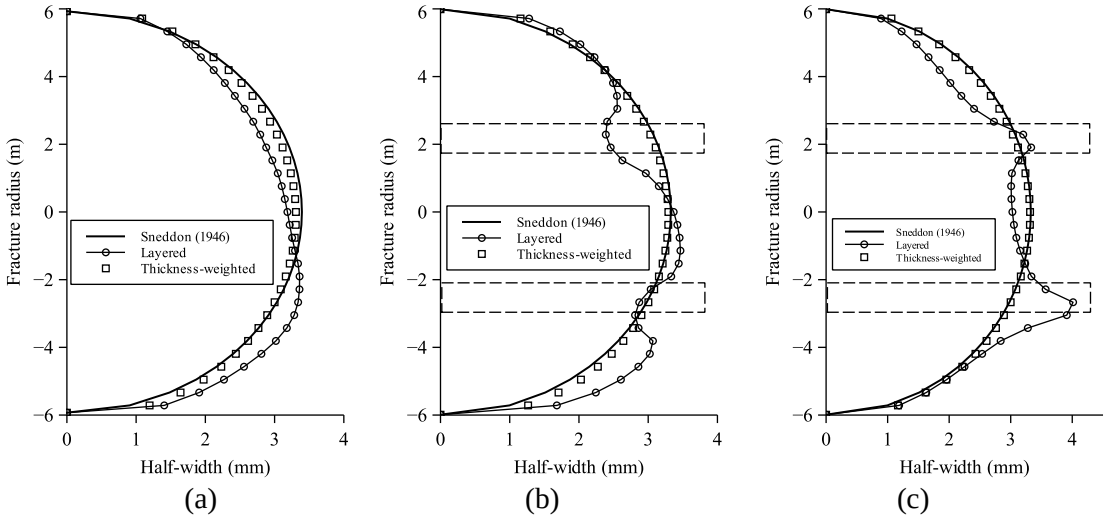

Figure 3.13 Aperture profiles plotted along fracture radius in vertical direction from simulations using layered modulus and thickness-weighted modulus (average modulus): (a) Based on well log data for Woodford shale; (b) Based on well log data with two synthetic layers having higher Young's modulus; (c) Based on well log data with two synthetic layers having lower Young's modulus. The two rectangle formed by dashed lines in (b) and (c) indicate the synthetic layers.

(2) Hydraulic fracture propagation in layered formations

Propagation of a hydraulic fracture is studied for the three scenarios in Figure 3.12. In this part, fractures form and propagate through continuous fluid injection. The parameters for the interface elements are the same as those used in the penny-shaped hydraulic fracturing in the

viscosity-dominated regime in the previous chapter. Fluid is injected for 11.5 s at a rate of 0.02 m^3/s. The injection point is located at 15.6 m. Figure 3.14 illustrates the aperture and pressure profiles in vertical direction passing through the injection point for the three scenarios. As can be seen, the aperture profiles from the simulation using the thickness-weighted modulus are not penny-shaped (unlike those from the simple pressurization of a stationary fracture-Figure 3.13).

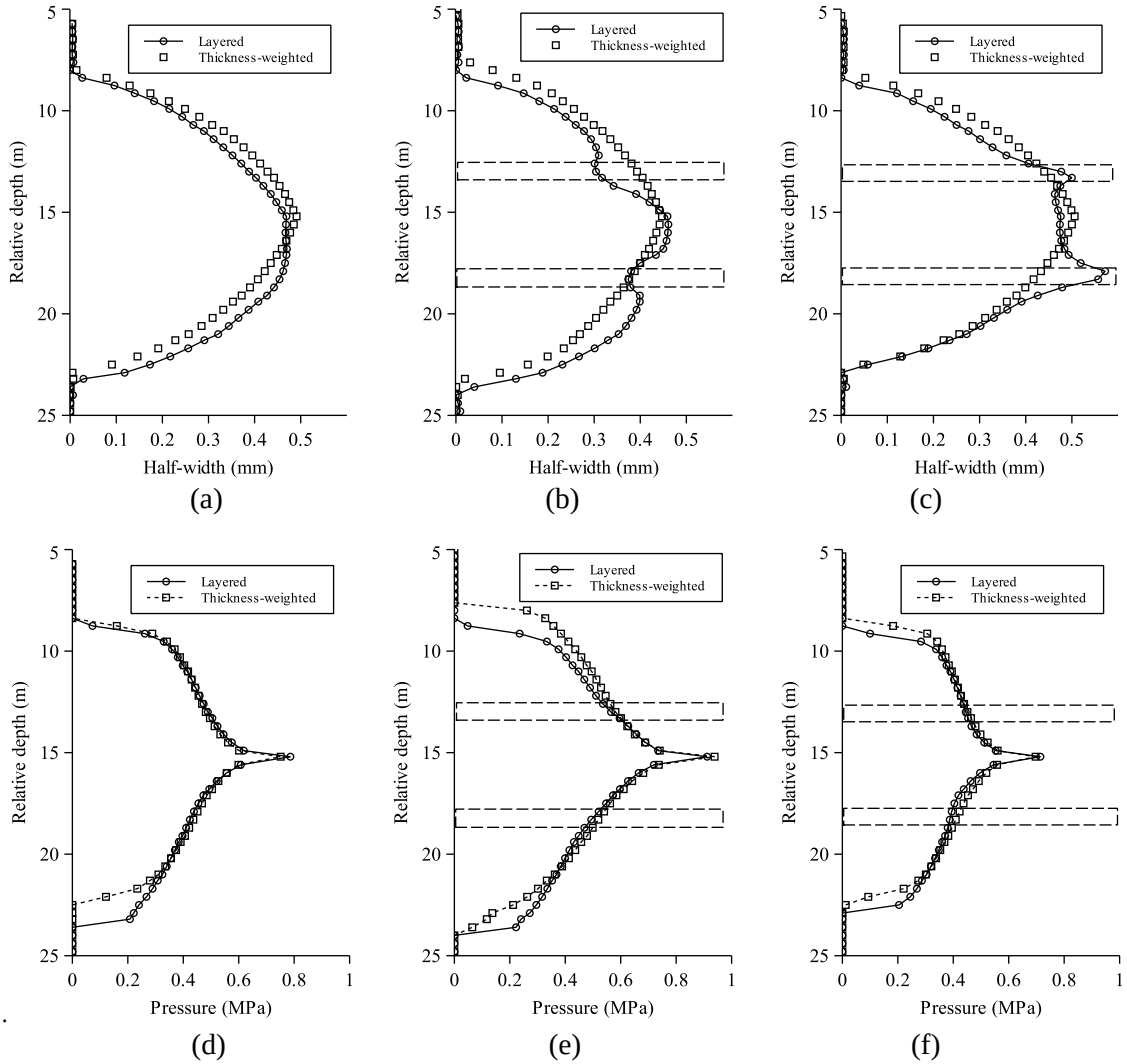

Figure 3.14 Aperture and pressure profiles from FEM plotted in vertical direction passing through the injection point after11.5 seconds of fracture propagation: (a)+(d) Based on well log data for Woodford shale; (b)+(e) Based on well log data with two synthetic layers having higher Young's modulus; (c)+(f) Based on well log data with two synthetic layers having lower Young's modulus. The two rectangle formed by dashed lines indicate the synthetic layers.

For the stationary fracture case, a uniform pressure is applied. However, in quasi-static hydraulic fracturing, the pressure within the hydraulic fracture decreases from the injection point to the fracture edges, as shown in Figure 3.14 (d), (e) and (f). Focusing on the results using layered moduli, a number of observations can be made. Comparing Figure 3.14 (b) to (a), the fracture aperture in a softer layer between two stiffer synthetic layers (having larger Young's modulus) is larger than the case without the synthetic layers. In other words, the presence of higher modulus layers makes the fracture in the softer rock layer between them experience more deformation. Comparing Figure 3.14 (c) to (a), the two softer synthetic layers generate a larger aperture fracture; the low modulus synthetic layers also influence the deformation of their surrounding formations through the leverage effect. Figure 3.14 (d), (e) and (f) illustrate the pressure profile within the hydraulic fracture. The maximum injection pressure from the simulations using thickness-weighted modulus is close to that when layered moduli are explicitly modeled though they have different profiles. The existence of layers with larger or lower Young's modulus does not cause too much variation in the pressure profiles.

To analyze the influence of Young's modulus on hydraulic fracture propagation, modulus contrasts are assumed to exist in the vertical direction. Two scenarios are considered. As shown in Figure 3.15, in one scenario the modulus above the injection location is 2 times larger than that below the injection location (Figure 3.15 (a)); in the other scenario, the modulus above the injection location is 4 times as large as that below the injection location (Figure 3.15 (b)). Fluid viscosity is 1.0 cp. The injection rate is 0.004 m^3/s. A fixed displacement in the direction perpendicular to the fracture is applied on the boundary surfaces.

The aperture distributions after 24 seconds of injection are shown in Figure 3.16. As illustrated, instead of propagating symmetrically about the injection point, the fracture mainly

propagates along the zone with lower Young's modulus, especially in the presence of a larger modulus layer (Figure 3.16 (b)). Although hydraulic fracture propagates into the higher Young's modulus layers above, its aperture size (≈ 0.2 mm) is much less than that (≈ 0.6 mm) that in the lowest Young's modulus layer. In addition, the simulation using a higher modulus contrast (Figure 3.16 (b)) generates a smaller fracture height when compared to the simulation with lower modulus contrast (Figure 3.16 (a)).

To further investigate the influence of Young's modulus contrast on the growth of fracture height and length, consider a scenario with one relatively higher Young's modulus (16 GPa) layer is confined by upper and lower layers having lower Young's moduli (4 GPa) (Figure 3.15 (c)). As shown, the fluid is injected into the layer having a higher Young's modulus. Other parameters are the same as those used in the previous example. For comparison purpose, an additional scenario using a uniform Young's modulus (16 GPa) is also modeled.

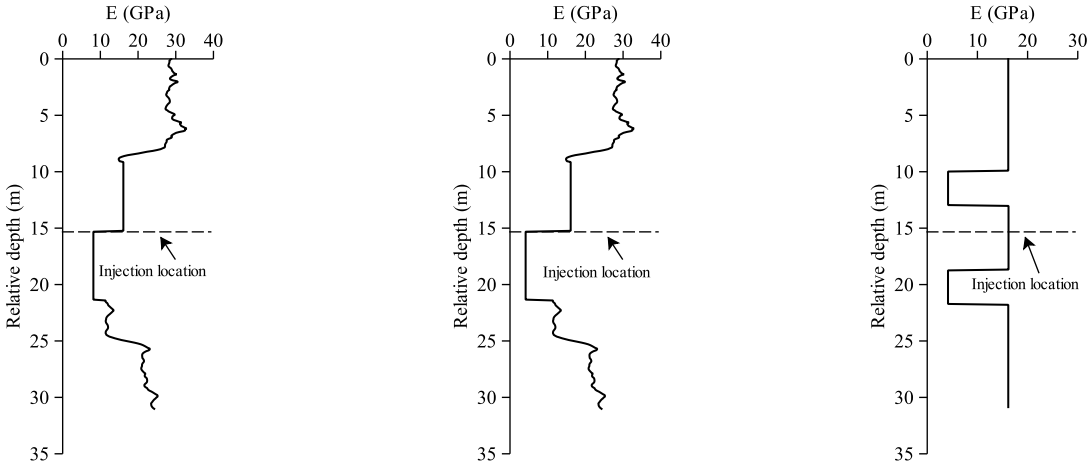

Figure 3.15 Distribution of layered Young's modulus in vertical direction: (a) modulus above the injection location is 2 times larger than that below the injection location; (b) modulus above the injection location is 4 times larger than that below the injection location; (c) fluid injected into the layer with relatively higher Young's modulus that is confined by top and bottom layers having lower Young's modulus.

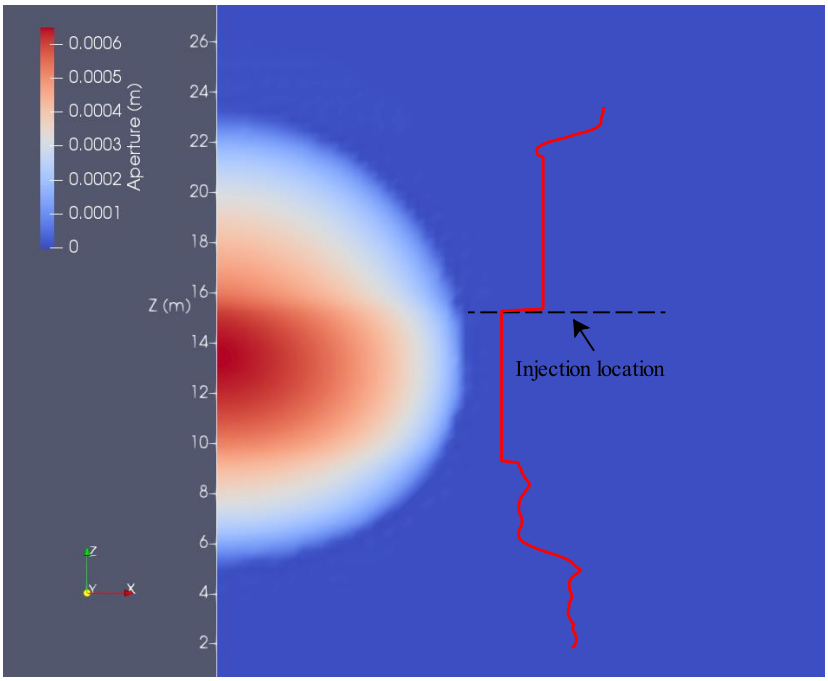

(a)

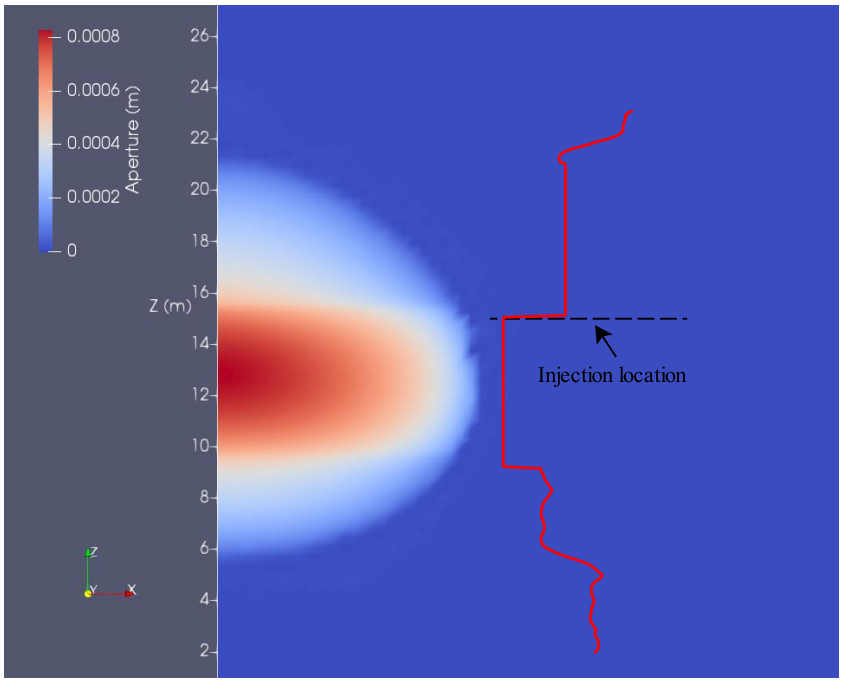

(b)

Figure 3.16 Aperture distribution on a vertical plane passing through the injection point: (a) lower modulus contrast; (b) higher modulus contrast. The red lines indicate the variation of Young's modulus.

Figure 3.17 illustrate the aperture distribution at two different time (time = 12 s and time = 24 s). It can be seen that the hydraulic fracture mainly propagates in the lower modulus layers. The aperture in the upper and bottom layers are larger than that in the middle layer where the injection point is located and having larger Young's modulus. After the hydraulic fracture reaches the upper and bottom layers, it propagates faster (in the lateral direction, i.e., length growth, not vertical growth) in those layers compared to its propagation in the middle layer. The aperture of the hydraulic fracture in the upper and lower layers favors the fracture opening in the middle layer, making it wider compared to the case with stiffer bounding layers, benefiting fluid flow, and hence making fracture propagation relatively easier in the middle layer through the leverage effect. As for the scenario with a uniform Young's modulus, the aperture distribution and fracture propagation are always symmetric to the injection point.

Another interesting phenomenon is related to the fracture height growth. After the hydraulic fracture reaches the upper and bottom layers, it mainly propagates laterally instead of vertically. The layers with lower Young's modulus act as barriers that prevent the fracture propagating in the vertical direction, thus limiting the height growth. It should be emphasized that all the scenarios in this section are for fracture propagating in viscosity-dominated regime. Most of energy is spent on fluid flow. The energy spent on creating new fracture or "conquering the fracture toughness" is negligible. Also, the layers are assumed to be fully bonded so that the interaction between the hydraulic fracture and bedding planes is not considered. This is the subject of another forthcoming study.

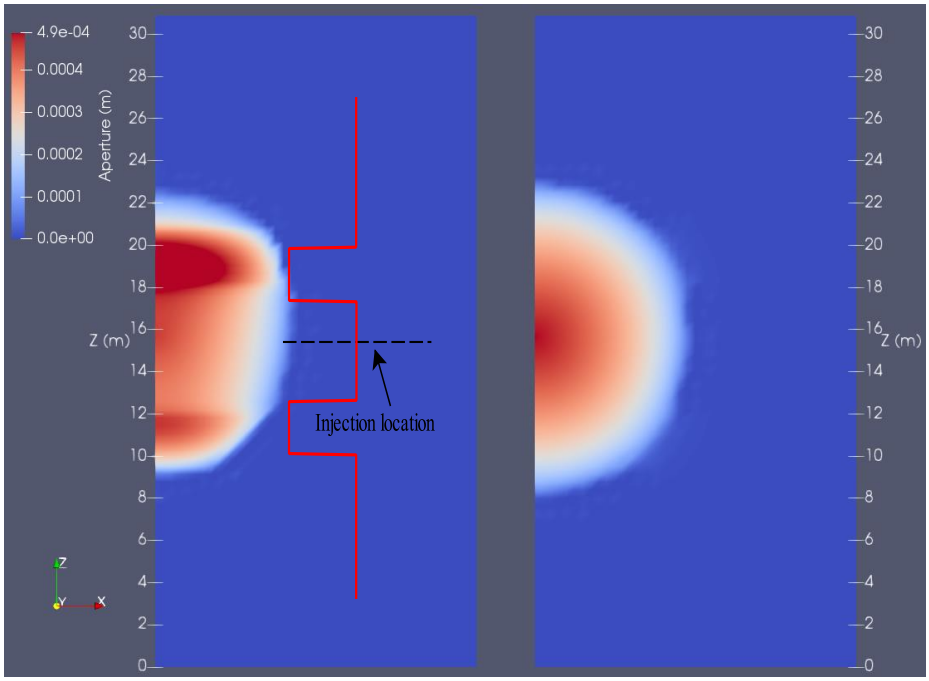

(a)

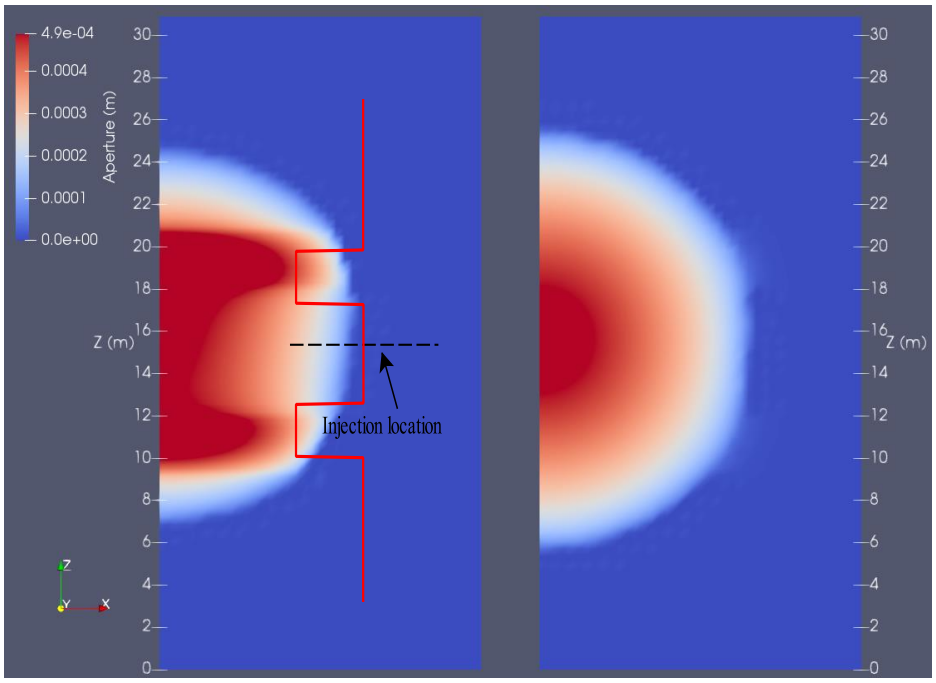

(b)

Figure 3.17 Aperture distribution on a vertical plane passing through the injection point: (a) time = 12 s; (b) time = 24 s. Left figures are for the simulation using layered modulus; right figures are for the simulation having a uniform Young's modulus (16.1 GPa).

3.4.2 Effects of in-situ stress

In-situ stress in a reservoir could vary in both vertical and horizontal directions. To simplify analyses, it is assumed that all the three principal stresses (minimum horizontal stress, maximum horizontal stress, vertical stress) are constant in each horizontally layered formation; differences in in-situ stress exist when changing from one layer to another. In equilibrium height model, a plane strain fracture (2D) is embedded in a homogeneous isotropic medium and is uniformly pressurized by a fluid. The layers surrounding the fracture have step variations in in-situ stress. The location of top and bottom tips of the fracture is determined by the requirement of equilibrium between the stress intensity factor and the fracture toughness. In this section, we first give the results obtained from static pressurization. Then hydraulic fracture propagation is modeled through fluid injection.

Figure 3.18 illustrates a symmetric configuration of a pressurized fracture in a three layer stress system. The center layer has a height of $2H$ with a minimum horizontal stress of σ_a. The top and bottom layers have the minimum horizontal stress of σ_b. The height of the hydraulic fracture is $2l$. The penetration depth of the hydraulic fracture in the adjacent layers is h ($h = l - H$). Based on the work of Simonson et al. (1978), the following equation, which relates fluid pressure p to the half-height of hydraulic fracture l, can be derived:

$$\frac{\sigma_b - p}{\sigma_b - \sigma_a} = \frac{2}{\pi}\sin^{-1}\left(\frac{H}{l}\right) - \frac{K_{Ic}}{\left(\sigma_b - \sigma_a\right)\sqrt{\pi l}} \tag{3.2}$$

Using the parameters given in Table 3.4, the net pressure ($p_{net} = p - S_{hmin}$) using Eq. (3.2) is plotted as a function of the fracture half-height (l) in Figure 3.19. Before the hydraulic fracture propagates into the formation with a higher in-situ stress (when $l < H$), the applied pressure gradually decreases as the fracture length and height increase. After the hydraulic fracture propagates across the boundary where the stress contrast exists, the net pressure begins to

increase dramatically, though it is still lower than the stress difference between the layers (σ_b - σ_a = 3MPa).

Table 3.4 Fracture radius, rock and fluid properties used for the verification test.

Poisson's Ratio, v:	0.15
Young's Modulus, E:	3.88×10^{10} Pa
Fracture toughness, K_{Ic}:	1.0×10^{6} Pa.m$^{1/2}$
Stress contrast, σ_b - σ_a:	3.0×10^{6} Pa
Height (center formation), $2H$:	40.0 m

Note: E and v are not needed in Eq. (3.2). But they are used in the numerical model.

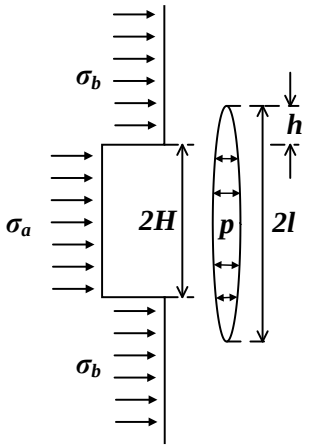

Figure 3.18 Pressurized vertical fracture in a layered-stress medium. *h* indicates the penetration depth of the pressurized fracture in the bounding layers.

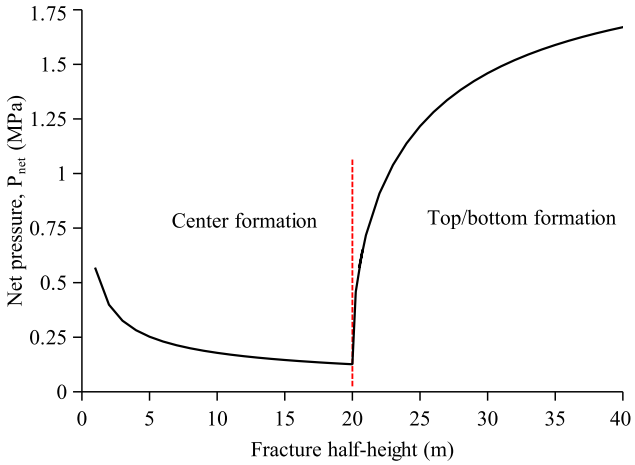

Figure 3.19 Net pressure, p_{net}, from Eq. (3.2) plotted as a function of the fracture half-height, l. The red dash line indicates the interface that separates the center formation from the top (or bottom) formation. When $l < H$ (H = 20 m), the hydraulic fracture is confined in the center formation as illustrated in Figure 3.18.

The finite element model is also utilized to simulate the pressurization test (Figure 3.18) using the parameters provided in Table 3.4. Instead of adjusting the fracture height to match the given fracture toughness under the applied fluid pressure, we apply the fluid pressure on a given fracture height and then check whether the calculated stress intensity factor equals the given fracture toughness (K_{Ic} = 1.0 MPa.m$^{1/2}$). Figure 3.20 illustrates the calculated stress intensity factor. As can been seen, the maximum relative error is less than +14%.

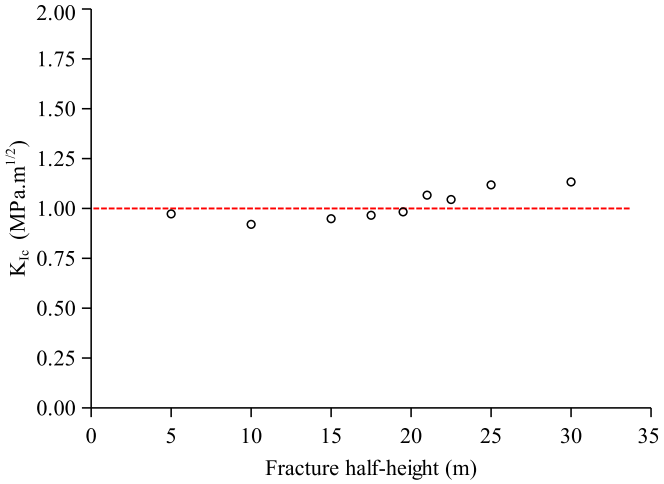

Figure 3.20 Calculated stress intensity factor in numerical simulations using the applied fluid pressure and the fracture half-height from Eq. (3.2), as shown in Figure 3.19. The red dash line indicates the assumed fracture toughness (K_{Ic} = 1.0 MPa.m$^{1/2}$), based on which the fluid pressure and the fracture half-height are obtained.

The aperture distribution during pressurization is also investigated in this study. Through comparison of aperture, a clearer picture about the "real" fluid pressure, which should be calculated based on a fully coupled hydro-mechanical model (rather than pressurization), could be obtained since the fluid pressure is strongly coupled with fracture conductivity which is proportional to the cube of aperture size. The relationship between in-situ stress and fluid pressure (Eq. (3.2)) is derived based on the superposition method according to the principles of fracture mechanics. However, the aperture size is rarely reported in works related to the equilibrium-height model since the analytical formulation for aperture involves a complex

integration and it is not easy to obtain in a straightforward manner. In numerical models, the aperture distribution is a natural part of the solution (no post-processing is needed). Figure 3.21 gives the aperture distribution plotted as a function of the fracture half-height. Before the pressurized fracture is extended across the formation boundary into the high stress zone, the analytical solution can be obtained from Sneddon and Elliot (1946). As shown in Figure 3.21 (a), our numerical results match well with the analytical solution. After the tips of the pressurized fracture penetrate the bounding layers where the higher minimum horizontal stress exists, the fluid pressure increases dramatically (Figure 3.19) provided that the calculated stress intensity factor is equal to the given fracture toughness; the corresponding aperture size also exhibits a jump (Figure 3.21 (b)). The stress contrast makes the aperture increases almost by one order of magnitude when the fracture propagation criterion is satisfied.

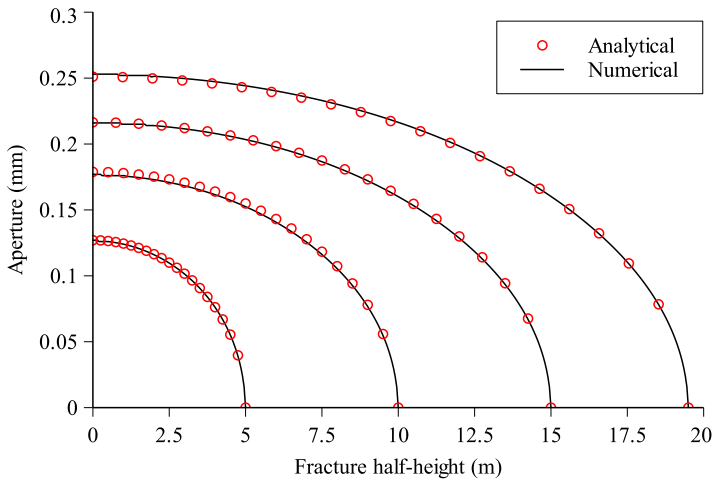

(a)

Figure 3.21 (a) aperture distribution before the pressurized fracture extends across the location where the stress contrast exists; (b) aperture distribution for the fracture half-height ranging from 5 m to 30 m. When fracture is confined in the center formation ($l \leq 20$ m), the analytical solution of aperture is available from Sneddon and Elliot (1946) as indicated by the red circles; after crossing into the layer with higher confining stress, the analytical solution for aperture is provided in an integral form, no straightforward expression exists. (continued)

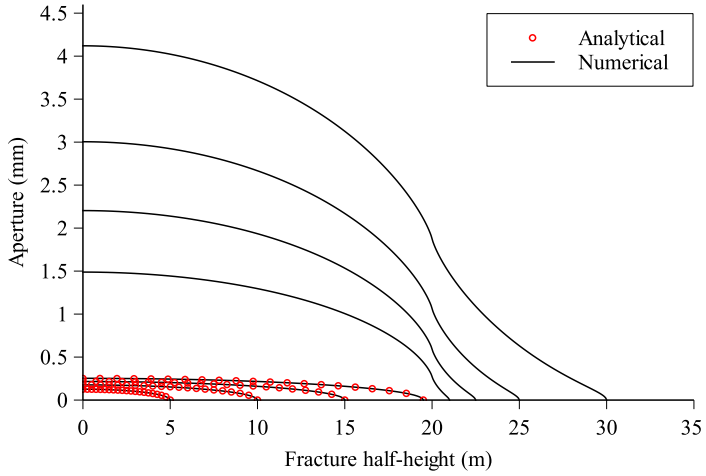

(b)

Figure 3.21 (continued). (Caption shown on previous page.)

(1) A KGD hydraulic fracture

To compare the behavior of the hydraulic fracture under static pressurization (equilibrium-height model) and the injection-induced propagation (fully coupled model), the KGD hydraulic fracture and 3D planar hydraulic fractures are modeled using the parameters provided in Table 3.4. This section details the analysis for the case of a KGD hydraulic fracture. The injection rate is 0.002 m^2/s (3D model is used to simulate the plane strain condition), fluid viscosity is 1.0 cp. The calculated dimensionless toughness is 0.51. The configuration of in-situ stress is the same as that shown in Figure 3.18. There are three layers. The minimum horizontal stress in the top and bottom layers is 3 MPa larger than that in the middle layer. The injection point is located at the center of the middle layer. For asymptotic analytical solutions (Detournay 2004), are applicable when no stress contrast exists so that numerical results can still be compared with the asymptotic solutions before the hydraulic fracture propagates into layers with higher in-situ stress.

Figure 3.22 gives the aperture size and fluid pressure at the injection point; it also shows the fracture half-height plotted as a function of time. At *time* = 14.5 s, the hydraulic fracture reaches the stress contrast boundaries. As shown, the numerical results match well with the

asymptotic solutions before 14.5 s; as the fracture penetrates into the top and bottom bounding layers, the numerical results deviate from the asymptotic analytical solutions. At the injection time of 50 s (after fracture crosses the stress boundaries), the fracture half-height, aperture size and net pressure at the injection point are 23.7 m, 2.94 mm and 1.32 MPa, each according to the numerical simulation. The corresponding values from the asymptotic solution are 45.6 m, 1.53 mm and 0.40 MPa. The difference is not small. When stress contrast exists, the hydraulic fracture almost stops propagating.

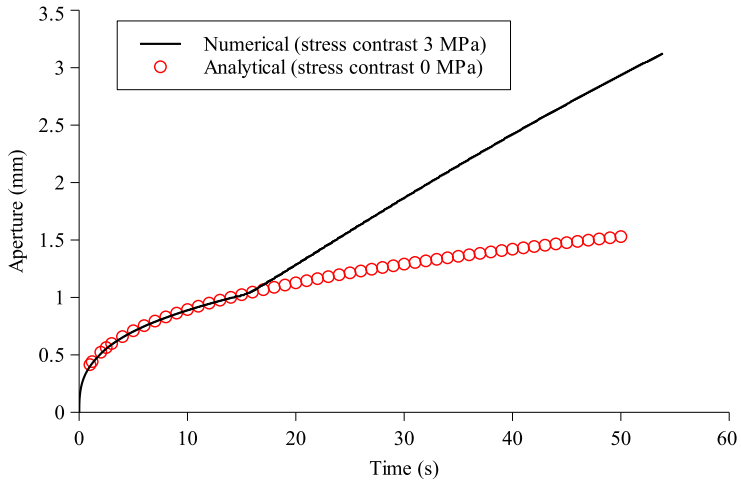

(a)

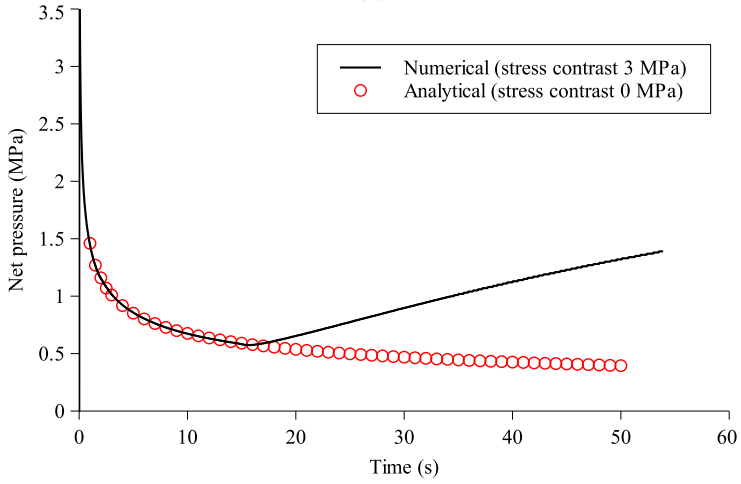

(b)

Figure 3.22 (a) Aperture distribution plotted as a function of time at the injection point; (b) Injection pressure plotted as a function of time at the injection point; (c) Fracture half-height plotted as a function of time. (continued)

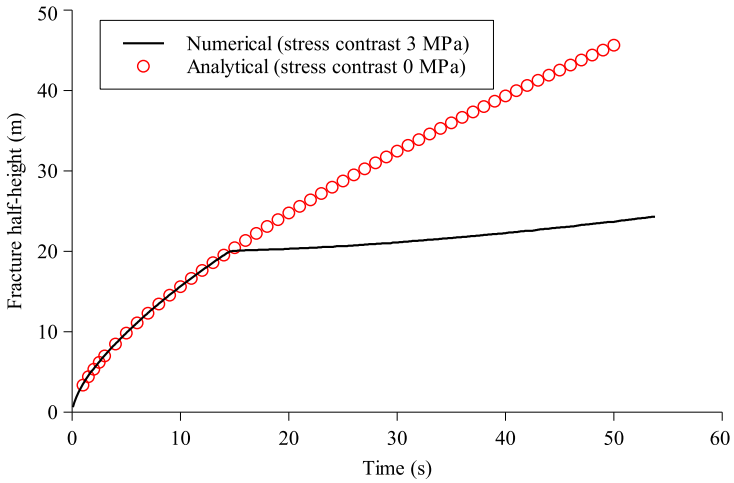

(c)

Figure 3.22 (continued). (Caption shown on previous page.)

The aperture and pressure profiles along the fracture height are plotted in Figure 3.23 (injection time ≤ 15 s) and Figure 3.24 (injection time ≥ 18 s). As illustrated, when injection time < 14.5 s, the hydraulic fracture is still confined in the middle layer (20 m of half-thickness); numerical results match well with the asymptotic analytical solutions. At injection time = 15 s, the hydraulic fracture slightly grows into the bounding layer (Figure 3.23a); the fluid pressure starts building up at tips (Figure 3.23b). As the injection is continued, the aperture and pressure profiles differ dramatically with those from the asymptotic analytical solutions. After the fracture propagates into the layers with higher in-situ stress, the fracture aperture and fluid pressure continuously increase; however, the fracture height growth is nearly impeded.

For comparison purpose, stress contrast of 1 MPa is also used in simulations. Figure 3.25 shows the aperture and net pressure profiles. The fracture half-height does not increase much when compared to the zero stress contrast solutions, though it is larger than that obtained with 3 MPa stress contrast.

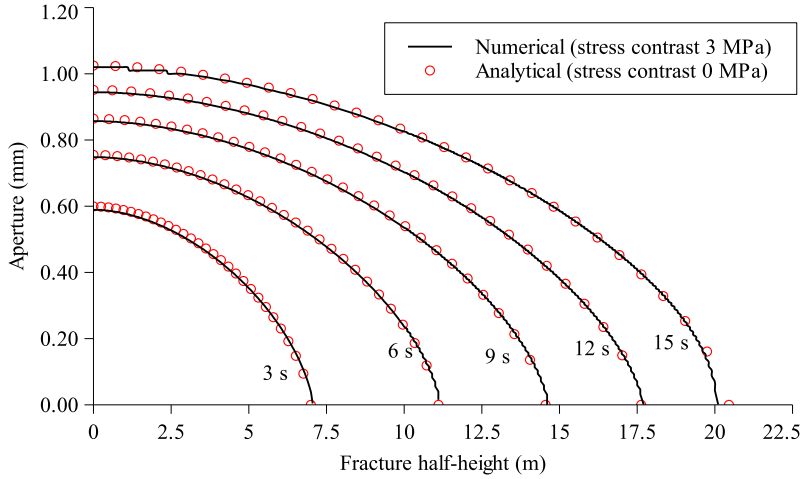

(a)

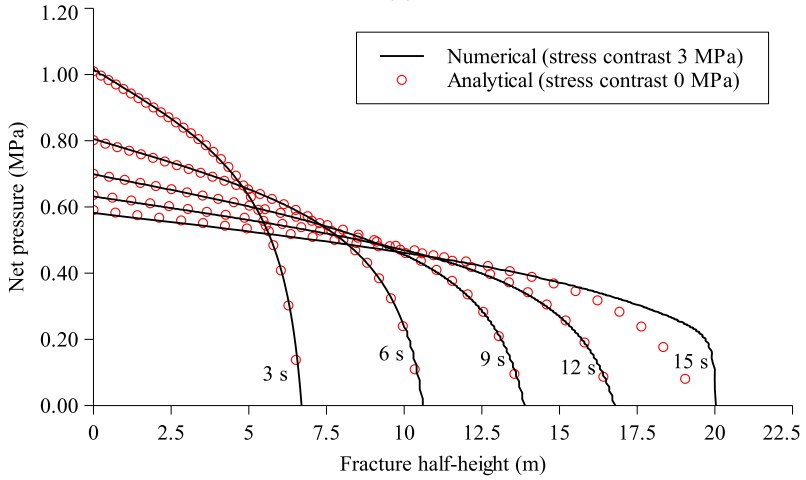

(b)

Figure 3.23 (a) Aperture profiles at different injection times; (b) Pressure profile at different injection times. At 14.5 second, the hydraulic fracture reaches the location where the stress contrast (3MPa) exists. When *time* < 14.5 s, the numerical results match well with the asymptotic analytical solutions (no stress contrast exists).

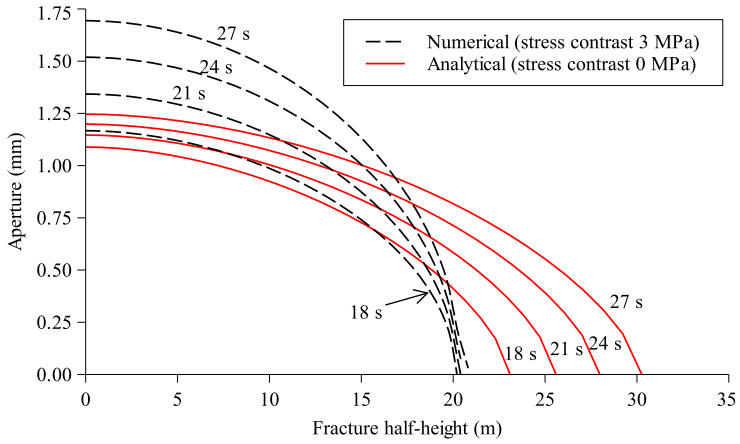

(a)

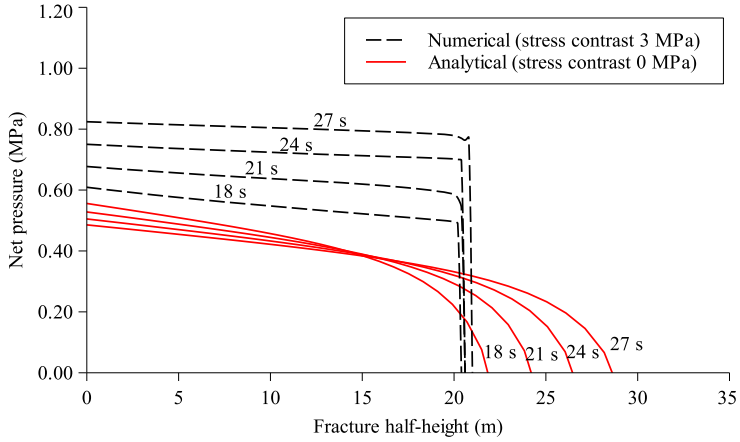

(b)

Figure 3.24 (a) Aperture profiles at different injection times; (b) Net pressure profiles at different injection times. When *time* > 14.5 s, the hydraulic fracture slightly passes across the stress contrast boundaries; the numerical results differ dramatically with the asymptotic analytical solutions. The stress contrast used in the numerical model is 3 MPa.

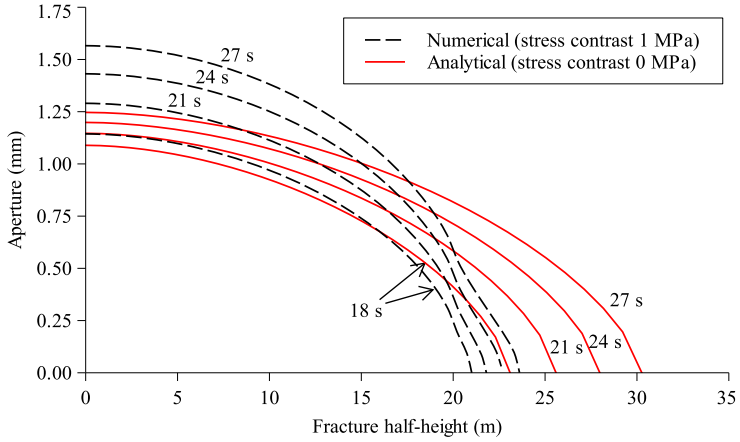

(a)

Figure 3.25 (a) Aperture profiles at different injection times; (b) Pressure profiles at different injection times. The stress contrast used in the numerical model is 1 MPa. (continued)

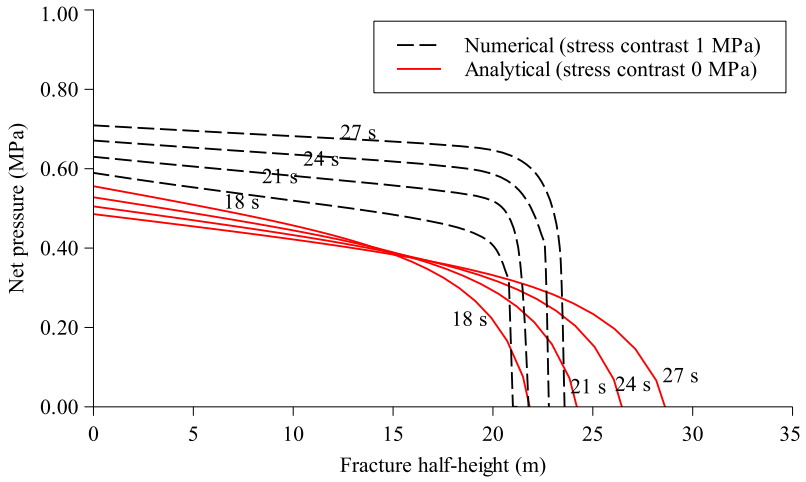

(b)

Figure 3.25 (continued). (Caption shown on previous page.)

Comparing the aperture size distribution obtained from the static pressurization (Figure 3.21b) to that from KGD hydraulic fracture with zero stress contrast (Figure 3.24a and Figure 3.25a) and to that from KGD hydraulic fracture with 1 MPa and 3 MPa stress contrast (Figure 3.24a and Figure 3.25a), the influence of in-situ stress contrast on aperture and fluid pressure is obvious. It restricts the height growth of the hydraulic fracture. It also reduces the aperture size in the higher in-situ stress layer. From simulations based on the fully coupled model, the growth of fracture height is almost impeded by the stress contrast and the fluid pressure in higher stress layers decreases dramatically. This fact underscores the inapplicability of the static pressurization approach (the equilibrium height model) in estimating the hydraulic fracture height in the viscosity-dominated regime.

(2) A 3D planner hydraulic fracture

In this section we consider the influence of in-situ stress contrast on the propagation of a planar 3D hydraulic fracture using the parameters provided in Table 3.4. The injection rate is 0.004 m^3/s, and fluid viscosity is 1.0 cp. The base case has a uniform confining stress of 10 MPa. Three additional scenarios having two bounding layers with confining stress higher than 10 MPa

are considered (Figure 3.26) with the stress contrasts of 0.5 MPa, 1.0 MPa, and 3.0 MPa, respectively.

The aperture profile for each scenario is plotted in Figure 3.26. The fracture propagates symmetrically in relation to the injection point in the absence of a stress contrast. As the confining stress in the top and bottom bounding layers increases, the fracture height growth is limited by the stress barriers and the fracture tends to grow in the lateral direction in the middle layer (where the injection interval is located). When the stress contrast = 3 MPa, the fracture is completely confined in the middle layer.

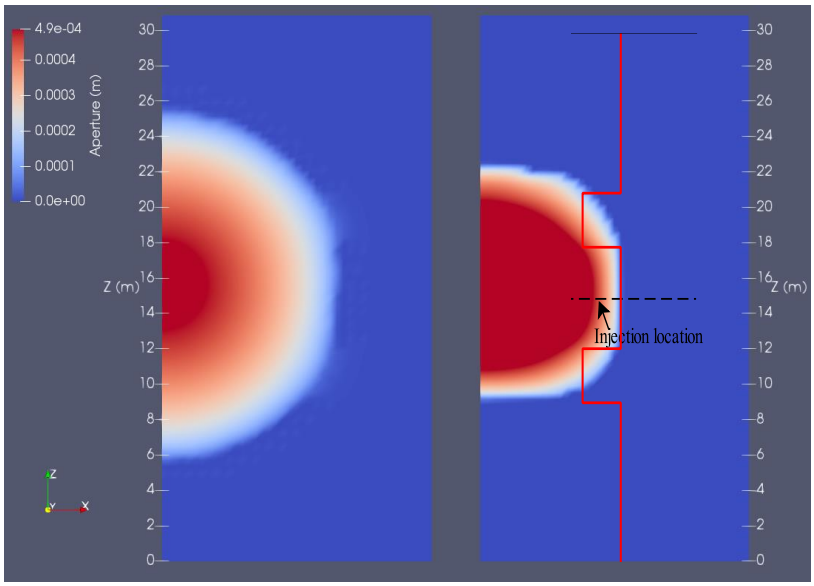

(a)

Figure 3.26 Aperture profiles at t = 24 s. (a) left figure has zero stress contrast, right figure has 0.5 MPa stress contrast; (b) left figure has 1.0 MPa stress contrast, right figure has 3.0 MPa stress contrast. The red line indicates the variation of confining stress as a function of depth. (continued)

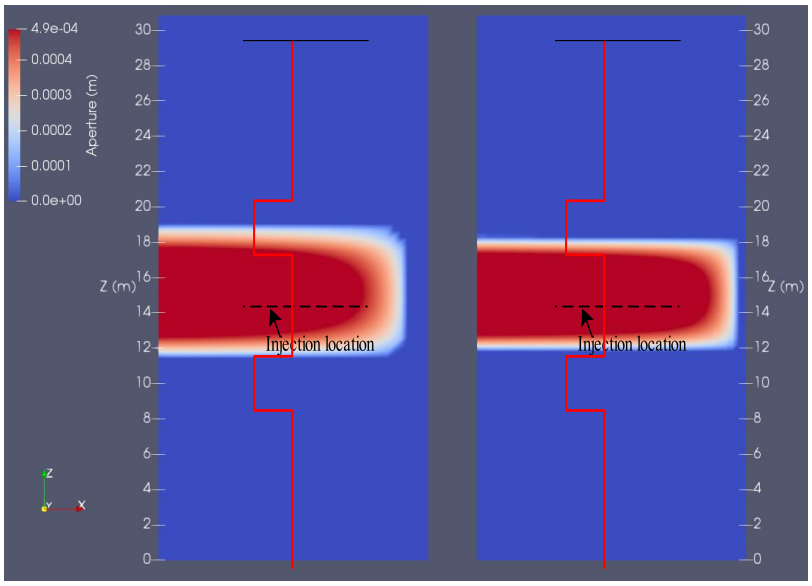

(b)

Figure 3.26 (continued). (Caption shown on previous page.)

3.4.3 The combined effects of the in-situ stress and Young's modulus heterogeneity

In previous sections, the factors that influence the height growth of hydraulic fractures are analyzed considering separately the Young's modulus and the in-situ stress. It is highly probable that layered rocks with different material properties have different confining stresses as well and vice versa. To gain some insights into the behavior of hydraulic fractures propagating in layered rock with variation of both Young's modulus and in-situ stress, a KGD hydraulic fracture is studied (to facilitate solution comparison). As shown in Figure 3.18, three layers in vertical direction are considered, with the center layer having a thickness of 20 m. The upper and lower bounding layers have the same properties. The injection point is located in the middle of the center layer. Under these configurations, the model is symmetric with respect to the injection point. The center layer has a minimum horizontal stress of 10 MPa. The bounding layers have a minimum horizontal stress of 10.5 MPa for one scenario and of 13 MPa for another scenario. Poisson's ratio is 0.15, the injection rate is 0.001 m^2/s, and the fluid viscosity is 1.0 cp. The

energy release rate G_{IC} is calculated using the fracture toughness K_{IC} being 1 MP.m$^{1/2}$. Three cases are considered for the distribution of Young's modulus:

- Case 1 Center layer E = 38 GPa Bounding layer E = 19 GPa
- Case 2 Center layer E = 38 GPa Bounding layer E = 38 GPa
- Case 3 Center layer E = 19 GPa Bounding layer E = 38 GPa

Figure 3.27 shows the aperture, net pressure and fracture half-height distributions for the 0.5 MPa stress contrast scenario. At about 5.2 seconds, the hydraulic fracture in case 1 and case 2 (Young's modulus in the center layer is 38 GPa for both cases) propagates to the formation boundary where the stress contrast and the modulus contrast exist. It arrives at the formation interface at about 7 seconds for case 3. After crossing the formation interface, the hydraulic fracture in case 1 (bounding layer E = 19 GPa) grows slower than that in case 2 (bounding layer E = 38 GPa), as indicated in Figure 3.27(c). Compared with case 1 and case 2, the case 3 hydraulic fracture has a larger aperture size and a smaller net pressure at the injection point, as well as a smaller half-height. Apparently these are caused by the relatively small Young's modulus in the center layer in case 3. These observations give us some hints about the selection of injection location in hydraulic fracture design. Injection in a zone having a relatively larger Young's modulus tends to generate larger fracture length and height under the plane strain condition shown in Figure 3.18(i.e., when fracture length is much larger than fracture height), and thus covers a relatively larger drainage area.

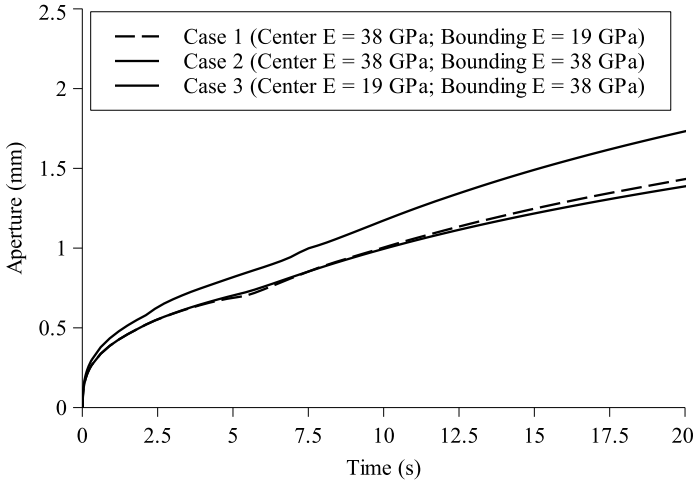

(a)

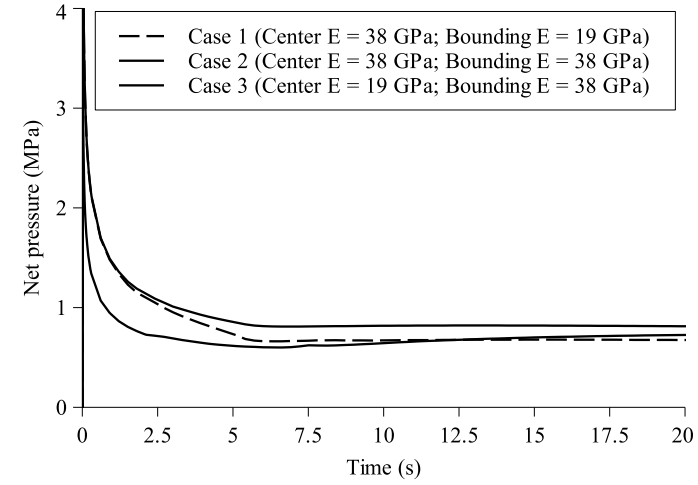

(b)

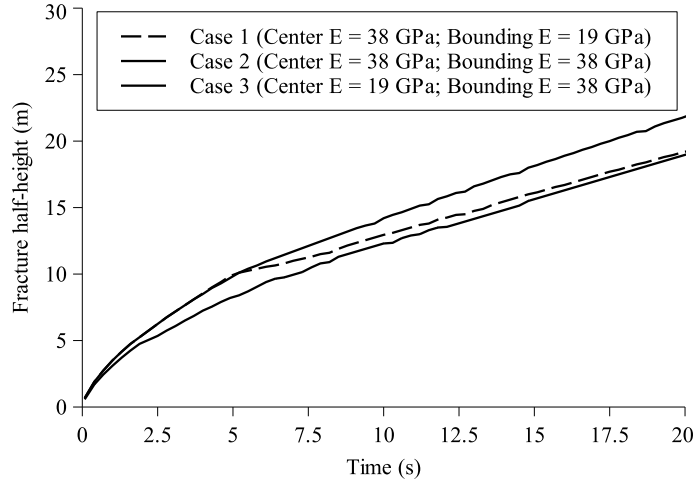

(c)

Figure 3.27 Aperture, net pressure and fracture half-height distributions plotted as a function of time for the scenario with the stress contrast of 0.5 MPa existing between the injection layer and the bounding layers. (a) aperture at the injection point; (b) net pressure at the injection point; (c) fracture half-height.

The results for the scenario with stress contrast being 3 MPa are illustrated in Figure 3.28. Before reaching the formation interface, they have the same behaviors as those shown in Figure 3.27. However, after the hydraulic fracture crosses the formation interface, the height growth is almost inhibited. We see the continuous increase of aperture and net pressure at the injection point. From the numerical results, it is observed that the Young's modulus mainly influence the aperture size, the corresponding net pressure and could limit fracture height growth; the stress contrast could, however, prevent the growth of hydraulic fractures when it is larger than a certain value, whether the modulus contrast exists or not.

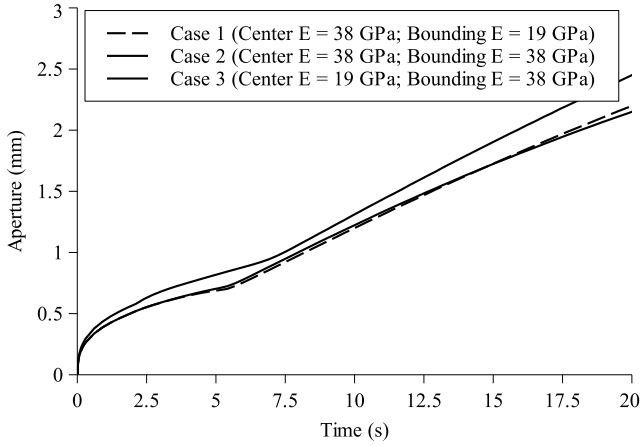

(a)

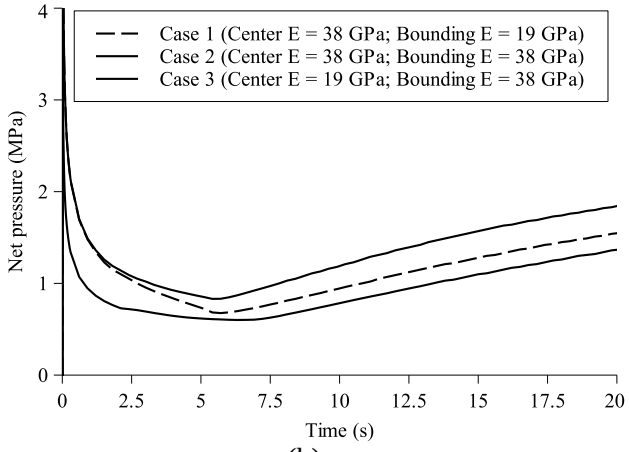

(b)

Figure 3.28 Aperture, net pressure and fracture half-height distributions plotted as a function of time for the scenario with the stress contrast of 3.0 MPa existing between the injection layer and the bounding layers. (a) aperture at the injection point; (b) net pressure at the injection point; (c) fracture half-height. (continued)

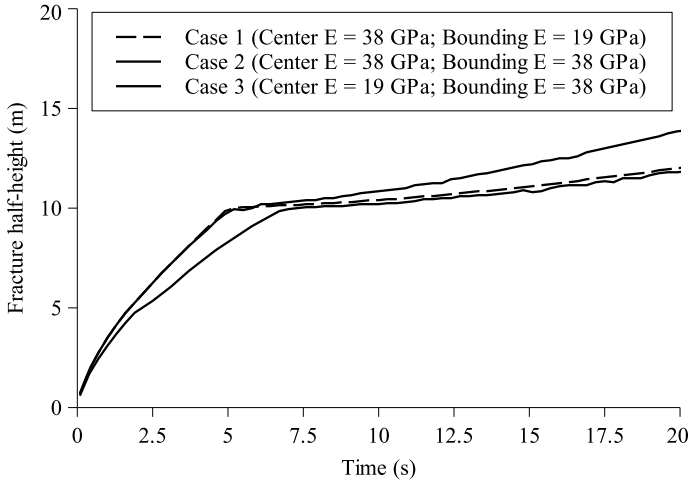

(c)

Figure 3.28 (continued). (Caption shown on previous page.)

3.4.4 Effects of rock ductility

For quasi-brittle rocks encountered in petroleum reservoir development, ductile behavior is often observed. When cracks propagate in salt, shale and coal, it is often considered that a small region in the vicinity of the crack tips experiences ductile deformation. In practical hydraulic fracturing operations, the injection pressure tends to be higher than that predicted according to the classical hydraulic fracturing simulators which are developed based on linear elastic fracture mechanics. It is considered that the higher injection pressure is partially caused by the ductile deformation during the fracture propagation. Through analyses considering elastic and plastic deformations, Papanastasiou (1999) demonstrated that more than an order of magnitude in the rock effective fracture toughness could be induced by the plastic yielding near the tips of a propagating fracture, and the results of plasticity could be matched well by an elastic model using the concept of effective fracture toughness. Tables of effective fracture toughness were given for a set of representative physical parameters including in-situ stress, rock strength, elastic modulus and injection parameters. Yao (2012) proposed a method to estimate the effective fracture toughness of ductile rock according to the size of the fracture process zone.

To analyze the influence of ductility on fracture height growth, two simulations are presented in this section. Relatively larger effective fracture toughness (G_{Ic} = 320 N/m, corresponding K_{Ic} is 2.3 MPa. $m^{1/2}$) is assumed for two ductile layers which are surrounded by layers with smaller fracture toughness (G_{Ic} = 32 N/m, corresponding K_{Ic} is 0.73 MPa. $m^{1/2}$). The Young's modulus is 16.1 GPa, Poisson's ratio 0.21, fluid viscosity 1.0 cp and injection rate 0.004 m^3/s. Figure 3.29 shows the profile of G_{Ic} distributed as a function of depth. A fixed displacement boundary is used to isolate the ductility effect.

Figure 3.30 illustrates the aperture profiles at different injection time. As shown, the aperture size in ductile layers is smaller than that in the confined layer which has smaller G_{IC}; the hydraulic fracture mainly propagates in the confined layer. The bounding ductile layers consume more energy during fracture propagating so it is reasonable for the hydraulic fracture to propagate in the confined layer which consumes less energy. The aperture and pressure at the injection point are plotted as a function of time in Figure 3.31. For comparison purpose, results from the scenario having uniform G_{IC} (= 32 N/m) are also given. The aperture profiles for the scenario having uniform G_{IC} are demonstrated through the right figures in Figure 3.17. In the presence of the ductile layers, the injection pressure is higher and the corresponding aperture at the injection point is larger than that obtained from the scenario using a uniform G_{IC}. Therefore, formation ductility promotes hydraulic fracture containment.

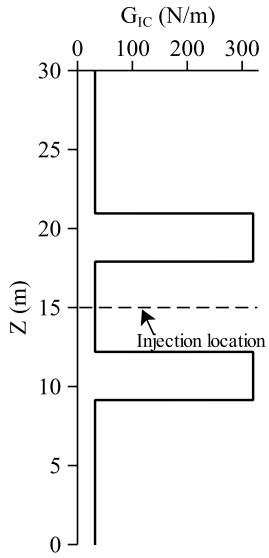

Figure 3.29 G_{IC} distributed as a function of depth.

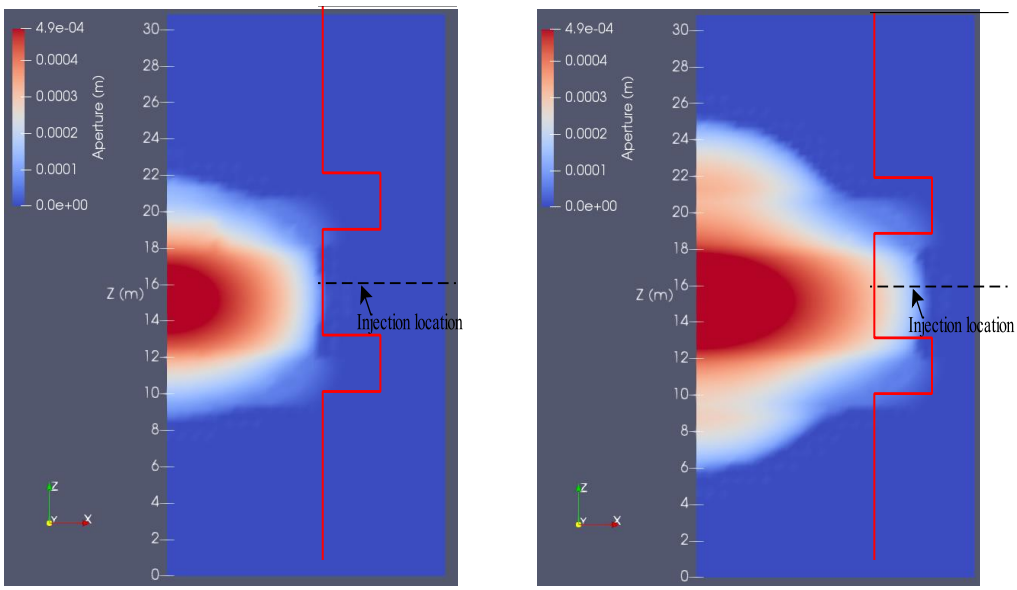

Figure 3.30 Aperture profiles at different time: (a) t = 12 s; (b) t = 24 s. The red line shows the variation of G_{IC} as given in Figure 3.29.

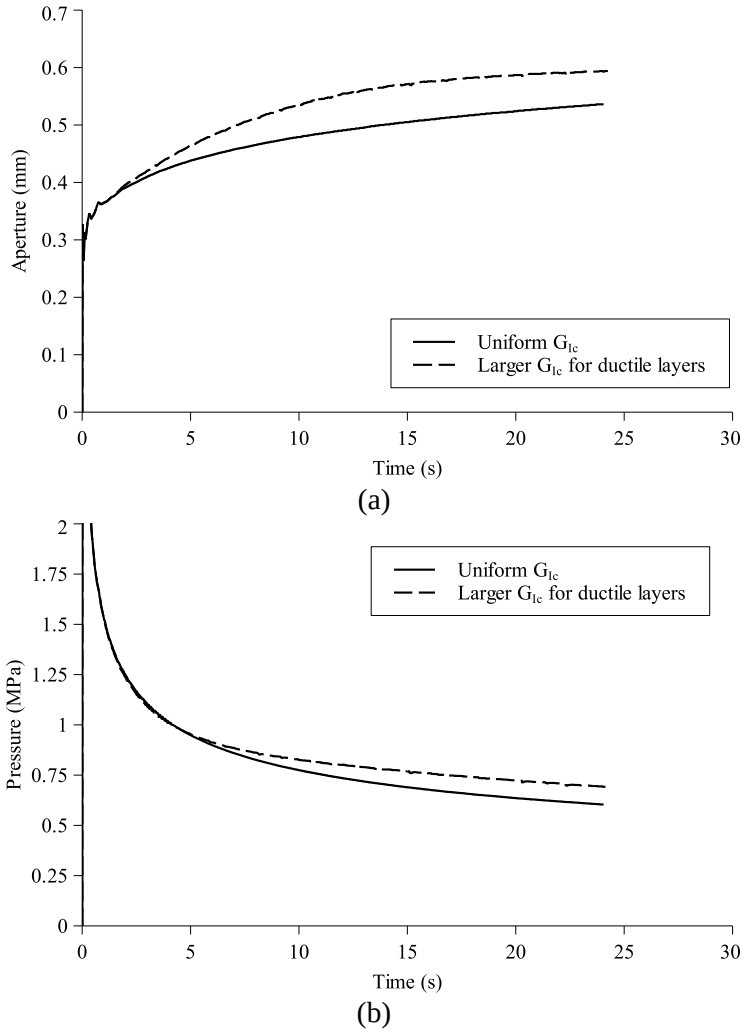

Figure 3.31 Aperture and pressure at the injection point plotted as a function of time for the case having ductile layers (Figure 3.29) and the case having uniform G_{IC} distribution (aperture profile is shown through the right figures on Figure 3.17).

3.5 Discussion

Due to the complexity involved in explicitly modeling hydraulic fractures in layered formations, different ways to obtain an "average Young's modulus" have been used in the literature. However, the repercussions of this approach are often not carefully considered. In this paper we have shown that the "average Young's modulus" produces different results in fluid pressure and especially in the fracture aperture, when compared to modeling that considered the presence of multiple layers having different moduli. The presence of a modulus contrast tends to make hydraulic fractures propagate in the layers having a relatively lower Young's modulus.

Thus, the modulus contrast could act as a potential barrier to prevent the fracture height growth though its effect is not significant than that caused by stress contrast.

Hydraulic fracturing involves coupled processes, such as rock deformation, fracture propagation, and fluid flow. They are strongly influence each other. Usually fully coupled models should be utilized to characterize the behaviors of a hydraulic fracture. However, often the "equilibrium height model" is utilized to simplify the problem. Since a uniform pressure is usually applied on the hydraulic fracture surface in this model, the pressure drop along the fracture surface is often not considered, so the model inevitably overestimates the hydraulic fracture height. As illustrated in this study, the influence of stress contrast on height growth of hydraulic fractures in the fully coupled model is much larger than that obtained according to the static pressurization. When the stress contrast is larger than a certain value in the fully coupled model, for example, 30% of in-situ minimum horizontal stress in this study, the fracture height growth is effectively inhibited. From in-situ experiments (Warpinski, Schmidt, et al. 1982), it has been found a stress contrast in the range of 1.4-3.5 MPa is sufficient to arrest the height growth of a hydraulic fracture. Experiments conducted to analyze hydraulic fracture containment also suggested that stress contrasts of 2-3 MPa are sufficient to prevent fracture growth in laboratory samples (Warpinski et al. 1982). Whether these stress contrasts would result to confine the fracture height growth depends on the designed hydraulic fracturing parameters, such as the fluid viscosity and the injection rate.

Rock properties usually are discontinuous across formation interfaces. We have also considered the simultaneous presence of a stress contrasts across formation interfaces. In reality, the stress contrasts may not necessarily be associated with modulus contrasts. Significant variation of in-situ stress could well exist in the same formation. Numerical simulations in this

study have mainly focused on analyzing the mechanisms involved in the height growth of hydraulic fractures considering the influence of layered material properties and in-situ stress. Other important factors, such as the slippage of on the formation interfaces and natural fractures, could also heavily affect the height growth. Additional studies are ongoing to investigate these effects.

3.6 Conclusions

The 3D fully coupled hydraulic fracturing model, developed in Part I of this paper, is validated through a laboratory experiment, which investigated the propagation of a hydraulic fracture under the influence of stress contrast. Through explicitly modeling of the wellbore, the influence of wellbore compressibility is demonstrated. Good agreements in fracture aperture, injection pressure and fracture footprint have been achieved. Numerical simulations are performed to analyze the influence of layered material properties and in-situ stress on hydraulic fracture height growth. Emphases are placed on the differences when comparing results obtained from the fully coupled model to those obtained based on the static pressurization manner. When the layered Young's modulus is explicitly simulated, its influences on aperture distribution and fracture propagation are captured. It is found that, given the same amount of injection volume in pressurization tests, the average modulus calculated through thickness-weighted method generates higher injection pressure than that obtained using the layered modulus. Hydraulic fractures tend to propagate in the layer with lower Young's modulus. This suggests the soft layers in reservoirs could potentially act as barriers to limit the height growth of hydraulic fractures. Since the height equilibrium model does not consider the pressure drop along the surface of hydraulic fractures, it yields larger aperture size and overestimates the fracture height. As shown in numerical simulations, when the stress contrast is larger than a certain value in the

fully coupled model, for example, 30% of the in-situ minimum horizontal stress in this study, the fracture height growth could be effectively inhibited under the assumed injection rate, fluid viscosity and in-situ stress. When ductile layers exist above and below the payzone, the injection pressure is higher and the corresponding aperture at the injection point is larger than that obtained from the scenario using uniform and homogenized rock properties.

References

Daneshy, A. A. 1978. Hydraulic Fracture Propagation in Layered Formations. *Society of Petroleum Engineers Journal* **18** (01): 33-41. http://dx.doi.org/10.2118/6088-pa.

Detournay, E. 2004. Propagation Regimes of Fluid-Driven Fractures in Impermeable Rocks. http://dx.doi.org/10.1061/(asce)1532-3641(2004)4:1(35).

Gao, Q. and Ghassemi, A. 2019. 3D thermo-poromechanical analysis of flow, heat transport and deformation in fractured rock with applications to a lab-scale geothermal system. submitted.

Gu, H. and Siebrits, E. 2008. Effect of Formation Modulus Contrast on Hydraulic Fracture Height Containment. *SPE Production & Operations* **23** (02): 170-176. http://dx.doi.org/10.2118/103822-PA.

Ghassemi, A. 2017. Application of rock failure simulation in design optimization of the hydraulic fracturing. Porous Rock Fracture Mechanics with Application to Hydraulic Fracturing, Drilling and Structural Engineering. Shojaei A.K., and Shao, J. (Eds). Pp. 3-23.

Huang, K., Ghassemi, A. and Zhang, Z. 2018. Simulation and Analysis of Laboratory Scale Hydraulic Fracturing Using 3D Virtual Multidimensional Internal Bonds Model With Fracture Energy Conservation. Paper presented at the 52nd U.S. Rock Mechanics/Geomechanics Symposium, Seattle, Washington, 2018/8/21/.

Jeffrey, R. G. and Bunger, A. 2007. A Detailed Comparison of Experimental and Numerical Data on Hydraulic Fracture Height Growth Through Stress Contrasts. Paper presented at

the SPE Hydraulic Fracturing Technology Conference, College Station, Texas, U.S.A., 2007/1/1/. http://dx.doi.org/10.2118/106030-ms.

Mendelsohn, D. A. 1984. A Review of Hydraulic Fracture Modeling—II: 3D Modeling and Vertical Growth in Layered Rock. *Journal of energy resources technology* **106** (4): 543-553. http://dx.doi.org/10.1115/1.3231121.

Moody, L. F. 1944. Friction factors for pipe flow. *Trans. ASME* **66** (8): 671-684.

Papanastasiou, P. 1999. The Effective Fracture Toughness in Hydraulic Fracturing. *International journal of fracture* **96** (2): 127. http://dx.doi.org/10.1023/a:1018676212444.

Simonson, E. R., Abou-Sayed, A. S. and Clifton, R. J. 1978. Containment of Massive Hydraulic Fractures. *SPE Journal*: 27-32. http://dx.doi.org/10.2118/6089-pa.

Smith, M. B., Bale, A. B., Britt, L. K. et al. 2001. Layered Modulus Effects on Fracture Propagation, Proppant Placement, and Fracture Modeling. Paper presented at the SPE Annual Technical Conference and Exhibition, New Orleans, Louisiana, 2001/1/1/. http://dx.doi.org/10.2118/71654-ms.

Sneddon, I. and Elliot, H. 1946. The Opening of a Griffith Crack Under Internal Pressure. *Quart. Appl. Math* **4** (3): 262-267.

Sneddon, I. N. 1946. The Distribution of Stress in the Neighbourhood of a Crack in an Elastic Solid. *Proceedings of the Royal Society of London Series a-Mathematical and Physical Sciences* **187** (1009): 229-260. http://dx.doi.org/10.1098/rspa.1946.0077.

Teufel, L. W. and Warpinski, N. R. 1983. In-Situ Stress Variations And Hydraulic Fracture Propagation In Layered Rock-Observations From A Mineback Experiment. Paper presented at the 5th ISRM Congress, Melbourne, Australia, 1983/1/1/.

van Eekelen, H. A. M. 1982. Hydraulic Fracture Geometry: Fracture Containment in Layered Formations. *Society of Petroleum Engineers Journal* **22** (03): 341-349. http://dx.doi.org/10.2118/9261-pa.

Warpinski, N. R., Branagan, P. T., Peterson, R. E. et al. 1998. An Interpretation of M-Site Hydraulic Fracture Diagnostic Results. Paper presented at the SPE Rocky Mountain Regional/Low-Permeability Reservoirs Symposium, Denver, Colorado, 1998/1/1/. http://dx.doi.org/10.2118/39950-ms.

Warpinski, N. R., Clark, J. A., Schmidt, R. A. et al. 1982. Laboratory Investigation on the -Effect of In-Situ Stresses on Hydraulic Fracture Containment. *Society of Petroleum Engineers Journal* **22** (03): 333-340. http://dx.doi.org/10.2118/9834-pa.

Warpinski, N. R., Schmidt, R. A. and Northrop, D. A. 1982. In-Situ Stresses: The Predominant Influence on Hydraulic Fracture Containment. *Journal of Petroleum Technology* **34** (03): 653-664. http://dx.doi.org/10.2118/8932-pa.

Wu, R., Bunger, A. P., Jeffrey, R. G. et al. 2008. A comparison of numerical and experimental results of hydraulic fracture growth into a zone of lower confining stress. Paper presented at the The 42nd U.S. Rock Mechanics Symposium (USRMS), San Francisco, California, June 29 - July 2.

Yao, Y. 2012. Linear Elastic and Cohesive Fracture Analysis to Model Hydraulic Fracture in Brittle and Ductile Rocks. *Rock Mechanics and Rock Engineering* **45** (3): 375-387. http://dx.doi.org/10.1007/s00603-011-0211-0.

Ye, Z., Sesetty, V. and Ghassemi, A. 2018. Experimental and Numerical Investigation of Shear Stimulation and Permeability Evolution in Shales. Paper presented at the SPE Hydraulic Fracturing Technology Conference and Exhibition, Woodland, TX.

4 3D planar hydraulic fracture propagation in an elastic medium: interaction between hydraulic fractures and discontinuities

Abstract

In recent years much research effort has focused on hydraulic fracture height growth because height containment is needed to ensure effective stimulation of target zones. In many cases, fracture height growth determines the success or failure of a hydraulic stimulation. For layered rock systems, material properties, interface's mechanical characteristics and its permeability, as well as the in-situ stresses influence both the lateral and height growth of hydraulic fractures. It is generally believed that stress contrast is a dominant factor that directly controls the fracture height. The influence of Young's modulus contrast on height growth is usually ignored. Simplified "average methods" are often proposed and utilized to homogenize layered modulus. Also, it is commonly assumed that the layer interfaces are perfectly bonded without slippage even when high stress contrast exits. Use of theses simplifying assumptions in modeling analysis are partially due to the difficulty in handling all the factors involved. In this study, a fully coupled 3D hydraulic fracture simulator based on finite element method is used to investigate the above factors and study how they impact hydraulic fracture propagation and height growth. The influence of modulus contrast, interface conditions, and in-situ stress on hydraulic fracturing and especially on fracture height growth is analyzed.

The numerical approach is a 3D finite element model with a special zero-thickness interface element based on the cohesive zone model (CZM) to simulate the fracture propagation and fluid flow in fractures. A local traction-separation law with strain-softening is used to capture tensile cracking. The nonlinear mechanical behavior of frictional sliding along interface surfaces is also considered. Since discontinuities are explicitly simulated through the use of the

interface element, details of the deformation processes are captured and revealed. For example, information related to aperture opening/sliding and stress distribution along the discontinuities is obtained in the simulations. After model verification and validation, it is used to simulate height growth in layered rock of practical interest. The numerical model is evaluated through a commonly used crossing/arrest criterion. Laboratory experiments on fracture-discontinuity interaction under triaxial-stress conditions are also studied. Numerical results match well with predictions of theoretical formulations and laboratory observations. Typical processes associated with fracture-discontinuity interaction are reveled. The recorded injection pressure increases when the hydraulic fracture reaches a bedding interface (or other discontinuities). Continuous opening and/or sliding along the interface requires higher injection pressure. With the existence of a horizontal interface, the influence of modulus contrast and stress contrast on hydraulic fracture height growth is analyzed. The combined effects of rock properties, mechanical properties of the interfaces, and in-situ stress can effectively inhibit hydraulic fracture height growth.

4.1 Introduction

Hydraulic fracture height growth is a key issue in hydraulic stimulation of unconventional reservoirs. Due to the complexity of geological conditions, prediction or determination of fracture height has been one of the challenge tasks when designing hydraulic fracturing. There are many factors that impact the height growth of hydraulic fractures in layered formations. In-situ stress contrast has been recognized as one of the most effective factors that can prevent the height growth. Other factors, such as modulus contrast and formation interface opening/slippage, have usually ignored in order to simplify analyses. There are both experimental and field observations suggesting that the growth of fractures can be impeded by

discontinuities (e.g. natural fracture, joint, layered formation interface/bedding plane). Depending on in-situ stress, properties of discontinuities and intact rock, a hydraulic fracture can cross or open the discontinuity; it can also be arrested. After the opening of a discontinuity, complex fracture paths could be created by fracture reinitiation or branching at flaws in the vicinity of the discontinuity interface. Formation interfaces and bedding planes can experience local stress disturbances as a hydraulic fracture approaches. It is highly possible that frictional sliding along the interfaces occurs. The induced stresses and pressurization by the fracturing fluid can make it open and thus take-in more fluid. Pressure loss due to fluid flow in the interface and local stress alteration due to reinitiation of fractures at flaws from the discontinuity would in turn impact the fracture propagation and height growth. Complex coupled hydro-mechanical processes are involved.

Many laboratory experiments on the interaction between hydraulic fractures and discontinuities can be found in the literature (Daneshy 1978; Warpinski and Teufel 1987; Anderson 1981; Teufel and Clark 1984). Daneshy (1978) performed experiments to study the fracture propagation in layered formations. The crossing and arrest of hydraulic fractures were demonstrated through experiments. Experimental results showed that the contrast of physical and mechanical properties on the two sides of an interface were not sufficient to stop the fracture propagation at the interface. It was suggested that confinement of fracture height may be caused more by low interface strength rather than by the contrast in rock properties. In addition, a lag between the fluid front and the fracture tip was observed.

One of the first studies of fracture crossing an interface was by Cook and Erdogan (1972) based on the principles of linear elastic fracture mechanics (LEFM). According to their results, a pressurized crack cannot grow across a bonded interface if the neighboring rock is stiffer than

the layer containing the crack (because the stress intensity factor would go to zero). On the other hand, for a softer neighboring material, the crack would cross the interface into the softer material because of the large stress intensity factor. These finding are not in agreement with the experimental observations cited above. This was explained by Roegiers and Wiles (1981) who argued that the conventional stress intensity factor does not hold for an interface and that the critical energy release rate is larger for a stiffer neighboring rock, hindering crossing. Vijayakumar and Cormack (1983) improved the solution of Cook and Erdogan (1972) and showed that a crack approaching an interface induces singular stresses in both the host layer and the stiffer neighboring layer; the singular stresses can potentially make the crack cross the interface. Utilizing formulations from LEFM, Renshaw and Pollard (1995) proposed a criterion for a fracture crossing an orthogonal interface. Through combing the stress state ahead of fracture tips and the Coulomb friction law, the crossing criterion was derived. The criterion assumes that rocks are linearly elastic, homogeneous and isotropic and no slip/opening occurs before the induced fracture contacts the interface (so that the mathematical stress singularity is still applicable at the tip of the approaching fracture). A series of laboratory experiments were conducted to evaluate the criterion and yielded results consistent with the criterion. Following Renshaw and Pollard (1995), Gu et al. (2012) extended the orthogonal criterion for nonorthogonal crossing. Laboratory experiments were designed to assess the extended criterion and produced results that were in agreement with those predicted by the extended crossing criterion. Laboratory experiments on interaction between hydraulic fractures and natural fractures can also be found in Hu and Ghassemi (2019). According to the observed displacement jump (slippage) across a natural fracture together with increasing AE activities, it was

demonstrated that the hydraulic fracture could cause slippage of the saw-cut fractures even before reaching them.

Mineback experiments, and exposed outcrops also provide valuable information for a better understanding of the interaction between hydraulic fractures and geological discontinuities. Warpinski and Teufel (1987) presented results from mineback experiments. The influence of geological discontinuities on hydraulic fracture propagation was analyzed. Offset of hydraulic fractures was observed after they crossed joints. Multiple fractures propagating side by side in a "zone of fracturing" were recorded. Through analyzing a hydraulic fracture slightly penetrating a bedding plane (2.5 to 5 cm), it was suggested that bedding plane and stress contrast together provide a fracture containment mechanism. Through mining the stimulated zones in a coal mine, Jeffrey et al. (1992) measured the size and geometry of hydraulic fractures. A propped horizontal hydraulic fracture was mapped at the interface between the coal and floor rock. The deflection of vertical fractures into formation interfaces forms the T-shaped fracture geometry.

In this study, we emphasize the impact of formation interfaces on fracture height growth. A fully-coupled hydro-mechanical model, which can simulate mixed-mode failure during fracture propagation, is developed and utilized. The numerical model is evaluated through a commonly utilized crossing/arrest criterion. 3D laboratory experiments on fracture-discontinuity interaction are studied. At last, the influence of material properties and in-situ stress together with the formation interface, on fracture height growth is studied.

4.2 Problem statement and methodology

4.2.1 Problem statement

Due to the complexity of fracture-discontinuity interactions, a large amount of efforts have been spent on understanding and modeling the physical mechanisms involved. It is still a

challenging task to accurately capture the main characteristics of the problem. Crossing/arrest criterions presented in the literature are usually derived based on 'static stress analyses' without considering the deformation of intact rock and discontinuities. The crossing criterion is mainly determined by the strength of rock. The energy criterion required for fracture initiation and propagation across a discontinuity is not considered. The coupled processes between mechanical deformation and fluid flow are often ignored. To use the existing formulations from LEFM, reservoir rock is commonly assumed to be linear elastic, homogeneous and isotropic. The material properties and in-situ stress across a discontinuity are also assumed as uniform (i.e. modulus contrast and stress contrast cannot exist in a model). These assumptions made in analytical or numerical models often limit the applications of them.

One of the main objectives of this study is trying to relax the above mentioned assumptions through reliable and robust numerical solutions. As a widely used method in engineering and scientific applications, finite element method is adopted in this work. A special hydro-mechanical interface element is developed to model the fully coupled hydro-mechanical processes. For mode I failure problem, the model has been successfully verified through penny-shaped hydraulic fracture and KGD hydraulic fracture for both viscosity- and toughness-dominated regimes (Gao and Ghassemi 2018, 2019b). When dealing with problems related to fracture-discontinuity interactions, mixed mode failure coupled with frictional sliding should be considered. Cohesive zone model (CZM) as a mature technique, has been proven to be a reliable and efficient way to simulate the mixed mode fracture (Park and Paulino 2013; Spring and Paulino 2015). Since the rock surrounding discontinuities is discretized through traditional volume elements (i.e. 3D 8-node hexahedron element in this model), the material heterogeneity, nonlinear mechanical behaviors and stress-contrast can all be considered. The effects of physical

properties of rock, mechanical properties of discontinuity, and in-situ stress will be analyzed in the following sections.

4.2.2 Fully coupled hydro-mechanical model

A fully coupled hydro-mechanical model is developed based on finite element method (FEM). The mechanical behaviors of pre-existing discontinuities and the freshly created hydraulic fractures are determined through a cohesive zone model (CZM), which is suitable to simulate both tensile and shear failure. In addition, frictional effects are considered when the two surfaces of fractures are in contact and under compression.

(1) Cohesive interface

Numerous studies on fracture propagation can be found in the literature. One of the most widely used approaches is the cohesive zone model. Due to its efficient and powerful algorithms, CZM has been successfully utilized in simulating mode I, mode II and mix mode fractures. In hydraulic fracturing modeling, mode I fracture is the most widely studied one; mix mode fracture is encountered in non-planar propagation. However, both of them usually assume the created fractures have opening space between the two facture surfaces. In other words, the fracture surfaces are separated and not in contact. Even for the cases in which fracture surface contact exists, the friction force exerting on the contact surfaces of hydraulic fractures are commonly ignored. One of the advantages of CZM lies not only in its power to efficiently handle the mix mode fracture, but also in its ability to couple the frictional slippage into the mixed-mode failure. Coupling a friction relation into CZM to simulate hydraulic fracturing in formations having discontinuities is one of the main targets of this study.

Like the stress-strain relationship in continuum mechanics, the behaviors of discontinuities in CZM are determined by a traction-separation law. There are mainly two kinds

of constitutive relationship for CZM that are able to handle the mixed-mode failure. One is effective displacement-based models; another one is potential-based models. A detailed comparison between the two can be found in Park and Paulino (2013). The PPR potential-based model (Park and Paulino 2012; Spring and Paulino 2015) is utilized in this work. Here we briefly summarize the thermodynamic consistent version of the PPR cohesive model (Spring et al. 2016) and the formulations pertinent to frictional sliding.

The cohesive tractions are related to the opening of fractures, and are written as following

$$T_n(\kappa_n, \kappa_t, \Delta_n) = T_n'(\kappa_n, \kappa_t)\frac{\Delta_n}{\kappa_n}, \text{ and } T_t(\kappa_n, \kappa_t, \Delta_t) = T_t'(\kappa_n, \kappa_t)\frac{\Delta_t}{\kappa_t}, \tag{4.1}$$

where Δ_n and Δ_t are normal opening and tangential opening, respectively; T_n and T_t normal and tangential traction, respectively; T_n' and T_t' are normal and tangential traction obtained using internal history parameters κ_n and κ_t., they have closed form expression and are derived from the PPR cohesive potential. The internal history parameters κ_n and κ_t are irreversible state variables and stand for the maximum normal opening and absolute tangential opening in the history of loading:

$$\kappa_n = \max\{\Delta_n\}, \text{ and } \kappa_t = \max\{\Delta_t\}. \tag{4.2}$$

When the two surfaces of a cohesive interface are in contact and under compression in the normal direction, a penalty method is activated to prevent the overlap of the two fracture surfaces; the corresponding resisting force is calculated at the same time. Frictional forces are then generated if the interface has the potential to slide. The onset of friction is coupled to the damage status of the interface and is assumed to occur when the maximum shear strength has been reached. The Coulomb friction law is adopted to calculate the frictional force:

$$T_f = \mu_f g(\kappa_t)|T_n| \text{ when } T_n < 0 \text{ and } \Delta_t > \Delta_t|_{T_t = T_t^{max}} (= \lambda_t \delta_t), \tag{4.3}$$

where μ_f is the coefficient of friction; δ_t the final tangential opening that is reached when shear strength equals to zero; λ_t the ratio of critical tangential opening δ_{tc} (when the maximum shear strength is reached) to the final tangential opening δ_t; $g(\kappa_t)$ varies monotonically from 0 to 1, its value depends on the internal history parameter κ_t:

$$g(\kappa_t) = \left(1 - \frac{T_t(0, \kappa_t, \kappa_t)}{D_0 \kappa_t}\right)^s \tag{4.4}$$

where s controls the shape of the monotonically increasing curve of $g(\kappa_t)$. D_0 is the stiffness of the interface when the maximum shear strength is reached.

The tangential opening (Δ_t) is composed by two perpendicular tangential openings (Δ_{t1} and Δ_{t2}) on the interface plane through the relationship $\Delta_t = \sqrt{{\Delta_{t1}}^2 + {\Delta_{t2}}^2}$. The normal and tangential tractions in the corresponding opening directions is determined by the following expression (Spring and Paulino 2015):

$$\boldsymbol{T} = \begin{Bmatrix} T_n \\ T_{t1} \\ T_{t2} \end{Bmatrix} = \begin{Bmatrix} T_n \\ T_t \dfrac{\Delta_{t1}}{\Delta_t} + T_f \left(\dfrac{|\Delta_{t1}|}{\Delta_t}\right) \dfrac{\dot{\Delta}_{t1}}{|\dot{\Delta}_{t1}|} \\ T_t \dfrac{\Delta_{t2}}{\Delta_t} + T_f \left(\dfrac{|\Delta_{t2}|}{\Delta_t}\right) \dfrac{\dot{\Delta}_{t2}}{|\dot{\Delta}_{t2}|} \end{Bmatrix} \tag{4.5}$$

The friction force on the interface plane is decomposed into two parts in directions corresponding to Δ_{t1} and Δ_{t2}. They are coupled to the cohesive force in Eq. (5).

The material tangent stiffness matrix, **D**, is given as

$$\boldsymbol{D} = \begin{bmatrix} \dfrac{\partial T_n}{\partial \Delta_n} & \dfrac{\partial T_n}{\partial \Delta_{t1}} & \dfrac{\partial T_n}{\partial \Delta_{t2}} \\ \dfrac{\partial T_{t1}}{\partial \Delta_n} & \dfrac{\partial T_{t1}}{\partial \Delta_{t1}} & \dfrac{\partial T_{t1}}{\partial \Delta_{t2}} \\ \dfrac{\partial T_{t2}}{\partial \Delta_n} & \dfrac{\partial T_{t2}}{\partial \Delta_{t1}} & \dfrac{\partial T_{t2}}{\partial \Delta_{t2}} \end{bmatrix} \tag{4.6}$$

Fluid flow in fractures is coupled to the CZM. As will be demonstrated by hydro-mechanical interface element, the injected fluid flows between the two surfaces of a cohesive interface element. On the interface surfaces, fluid pressure acts as traction in the normal direction. There is a nonlinear fracture process zone in front of the fracture tips, where elastic and inelastic cohesive tractions characterized by Eq. (4.5) exist (Figure 2.1). Similar to the theory of poroelasticity, the concepts of effective traction ($\boldsymbol{T}$) and total traction ($\boldsymbol{T_{total}}$) are introduced. They are related to the fluid pressure (p_f) through the following formulation:

$$\boldsymbol{T_{total}} = \boldsymbol{T} - p_f \boldsymbol{n} \tag{4.7}$$

where $\boldsymbol{n}$ is the normal of the cohesive interface. The effective traction $\boldsymbol{T}$ is the one that given in Eq. (4.5).

(2) Fluid flow in fractures

Fluid flow and heat transport in fractures surrounding by elastic and thermo-poroelastic media are presented in detail in Gao and Ghassemi (2019a) and Gao and Ghassemi (2019b). Here we briefly present the governing equations and boundary conditions. In this study, we assume the reservoir formation is elastic. The leak-off and poroelastic effects are ignored considering the extremely low permeability of unconventional petroleum and geothermal reservoirs. Incompressible, linear (Newtonian) viscous fluid is assumed. The fluid pressure is considered to be constant over normal opening along the direction perpendicular to the fracture surfaces. It has pressure gradient in the tangential direction parallel to the facture surfaces.

The longitudinal flow within hydraulic fractures is treated as fluid flow between two parallel plates. It is governed by the lubrication equation:

$$\boldsymbol{q} = \boldsymbol{v}w = -\frac{w^3}{12\mu}\nabla p_f \tag{4.8}$$

where μ is the fluid viscosity, $w(\boldsymbol{x}, t)$ is the normal opening, $\boldsymbol{v}$ is the average flow velocity, $\boldsymbol{q}$ is the fluid flow rate.

The mass balance equations is written as

$$\frac{\partial w}{\partial t} + \nabla \cdot \boldsymbol{q} = Q(t) \tag{4.9}$$

where $Q(t)$ is the sink/source term, it represents injection rate in this study.

The following equation is obtained after substituting Eq. (4.8) to (4.9):

$$\frac{\partial w}{\partial t} - \nabla \cdot \frac{w^3}{12\mu} \nabla p_f = Q(t) \tag{4.10}$$

At the injection point, we have

$$\boldsymbol{q}(x,t)|_{x=0} = Q(t) \tag{4.11}$$

At the fracture tips, the normal opening and fluid flux equal to zero, they are expressed as following:

$$\begin{aligned} w(x,t)|_{x=tips} &= 0 \\ \boldsymbol{q}(x,t)|_{x=tips} &= 0 \end{aligned} \tag{4.12}$$

(3) Hydro-mechanical interface element

A triple-node zero-thickness interface element is developed to simulate the coupled hydro-mechanical behaviors of fractures. The mechanical responses of the interface element are governed by CZM. As shown in Figure 2.3, the hydro-mechanical interface element has three layers and is composed by isoparametric and quadrilateral elements. There are 12 nodes: 1 ~ 8 have degree of freedoms for displacement (u_x, u_y, u_z); 9 ~ 12 have degree of freedoms for fluid pressure (p_f). The fluid flows on the center plane (9-10-11-12). The top and bottom planes (1-2-3-4 and 5-6-7-8) represent the surfaces of a fracture and share the nodes with traditional 8-node hexahedron elements discretizing surrounding rock. Figure 4.1 illustrates the insertion of 12-

node zero-thickness elements into the 8-node hexahedron elements where a vertical interface intersects a horizontal interface. The shadow area circled by the red dash lines indicates the center plane in a cohesive interface element. We exclusively use 8-node hexahedron elements (3D) for discretizing the rock matrix. When modeling a plane strain condition using the 3D elements, the displacement is fixed in the direction perpendicular to the plane on which the plane strain condition is satisfied.

When cohesive interface elements are under compression, the two surfaces of the interface elements come into contact. To prevent the overlap of the two surfaces when they are in contact, the penalty method is used. The penalty method utilizes a large interface stiffness to prevent the overlap of the surfaces. It should be emphasized that the stiffness used to prevent the overlap in the penalty method is different with the well-known joint stiffness. In the numerical model, when the surfaces of interface elements are in contact, the mechanical aperture is zero. However, due to the rough surfaces of geological discontinuities, the contact of two surfaces of a geological discontinuity, such as joint, does not indicate it zero aperture. In other words, a geological discontinuity can still be permeable when it is under compression; hydraulic aperture is used to account for the permeability of the discontinuity. Hydraulic aperture is a function of the "joint stiffness". In the coupled hydro-mechanical model, the aperture used in (4.10) is the sum of mechanical aperture and hydraulic aperture. When the surfaces of an interface element are in contact, the mechanical aperture is zero; when it is open, the mechanical aperture is usually orders of magnitude larger than the hydraulic aperture, and makes the hydraulic aperture negligible. During the closure of an interface element, the compressive stress gradually increases in the normal direction of the interface element; the corresponding hydraulic aperture gradually decreases and is calculated according to the normal stress and the joint stiffness until reaching

the residual aperture of the interface element. The reversed process applies for the opening of an interface element which is under compression initially and is subjected to fluid pressurization subsequently.

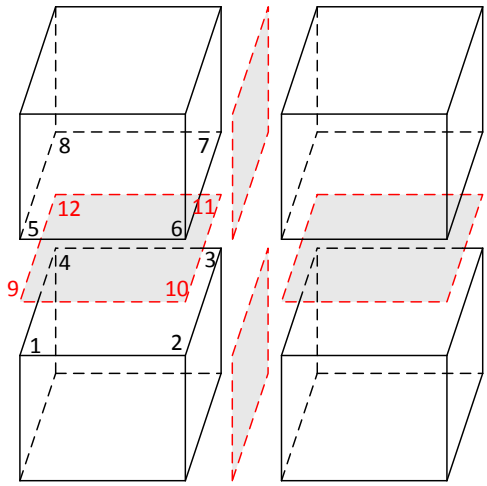

Figure 4.1 12-node zero-thickness elements embedded in the traditional 8-node hexahedron elements at the intersection part of a vertical interface and a horizontal interface. The shadow area circled by red dash lines indicates the center plane of a zero-thickness element. The three layers of quadrilateral (1-2-3-4; 5-6-7-8; 9-10-11-12) in a cohesive interface element are initially overlapped with each other and have zero thickness. They are separately illustrated for visualization purpose.

According to the principle of virtual work, the following weak form of the governing equations is derived

$$\int_{\Omega} \delta\boldsymbol{\varepsilon} : \boldsymbol{\sigma} dV + \int_{\Gamma} \delta\boldsymbol{\Delta} \cdot \left(\boldsymbol{T} - p_f \boldsymbol{n}\right) ds = \int_{\partial\Omega} \delta\boldsymbol{u} \cdot \boldsymbol{T}_{ext} ds$$
$$\int_{\Gamma} \delta p_f \frac{\partial w}{\partial t} ds - \int_{\Gamma} \delta p_f \nabla \cdot \frac{w^3}{12\mu} \nabla p_f ds = \int_{\Gamma} \delta p_f Q(t) ds \tag{4.13}$$

A standard Galerkin finite element method is adopted to discretize the weak form of equations. Detailed procedures can be found in Gao and Ghassemi (2019b). Newton-Raphson method is utilized to solve the nonlinear system equations assembled at each time step. The unknowns for displacement and fluid pressure are solved simultaneously. For mode I failure, the hydro-mechanical model has been successfully verified. Interested readers are referred to Gao and Ghassemi (2018) and Gao and Ghassemi (2019b) for details.

4.3 Mechanical behaviors of the interface element

Numerical experiments are performed to illustrate and analyze the behaviors of the cohesive interface element. Since the interaction between hydraulic fractures and discontinuities involves complex processes, such as mixed-mode failure coupled with frictional sliding, loading/unloading stress conditions, special attentions are spent on investigating the reliability of the CZM in handling these failure processes.

Typical loading paths for mode I, mode II and mixed-mode failure are studied and demonstrated. The same input parameters are used for examples presented in this section. The difference between them lies in the loading paths. Table 4.1 gives the input values, the physical meaning of each parameter is consistent with those given in Park and Paulino (2012) and Spring et al. (2016).

Table 4.1 Basic input parameters for PPR cohesive interface element.

Normal fracture energy, ϕ_n or G_{c_I}	100 J/m^2
Tangential fracture energy, ϕ_t or G_{c_II}	200 J/m^2
Normal cohesive strength, σ_{max}	2.0×10^6 Pa
Shear cohesive strength, τ_{max}	4.0×10^6 Pa
Normal shape parameter, α	5.0
Tangential shape parameter, β	2.0
Normal initial slope indicator, λ_n	0.1
Normal initial slope indicator, λ_t	0.2
Shape parameter for $g(\kappa_t)$ in Eq. (4), s	3.0
Coefficient of friction, μ	0.5

4.3.1 Mode I fracture

For mode I fracture, only the normal opening is considered. The tangential opening is zero. As shown in Figure 4.2, the interface element is first loaded to near its maximum tensile strength of 2 MPa causing it to enter the softening zone (Δ_n = 0.03 mm); then it is unloaded to the original state (zero normal opening) (Δ_n = 0 mm) along the line connecting the unloading point on the traction-separation curve and the original point. After unloading, it is reloaded to the

original traction-separation curve (Δ_n = 0.03 mm). The unloading and reloading curves are overlapped for mode I fracture. This is one of the properties of the thermodynamic consistent CZM. Continuously reloading brings it to the complete failure status where zero traction exists (Δ_n = 0.13 mm).

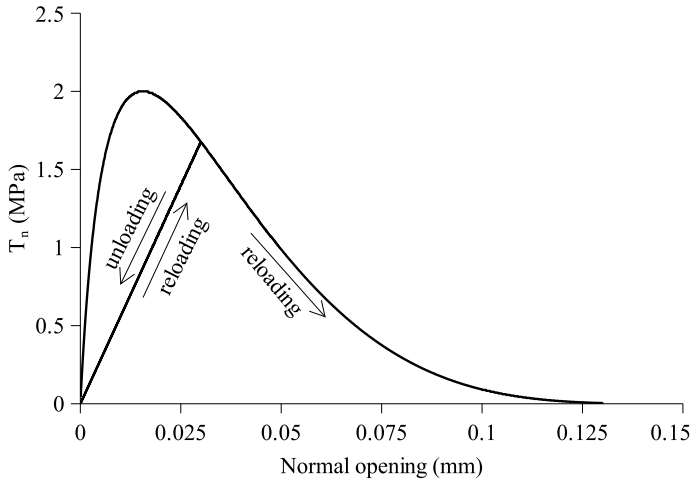

Figure 4.2 Normal traction plotted as a function of normal opening. During the loading-unloading-reloading process, the tangential opening is maintained as zero. No tangential opening occurs.

4.3.2 Mode II fracture with friction coupling

As stated in Eq. (4.3), the frictional force can only take effect when the cohesive interface is under compression in the normal direction. To illustrate the mode II failure and the evolution of coupled frictional force as a function of cohesive damage, a predefined normal opening (Δ_n = -7.0 × 10^{-6} m) is applied to a single element to create a compressive stress on the interface. It should be noted that the penalty method is utilized in PPR cohesive model when the two surfaces of an interface element are in contact. Small penetration of two contacting surfaces is allowed.

In Figure 4.3, the tangential opening (Δ_t) is continuously increased to 0.1 mm. The cohesive traction (T_t) initially increases; it then enters into the softening stage until complete failure of the interface. The tangential traction generated by the frictional force (T_f) initiates when the maximum tangential strength is reached and gradually increases. When the interface

failures completely (T_t = 0), the frictional traction arrives at a maximum value ($T_f = \mu_f |T_n|$) and maintains at it as the frictional sliding on the interface occurs continuously.

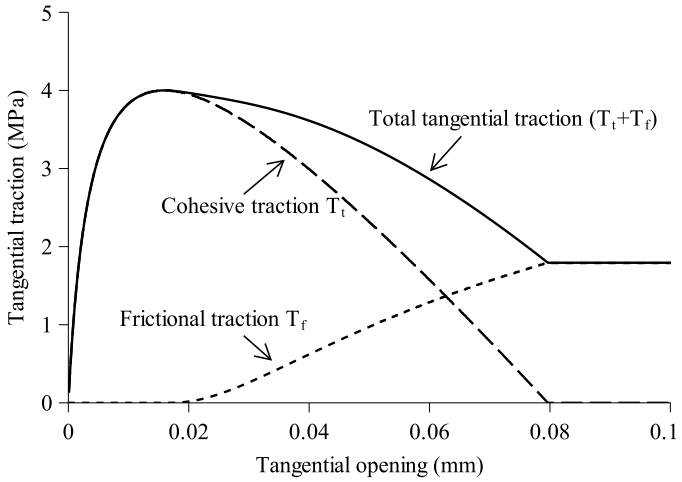

Figure 4.3 Tangential traction (shear) decomposed into cohesive traction component (T_t) and frictional traction component (T_f) and plotted as a function of tangential (shear) opening (Δ_t).

Numerical experiments are also carried out to investigate the behaviors of the coupled cohesive – friction relation under one cycle of loading-unloading-reloading. A predefined normal opening is set as Δ_n = - 7.0 × 10^{-6} m. One cycle of tangential loading is applied, as shown in Figure 4.4. Figure 4.4 (a) illustrates the cohesive (T_t) and frictional (T_f) components of the tangential traction. Following the arrow, which indicates "loading direction", some typical deformation stages are identified: (1) elastic loading, (2) softening, (3) unloading, (4) softening in the reverse direction, (5) reloading, (6) softening, and (7) complete failure. When the loading direction is reversed, the sign of frictional force is changed into an opposite one correspondingly, as marked by '2-3' and '4-5' on Figure 4.4 (b). The total tangential traction (T_t + T_f) is obtained by combining the frictional and cohesive components according to Eq. (4.5).

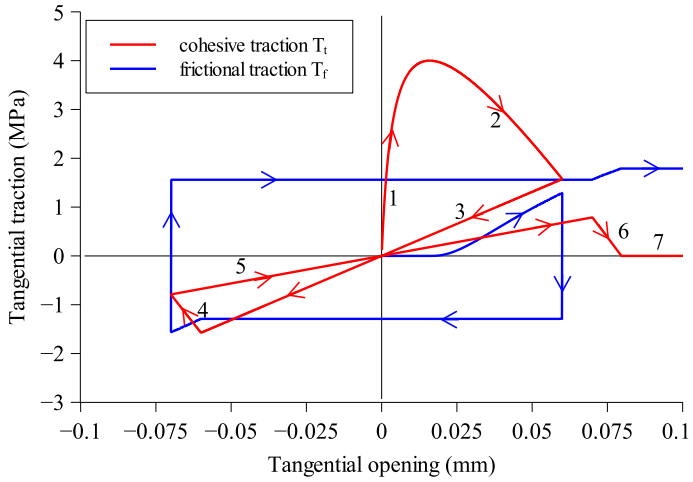

(a)

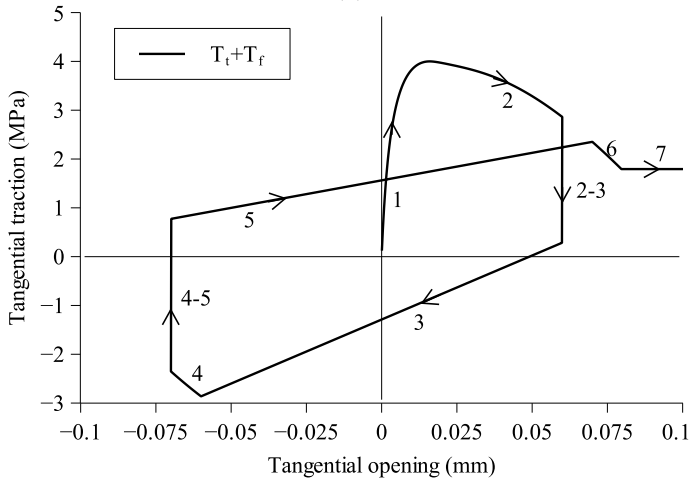

(b)

Figure 4.4 Tangential traction plotted as a function of tangential opening (Δ_t) during one cycle of loading. (a) cohesive traction (T_t) and frictional traction (T_f) vs. tangential opening (Δ_t); (b) total tangential traction ($T_t + T_f$) vs. tangential opening (Δ_t). The arrows indicate the "loading directions". The number gives the deformation stages: (1) elastic loading, (2) softening, (3) unloading, (4) softening in the reverse direction, (5) reloading, (6) softening, and (7) complete failure. '2-3' and '4-5' mark the reverse of loading direction.

4.3.3 Mixed-mode fracture

The behaviors of the cohesive interface under mixed-mode failure are demonstrated through three examples. They all have the same loading/unloading paths. The reloading path is different among them. At first, a mixed-mode loading is applied proportionally with $\Delta_n = \Delta_t =$ 0.02 mm; then a mixed-mode unloading is performed proportionally until $\Delta_n = \Delta_t = 0$. At last, the

reloading is carried out until complete failure. During the reloading stage, case 1 has proportional opening with $\Delta_n = \Delta_t$; case 2 $\Delta_n > 0$ and $\Delta_t = 0$; case 3 $\Delta_n = 0$ and $\Delta_t > 0$.

The critical energy release rate in mode I (G_{c_I}) is two times larger than that in mode II (G_{c_II}). As shown in Figure 4.5 (a), under proportional reloading in case 1, the complete failure in mode I is achieved first, which makes the tangential traction equal to zero in mode II failure. It should be remembered that the *complete* failure in either mode I or mode II makes the cohesive interface fail completely. For example, if an interface element has an ultimate failure in the normal direction (mode I), the tangential cohesive strength of the interface element will also be reduced to zero. In mixed-model, the mode I and II failures influence each other, three reloading paths produces distinctive behaviors of the cohesive interface. The maximum normal and tangential tractions in mixed-mode are less than that in mode I and mode II failures, respectively. The complex mechanical behaviors in mixed-mode failure could impact hydraulic fracturing when the mixed-mode failure, rather than commonly analyzed tensile failure (mode I), exists in this treatment.

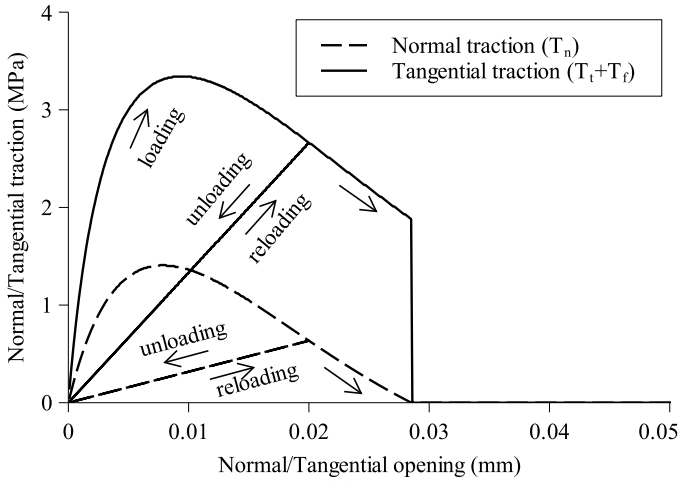

(a)

Figure 4.5 Mixed-mode failure under three different reloading conditions: (a) $\Delta_n = \Delta_t$; (b) $\Delta_n > 0$ and $\Delta_t = 0$; (c) $\Delta_n = 0$ and $\Delta_t > 0$. The frictional component of tangential traction is actually zero, since the normal opening is positive, the cohesive interface is in tensile stress state. (continued)

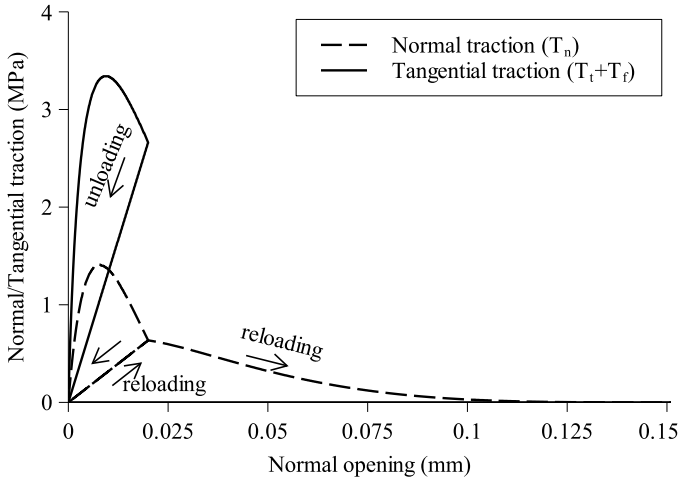

(b)

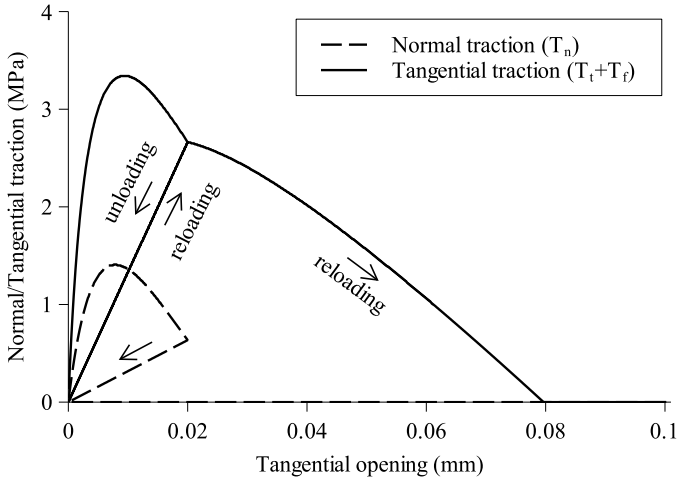

(c)

Figure 4.5 (continued). (Caption shown on previous page.)

4.4 Numerical analyses

The hydro-mechanical model is first evaluated through the commonly used Renshaw and Pollard's criterion. Then laboratory experiments on fracture-discontinuity interaction under triaxial-stress conditions are studied. With the existence of formation interface, the influence of modulus contrast and stress contrast on hydraulic fracture height growth is analyzed at last.

4.4.1 Comparison of model predictions with analytical crossing criterion

For interaction between an induced fracture and a pre-existing discontinuity (e.g. natural fracture, formation interface), multiple criterions existing in the literature can be used to determine whether an induced fracture could cross a frictional interface. A commonly used one

is that proposed by Renshaw and Pollard (1995), which was successfully verified through laboratory experiments for its conditions of applicability. The criterion was derived based on the theory of linear elastic fracture mechanics (LEFM). It suggests fracture reinitiation on the opposite side of the interface could occur when the stress singularity still exists at fracture tips as the fracture is approaching the interface but not in contact yet. Analyses indicate that there is no mathematical stress singularity at the fracture tips when they are in contact with a frictional interface. In other words, if reinitiation prior to contact does not occur, a fracture may not be able to cross an interface since the loss of stress singularity at the contact points with a frictional interface reduces the stress concentration around the tips. To use formulations derived based on LEFM, linear elastic, homogeneous and isotropic material properties are assumed on both sides of the interface; the elastic properties across the interface should not have a strong contrasts (i.e., the ratio of Young's modulus on the two sides should range from 0.4 to 2.0 given identical Poisson's ratio); a uniform in-situ stress field is assumed (i.e. no stress contrast exists at the interface); the criterion also assumes the interface is perfectly bonded, no slippage or opening exists along the interface. As will be illustrated in following sections, slippage or opening would inevitably occur when an induced hydraulic fracture is approaching and is in contact with a formation interface.

For a vertical hydraulic fracture propagating towards a horizontal interface, the criterion for the hydraulic fracture crossing the interface has the following form (Renshaw and Pollard 1995) (note: tension is positive; compression negative):

$$\frac{-\sigma_v^r}{T_0 - \sigma_{hmin}^r} > \frac{0.35 + \frac{0.35}{\mu}}{1.06} \tag{4.14}$$

where σ_v^r is remote vertical stress (in-situ vertical stress), σ_{hmin}^r remote minimum horizontal stress, T_0 tensile strength of intact rock, μ coefficient of friction. Eq. (4.14) involves in-situ stresses, tensile strength and coefficient of friction. Other elastic properties of rock, such as Young's modulus, Poisson's ratio, and critical energy release rate/fracture toughness, are not considered.

Two cases are studied in order to evaluate our numerical model. The schematic geometry of the model is illustrated in Figure 4.6. A hydraulic fracture is approaching vertically to a horizontal formation interface (indicated by the red line). Homogeneous, isotropic material properties (Young's modulus E = 38.8 GPa, Poisson's ratio ν = 0.15) and uniform in-situ stress are used here though there are two layers indicated in Figure 8. In the first case, the vertical stress σ_v^r is set as 10.0 MPa; the minimum horizontal stress σ_{hmin}^r = 9.0 MPa; the tensile strength of intact rock T_0 = 1.0 MPa; the critical energy release rate of intact rock G_{IC} = 100 N/m (corresponding fracture toughness K_{IC} = 2.0 Pa.m$^{1/2}$); the coefficient of friction μ = 0.6. The formation interface has negligible tensile strength and critical energy release rate. Injection rate is 4.0 × 10^{-5} m^3/(s.m) (plain strain condition is simulated in a 3D domain), fluid viscosity 1.0 Pa.s. For the given parameters, the left side of Eq. (4.14) equals 1.0, the right side equals 0.88. The criterion predicts the hydraulic fracture crosses the formation interface.

Numerical results for the first case are shown in Figure 4.7. The hydraulic fracture crosses the horizontal formation interface. It is consistent with the analytical prediction. Analyzing the variation of net pressure and aperture on the curves in Figure 4.7 (a) and (b), several processes related to fracture propagation can be observed. Initially the hydraulic fracture propagates in both the upward and downward directions (t < 34 s). During this stage, the numerical results match well with asymptotic analytical solutions for a plane strain KGD

hydraulic fracture (Detournay 2004). At t = 34 s (t_1), the lower tip of the hydraulic fracture reaches a zone with a higher lateral stress set intentionally to prevent the fracture propagating in the downward direction and to force it to propagate in the upward direction where the horizontal interface exists. At t = 66 s (t_2), the hydraulic fracture reaches the formation interface (bedding plane). After 66 s, the injection net pressure continuously increases; the formation interface starts sliding and the top tip of the hydraulic fracture is widened, as illustrated by the fracture profile at t_3. At t = 86 s (t_4), the shear force on the interface is large enough to initiate the tensile failure in rock on the opposite side of the interface (t_4 in Figure 4.7); the hydraulic fracture starts crossing the interface and propagating again in the upward direction. After 86 s, the injection net pressure experiences decrease as the hydraulic fracture propagates continuously in the upward vertical direction (t_5 and t_6 in Figure 4.7). Similar phenomenon was reported in a laboratory study on hydraulic fracture propagation crossing a formation interface (Daneshy 1978). Injection pressure was observed to be accumulated when the hydraulic fracture reached the formation interface. After hydraulic fracture penetrated into the bounding layers, injection pressure began once again to decrease.

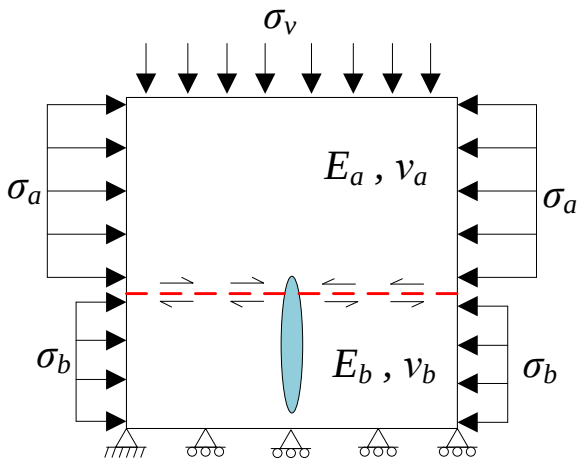

Figure 4.6 Illustration of the interaction between a hydraulic fracture and a formation interface (bedding plane) in a layered medium. Formation a and b have different material properties and in-situ stress. The red line indicates the formation interface.

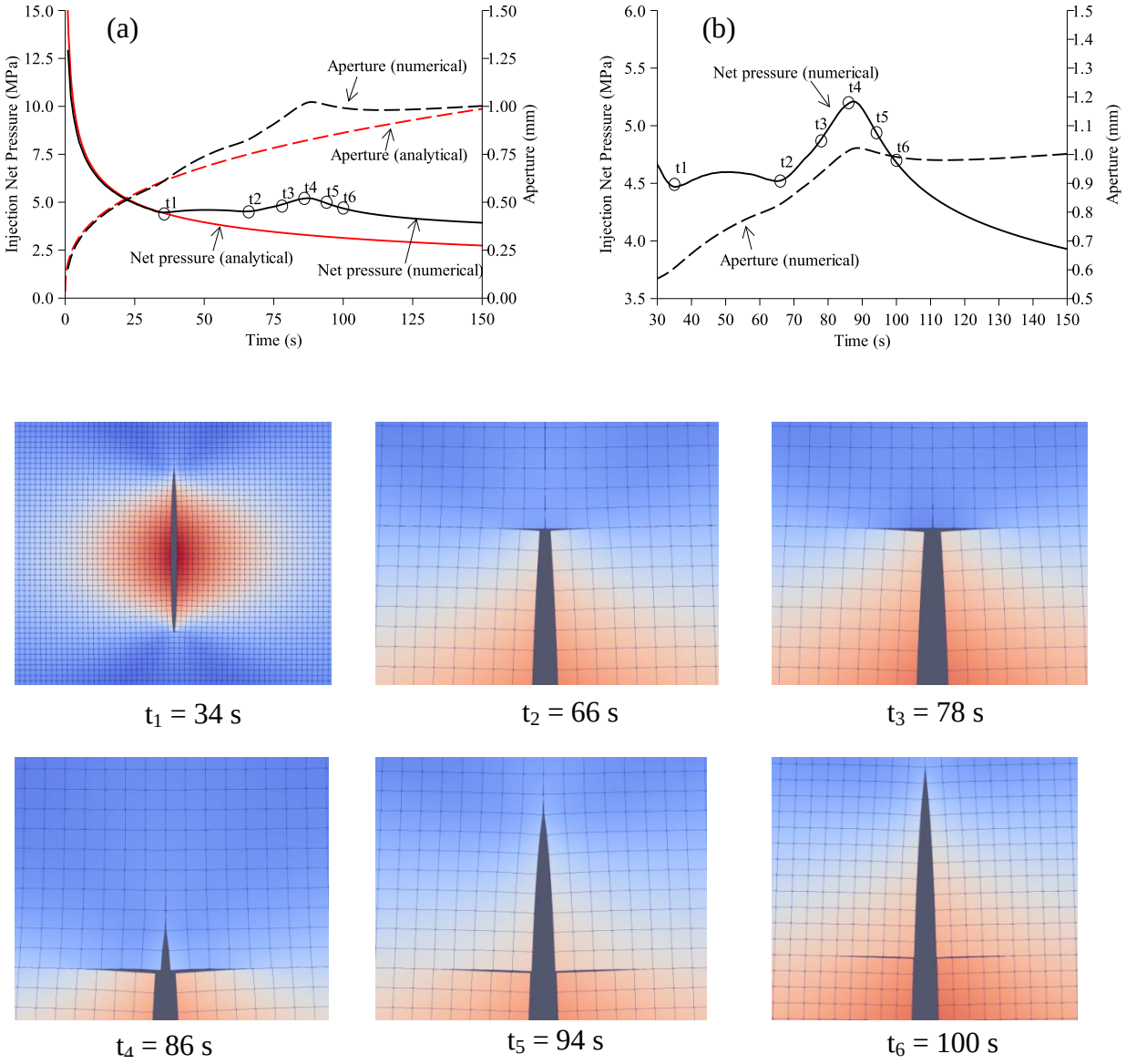

Figure 4.7 Net pressure, aperture and corresponding fracture profiles vs. time for the first case. (a) Net pressure and aperture at the injection point plotted as functions of time for $0 \leq time \leq 150$ s. The red lines show the asymptotic analytical solution, which is applicable ($time < 34$s) before the hydraulic fracture (HF) is restricted by high stress contrast in order to stop it propagating in the downward direction and before it reaches the horizontal formation interface in the upward direction; (b) Variation of net pressure and aperture at the injection point when $time > 30$s. The HF profiles are shown by color contours, the deformation is enlarged by a factor of 200: t_1: HF stops propagating downward; t_2: HF reaches the horizontal interface; t_3: Interface slips due to pressurization of HF; t_4: HF initiates at the intersection point; t_5: HF crosses the formation interface and propagates in the upward direction; t_6: HF propagates continuously. The mesh is uniform in horizontal and vertical directions and each grid is 0.1 m by 0.1 m.

In the second case, the vertical stress σ_v^r is lower, 9.1 MPa; the minimum horizontal stress σ_{hmin}^r = 9.0 MPa; the tensile strength of intact rock is higher, T_0 = 2.0 MPa. All the other parameters are the same as those used in the first case. For the given parameters, the left side of Eq. (4.14) equals 0.83. The crossing criterion of Eq. (4.14) is not satisfied. Arrest of the hydraulic fracture is predicted through Eq. (4.14). As expected, the numerical results are consistent with the analytical criterion, the vertical growth of the hydraulic fracture is inhibited by the formation interface, as illustrated in Figure 4.8. The net pressure and aperture at the injection point are plotted as functions of time in Figure 4.8 (a) and (b). The variation of net pressure and aperture at the injection point is associated with several processes related to fracture propagation. As in the first case, the hydraulic fracture is free to propagate upward and downward until it reaches the stress contrast at t = 34 s. The stress contrast is set to restrict its propagation in the downward direction. After downward growth stops, the hydraulic fracture propagates upward and approaches the formation interface above it. At t = 66 s, the hydraulic fracture reaches the interface. Because of the lower vertical stress, frictional force on the interface is insufficient to initiate the tensile failure of rock above the interface, the hydraulic fracture is arrested by the formation interface. Continued pumping causes the interface to open, as shown by the fracture profile at t_3 = 140 s. Field mapping of fracture geometry in a coal mine revealed the propagation of hydraulic fractures along formation interfaces (Jeffrey et al. 1992). The deflection of a vertical hydraulic fracture into a horizontal formation interface between coal and roof-rock generated the T-shaped fracture geometry.

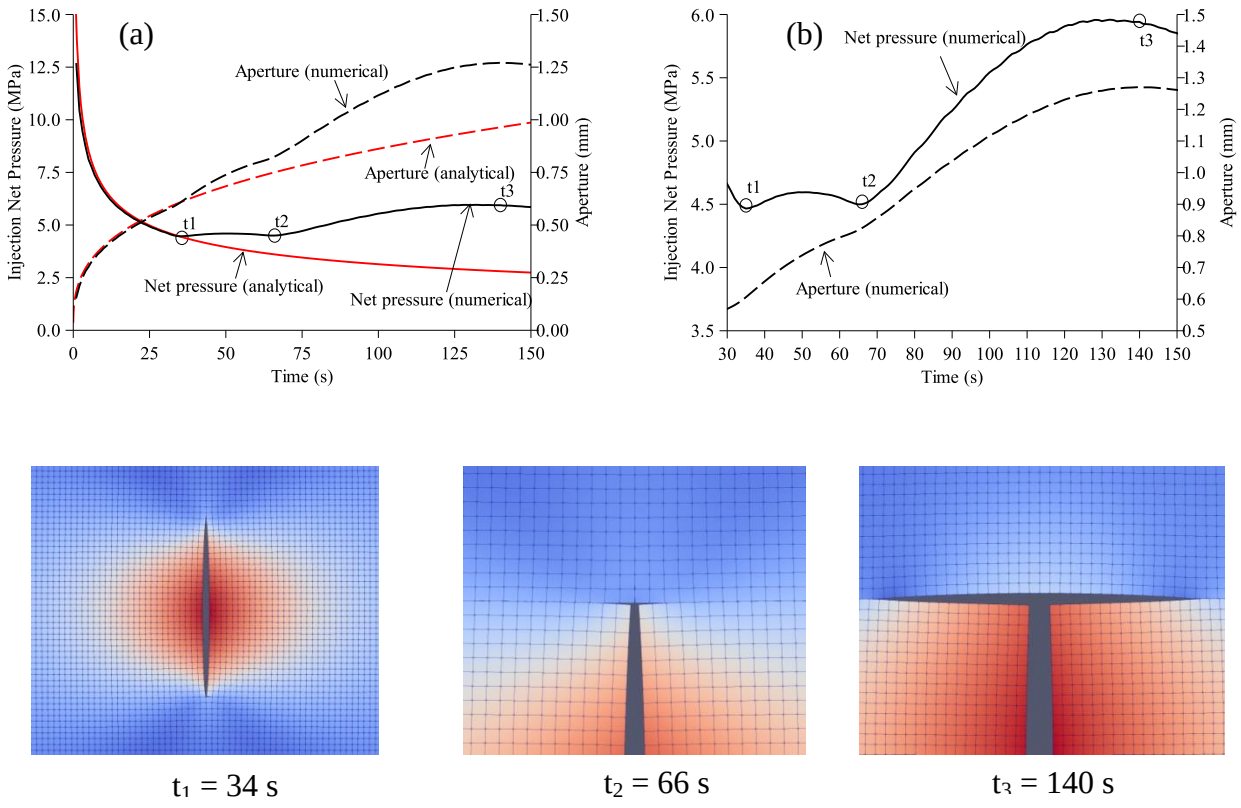

Figure 4.8 Net pressure, aperture and corresponding fracture profiles vs. time for the second case. (a) Net pressure and aperture at the injection point plotted as functions of time for $0 \leq time \leq 150$ s. The red lines show the asymptotic analytical solution, which is applicable (*time* < 34s) before the HF is restricted by high stress contrast in order to stop it propagating in the downward direction and before it reaches the horizontal formation interface in the upward direction; (b) Variation of net pressure and aperture at the injection point when *time* > 30s. The HF profiles are shown by color contours, the deformation is enlarged by a factor of 200: t_1: HF stops propagating downward; t_2: HF reaches the horizontal interface; t_3: Slippage and opening of the formation interface. The mesh is uniform in horizontal and vertical directions and each grid is 0.1 m by 0.1 m.

The stress distribution at t = 140 s around the opening section of the formation interface for the second case is illustrated in Figure 4.9. As shown, on the opposite side of the hydraulic fracture, the stress in the horizontal direction (σ_{yy}) in rock above the interface is under tension at tips, and is under compression at the center part of the opening section. The compressive stress would prevent the initiation of new hydraulic fractures at the center part above the interface. However, if flaws (e.g. natural fracture, joint) exist at the regions close to fracture tips, reinitiation of hydraulic fractures along the flaws in rock above the interface may occur. Below

the interface, the rock is under compression. On-site mineback and coring showed hydraulic fractures are offset when they cross joints (Warpinski and Teufel 1987; Jeffrey et al. 1992). Exposed outcrops also demonstrate the reinitiation of fractures from pre-existing flaws along bedding planes or natural fractures (Helgeson and Aydin 1991; Underwood et al. 2003).

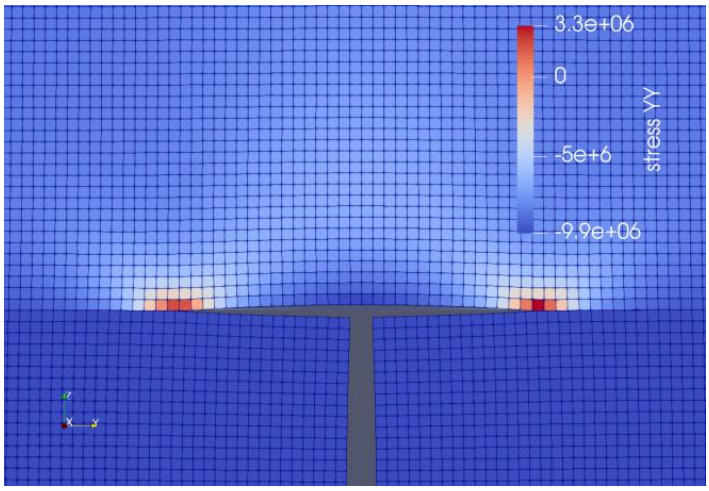

(a)

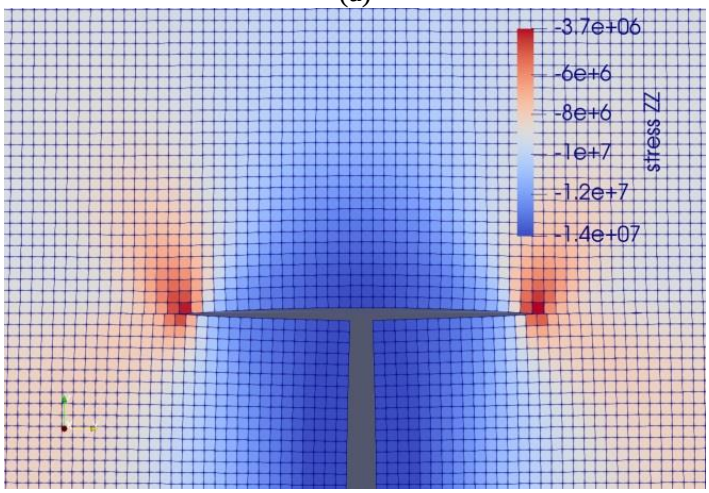

(b)

Figure 4.9 Stress distribution at t = 140 s around the opening portion of the formation interface: (a) σ_{yy} (horizontal) distribution; (b) σ_{zz} (vertical) distribution.

It should be noted that our numerical model is built through FEM-based CZM so that the more realistic interactions can be studied by relaxing the limiting assumptions in the analytical approach. For example, when an induced hydraulic fracture is approaching the interface, the interface can experience either frictional slippage (mode II failure) or opening (mode I failure) or

both (mixed mode failure). Both modulus contrast and stress contrast can exist at the interface. One of the important parameters lacking in Eq. (4.14) is the critical energy release rate (or fracture toughness). Fracture propagation is determined by the critical energy release rate.

4.4.2 Simulation of laboratory tests on hydraulic fracture crossing a pre-existing discontinuity

In this section we simulate laboratory experiments conducted by Gu et al. (2012) to study the crossing/arrest criterion for fracture-discontinuity interaction. The block samples were tested under triaxial-stress conditions. A discontinuity was created by cutting the block samples at specified angles (i.e. 90°, 75°, and 45°) with respect to the designed direction for hydraulic fracture propagation. The two faces of the discontinuity were ground smooth and flat. Here we focus on the orthogonal interaction. The hydraulic fracture propagates toward the created discontinuity perpendicularly. Same type of rock (Colton sandstone) is used in all the tests. The Young's modulus is 20 GPa; Poisson's ratio 0.15; tensile strength of rock 4 MPa; critical energy release rate (G_{IC}) 115 N/m (corresponding fracture toughness K_{IC} = 1.6 MPa.m$^{1/2}$); fluid viscosity 1.0 Pa.s; injection rate 0.5 × 10^{-6} m^3/s. The coefficient of friction for the discontinuities was measured to be 0.615. The cohesive strength and critical energy release rate (G_{IC}) for discontinuities are negligible. The coupled hydro-mechanical model is utilized to simulate two of the laboratory tests, which have the same laboratory configurations but have different stresses applied on the boundaries. In the first test, S_v = 27.6 MPa (4000 psi), S_{Hmax} = 13.8 MPa (2000 psi), S_{hmin} = 6.89 MPa (1000 psi). The only difference between the first and second test lies in the S_{Hmax}, which is equal to 7.58 MPa in the second one.

The geometry and the location of the discontinuity are shown in Figure 4.10. The injection point is located at the center point of the block. Figure 4.11 illustrates the fracture footprint and the distribution of aperture at t = 7.3 s for the first and second tests. As shown, in

the first numerical simulation, the hydraulic fracture crosses the discontinuity; in the second test, the hydraulic fracture is arrested at the discontinuity. Numerical results are consistent with the laboratory observations.

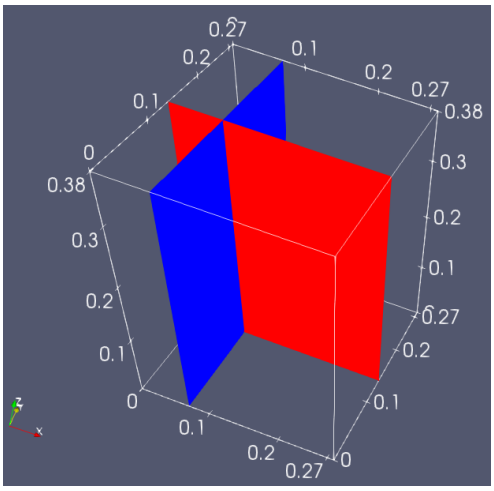

Figure 4.10 Geometry of the block sample and locations of the cutting discontinuity and the designed fracture propagation path. Red color indicates the designed fracture propagation path; blue color indicates the discontinuity. The minimum horizontal stress (S_{hmin}) is perpendicular to the red plane. Unit: m.

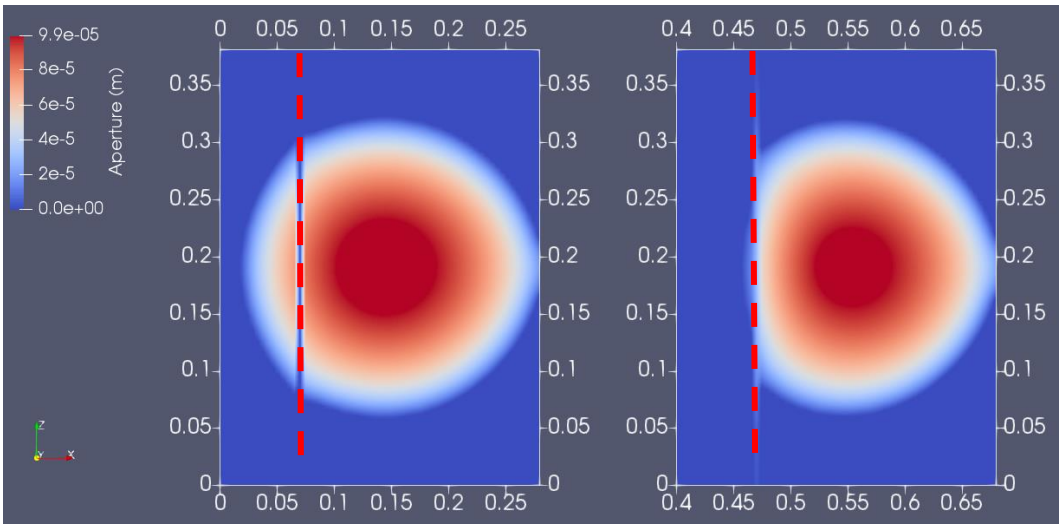

Figure 4.11 Fracture foot print and aperture distribution after 7.3 seconds of injection. The left figure is for the first test; the right one is for the second test. The red dash line shows the location of the discontinuity that is orthogonal to the plane (x-z plane) of fracture propagation.

The injection pressure and aperture at the injection point are plotted as functions of time in Figure 4.12. Before the hydraulic fractures reach the discontinuity (t < 1.36 s), the results from the two numerical simulations are identical in pressure and aperture distribution and should

match the asymptotic analytical solution (Savitski and Detournay 2002) for penny-shaped hydraulic fracture. The numerical results have larger aperture and higher net pressure than those in analytical solutions. Simple calculation reveals that the hydraulic fracture propagates in a viscosity-dominated regime. The analytical solutions for viscosity-dominated regime work for idealized situations in which the influence of tensile strength (or fracture toughness) on fracture propagation is negligible. The rock samples studied here have a tensile strength = 4 MPa, which is too large to be ignored and causes the differences between the numerical results and analytical solutions. Detailed analyses on the effects of tensile strength in the hydro-mechanical model can be found in Gao and Ghassemi (2019b). At t = 3.36 s, the hydraulic fracture starts crossing the discontinuity in the first test. At t = 7.30 s, the hydraulic fracture in both the first test and the second test reaches the boundary of the rock samples (Figure 4.11). Before reaching boundaries, the crossing scenario (first test) has larger aperture and smaller net pressure at the injection point.

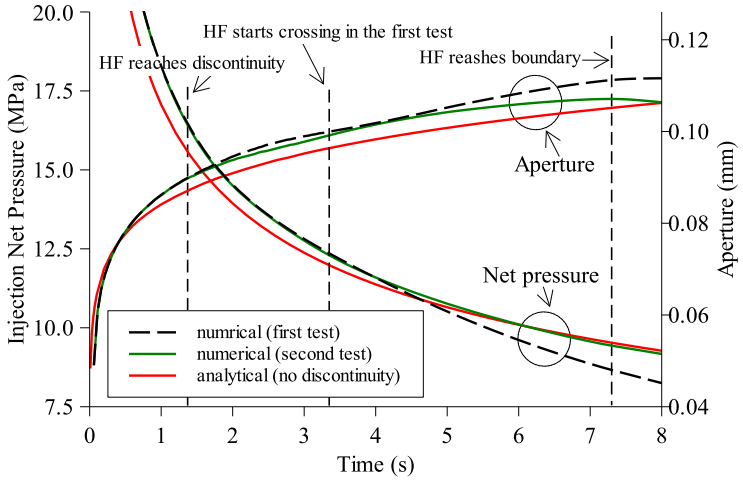

Figure 4.12 Net pressure and aperture at the injection point vs. time. The asymptotic analytical solution for penny-shaped hydraulic fracture is given for reference. The solution assumes no existence of discontinuities.

4.4.3 Effect of Young's modulus

In traditional modeling on hydraulic fracturing in layered formations, the formation interfaces are commonly assumed to be perfectly bonded without slippage during hydraulic

fracturing; the influence of layered Young's modulus is often ignored or an uniform Young's modulus obtained from a certain kind of average method (e.g., thickness-weighted average) is used instead. It is suggested in the literature that, compared to stress-contrast, modulus contrast is negligible. Through laboratory tests, Daneshy (1978) demonstrated that the variation of modulus on the two sides of cemented interfaces is insufficient to terminate fracture growth across the interfaces. In many situations, the change of modulus occurs on the two sides of a formation interface which could be weakly bounded. The slippage along weakly bounded interfaces together with modulus contrast could yield results different with observations or simulations that have strongly bounded formation interfaces.

The influence of modulus contrast on hydraulic fracture-discontinuity interaction is studied here. The example shown in Figure 4.7 is used as a base case, which has a uniform distribution of Young's modulus (38.8 GPa). A scenario is created that has Young's modulus = 38.8 GPa for the layer above the interface and has Young's modulus = 19.4 GPa for the layer below the interface within which the hydraulic fracture propagates (as illustrated in Figure 4.6). All the other parameters are the same as those used in the base case. As shown in Figure 4.13 (a) about σ_{yy} distribution at t = 112 s, the hydraulic fracture is arrested by the formation interface. Tensile stress develops across the interface due to the frictional slippage along the interface; the maximum tensile stress in the horizontal direction (σ_{yy}) in rock above the interface is about 1.4 MPa. If there are flaws with tensile strength less than the tensile stress, reinitiation of fractures could take place along the interface. The modulus contrast together with the interface causes the arrest of the hydraulic fracture. For comparison purpose, an additional scenario not having the horizontal interface in the model is also simulated. At t_2 = 89 s, the hydraulic fracture reaches the interface. When the horizontal interface does not exist, the hydraulic fracture crosses the

interface, just as those shown in Figure 4.7. For the scenario having the horizontal interface, the injection net pressure is larger than that in the scenario without the interface (Figure 4.13(b)).

When the layer above the horizontal interface has Young's modulus = 19.4 GPa and the layer below the interface has Young's modulus = 38.8 GPa, the hydraulic fracture crosses the interface just as those shown in Figure 4.7.

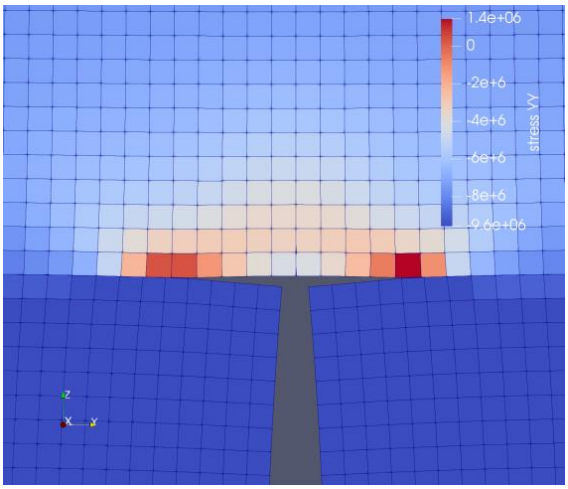

(a)

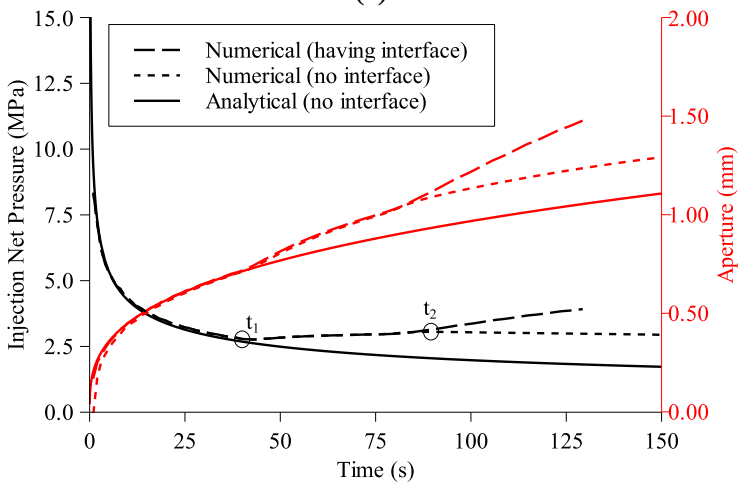

(b)

Figure 4.13 (a) σ_{yy} distribution at t = 112 s around the opening section of the formation interface; (b) Aperture, injection net pressure vs. time for numerical results and asymptotic analytical solutions (t_1: HF stops propagating downward; t_2: HF reaches the location where Young's modulus contrast exists).

Due to the existence of the horizontal interface and the modulus contrast, the stress distribution is not continuous across the interface. Figure 13 illustrates the induced σ_{yy} distribution before the

fracture tip reaches the interface for the above mentioned two different scenarios. Figure 4.14 (a) is for the scenario with E = 38.8 GPa for the upper layer and E = 19.4 GPa for the lower layer. Figure 4.14 (b) is for the scenario with reversed distribution of Young's modulus. As can be seen, the range of induced σ_{yy} around the fracture tip in Figure 4.14 (b) (upper layer E = 19.4 GPa, lower layer E = 38.8 GPa) is larger than that in Figure 4.14 (a) (upper layer E = 38.8 GPa, lower layer E = 19.4 GPa). The induced σ_{yy} along a line (red dash line in Figure 4.14 (a) and (b)) above the interface is shown in Figure 4.14 (c). The maximum induced tensile stress is not located ahead of the fracture tip (the symmetric point of the model) (y = 215 m), but located at a distance away from it. The distribution of induced stresses in the upper layer could reinitiate fractures at locations away from the intersection point (y = 215 m) between the vertical hydraulic fracture and the horizontal interface, thus creates an offset between the intersection point and the reinitiation points. Laboratory experiments and in-situ observations have well documented the offset phenomena for fracture-discontinuity interaction (Jeffrey et al. 1992; Warpinski and Teufel 1987).

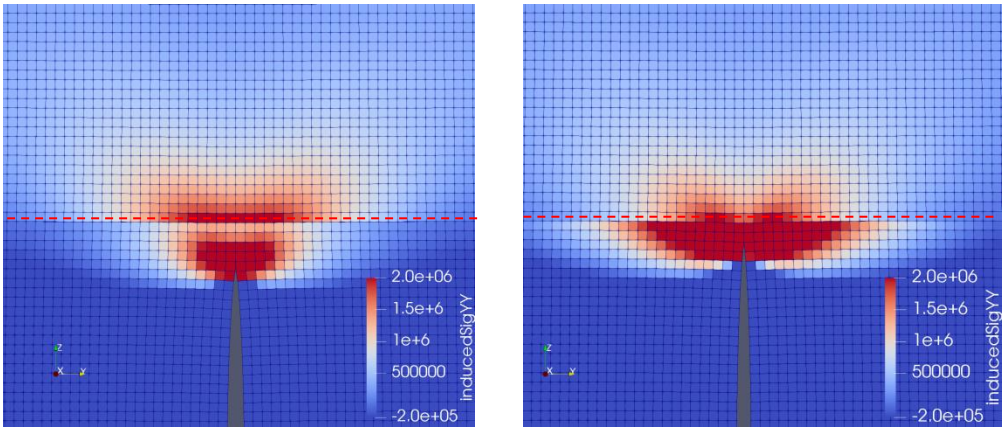

(a) (b)

Figure 4.14 (a) Induced σ_{yy} distribution at t = 60 s before the fracture tip reaches the formation interface, upper layer E = 38.8 GPa, lower layer E = 19.4 GPa; (b) Induced σ_{yy} distribution at t = 54 s before the fracture tip reaches the formation interface, upper layer E = 19.4 GPa, lower layer E = 38.8 GPa; (c) Induced σ_{yy} along a line parallel to the horizontal interface in the upper layer (red dash line in (a) and (b)). (y is the horizontal direction; z is the vertical direction.) (continued)

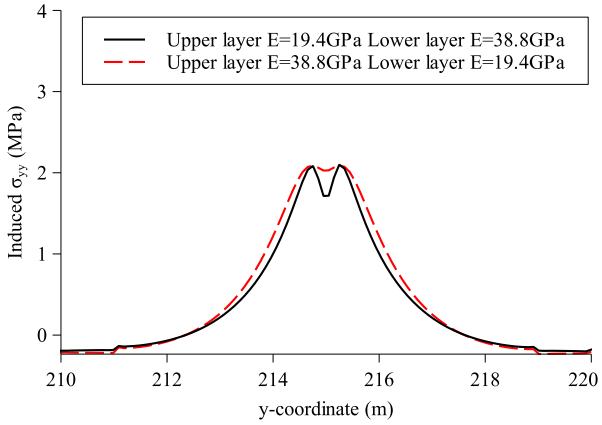

(c)

Figure 4.14 (continued). (Caption shown on previous page.)

4.4.4 Effect of stress contrast

Stress contrast in a layered formation is often considered as the dominating factor that controls the hydraulic fracture height growth. Laboratory and on-site experiments have demonstrated that stress contrast larger than a certain value can completely inhibit the growth of hydraulic fractures. When in-situ stress contrast is combined with the weakly bounded interfaces (or other discontinuities, such as natural fracture, joint), their effects on fracture height growth could become more significant.

The example shown in Figure 4.7 is used again as a base case, which has a uniform distribution of minimum horizontal stress (S_{hmin}). A case is created with stress contrast of 0.5 MPa existing at the horizontal interface (see Figure 4.6 for illustration). The top layer has 0.5 MPa larger S_{hmin} than the bottom layer. All the other parameters are the same as those used in the base case. Figure 4.15 gives the distribution of σ_{yy} and the curves for the net pressure and the aperture at the injection point vs. time. As shown, the hydraulic fracture is arrested; the minimum value of σ_{yy} is at the fracture tips and still under compression (≈ - 0.26 MPa). An additional scenario without the existence of the horizontal interface is considered for comparison purpose. At t_2 = 68 s, the hydraulic fracture reaches the stress contrast. The injection net pressure for the

scenario having the horizontal interface is larger than that in the case without the interface after reaching the stress contrast.

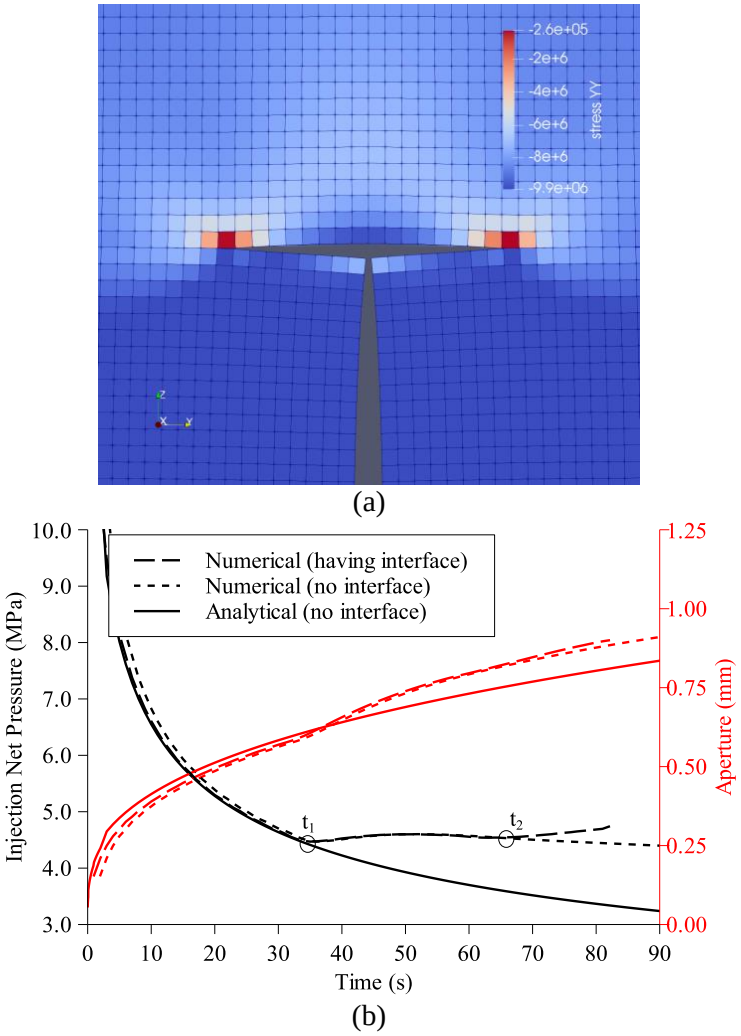

Figure 4.15 (a) σ_{yy} distribution at t = 82 s around the opening section of the formation interface; (b) Aperture, injection net pressure vs. time for numerical results and asymptotic analytical solutions (t_1: HF stops propagating downward; t_2: HF reaches the location where stress contrast exists).

4.5 Discussion

Multiple key factors influence and control the height growth of hydraulic fractures in layered formations. Effects of material properties, in-situ stress, and mechanical properties of discontinuities are analyzed in this study. The emphasis is placed on the mechanical behaviors of discontinuities considering the effects of modulus contrast and stress contrast. As we know, the change of material properties usually occurs at a discontinuity (e.g. formation interface/bedding

plane). The effects of layered modulus (or modulus contrast) on fracture propagation are often not considering in many analyses. Since the fracture-discontinuity interaction involves complex mechanical behaviors, the formation interface/bedding plane is commonly assumed to be perfectly bounded without frictional slippage; its influence on hydraulic fracture height growth is thus weakened when the discontinuities are not considered. As shown in previous analyses, the combination of modulus contrast and frictional slippage could produce results that are different with those using single uniform modulus. In-situ stress contrast can directly control the fracture height growth. When stress-contrast is considered together with the existence of discontinuities, their influence on height growth or fracture propagation is significant. A slight stress contrast (0.5 MPa in this study) at a discontinuity could effectively inhibit the propagation of fractures. On-site experiments demonstrated that neither the material properties nor the in-situ stress contrast is sufficient to explain the observed relatively longer fracture lengths compared to their height. The combined effects from material properties, in-situ stress and the existence of discontinuities should be considered in analyzing height confinement mechanisms (Warpinski et al. 1998).

Based on FEM and Newton-Raphson solution scheme, all the hydro-mechanical processes in this study are modelled in a fully coupled manner. Fully coupled scheme is crucial to accurately predict the behaviors of hydraulic fractures, especially for fracture propagation in viscosity-dominated regime. All the examples in previous sections are in the viscosity-dominated regime. Within this regime, the pressure within hydraulic fractures varies significantly as a function of fracture aperture. After the form of "T-shaped" hydraulic fractures, the opening along formation interface/bedding plane is usually smaller than the vertical part of the "T-shaped" hydraulic fractures, partly due to the relatively larger vertical in-situ stress. Smaller aperture

along formation interface/bedding plane causes larger pressure drop, which in turn requires higher injection pressure for further propagation along the interface. This phenomenon has been well demonstrated on the injection pressure curves in the previous examples. On the curves for the injection net pressure vs. time, higher injection pressure is always observed when the vertical hydraulic fractures reach the horizontal interface. The injection pressure continuously increases when the horizontal interface experience slippage and/or opening. The mechanism of frictional slippage could potentially be used to explain the relative higher injection pressure observed in field than those predicted by traditional hydraulic fracturing simulators without considering the existence of discontinuities. In addition, it should be emphasized that the frictional slippage in this work is coupled into the nonlinear solution scheme, based on which the frictional slippage is a part of the solutions but not evaluated subsequently according to the solutions.

4.6 Conclusions

A coupled hydro-mechanical model utilizing a cohesive interface element is developed and utilized to study the hydraulic fracture height growth in layered formations. The cohesive interface element is suitable to simulate mode I, mode II and mixed mode fractures. Mechanical behaviors of the interface element are determined by a cohesive zone model that can account for frictional slippage. A series of numerical tests are performed to evaluate the mechanical behaviors of the interface element under different typical loading paths. The demonstrated loading, unloading and reloading paths illustrate the versatility of the model and reveal its capability to handle many different working conditions. To study the height growth of hydraulic fractures in layered formations considering modulus contrast, in-situ stress contrast and the existence of discontinuities, the model is evaluated through the commonly used Renshaw and Pollard's criterion for an induced fracture orthogonally crossing a pre-existing fracture/interface.

The numerical model produces results being in agreement with those predicted by the criterion. The responses of injection pressure and aperture at the injection point are recorded. Several processes related to the fracture-interface interaction are reveled. When the vertical hydraulic fractures reach the horizontal interface, the injection pressure increases. Continuous opening and sliding of the interface causes the need of higher injection pressure. Stress distribution around the tips of "T-shaped" hydraulic fractures indicates the potential of fracture reinitiation along the interface if flaws exist. The model is also utilized to study laboratory experiments on fracture-discontinuity interaction under triaxial-stress conditions. The numerical results match well with the experiments in terms of hydraulic fractures crossing of or being arrested by a pre-existing discontinuity.

The influence of interface on fracture height growth is studied under the existence of modulus contrast and in-situ stress contrast at the interface. For a hydraulic fracture propagates in a lower layer, which has one-half of the Young's modulus as that in the upper layer, the hydraulic fracture is arrested by the interface existing between the two layers. However, it crosses the interface when a uniform modulus is used for the two layers (the modulus contrast does not exist). The effects of stress contrast yield the similar results. A hydraulic fracture is arrested when adding slightly higher in-situ stress (0.5 MPa) in the upper layer. When combining together the effects of modulus contrast, stress contrast, and the existence of discontinuities, the propagation of fractures and the height growth of hydraulic fractures could be effectively impeded.

References

Anderson, G. D. 1981. Effects of Friction on Hydraulic Fracture Growth Near Unbonded Interfaces in Rocks. *Society of Petroleum Engineers Journal* **21** (01): 21-29. http://dx.doi.org/10.2118/8347-pa.

Cook, T. S. and Erdogan, F. 1972. Stresses in bonded materials with a crack perpendicular to the interface. *International Journal of Engineering Science* **10** (8): 677-697. https://doi.org/10.1016/0020-7225(72)90063-8.

Daneshy, A. A. 1978. Hydraulic Fracture Propagation in Layered Formations. *Society of Petroleum Engineers Journal* **18** (01): 33-41. http://dx.doi.org/10.2118/6088-pa.

Detournay, E. 2004. Propagation Regimes of Fluid-Driven Fractures in Impermeable Rocks. *International Journal of Geomechanics* **4** (1): 35-45. http://dx.doi.org/10.1061/(ASCE)1532-3641(2004)4:1(35).

Gao, Q. and Ghassemi, A. 2018. Parallel Finite Element Simulations of 3D Hydraulic Fracture Propagation Using a Coupled Hydro-mechanical Interface Element. Paper presented at the 52nd US Rock Mechanics / Geomechanics Symposium, Seattle, Washington, USA, 17 June-20 June.

Gao, Q. and Ghassemi, A. 2019a. 3D thermo-poromechanical analysis of flow, heat transport and deformation in fractured rock with applications to a lab-scale geothermal system. **submitted**.

Gao, Q. and Ghassemi, A. 2019b. Finite element simulations of 3D planar hydraulic fracture propagation using a coupled hydro-mechanical interface element. **submitted**.

Gao, Q. and Ghassemi, A. 2019c. Three dimensional finite element simulations of hydraulic fracture height growth in layered formations using a coupled hydro-mechanical model. **submitted**.

Gu, H., Weng, X., Lund, J. B. et al. 2012. Hydraulic Fracture Crossing Natural Fracture at Nonorthogonal Angles: A Criterion and Its Validation. *SPE Production & Operations* **27** (01): 20-26. http://dx.doi.org/10.2118/139984-pa.

Helgeson, D. E. and Aydin, A. 1991. Characteristics of joint propagation across layer interfaces in sedimentary rocks. *Journal of Structural Geology* **13** (8): 897-911. https://doi.org/10.1016/0191-8141(91)90085-W.

Hu, L. and Ghassemi, A. 2019. Lab-scale Experiments Investigating the Possibility of Bedding Plane Slip Events During Microseismic Monitoring of Hydraulic Fracturing. Paper presented at the 53rd US Rock Mechanics / Geomechanics Symposium, New York City, NY, USA, 23 June-26 June.

Jeffrey, R. G., Jr., Brynes, R. P., Lynch, P. J. et al. 1992. An Analysis of Hydraulic Fracture and Mineback Data for a Treatment in the German Creek Coal Seam. Paper presented at the SPE Rocky Mountain Regional Meeting, Casper, Wyoming, 1992/1/1/. http://dx.doi.org/10.2118/24362-ms.

Park, K. and Paulino, G. H. 2012. Computational implementation of the PPR potential-based cohesive model in ABAQUS: Educational perspective. *Engineering Fracture Mechanics* **93** (0): 239-262. http://dx.doi.org/10.1016/j.engfracmech.2012.02.007.

Park, K. and Paulino, G. H. 2013. Cohesive Zone Models: A Critical Review of Traction-Separation Relationships Across Fracture Surfaces. *Applied Mechanics Reviews* **64** (6): 060802-060802-20. http://dx.doi.org/10.1115/1.4023110.

Renshaw, C. E. and Pollard, D. D. 1995. An experimentally verified criterion for propagation across unbounded frictional interfaces in brittle, linear elastic materials. *International Journal of Rock Mechanics and Mining Sciences & Geomechanics Abstracts* **32** (3): 237-249. http://dx.doi.org/10.1016/0148-9062(94)00037-4.

Savitski, A. A. and Detournay, E. 2002. Propagation of a penny-shaped fluid-driven fracture in an impermeable rock: asymptotic solutions. *International Journal of Solids and Structures* **39** (26): 6311-6337. http://dx.doi.org/10.1016/S0020-7683(02)00492-4.

Spring, D. W., Giraldo-Londoño, O. and Paulino, G. H. 2016. A study on the thermodynamic consistency of the Park–Paulino–Roesler (PPR) cohesive fracture model. *Mechanics Research Communications* **78**: 100-109. http://dx.doi.org/10.1016/j.mechrescom.2016.05.006.

Spring, D. W. and Paulino, G. H. 2015. Computational homogenization of the debonding of particle reinforced composites: The role of interphases in interfaces. *Computational Materials Science* **109**: 209-224. http://dx.doi.org/10.1016/j.commatsci.2015.07.012.

Teufel, L. W. and Clark, J. A. 1984. Hydraulic Fracture Propagation in Layered Rock: Experimental Studies of Fracture Containment. *Society of Petroleum Engineers Journal* **24** (01): 19-32. http://dx.doi.org/10.2118/9878-pa.

Underwood, C. A., Cooke, M. L., Simo, J. A. et al. 2003. Stratigraphic controls on vertical fracture patterns in Silurian dolomite, northeastern Wisconsin. *AAPG bulletin* **87** (1): 121-142.

Vijayakumar, S. and Cormack, D. E. 1983. Stress behaviour in the vicinity of a crack approaching a bimaterial interface. *Engineering Fracture Mechanics* **17** (4): 313-321. https://doi.org/10.1016/0013-7944(83)90082-6.

Warpinski, N. R., Branagan, P. T., Peterson, R. E. et al. 1998. An Interpretation of M-Site Hydraulic Fracture Diagnostic Results. Paper presented at the SPE Rocky Mountain Regional/Low-Permeability Reservoirs Symposium, Denver, Colorado, 1998/1/1/. http://dx.doi.org/10.2118/39950-ms.

Warpinski, N. R. and Teufel, L. W. 1987. Influence of Geologic Discontinuities on Hydraulic Fracture Propagation (includes associated papers 17011 and 17074). *Journal of Petroleum Technology* **39** (02): 209-220. http://dx.doi.org/10.2118/13224-pa.

5 3D thermo-poromechanical analysis of flow, heat transport and deformation in fractured rock with applications to a lab-scale geothermal system

Abstract

Fluid flow in subsurface rock with either pre-existing fractures or newly created ones, involves coupled thermal-hydro-mechanical processes. Fractures and other discontinuities, such as joints, bedding planes, and faults, usually act as highly permeable flow paths, which dominate the fluid flow and heat transport underground. Better description and understanding of the fracture response to flow and heat transport is of crucial importance in developing underground energy resources. In this work we investigate this problem within the framework of the governing equations for the theory of thermo-poroelasticity, together with the equations describing fluid flow and heat transport in fractures, and the equation for fluid flow in wellbore. The finite element method (FEM) is utilized to discretize the governing equations in a fully coupled manner. A special zero-thickness interface element is implemented to simulate the thermo-hydro-mechanical behaviors of a fracture/matrix system. The constitutive law of the interface element is built based on the cohesive zone model (CZM), which is suitable for simulating both tensile and shear failures. Fracture flow is formulated through the commonly used "cubic law". The fluid flux exchange between the fractures and the surrounding permeable rock matrix is determined by a fluid transfer coefficient. A convective heat transfer coefficient is introduced in the equation governing heat transport in the fractures. When discontinuities in porous rock are treated as interior boundaries, fluid and heat flux equilibrium is maintained. However, the corresponding fluid pressure and temperature are not necessarily continuous across the interior boundaries. The introduction of fluid transfer coefficient and heat transfer coefficient

satisfies the mass balance and energy balance across the interior boundaries, while at the same time allowing for a temperature drop and pressure drop across the interface connecting the fractures and the surrounding rock matrix. Numerical analyses are performed to verify the model, to illustrate some fundamental phenomena, and to provide some applications to laboratory injection and circulation experiments to further validate the model. In particular, three lab-scale EGS (enhance geothermal system) experiments are studied. Numerical simulations reveal the role of mechanical, hydraulic and thermal properties and the coupled processes in the experiments.

5.1 Introduction

The coupled thermo-hydro-mechanical (THM) processes in porous and fractured rock are associated with a wide range of applications. These include geothermal energy extraction, fluid injection induced seismicity, stimulation of petroleum reservoirs, and design of nuclear waste repository in rock, etc. All of these problems involve strong coupling among pressure diffusion, transport of heat, and the change of in-situ stresses and rock deformation.

Since Biot (1941) proposed the isothermal theory of poroelasticity for fluid-saturated porous media, extensive and excellent efforts have been spent to extend the theory to investigate a wide variety of subsurface phenomena. Rice and Cleary (1976) have recast Biot's theory in terms with straightforward physical concepts. A substantial literature exists on extending the well-known isothermal theory to include the thermal effects (Schiffman 1971; Booker and Savvidou 1984, 1985; Kurashige 1989; McTigue 1986; McTigue 1990). The governing equations derived in these papers are different only in some details (McTigue 1986). For example, the expressions for fluid content and fluid pressure are presented in different forms. Both analytic

and numerical methods are developed to derive solutions for the coupled thermal-hydro-mechanical problems in porous media.

Compared to continuous porous media, one distinguishing feature of underground rock mass is the presence of discontinuities (e.g., joints, fractures and faults) which are widely distributed. Problems related to discontinuities are commonly encountered in engineering applications. Pre-existing or newly-created fractures are crucial in the development of geothermal and petroleum reservoir. Discontinuities usually act as highly permeable flow paths, which dominate the fluid flow and heat transfer in reservoirs. Interaction between the discontinuities and the porous matrix is a multi-physics problem. At the interface between the discontinuity and the rock matrix, fluid transfer and convective heat transfer occur and contribute to the mechanical deformation (opening or closing of discontinuities) of the fracture resulting in a coupled system.

There are mainly two kinds of numerical approaches to handle the coupled thermo-hydro-mechanical processes in fractured porous rock. One is based on boundary element method (BEM), which uses integral equation representations of the governing partial differential equations to solve problems of interest (Ghassemi et al. 2013). Since it uses boundary-only discretization, significant reduction in generalized linear algebraic equations is achieved. Extensive work has been done on the thermo-poroelastic formulation of BEM and its usage, especially the displacement discontinuity method (a branch of BEM), to study the coupled processes related to discontinuities in petroleum and geothermal reservoirs. The thermo-poroelastic responses of a stationary crack were studied by Ghassemi and Zhang (2006) using the displacement discontinuity method (DD). Ghassemi et al. (2013) and Ge and Ghassemi (2008) utilizing elastic and poroelastic models based on DD to study the failure processes around a

hydraulic fracture. Simulation results showed the dominant failure mode to be tension in the close vicinity of the fracture where the pore pressure reaches its highest values. Shear failure potential exists away from the fracture walls and near the tips. 3D thermo-poroelastic analyses of fractured network deformation in enhanced geothermal systems were performed by Ghassemi and Zhou (2011), Rawal and Ghassemi (2014) and Safari and Ghassemi (2015). The nonlinear characteristics of the fracture deformation in the normal and shear deformations were considered. In addition, the DD method has been widely used in hydraulic fracturing. Interested readers are referred to Vandamme and Curran (1989), Sesetty and Ghassemi (2015), Kumar and Ghassemi (2016) and Kumar and Ghassemi (2018) for further reading.

The second type of numerical approach is domain mesh-based, such as finite element method, finite volume method and discrete element method. The entire spatial domain of interest needs to be discretized when these methods are adopted. In the FEM, the generated stiffness matrix is sparse, instead of full in the DD, but is relatively larger than that generated from DD method. When simulating discontinuities based on the FEM, interface elements and enriched elements in the framework of extended finite element method (XFEM) are usually utilized. The usage of 2D XFEM to simulate hydro-mechanical problems is often reported; however, the utilization of 3D XFEM to study fully coupled thermo-hydro-mechanical problems is rarely found. In this study we concentrate on using ‘zero-thickness’ interface element to discretely represent discontinuities and to study the fully coupled processes in 3D.

Initially the zero-thickness interface element was developed for rock joints without considering fluid flow and heat transport in discontinuities (Goodman et al. 1968). Many nonlinear mechanical constitutive laws from rock and soil mechanics were successfully implemented into the interface element (Beer 1985; Potts and Zdravkovic 1999). They were

utilized to reproduce a wide range of observed joint stress-strain behavior. For example, Gens et al. (1990) developed an elastoplastic constitutive law to describe the 3D mechanical behavior of joints. A hyperbolic failure criterion was adopted and the hardening/softening evolution was considered. Based on the Mohr-Coulomb failure theory, Lotfi Hamid and Shing (1994) proposed an interface constitutive model capable of simulating the interface fracture under combined normal and shear stresses; the shear dilation phenomenon was also considered. In addition to model the behavior of pre-existing discontinuities, interface elements are also used to analyze cracking phenomena. One of the most commonly used constitutive models capable of capturing the main characteristics of crack initiation and propagation in quasi-brittle materials (e.g. rock, concrete, ceramics) is the cohesive zone model (CZM). There are numerous publications related to CZM since Hillerborg et al. (1976) used it to analyze the cracking behavior in concrete.

To couple the rock matrix and fracture mechanical deformation with the fluid flow and the heat transport in the interface element, different numerical strategies can be found in the literature (Noorishad et al. 1984; Rutqvist et al. 2002). Here we focus on fully coupled approaches, not iteratively coupled (or staggered). Depending on particular physical mechanisms that are considered, double-node zero-thickness interface elements or triple-node zero-thickness interface elements are usually adopted. For example, Noorishad et al. (1982) proposed a fully coupled hydro-mechanical interface element. It is double-nodded and assumes the fluid pressure is continuous across the interface (no pressure drop exists across the interface). Segura and Carol (2008) formulated an interface element with double nodes. Pressure drop across the interface was considered. Cerfontaine et al. (2015) proposed a 3D zero-thickness interface element with triple nodes to simulate coupled hydro-mechanical processes. The fluid flow in discontinuities was discretized by the nodes located on the center plane of the interface and the central plane nodes

were used for fluid flow and top and bottom planes nodes for deformation of fractures. The theory of contact mechanics was utilized to simulate discontinuity behaviors.

When thermal effects need to be considered, additional degrees of freedom for temperature should be defined to simulate heat transport in discontinuities. Considering the discontinuities as internal boundaries, a thermal boundary layer would exist between the discontinuity and the porous matrix (Bergman et al. 2011) and thus a convective heat transfer boundary condition should be applied at the interface. This will cause a temperature drop across the interface. Depending on the value of the convective heat transfer coefficient, the temperature in the discontinuity may be close to that on the two walls of the discontinuity due to high heat flux; or it could have little influence on the wall temperature because of low heat flux. As will be shown here in, the triple-node zero-thickness interface element can handle the convective heat transfer within discontinuities quite well.

In this work, a triple-node zero-thickness interface element is developed to describe the fully coupled thermo-hydro-mechanical behavior of discontinuities. The mechanical constitutive law of the interface element is built based on the CZM, which is suitable for characterizing both pre-existing discontinuities and developing fractures. The transfer of fluid and heat from the interface element to the surrounding continuum elements (8-node hexahedron elements) representing reservoir matrix are determined by transfer coefficients for fluid and heat, respectively. In the following, the governing equations for thermo-poroelasticity, fluid flow and heat transport in fracture, and for fluid flow in wellbore are given first. Then the θ-method and the standard Garlerkin method are adopted to perform temporal and spatial discretization of the given equations. Finally, simulations and analyzes of a few problems are discussed and the model is applied and validated against a lab-scale enhanced geothermal system.

5.2 Governing equations

The formulations for coupled thermo-hydraulic-mechanical model are presented in this section. We first give the strong form of the governing equations. After temporal discretization, the weak form is derived. Through spatial discretization, a system of nonlinear equations is generated. The Newton-Raphson method is adopted to solve the linearized system of equations iteratively.

5.2.1 Thermo-poroelastic theory for porous, permeable rock

By extending Rice and Cleary (1976) or Cleary (1977) theory, McTigue (1986) and Kurashige (1989) developed a themoelastic theory for fluid-saturated porous media. The quasi-linear and quasi-static theory assumes constant material properties. Inelastic terms are ignored. The thermo-poroelastic governing equations consist of the following (McTigue, 1986; Kurashige 1989)

• Constitutive equations:

$$\sigma_{ij} = 2G\left(\varepsilon_{ij} + \frac{\nu}{1-2\nu}\varepsilon_{kk}\delta_{ij}\right) - \alpha p\delta_{ij} - \frac{2G(1+\nu)\alpha_m^T}{3(1-2\nu)}T\delta_{ij}$$
$$\zeta = \alpha\varepsilon_{kk} + \frac{1}{M}p - \left[\alpha\alpha_m^T + \phi\left(\alpha_f^T - \alpha_m^T\right)\right]T \tag{5.1}$$

• Conservation equations:

$$\sigma_{ij,j} = -F_i \quad \text{(Momentum balance)}$$
$$\frac{\partial\zeta}{\partial t} + q_{i,i} = \gamma \quad \text{(Fluid mass balance)} \tag{5.2}$$
$$\frac{\partial\left(\rho_t C_t T\right)}{\partial t} = -h_{i,i} - \left(\rho_f C_f T q_i\right)_{,i} \quad \text{(Energy balance)}$$

• Darcy's law:

$$v_i = -\frac{k}{\mu}\left(p_{,i} - f_i\right) \tag{5.3}$$

• Fourier's law:

$$h_i = -\kappa^T T_{,i} \tag{5.4}$$

In the above equations, a set of five parameters for the theory of linear isotropic poroelasticity consist of the shear modulus G, the drained and undrained Poisson's ratios v and v_u, the Biot's effective stress coefficient α, and the permeability coefficient κ ($\kappa = k/\mu$, where k is the intrinsic permeability and μ the dynamic fluid viscosity). ϕ is porosity, ρ_f fluid density, ρ_t matrix density. M is Biot's modulus (Cheng 2016):

$$M = \frac{2G\left(v_u - v\right)}{\alpha^2\left(1-2v_u\right)\left(1-2v\right)} \tag{5.5}$$

The thermal related parameters are the volumetric thermal expansion coefficient of the porous matrix $\alpha_m{}^T$ and the pore fluid α_f^T, thermal conductivity κ^T, matrix specific heat C_t, and specific heat of pore fluid C_f. The indices take the values 1, 2 and 3, and repeated indices imply summation. So, in total 9 independent parameters are need to describe the rock thermo-poroelastic response.

After some algebraic operations, the field equations for the theory of thermo-poroelasticity can be obtained:

$$Gu_{i,jj} + \frac{G}{1-2v}u_{j,ji} - \alpha p_{,i} - \frac{2G\alpha_m^T\left(1+v\right)}{3\left(1-2v\right)}T_{,i} + F_i = 0$$

$$\frac{\partial p}{\partial t} = M\left[\kappa p_{,jj} - \alpha\frac{\partial \varepsilon_{kk}}{\partial t} + \left(\alpha\alpha_m^T + \phi_0\left(\alpha_f^T - \alpha_m^T\right)\right)\frac{\partial T}{\partial t} + \gamma\right] \tag{5.6}$$

$$\frac{\partial T}{\partial t} = \frac{1}{\rho_t C_t}\left(k^T T_{,i}\right)_{,i} - \frac{\rho_f C_f}{\rho_t C_t}v_i T_{,i}$$

In derivation of Eq. $(5.6)_3$, it is assumed that the fluid and solid densities are independent of temperature and pressure. The variation of porosity due to heating-induced expansion of solid is not considered (Placiauskas and Domenico, 1982). Also, the influences of elastic deformation of solid and dilatation of the fluid on energy generation or consumption are neglected. The thermoelastic coupling effect could be included after considering the solid deformation energy, $[\beta\partial/\partial t]\varepsilon_{ii}$ (Noorishad et al. 1984). The derived energy balance equation is identical to those utilized by Lewis et al. (1986) and Noorishad et al. (1984), which states the energy balance between the rate of inflow into a control volume and the increase in the internal energy.

Considering a closed domain denoted by $\bar{\Omega} = \Omega \bigcup \Gamma$, where Ω is an open domain with boundary Γ. The boundary domain is decomposed into different parts on which essential and natural boundary conditions are specified for displacement or stress, pressure or fluid flow, and temperature or heat flow (Figure 5.1). The decomposed boundaries are subject to the restrictions:

$$\begin{aligned} \Gamma &= \overline{\Gamma_u \bigcup \Gamma_t} = \overline{\Gamma_p \bigcup \Gamma_q} = \overline{\Gamma_T \bigcup \Gamma_{qT}} \\ \varnothing &= \Gamma_u \bigcap \Gamma_t = \Gamma_p \bigcap \Gamma_q = \Gamma_T \bigcap \Gamma_{qT} \end{aligned} \tag{5.7}$$

where Γ_u is the displacement boundary; Γ_t is the stress traction boundary; Γ_p is the fluid pressure boundary; Γ_q is the fluid flux boundary; Γ_T is the temperature boundary; Γ_{qT} is the heat flux boundary.

The boundary conditions for the thermo-poroelastic model are given as

$$u_i = \bar{u}_i \quad \text{on } \Gamma_u \quad \text{(specified displacement)} \tag{5.8}$$

$$\sigma_{ij} n_j = \bar{t}_i \quad \text{on } \Gamma_t \quad \text{(specified traction)} \tag{5.9}$$

$$p = \bar{p} \quad \text{on } \Gamma_p \quad \text{(specified pressure)} \tag{5.10}$$

$$q_i n_i = \bar{q} \quad \text{on } \Gamma_q \quad \text{(specified fluid flux)} \tag{5.11}$$

$$T = \bar{T} \quad \text{on } \Gamma_T \quad \text{(specified temperature)} \tag{5.12}$$

$$q_{Ti} n_i = \bar{q}_T \quad \text{on } \Gamma_{qT} \quad \text{(specified heat flux)} \tag{5.13}$$

The initial conditions at $t = 0$ are given as

$$u_i = u_{i0} \qquad p = p_0 \qquad T = T_0 \tag{5.14}$$

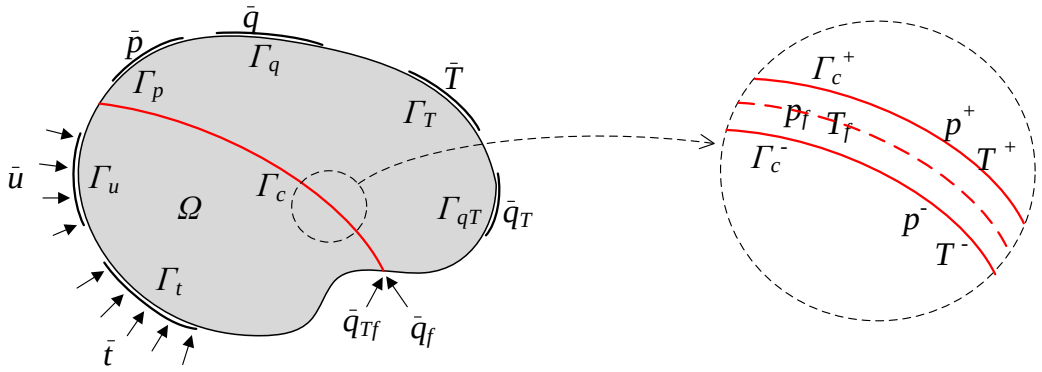

Figure 5.1 Schematic illustration of domain Ω and boundary Γ.

5.2.2 Mechanical behaviors of fracture

Natural fractures have a variety of strength and deformation characteristics. Some pre-existing fractures have cohesive strength and resist opening during pressurization. For newly created hydraulic fractures, enough energy should be provided to maintain the propagation of the fractures. In this work, a cohesive law is adopted to govern the mechanical behaviors of natural and hydraulic fractures, based on which a cohesive zone model (CZM) is built. Other nonlinear mechanical constitutive laws for discontinuities, e.g. elasto-plastic constitutive model based on Mohr-Coulomb theory, can be implemented in the same manner.

Since the introduction of CZM by Barenblatt (1962) and Dugdale (1960) for analyzing elastic-plastic fracture in ductile metals, and by Hillerborg et al. (1976) for simulating fracture

and fragmentation processes in quasi-brittle materials, extensive literature related to CZM has been published. The approach has attracted considerable attention because it provides an efficient and powerful algorithm to describe the behaviors of fracture. By modifying material parameters, the CZM can be used to simulate both newly created fractures and pre-existing natural fractures. In this work we couple thermo-hydro-mechanical processes, fluid flow, and thermal transfer with CZM through an interface element.

Similarly to the theory of poroelasticity, the effective cohesive stress (***T'***) is introduced and is related to the total cohesive stress (***T***) and fluid pressure (p_f) through the following equation:

$$\boldsymbol{T} = \boldsymbol{T}' - p_f \boldsymbol{n} \tag{5.15}$$

where ***n*** is the local normal of the cohesive zone interface. When the cohesive zone is completely damaged, the cohesive traction (***T'***) is zero and the fluid pressure (p_f) is acting as traction on the open fracture surfaces.

A cohesive law relates the traction (***T'***) to the displacement jump (***Δ***) across a cohesive interface through a potential function (***ψ***) (Park and Paulino 2012):

$$\boldsymbol{T}' = \frac{\partial \psi}{\partial \boldsymbol{\Delta}} \tag{5.16}$$

A second derivative of the potential function with respect to the displacement jump provides the constitutive relationship (material tangent modulus). The traction-separation relationship governs the behaviors of fractures. In this study, the PPR, potential-based cohesive law (Park and Paulino 2012; Spring and Paulino 2014), is adopted; the traction and separation in both the normal and shear directions of the fracture surfaces can be considered. As shown in Figure 2.2, four deformation stages exist on the traction-separation curve. They are elastic

deformation, fracture initiation, softening deformation and complete failure. The area under the pure normal traction-separation curve represents the fracture energy G_{IC} in the normal direction:

$$G_{IC} = \int_0^{\delta_n} T_n(\Delta_n) d\Delta_n \tag{5.17}$$

where δ_n is the final normal opening width between two fracture surfaces. The fracture energy G_{IC} is an independent input parameter to the model. When the size of cohesive zone is much smaller than the fracture length, the cohesive energy (G_{IC}) can be related to the fracture toughness in mode-I (K_{IC}) in linear elastic fracture mechanics (LEFM) through Irwin's formula (Irwin 1957):

$$G_{IC} = \frac{K_{IC}^2}{E}\left(1-\upsilon^2\right) \tag{5.18}$$

where E is Young's modulus and υ the Poisson's ratio.

During injection operations, the response of the fluid flow is coupled with the fracture deformation. Figure 2.1 illustrates the fluid pressure and cohesive traction distributions in CZM considering the coupled hydro-mechanical effects as given by Eq. (5.15). On fracture surfaces, either nonzero cohesive traction or zero cohesive traction exists depending on the deformation stage of a particular region. The fluid pressure is applied on the two surfaces of a fracture.

5.2.3 Fluid flow in fracture

For liquid flow within discontinuities, the compressibility is negligible when compared with the deformation of discontinuities (opening or closure), so that the fluid within discontinuities is assumed to be incompressible. Linear (Newtonian) viscous fluid is adopted in this study. The longitudinal flow within the space between two surfaces of a fracture is derived from conservation of momentum and approximated through the lubrication equation, which is also known as cubic law:

$$\boldsymbol{q} = \boldsymbol{v}w = -\frac{w^3}{12\mu}\nabla p_f \tag{5.19}$$

where $\boldsymbol{q}$ is the fluid flux of the longitudinal flow; $\boldsymbol{v}$ is the average fluid velocity; μ is the viscosity of the Newtonian fluid; w is the local fracture width, which is equal to the displacement jump (Δ_n) in the normal direction of the surface for a freshly created fracture; for pre-existing fractures, the hydraulic aperture at zero mechanical opening (Δ_n) should be used for the local fracture width.

Deriving from mass conservation in a fracture, the fluid mass balance equation is formulated as

$$\frac{\partial w}{\partial t} + \nabla \cdot \boldsymbol{q} + q^+ + q^- = Q(t) \tag{5.20}$$

where q^+ and q^- are the transversal flow rates to account for the fluid transfer through two fracture surfaces into the surrounding rock (leak-off), $Q(t)$ is the injection rate into the fracture.

The fluid transfer terms in Eq. (5.20) can be expressed as:

$$\begin{aligned} q^+ &= c\left(p_f - p^+\right) \\ q^- &= c\left(p_f - p^-\right) \end{aligned} \tag{5.21}$$

where c is the fluid transfer coefficient, p^+ and p^- are pore pressure on the two fracture surfaces.

Combining equations (5.19) and (5.20), it is obtained:

$$\frac{\partial w}{\partial t} - \nabla \cdot \frac{w^3}{12\mu}\nabla p_f + q^+ + q^- = Q(t) \tag{5.22}$$

When the model is used to simulate hydraulic fracturing, during which new fractures are created, we have the following boundary conditions at the fracture tips:

$$w(x,t)\big|_{x=R} = 0$$
$$q(x,t)\big|_{x=R} = 0 \tag{5.23}$$

At the injection point, the fluid flux is

$$q(x,t)\big|_{x=0} = q_0 \tag{5.24}$$

5.2.4 Heat transport in fracture

There are several mechanisms involved in the heat transport in a fracture, such as heat storage, advection, longitudinal dispersion, and conduction from surrounding rocks to fracture surfaces (Cheng et al. 2001). Due to the complexity of the problem, simplified assumptions are often made in analytical and numerical solutions. One commonly assumed condition is that the temperature is continuous across the fracture surfaces. In other words, it is assumed that the temperature in the space between the two fracture surfaces is equal to the temperature on the surfaces of the fracture (i.e., the surfaces of surrounding rock matrix). However, in advection-dominated heat transport, this assumption is not necessarily valid. In this study, the temperature is assumed uniform within the fracture in transverse direction (perpendicular to fracture surfaces) since the fracture aperture size is relatively small comparing to the length of fractures. The possibility of a discontinuity in temperature across the fracture surfaces is considered. In other words, the temperature within the fracture could be different than that on the surfaces of surrounding rock matrix. The equation governing heat transport, which is modified from Cheng et al. (2001), is expressed as

$$\frac{\partial T_f}{\partial t} + \boldsymbol{v}\cdot\nabla T_f - D\nabla^2 T_f + \frac{1}{\rho_w c_w w}\left(q_T^+ + q_T^-\right) = 0 \tag{5.25}$$

where T_f is the fluid temperature in the space between two fracture surfaces, ρ_w is the fluid density, c_w is the specific heat of fluid, D is the dispersion coefficient, q^+_T and q^-_T are the heat fluxes from the fracture to the surrounding rock matrix through the two fracture surfaces.

The heat transfer terms in Eq. (5.25) can be expressed as:

$$\begin{aligned} q_T^+ &= h\left(T_f - T^+\right) \\ q_T^- &= h\left(T_f - T^-\right) \end{aligned} \tag{5.26}$$

where h is the convective heat transfer coefficient, T^+ and T^- are rock temperature on the two fracture surfaces.

The dispersion coefficient D is a function of flow velocity (Zhao et al. 2010):

$$D = \alpha|\boldsymbol{v}| + D_m \tag{5.27}$$

where α is dispersion, D_m is molecular diffusion coefficient.

5.2.5 Fluid flow in wellbore

As mentioned before, the thermo-hydro-mechanical interface element can be used to model pre-existing discontinuities and it can simulate newly created hydraulic fractures as well. From analytical and numerical hydraulic fracturing models, we know that the fluid pressure at the injection point could be infinitely large in the beginning of injection, since the compressibility effects from the injection system are not considered. After considering the compressibility effects, an initial pressure buildup stage would usually exist in the pressure record, as demonstrated in many laboratory experiments (Hu and Ghassemi 2018a; Wu et al. 2008) or field observations.

The compressibility effects of the whole injection system could be induced by the deformation of fluid pipe and wellbore during pressurization. In this study, these are considered by introducing a wellbore in numerical simulations. Fluid flow through wellbores and the

corresponding compressibility and pressure drop in the whole injection system are characterized by the mass balance equation and the momentum balance equation. By averaging the conservation of mass and the balance of momentum at the cross-section of wellbore (Lecampion and Desroches 2015), the fluid flow in wellbores is simplified into a one-dimensional problem.

For pipe flow, the conservation of mass in 1D is given as:

$$\frac{\partial \rho A}{\partial t} + \frac{\partial \rho AV}{\partial x} = \rho Q(t) \tag{5.28}$$

where ρ is the fluid density and $\rho \approx \rho_0(1 + c(p_w - p_0))$, ρ_0 is the fluid density under the fluid pressure of p_0, c the fluid compressibility; A the cross-section area of wellbore, $A = \pi r^2$, r the internal radius of wellbore; V the average velocity through the cross-section area; $Q(t)$ the sink/source term. Strictly speaking, both the fluid density ρ and the cross-section area A are functions of time and the spatial coordinates. In this work, we assume the wellbore is rigid and its compressibility effects are considered through the fluid compressibility parameter c representing the total system compressibility. Through the linearization of Eq. (5.28), the following continuity equation is obtained:

$$Ac\frac{\partial p_w}{\partial t} + A\frac{\partial V}{\partial x} + AVc\frac{\partial p_w}{\partial x} = Q(t) \tag{5.29}$$

The balance of momentum for 1D pipe flow is given as:

$$\frac{\partial p_w}{\partial x} = -\frac{2}{r}\tau_w \tag{5.30}$$

where τ_w is the shear stress on the pipe wall. Empirical correlations should be used to determine the frictional pressure loss when the flow pattern is recognized as turbulent in pipe. After introducing the dimensionless friction factor, the Fanning equation is derived (Bourgoyne et al. 1991):

$$\frac{\partial p_w}{\partial x} = -\frac{\rho V|V|}{r} f_{Fan} = -\frac{\rho V|V|}{r}\frac{f_D}{4} \tag{5.31}$$

where f_{Fan} is called the Fanning friction factor; f_D the Darcy-Weisbach friction factor. The Darcy-Weisbach friction factor can be approximated numerically for laminar, transitional and turbulent flow based on Moody's chart (Moody, 1944):

$$\begin{aligned} f_D &= \frac{64}{\mathrm{Re}}, \quad \mathrm{Re} \le 2100 \\ \frac{1}{\sqrt{f_D}} &= -1.8\log\left(\left(\frac{\varepsilon}{3.7}\right)^{1.11} + \frac{6.9}{\mathrm{Re}}\right), \quad \mathrm{Re} \ge 4000 \end{aligned} \tag{5.32}$$

Substituting Eq. (5.31) into (5.29), the following non-linear equation characterizing fluid flow in the wellbore is obtained:

$$Ac\frac{\partial p_w}{\partial t} + A\frac{\partial}{\partial x}\left(-\frac{4r}{\rho f_D|V|}\frac{\partial p_w}{\partial x}\right) + AVc\frac{\partial p_w}{\partial x} = Q(t) \tag{5.33}$$

The boundary condition at the injection point of the wellbore is:

$$-\frac{4rA}{\rho f_D|V|}\frac{\partial p_w}{\partial x}\bigg|_{x=0} = q_{w0} \tag{5.34}$$

5.3 Finite element implementation

The finite element method is utilized to discretize the governing equations. A fracture in a thermo-poroelastic medium gives rise to discontinuities in displacements, fluid pressure and temperature. When dealing with fluid flow and heat transport in a fracture, a multi-physics process is encountered since aperture variations are connected with fluid pressure and temperature changes in space and time. In this study, a zero-thickness interface element is developed to handle the complex thermo-hydro-mechanical processes in fracture.

5.3.1 Zero-thickness interface (ZTI) element

A triple-node interface element with zero thickness is developed (Figure 5.2), which is similar to that proposed in Cerfontaine et al. (2015). The mechanical behavior of the ZTI is governed by CZM. The interface element allows for pressure and temperature discontinuity across the interface. To simulate hydraulic fracture propagation, assuming fluid pressure is continuous across newly created fractures, larger value of fluid transport coefficient, *c*, should be used. To simulate the situations where fluid pressure or temperature is required to be continuous across newly created fractures, a relatively large value of the fluid transport coefficient or the convective heat transfer coefficient should be used. The influence of transport coefficient on temperature distribution is analyzed in detail in following sections. Initially the three layers have zero thickness and are overlapped with each other. In Figure 5.2, the top and bottom planes (1-2-3-4 and 5-6-7-8) represent the surfaces of the fracture. Fluid flow and heat transport are discretized on the center plane (9-10-11-12) of the three layers where the quadrilateral elements used. Each of the nodes 1 ~ 8 has five degrees of freedom; 3 for displacements (u_x, u_y, u_z), 1 for pore pressure (p), and 1 for temperature (T). Each of the nodes 9 ~ 12 has two degrees of freedom; 1 for fluid pressure (p_f) and 1 for temperature (T_f) in the fracture. To summarize, the mechanical, hydraulic, and thermal degrees of freedom are written in vector form at each node:

$$\begin{aligned} \boldsymbol{u} &= \left[u_x, u_y, u_z, p, T \right]^T \text{ for nodes 1~8} \\ \boldsymbol{u_f} &= \left[p_f, T_f \right]^T \text{ for nodes 9~12} \end{aligned} \tag{5.35}$$

As an example, Figure 2.4 shows the deformation of the interface elements after fluid is injected into the ZTI elements. The interface elements are linked to and bounded by conventional thermo-poroelastic rock matrix elements through 4 shared nodes on the surface of rock matrix.

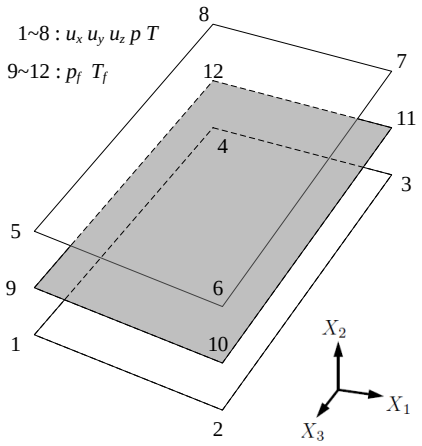

Figure 5.2 12-node interface element. Nodes 1 ~ 8 have degrees of freedom for displacement, pore pressure and temperature; nodes 9 ~ 12 have degrees of freedom for fluid pressure and temperature. Initially the three layers have zero thickness and overlap each other in numerical models. Here they are separated for visualization purpose.

5.3.2 Discretization in time

For finite element analysis of time-dependent problems, the usual practice is to perform the spatial discretization before the time discretization. However, for stabilization techniques in transient analysis, it is preferable that the time discretization be performed first (Donea and Huerta, 2003). As we will see later, the residual term in stabilization analyses involves a time derivative of temperature, which results in a rather cumbersome implementation if the spatial discretization is performed first.

The θ family of methods is adopted to perform the time discretization. No time-derivatives are included in the momentum balance equation $(5.2)_1$, so it is implicitly evaluated at step $n + 1$.

Let Δt be the time step size of a time interval $[0, t]$. We use a superscript to refer to the time step counter, and define:

$$u^{n+\theta} = \theta u^{n+1} + (1-\theta) u^{n} \quad (0 \le \theta \le 1),$$
$$\Delta u = u^{n+1} - u^{n} . \tag{5.36}$$

The θ family of methods consist of, finding u^{n+1} given u^n and by satisfying the boundary conditions:

$$\frac{\Delta u}{\Delta t} - \theta \Delta u_t = u_t^{\,n} \tag{5.37}$$

where $\Delta u_t = u_t^{n+1} - u_t^n$. Substituting u_t by p_t and T_t using Eqs. $(5.6)_2$ and $(5.6)_3$, we obtain the following semi-discrete equations:

$$\begin{aligned} \frac{\Delta p}{\Delta t} &= M\left[\kappa p_{,jj}^{\;n+\theta} - \alpha \frac{\Delta u_{i,i}}{\Delta t} + \left(\alpha\alpha_m^T + \phi_0\left(\alpha_f^T - \alpha_m^T\right)\right)\frac{\Delta T}{\Delta t} + \gamma^{n+\theta}\right], \\ \frac{\Delta T}{\Delta t} &= \frac{1}{\rho_t C_t}\left(k^T T_{,i}\right)_{,i}^{\;n+\theta} - \frac{\rho_f C_f}{\rho_t C_t} v_i T_{,i}^{\;n+\theta}. \end{aligned} \tag{5.38}$$

Particular cases of interest are $\theta = 1$ (backward Euler), $\theta = 1/2$ (Crank-Nicolson) and $\theta = 0$ (forward Euler). The Crank-Nicolson scheme is of second-order accuracy and the rest of the cases are of first-order accuracy.

For equations governing fluid flow (Eq. (5.22)) and heat transport (Eq. (5.25)) in fractures and for the equation characterizing fluid flow in wellbores (Eq. (5.33)), the same method is used. The following semi-discrete equations are obtained:

$$\begin{aligned} &\frac{\Delta w}{\Delta t} - \nabla \cdot \frac{\left(w^3\right)^{n+\theta}}{12\mu} \nabla p_f^{\,n+\theta} + q^{+\;n+\theta} + q^{-\;n+\theta} = Q(t)^{n+\theta}, \\ &\frac{\Delta T_f}{\Delta t} + \boldsymbol{v} \cdot \nabla T_f^{n+\theta} - D\nabla^2 T_f^{n+\theta} + \frac{1}{\rho_w c_w w^{n+\theta}}\left(q_T^{+\;n+\theta} + q_T^{-\;n+\theta}\right) = 0, \\ &Ac\frac{\Delta p_w}{\Delta t} + A\frac{\partial}{\partial x}\left(-\frac{4r}{\rho f_D |V|}\frac{\partial p_w}{\partial x}^{n+\theta}\right) + AVc\frac{\partial p_w}{\partial x}^{n+\theta} = Q\left(t\right)^{n+\theta}. \end{aligned} \tag{5.39}$$

5.3.3 The Weak form

If the temporal truncation error is neglected, the time-discretized equations (Eqs. (5.38) - (5.39)) could be interpreted as a set of spatial differential operators representing the strong form, and must be solved at each time step. The standard Galerkin method of weighted residuals is employed for spatial discretization of the time discretized equations (Eq. (5.38) and Eq. (5.39)). To develop the weak form of the boundary value problem, we define two classes of functions: the trial functions and the test functions.

The spaces of trial function consist of all functions have square integrable first derivatives over the solution domain Ω for rock deformation in 3D thermo-poroelastic medium, over the solution domain Γ_c for fluid flow and heat transport on 2D fracture surface, and over the solution domain s_w for 1D fluid flow in wellbore, and are required to satisfy the essential boundary conditions. They are defined as:

$$
\begin{aligned}
S_u &= \left\{ u_i : \Omega \to R \middle| u_i \in H^1(\Omega), u_i = \bar{u}_i \ \text{ on } \Gamma_{u_i} \right\}, \\
S_p &= \left\{ p : \Omega \to R \middle| p \in H^1(\Omega), p = \bar{p} \ \text{ on } \Gamma_p \right\}, \\
S_T &= \left\{ T : \Omega \to R \middle| T \in H^1(\Omega), T = \bar{T} \ \text{ on } \Gamma_T \right\}, \\
S_{p_f} &= \left\{ p_f : \Gamma_c \to R \middle| p_f \in H^1(\Gamma_c), p_f = \bar{p}_f \ \text{ on } s_{p_f} \right\}, \\
S_{T_f} &= \left\{ T_f : \Gamma_c \to R \middle| T_f \in H^1(\Gamma_c), T_f = \bar{T}_f \ \text{ on } s_{T_f} \right\}, \\
S_{p_w} &= \left\{ p_w : s_w \to R \middle| p_w \in H^1(s_w), p_w = \bar{p}_w \ \text{ on } \partial s_w \right\}.
\end{aligned}
\tag{5.40}
$$

where $H^l(\Omega)$ represents a Sobolev space of order one. The corresponding spaces of test function are similar to the trial functions except that they are vanished on the essential boundaries. They are defined as follows:

$$
\begin{aligned}
V_u &= \left\{ \omega_{u_i} : \Omega \to R \middle| \omega_{u_i} \in H^1(\Omega), \omega_{u_i} = 0 \ \text{ on } \Gamma_{u_i} \right\}, \\
V_p &= \left\{ \omega_p : \Omega \to R \middle| \omega_p \in H^1(\Omega), \omega_p = 0 \ \text{ on } \Gamma_p \right\}, \\
V_T &= \left\{ \omega_T : \Omega \to R \middle| \omega_T \in H^1(\Omega), \omega_T = 0 \ \text{ on } \Gamma_T \right\}, \\
V_{p_f} &= \left\{ p_f : \Gamma_c \to R \middle| p_f \in H^1(\Gamma_c), \omega_{p_f} = 0 \ \text{ on } s_{p_f} \right\}, \\
V_{T_f} &= \left\{ T_f : \Gamma_c \to R \middle| T_f \in H^1(\Gamma_c), \omega_{T_f} = 0 \ \text{ on } s_{T_f} \right\}, \\
V_{p_w} &= \left\{ p_w : s_w \to R \middle| p_w \in H^1(s_w), \omega_{p_w} = 0 \ \text{ on } \partial s_w \right\}.
\end{aligned}
\tag{5.41}
$$

For the θ family of methods, the weak form for the problem of rock deformation in 3D porous medium consists in finding $\{u_i, p, T\} \in S_u \times S_p \times S_T$ such that for all $\{\omega_{u_i}, \omega_p, \omega_T\} \in V_u \times V_p \times V_T$,

$$
\begin{aligned}
R_{u_i}^{n+1} = &\int_\Omega \omega_{u_{i,j}} \left(\sigma_{ij}' - \alpha p \delta_{ij} - \alpha_m^T K T \delta_{ij} \right)^{n+1} \mathrm{d}\Omega + \int_{\Gamma_c} \omega_{\Delta_n} \left(T_n' - p_f \right)^{n+1} \mathrm{d}\Gamma_c \\
&- \int_\Omega \omega_{u_i} F_i^{n+1} \mathrm{d}\Omega - \int_{\Gamma_t} \omega_{u_i} \bar{t}_i^{n+1} \mathrm{d}\Gamma_t = 0
\end{aligned},
$$

$$
\begin{aligned}
R_p^{n+1} = &\int_\Omega \omega_{p,i} \kappa p_{,i}^{n+\theta} \mathrm{d}\Omega + \int_\Omega \omega_p \left[\alpha \frac{\Delta u_{i,i}}{\Delta t} - \left(\alpha \alpha_m^T + \phi_0 \left(\alpha_f^T - \alpha_m^T \right) \right) \frac{\Delta T}{\Delta t} + \frac{1}{M} \frac{\Delta p}{\Delta t} \right] \mathrm{d}\Omega \\
&- \int_\Omega \omega_p \gamma^{n+\theta} \mathrm{d}\Omega - \int_{\Gamma_q} \omega_p \bar{q}^{n+\theta} \mathrm{d}\Gamma_q = 0
\end{aligned},
\tag{5.42}
$$

$$
\begin{aligned}
R_T^{n+1} = &\int_\Omega \left(\omega_T \frac{\Delta T}{\Delta t} + \omega_{T,i} \frac{1}{\rho_t C_t} \left(k^T T_{,i} \right)^{n+\theta} + \omega_T \frac{\rho_f C_f}{\rho_t C_t} v_i T_{,i}^{n+\theta} \right) \mathrm{d}\Omega \\
&- \int_{\Gamma_{qT}} \omega_T \frac{1}{\rho_t C_t} \bar{q}_T^{n+\theta} \mathrm{d}\Gamma_{qT} = 0
\end{aligned}.
$$

The equations for fluid flow and heat transport are discretized on 2D surfaces representing discontinuities in a 3D domain. Using similar procedures, it is obtained:

$$
\begin{aligned}
R_{p_f}{}^{n+1} &= \int_{\Gamma_c}\left(\omega_{p_f}\frac{\Delta w}{\Delta t}\right)\mathrm{d}\Gamma_c + \int_{\Gamma_c}\omega_{p_{f,i}}\frac{(w)^3}{12\mu}{}^{n+\theta} p_{f,i}{}^{n+\theta}\mathrm{d}\Gamma_c + \int_{\Gamma_c}\omega_{p_f} q^{+\,n+\theta}\mathrm{d}\Gamma_c \\
&+\int_{\Gamma_c}\omega_{p_f} q^{-\,n+\theta}\mathrm{d}\Gamma_c - \int_{\Gamma_c}\omega_{p_f} Q(t)^{n+\theta}\mathrm{d}\Gamma_c - \int_{s_q}\omega_{p_f}\bar{q}_f{}^{n+\theta}\mathrm{d}s_q = 0
\end{aligned}
$$

$$
\begin{aligned}
R_{T_f}{}^{n+1} &= \int_{\Gamma_c}\left(\omega_{T_f}\frac{\Delta T_f}{\Delta t}\right)\mathrm{d}\Gamma_c + \int_{\Gamma_c}\left(\omega_{T_f}\left(\boldsymbol{v}\cdot\nabla T_f^{n+\theta}\right)\right)\mathrm{d}\Gamma_c + \int_{\Gamma_c}\omega_{T_{f,i}} DT_{f,i}{}^{n+\theta}\mathrm{d}\Gamma_c \\
&+\int_{\Gamma_c}\omega_{T_f}\frac{1}{\rho_w c_w w^{n+\theta}} q_T^{+\,n+\theta}\mathrm{d}\Gamma_c + \int_{\Gamma_c}\omega_{T_f}\frac{1}{\rho_w c_w w^{n+\theta}} q_T^{-\,n+\theta}\mathrm{d}\Gamma_c - \int_{s_{qT}}\omega_{T_f}\bar{q}_{Tf}{}^{n+\theta}\mathrm{d}s_{qT} = 0
\end{aligned}
\qquad (5.43)
$$

where Γ_c is fracture surface, *s* is the boundary of fracture surface; $\omega_{u_{i,j}}$, ω_{Δ_n}, ω_{u_i}, ω_p, ω_{p_f}, ω_T and ω_{T_f} are virtual strain, virtual separation normal to fracture surface, virtual displacement, virtual pore pressure in porous medium, virtual fluid pressure in fracture, virtual temperature in porous medium and virtual fluid temperature in fracture, respectively. Scripts $n + 1$ and $n + \theta$ refer to the time step counter.

The equation for 1D fluid flow in wellbore has the following weak form:

$$
\begin{aligned}
R_{p_w}{}^{n+1} &= \int_{s_w}\left(\omega_{p_w} Ac\frac{\Delta p_w}{\Delta t}\right)\mathrm{d}s_w + \int_{s_w}\frac{\partial\omega_{p_w}}{\partial x}\left(\frac{4rA}{\rho f_D|V|}\right)\frac{\partial p_w}{\partial x}{}^{n+\theta}\mathrm{d}s_w + \int_{s_w}\omega_{p_w} AVc\frac{\partial p_w}{\partial x}{}^{n+\theta}\mathrm{d}s_w \\
&-\int_{s_w}\omega_{p_w} Q(t)^{n+\theta}\mathrm{d}s_w - \int_{\partial s_w}\omega_{p_w} A\bar{V}^{n+\theta}\mathrm{d}s_w = 0
\end{aligned}
\qquad (5.44)
$$

5.3.4 Discretization in space

Following the standard Galerkin approximation for spatial discretization, the displacement, pressure and temperature are discretized through spatial interpolation functions (shape functions) in the domain of interest and expressed as:

$$
\begin{aligned}
&\boldsymbol{u}^h = \boldsymbol{N}^u\boldsymbol{u}, \quad p^h = \boldsymbol{N}^p\boldsymbol{p}, \quad T^h = \boldsymbol{N}^{th}\boldsymbol{T} \\
&p_f^h = \boldsymbol{N}^{p_f}\boldsymbol{p_f}, \quad T_f^h = \boldsymbol{N}^{T_f}\boldsymbol{T_f}, \quad p_w^h = \boldsymbol{N}^{p_w}\boldsymbol{p_w}
\end{aligned}
\qquad (5.45)
$$

where $\boldsymbol{N^u}$, $\boldsymbol{N^p}$, and $\boldsymbol{N^{th}}$ are displacement, pore pressure and temperature shape functions for 3D porous medium, $\boldsymbol{N^{pf}}$ and $\boldsymbol{N^{Tf}}$ are fluid pressure and temperature shape functions in 2D fracture,

$\boldsymbol{N}^{pw}$ is the shape function for 1D fluid flow in wellbore, and $\boldsymbol{u}$, $\boldsymbol{p}$, $\boldsymbol{T}$, $\boldsymbol{p_f}$, $\boldsymbol{T_f}$, $\boldsymbol{p_w}$ are corresponding unknown nodal values. The test functions are written in a similar manner:

$$\begin{aligned} \boldsymbol{\omega}_{\boldsymbol{u}}^{h} &= \boldsymbol{N}^{u}\boldsymbol{\omega}_{\boldsymbol{u}}, \quad \omega_{p}^{h} = \boldsymbol{N}^{p}\boldsymbol{\omega}_{\boldsymbol{p}}, \quad \omega_{T}^{h} = \boldsymbol{N}^{th}\boldsymbol{\omega}_{\boldsymbol{T}} \\ \omega_{p_f}^{h} &= \boldsymbol{N}^{p_f}\omega_{\boldsymbol{p_f}}, \quad \omega_{T_f}^{h} = \boldsymbol{N}^{T_f}\omega_{\boldsymbol{T_f}}, \quad \omega_{p_w}^{h} = \boldsymbol{N}^{p_w}\boldsymbol{\omega}_{\boldsymbol{p_w}} \end{aligned} . \tag{5.46}$$

Using Eq. (5.45), the gradient and divergence of the unknown variables could be obtained and represented in the following format:

$$\begin{aligned} \nabla \boldsymbol{u}^{h} &= \nabla \boldsymbol{N}^{u}\boldsymbol{u} = \boldsymbol{B}^{u}\boldsymbol{u}, \\ \nabla \cdot \boldsymbol{u}^{h} &= I^{T}\boldsymbol{B}^{u}\boldsymbol{u}, \\ \nabla p^{h} = \nabla \boldsymbol{N}^{p}\boldsymbol{p} = \boldsymbol{B}^{p}\boldsymbol{p}, &\quad \nabla p_f^{h} = \nabla \boldsymbol{N}^{p_f}\boldsymbol{p_f} = \boldsymbol{B}^{p_f}\boldsymbol{p_f}, \\ \nabla T^{h} = \nabla \boldsymbol{N}^{th}\boldsymbol{T} = \boldsymbol{B}^{th}\boldsymbol{T}, &\quad \nabla T_f^{h} = \nabla \boldsymbol{N}^{T_f}\boldsymbol{T_f} = \boldsymbol{B}^{T_f}\boldsymbol{T_f}, \\ I^{T} &= \begin{bmatrix} 1 & 1 & 1 & 0 & 0 & 0 \end{bmatrix}^{T}. \end{aligned} \tag{5.47}$$

The local separation of fracture surfaces (Δ_n) is related to the global nodal displacements (u_i) on the fracture surfaces and is given as

$$\Delta_n = \boldsymbol{B}^{c}\boldsymbol{u} \tag{5.48}$$

Substituting the trial and test functions into Eqs. (5.42) and (5.43), invoking the arbitrariness of the test functions, we obtain the following residual equations:

(1) Balance of linear momentum

$$\begin{aligned} R_u^{n+1} = &\int_{\Omega}\left(\boldsymbol{B}^{u}\right)^{T}\left(\boldsymbol{D}\boldsymbol{B}^{u}\boldsymbol{u} - \alpha I\boldsymbol{N}^{p}\boldsymbol{p} - \alpha_m^{T}KI\boldsymbol{N}^{th}\boldsymbol{T}\right)^{n+1}\mathrm{d}\Omega + \int_{\Gamma_c}\left(\boldsymbol{B}^{c}\right)^{T}\left(T'_n\right)^{n+1}\mathrm{d}\Gamma_c \\ &-\int_{\Gamma_c}\left(\boldsymbol{B}^{c}\right)^{T} I_d\boldsymbol{N}^{p}\left(\boldsymbol{p_f}\right)^{n+1}\mathrm{d}\Gamma_c - \int_{\Omega}\left(\boldsymbol{N}^{u}\right)^{T}\boldsymbol{F}^{n+1}\mathrm{d}\Omega - \int_{\Gamma_t}\left(\boldsymbol{N}^{u}\right)^{T}\bar{\boldsymbol{t}}^{n+1}\mathrm{d}\Gamma_t = 0 \end{aligned} \tag{5.49}$$

(2) Balance of mass

$$
\begin{aligned}
R_p^{n+1} &= \int_\Omega \left(\boldsymbol{B}^p\right)^T \boldsymbol{\kappa}\theta \boldsymbol{B}^p \Delta \boldsymbol{p} \mathrm{d}\Omega \\
&+ \int_\Omega \left(\boldsymbol{N}^p\right)^T \left[\alpha I^T \boldsymbol{B}^u \frac{\Delta \boldsymbol{u}}{\Delta t} - \left(\alpha \alpha_m^T + \phi_0 \left(\alpha_f^T - \alpha_m^T\right)\right) \boldsymbol{N}^{th} \frac{\Delta \boldsymbol{T}}{\Delta t} + \frac{1}{M} \boldsymbol{N}^p \frac{\Delta \boldsymbol{p}}{\Delta t} \right] \mathrm{d}\Omega \\
&+ \int_\Omega \left(\boldsymbol{B}^p\right)^T \boldsymbol{\kappa} \boldsymbol{B}^p \boldsymbol{p}^{\boldsymbol{n}} \mathrm{d}\Omega - \int_\Omega \left(\boldsymbol{N}^p\right)^T \gamma^{n+\theta} \mathrm{d}\Omega - \int_{\Gamma_q} \left(\boldsymbol{N}^p\right)^T \bar{q}^{n+\theta} \mathrm{d}\Gamma_q = 0
\end{aligned}
\tag{5.50}
$$

(3) Balance of energy

$$
\begin{aligned}
R_T^{n+1} &= \int_\Omega \left(\left(\boldsymbol{N}^{th}\right)^T \boldsymbol{N}^{th} \frac{\Delta \boldsymbol{T}}{\Delta t} + \theta \frac{1}{\rho_t C_t} \left(\boldsymbol{B}^{th}\right)^T \kappa^T \boldsymbol{B}^{th} \Delta \boldsymbol{T} + \theta \frac{\rho_f C_f}{\rho_t C_t} \left(\boldsymbol{N}^{th}\right)^T \left(\boldsymbol{q} \cdot \boldsymbol{B}^{th}\right) \Delta \boldsymbol{T} \right) \mathrm{d}\Omega \\
&+ \int_\Omega \left(\frac{1}{\rho_t C_t} \left(\boldsymbol{B}^{th}\right)^T \kappa^T \boldsymbol{B}^{th} \boldsymbol{T}^n + \frac{\rho_f C_f}{\rho_t C_t} \left(\boldsymbol{N}^{th}\right)^T \left(\boldsymbol{v} \cdot \boldsymbol{B}^{th}\right) \boldsymbol{T}^n \right) \mathrm{d}\Omega \\
&- \int_{\Gamma_{qT}} \frac{1}{\rho_t C_t} \left(\boldsymbol{N}^{th}\right)^T \bar{q}_T^{n+\theta} \mathrm{d}\Gamma_{qT} = 0
\end{aligned}
\tag{5.51}
$$

(4) Fluid flow in fracture

$$
\begin{aligned}
R_{p_f}^{n+1} &= \int_{\Gamma_c} \left(\boldsymbol{N}^{p_f}\right)^T \left(\boldsymbol{B}^c \frac{1}{\Delta t} \right) \left((w)^{n+1} - (w)^n \right) \mathrm{d}\Gamma_c + \int_{\Gamma_c} \left(\boldsymbol{B}^{p_f}\right)^T \frac{(w)^3}{12\mu}^{n+\theta} \boldsymbol{B}^{p_f} \boldsymbol{p}_{\boldsymbol{f}}^{n+\theta} \mathrm{d}\Gamma_c \\
&+ \int_{\Gamma_c} \left(\boldsymbol{N}^{p_f}\right)^T q^{+\ n+\theta} \mathrm{d}\Gamma_c + \int_{\Gamma_c} \left(\boldsymbol{N}^{p_f}\right)^T q^{-\ n+\theta} \mathrm{d}\Gamma_c \\
&- \int_{\Gamma_c} \left(\boldsymbol{N}^{p_f}\right)^T Q(t)^{n+\theta} \mathrm{d}\Gamma_c - \int_{s_q} \left(\boldsymbol{N}^{p_f}\right)^T \bar{q}_f^{\ n+\theta} \mathrm{d}s_q = 0
\end{aligned}
\tag{5.52}
$$

(5) Heat transport in fracture

$$
\begin{aligned}
R_{T_f}^{n+1} &= \int_{\Gamma_c} \left(\boldsymbol{N}^{T_f}\right)^T \boldsymbol{N}^{T_f} \frac{\Delta T_f}{\Delta t} \mathrm{d}\Gamma_c + \int_{\Gamma_c} \left(\boldsymbol{N}^{T_f}\right)^T \left(\boldsymbol{v} \cdot B^{T_f} T_f^{n+\theta}\right) \mathrm{d}\Gamma_c \\
&+ \int_{\Gamma_c} \left(B^{T_f}\right)^T D B^{T_f} T_f^{n+\theta} \mathrm{d}\Gamma_c + \int_{\Gamma_c} \frac{1}{\rho_w c_w w^{n+\theta}} \left(\boldsymbol{N}^{T_f}\right)^T q_T^{+\ n+\theta} \mathrm{d}\Gamma_c \\
&+ \int_{\Gamma_c} \frac{1}{\rho_w c_w w^{n+\theta}} \left(\boldsymbol{N}^{T_f}\right)^T q_T^{-\ n+\theta} \mathrm{d}\Gamma_c - \int_{s_{qT}} \left(\boldsymbol{N}^{T_f}\right)^T \bar{q}_{Tf}^{\ n+\theta} \mathrm{d}s_{qT} = 0
\end{aligned}
\tag{5.53}
$$

It should be noted that the $\boldsymbol{v}$ in Eq. (5.51) is for flow rate in porous medium; $\boldsymbol{v}$ in Eq. (5.53) is for flow rate in fracture.

(6) Fluid flow in wellbore

$$R_{p_w}^{n+1} = \int_{s_w} \left(Ac\left(\boldsymbol{N}^{p_w}\right)^T \boldsymbol{N}^{p_w} \frac{\Delta \boldsymbol{p_w}}{\Delta t} \right) \mathrm{d}s_w + \int_{s_w} \left(\frac{4rA}{\rho f_D |V|} \right) \left(\frac{\partial \boldsymbol{N}^{p_w}}{\partial x} \right)^T \left(\frac{\partial \boldsymbol{N}^{p_w}}{\partial x} \right) \boldsymbol{p_w}^{n+\theta} \mathrm{d}s_w$$
$$+ \int_{s_w} AVc\left(\boldsymbol{N}^{p_w}\right)^T \left(\frac{\partial \boldsymbol{N}^{p_w}}{\partial x} \right) \boldsymbol{p_w}^{n+\theta} \mathrm{d}s_w - \int_{s_w} \left(\boldsymbol{N}^{p_w}\right)^T Q(t)^{n+\theta} \mathrm{d}s_w \qquad (5.54)$$
$$- \int_{\partial s_w} \left(\boldsymbol{N}^{p_w}\right)^T A\bar{V}^{n+\theta} \mathrm{d}s_w = 0$$

5.3.5 Newton-Raphson method

When failure processes, such as generation of new fractures, reactivation of natural fractures or plastic deformation (shear slip), are generated during fluid injection or production, the constitutive laws for the solid deformation and fluid flow would be nonlinear. Fluid flow and heat transport are nonlinear with respect to aperture size and flow rate in the fracture. Another nonlinear behavior commonly encountered in reservoir simulations is the stress (or strain)-dependent permeability. In these scenarios, the residual terms above, R_u^{n+1}, R_p^{n+1}, R_T^{n+1}, R_{pf}^{n+1}, R_{Tf}^{n+1}, and R_{pw}^{n+1} are nonlinear with respect to the primary variables $\boldsymbol{u}$, p, T, p_f, T_f and p_w.

The Newton-Raphson method is utilized to solve the system of nonlinear equations (5.49), (5.50), (5.51), (5.52), (5.53) and (5.54) iteratively at each time step. The residual in each iteration can be approximated as:

$$\boldsymbol{R}\left(\boldsymbol{x}_{k+1}\right) \approx \boldsymbol{R}\left(\boldsymbol{x}_k\right) + \left.\frac{d}{d\varepsilon}\right|_{\varepsilon=0} \boldsymbol{R}\left(\boldsymbol{x}_k + \varepsilon \Delta \boldsymbol{x}\right) = \boldsymbol{R}\left(\boldsymbol{x}_k\right) + \boldsymbol{K}\Delta \boldsymbol{x} = \boldsymbol{0}$$
$$\Delta \boldsymbol{x} = \boldsymbol{x}_{k+1} - \boldsymbol{x}_k \qquad (5.55)$$

From above approximation, a linear set of equations for $\boldsymbol{\Delta x}$ are to be solved at each Newton-Raphson iteration:

$$\boldsymbol{K}\Delta \boldsymbol{x} = -\boldsymbol{R}\left(\boldsymbol{x}_k\right)$$
$$\boldsymbol{x}_{k+1} = \boldsymbol{x}_k + \Delta \boldsymbol{x} \qquad (5.56)$$

Performing the linearization, the matrix-vector form of equations (5.49), (5.50), (5.51), (5.52), (5.53) and (5.54) is derived as:

$$\begin{bmatrix} \frac{\partial R_u}{\partial \boldsymbol{u}} & \frac{\partial R_u}{\partial \boldsymbol{p}} & \frac{\partial R_u}{\partial \boldsymbol{T}} & \frac{\partial R_u}{\partial \boldsymbol{p}_f} & \frac{\partial R_u}{\partial \boldsymbol{T}_f} & \frac{\partial R_u}{\partial \boldsymbol{p}_w} \\ \frac{\partial R_p}{\partial \boldsymbol{u}} & \frac{\partial R_p}{\partial \boldsymbol{p}} & \frac{\partial R_p}{\partial \boldsymbol{T}} & \frac{\partial R_p}{\partial \boldsymbol{p}_f} & \frac{\partial R_p}{\partial \boldsymbol{T}_f} & \frac{\partial R_p}{\partial \boldsymbol{p}_w} \\ \frac{\partial R_T}{\partial \boldsymbol{u}} & \frac{\partial R_T}{\partial \boldsymbol{p}} & \frac{\partial R_T}{\partial \boldsymbol{T}} & \frac{\partial R_T}{\partial \boldsymbol{p}_f} & \frac{\partial R_T}{\partial \boldsymbol{T}_f} & \frac{\partial R_T}{\partial \boldsymbol{p}_w} \\ \frac{\partial R_{p_f}}{\partial \boldsymbol{u}} & \frac{\partial R_{p_f}}{\partial \boldsymbol{p}} & \frac{\partial R_{p_f}}{\partial \boldsymbol{T}} & \frac{\partial R_{p_f}}{\partial \boldsymbol{p}_f} & \frac{\partial R_{p_f}}{\partial \boldsymbol{T}_f} & \frac{\partial R_{p_f}}{\partial \boldsymbol{p}_w} \\ \frac{\partial R_{T_f}}{\partial \boldsymbol{u}} & \frac{\partial R_{T_f}}{\partial \boldsymbol{p}} & \frac{\partial R_{T_f}}{\partial \boldsymbol{T}} & \frac{\partial R_{T_f}}{\partial \boldsymbol{p}_f} & \frac{\partial R_{T_f}}{\partial \boldsymbol{T}_f} & \frac{\partial R_{T_f}}{\partial \boldsymbol{p}_w} \\ \frac{\partial R_{p_w}}{\partial \boldsymbol{u}} & \frac{\partial R_{p_w}}{\partial \boldsymbol{p}} & \frac{\partial R_{p_w}}{\partial \boldsymbol{T}} & \frac{\partial R_{p_w}}{\partial \boldsymbol{p}_f} & \frac{\partial R_{p_w}}{\partial \boldsymbol{T}_f} & \frac{\partial R_{p_w}}{\partial \boldsymbol{p}_w} \end{bmatrix}^{n+1,k} \begin{pmatrix} \Delta \boldsymbol{u} \\ \Delta \boldsymbol{p} \\ \Delta \boldsymbol{T} \\ \Delta \boldsymbol{p}_f \\ \Delta \boldsymbol{T}_f \\ \Delta \boldsymbol{p}_w \end{pmatrix}^{k+1} = - \begin{pmatrix} R_u \\ R_p \\ R_T \\ R_{p_f} \\ R_{T_f} \\ R_{p_w} \end{pmatrix}, \tag{5.57}$$

$$\boldsymbol{u}_{n+1} = \boldsymbol{u}_n + \Delta \boldsymbol{u}\ ,\ \boldsymbol{p}_{n+1} = \boldsymbol{p}_n + \Delta \boldsymbol{p}\ ,\ \boldsymbol{T}_{n+1} = \boldsymbol{T}_n + \Delta \boldsymbol{T}\ ,$$

$$\boldsymbol{p}_{f\,n+1} = \boldsymbol{p}_{f\,n} + \Delta \boldsymbol{p}_f\ ,\ \boldsymbol{T}_{f\,n+1} = \boldsymbol{T}_{f\,n} + \Delta \boldsymbol{T}_f\ ,\ \boldsymbol{p}_{w_{n+1}} = \boldsymbol{p}_{w_n} + \Delta \boldsymbol{p}_w\ .$$

The terms in the stiffness matrix can be calculated straightforward from the given residual equations. Usually, the residual terms would not strictly equal to zero during iterations. An error tolerance needs to be chosen as a convergent criterion.

5.4 Stabilized finite element method for thermal convection

In problems which involve coupled thermal-poro-mechanical processes, the value of heat diffusivity is usually smaller by several orders of magnitude compared to convection velocity (also known as advection). This means the coupled equations become convection-dominated. It is well known in practice that spurious oscillations would occur in numerical simulations involving convection-dominated flow (Brooks and Hughes 1982). Though these oscillations could be removed by severe mesh refinement, it is clearly not economical with respect to the

computation time to use finer meshes, especially when coefficient of diffusivity is extremely small. By modifying the standard Galerkin formulation, various numerical techniques have been proposed to eliminate the spurious oscillations caused by advection-dominated transport (Codina 1998). These include streamline-upwind Petrov-Galerkin method (SUPG), Space-time Galerkin/least-squares method (ST-GLS), subgrid scale method (SGS), characteristic Galerlin method (CG), Taylor-Galerkin method, and so on. Among these, stabilized finite element methods are more commonly used. The SUPG stabilization technique will be described and applied in the following.

Comparison of the standard Galerkin discrete equations with the exact solution of the heat transport equation $(5.6)_3$, indicates that the Galerkin method introduces a truncation error in the form of a diffusion operator (Donea and Huerta 2003). The magnitude of the truncation error is a function of the Peclet number (P_e), which expresses the ratio of convection to diffusive transport:

$$P_e = \frac{ah}{2v} \tag{5.58}$$

where a is the convection velocity, v is the coefficient of diffusivity, and h is the characteristic length. This truncation error is systematically negative for all value of P_e. Because of the introduction of a negative truncation error, in effect, a modified equation with a reduced diffusion coefficient is actually solved. The diffusion coefficient may become negative when P_e increases. No stable solution is guaranteed in this situation. To reduce spurious oscillations, an additional stabilizing term is added into the original Galerkin formulation of the thermal transport equation $(5.6)_3$.

The stabilization techniques can be expressed in a general form (Brooks and Hughes 1982; Codina 1998; Donea and Huerta 2003):

$$\underbrace{\int_{\Omega}\left(\omega_T\frac{\Delta T}{\Delta t}-\omega_{T,i}\frac{1}{\rho_t C_t}\left(k^T T_{,i}\right)_{,i}^{n+\theta}+\omega_T v_i\frac{\rho_f C_f}{\rho_t C_t}T_{,i}^{n+\theta}\right)d\Omega}_{\text{Standard Galerkin}}+\underbrace{\sum_e\int_{\Omega^e}P(\omega_T^h)\tau R(T^h)d\Omega}_{\text{Stabilization term}}=0 \tag{5.59}$$

where ω is the weighting functions, τ stabilization parameter.

For coupled phenomena studied in this work, two convection-dominated processes could exist. The first one is the heat transport in the porous matrix (Eq. $(5.6)_3$), and the other one is the heat transport in the fracture fluid (Eq. (5.25)). They share the same basic formulation although they have different coefficients and additional terms.

5.4.1 Stabilization of heat transport in the porous matrix

For heat transport in the porous rock matrix, the stabilization terms introduced by the SUPG method have the following forms:

$$\begin{aligned}
P_{\text{SUPG}}(\omega_T^h)&=\frac{\rho_f C_f}{\rho_t C_t}v_i\omega_{T,i}^h\\
R_{\text{SUPG}}(T^h)&=\frac{\Delta T^h}{\Delta t}-\frac{1}{\rho_t C_t}\left(k^T T_{,i}\right)_i^{n+\theta}+\frac{\rho_f C_f}{\rho_t C_t}v_i\left(T^h{}_{,i}\right)^{n+\theta}.\\
\tau&=\left(\frac{1}{\theta\Delta t}+\frac{2}{h}\frac{k^T}{\rho_t C_t}+\frac{4}{h^2}\frac{\rho_f C_f}{\rho_t C_t}v\right)^{-1}
\end{aligned} \tag{5.60}$$

Using the same procedures for the spatial and temporal discretization of the thermal transport equations $(5.6)_3$ in the porous matrix, the following discretized stabilization terms, which should be added to the standard Galerkin formulations (Eq. $(5.42)_3$), are obtained:

$$M^{SUPG}_{porous\ medium}=\int_{\Omega^e}\frac{\tau}{\Delta t}\left(\frac{\rho_f C_f}{\rho_t C_t}\left(\boldsymbol{v}\cdot\boldsymbol{B}^{th}\right)w_T\right)\times\left(N^{th}\Delta T+\Delta t\theta\frac{\rho_f C_f}{\rho_t C_t}\left(\boldsymbol{v}\cdot\boldsymbol{B}^{th}\right)\Delta T+\Delta t\frac{\rho_f C_f}{\rho_t C_t}\left(\boldsymbol{v}\cdot\boldsymbol{B}^{th}\right)T^n\right)\mathrm{d}\Omega\,. \tag{5.61}$$

The terms related to thermal diffusivity are neglected in the stabilization derivation due to the usage of trilinear 8-node hexahedron element (second order partial derivative of linear shape function with respect to spatial coordinate equals to zero).

5.4.2 Stabilization of heat transport in fracture

Fractures in a porous rock often act as major flow paths, which dominate fluid flow underground. Under the condition of continuous injection of fluid, heat transport in a fracture is usually convection-dominated. The stabilization terms based on SUPG method to reduce the numerical oscillation caused by convection-dominated flow have the following forms:

$$\begin{aligned} &P_{\mathrm{SUPG}}(\omega_T^h) = v_i \omega_{T,i}^h \\ &R_{\mathrm{SUPG}}(T^h) = \frac{\Delta T_f}{\Delta t} + v_i \left(T_f{}^h{}_{,i}\right)^{n+\theta} - D T_{f,ii}{}^{n+\theta} + \frac{1}{\rho_w c_w w^{n+\theta}} \left(q_T^{+\ n+\theta} + q_T^{-\ n+\theta}\right). \\ &\tau = \left(\frac{1}{\theta \Delta t} + \frac{D}{h} + \frac{4v}{h^2} + \frac{1}{\rho_w c_w w^{n+\theta}} \right)^{-1} \end{aligned} \tag{5.62}$$

After spatial and temporal discretization of the above equations, the following discretized stabilization terms are obtained:

$$M_{fracture}^{SUPG} = \int_{\Omega^e} \frac{\tau}{\Delta t} \left(\left(\boldsymbol{v} \cdot \boldsymbol{B}^{th} \right) w_T \right) \times \begin{pmatrix} N^{th} \Delta T + \Delta t \theta \left(\boldsymbol{v} \cdot \boldsymbol{B}^{th} \right) \Delta T_f \\ + \Delta t \left(\boldsymbol{v} \cdot \boldsymbol{B}^{th} \right) T_f{}^n + \dfrac{1}{\rho_w c_w w^{n+\theta}} \left(q_T^{+\ n+\theta} + q_T^{-\ n+\theta} \right) \end{pmatrix} \mathrm{d}\Omega \,. \tag{5.63}$$

5.5 Numerical analyses: verification and illustration

Several typical problems with analytical solutions related to thermal-hydro-mechanical processes are studied to verify and analyze the proposed numerical schemes. A KGD Hydraulic fracture in 3D domain is studied first. With the consideration of the compressibility effects of wellbore, the initiation and propagation of the hydraulic fracture are demonstrated and analyzed. A thermo-poroelastic consolidation problem is utilized to illustrate the coupled processes in porous rock. Then, the convective-dominated transport problem and its corresponding SUPG

stabilization technique are studied. At last, a heat transport problem in fractured porous rock is simulated; methods commonly used in simulating fractures in porous rock are analyzed.

5.5.1 Initiation and propagation of a KGD hydraulic fracture

A KGD hydraulic fracture in 3D domain is utilized to study the initiation and propagation of hydraulic fractures. 3D 8-node hexahedron elements are used. The displacement in thickness direction (*x*-direction in Figure 5.3) is fixed with zero value in order to simulate the plane strain condition under which the KGD hydraulic fracture is developed. The compressibility effects are considered by simulating the wellbore using 1D elements, which are connected to the zero-thickness interface elements discretizing the hydraulic fracture. As shown in Figure 5.3, there are two nodes in the *x*-direction. The thickness in the *x*-direction is 1 m. To make all the variables uniformly distributed in the *x*-direction, a wellbore with flow rate of $Q_0/2$ is used at each of the two nodes at the boundary of zero-thickness elements. Table 5.1 gives the input parameters.

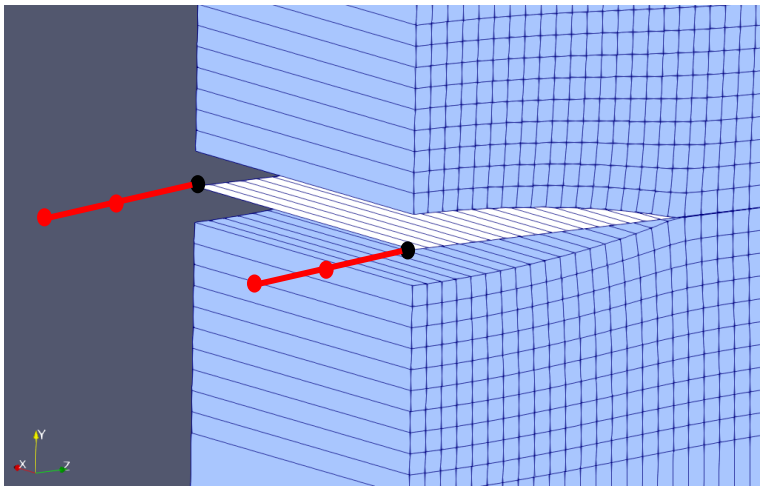

Figure 5.3 Connection of 1D elements for wellbore to the zero-thickness interface element in 3D. The red bar and circles indicate the 1D elements and their corresponding nodes; the white color shows the zero-thickness interface elements; the light blue color shows the 8-node hexahedron elements after deformation. The dark nodes connect the 1D element representing the wellbore to the zero-thickness element representing the hydraulic fracture.

For comparison purpose, the KGD hydraulic fracture without considering wellbore compressibility effects is also simulated. Figure 5.4 gives the aperture, fluid pressure and fracture

half-length evolution as a function of time. The aperture and net pressure profiles at different injection times are plotted in Figure 5.5. The numerical results when no compressibility effects exist match well with the asymptotic analytical solutions. As we know from both numerical simulations and asymptotic analytical solutions for the cases without compressibility effects, the fluid pressure at the injection point is infinite large at the very beginning of the injection; it then gradually decreases as the fracture length grows.

Table 5.1 Wellbore parameters, rock and fluid properties used for the KGD hydraulic fracture.

Poisson's ratio, v	0.15
Young's modulus, E	3.88×10^{10} Pa
Fracture toughness, K_{IC}	1.0×10^{6} Pa.m$^{1/2}$
Tensile strength, T_n	1.0×10^{6} Pa
Energy release rate, G_{IC}	25.2 N/m
Confining stress,	10.0×10^{6} Pa
Compressibility of wellbore, c	1.0×10^{-9} Pa^{-1}
Length of wellbore, L	1.0 m
Diameter of wellbore, $2r$	0.12 m
Fluid viscosity, μ	1.0 cp
Injection rate, Q_0 (half-wing)	0.001 m^2/s
Dimensionless toughness, κ	0.513

Note: Fracture toughness, K_{IC} , and dimensionless toughness κ are not input parameters for CZM, they are calculated for reader's convenience.

After considering the compressibility effects, a linear pressurization stage exists before the break down happens, as shown in Figure 5.4 (b). There is no propagation of the hydraulic fracture for the majority part of the pressurization stage. The slope of the curve during the linear pressurization on the fluid pressure vs. time plot can be calculated according to Eq. (5.29) when no fluid enters the fracture:

$$\frac{\partial p_w}{\partial t} = \frac{Q(t)}{Ac}. \tag{5.64}$$

$Q(t)$ is the injection rate at the inlet of wellbore, and has unit of m^2/s. The slop is calculated as 4.42×10^7 Pa/s based on data in Table 5.1. From numerical simulation, it is

calculated as 4.40×10^7 Pa/s. The fluid flux entering from the wellbore to the hydraulic fracture is illustrated in Figure 5.6. As shown, at the time close to break down, there is a jump in the fluid flux ($\approx 12.5 \times 10^{-4}$ m^2/s), which is 2.5 times higher than the given injection rate at the inlet of wellbore (5.0×10^{-4} m^2/s). The jump in fluid flux is apparently caused by the compressibility effects. A similar phenomenon is also observed in laboratory experiments (Hu and Ghassemi 2018a; Wu et al. 2008).

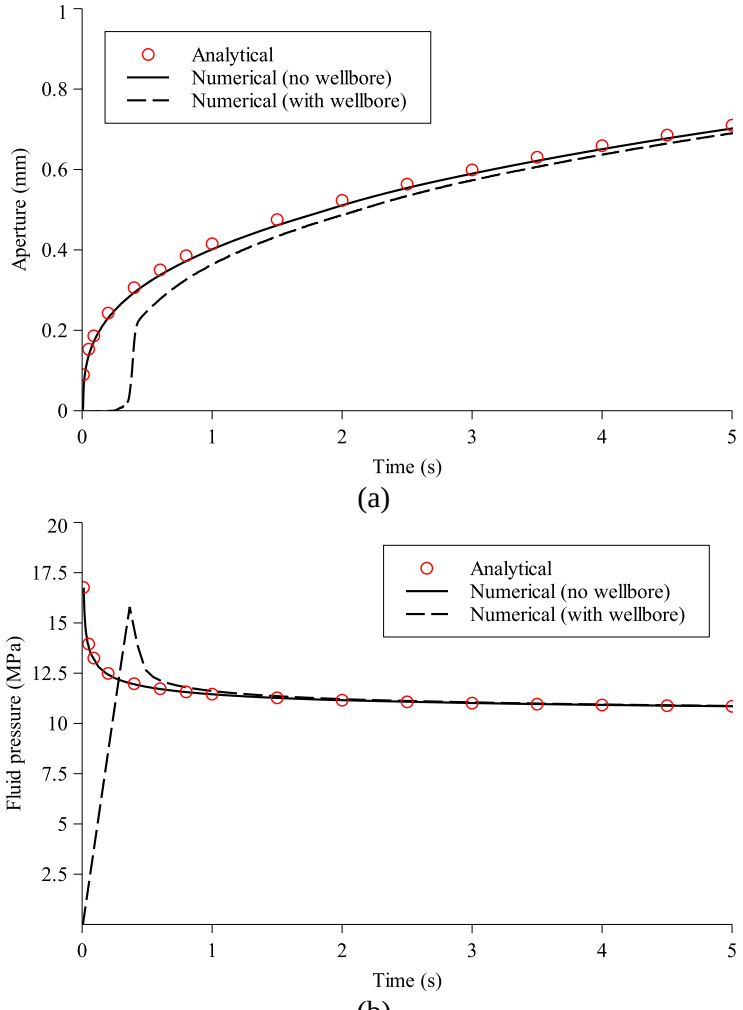

Figure 5.4 Hydraulic fracture variables plotted as a function of time. (a) Aperture at the fluid inlet point of the hydraulic fracture; (b) fluid pressure at the fluid inlet point of the hydraulic fracture; (c) fracture half-length. The fluid inlet point connects the 1D element for wellbore to the 3D zero-thickness interface element for hydraulic fracture as indicated by the black circles in Figure 5.3. (continued)

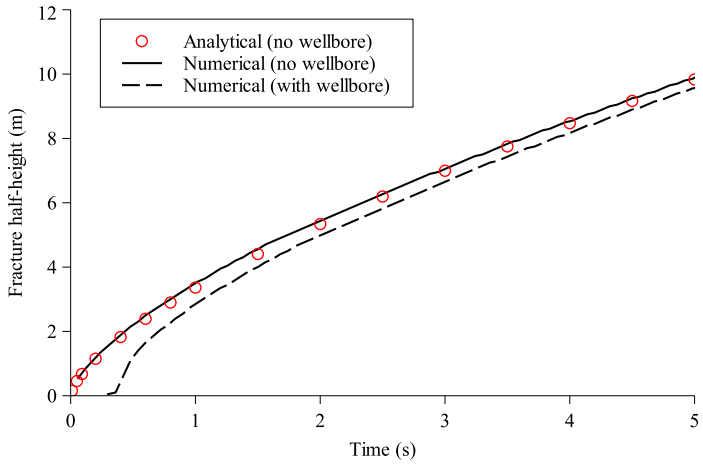

(c)

Figure 5.4 (continued). (Caption shown on previous page.)

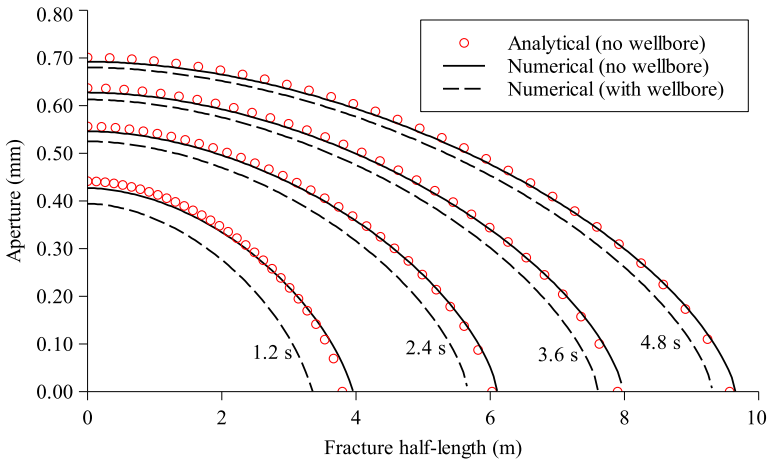

(a)

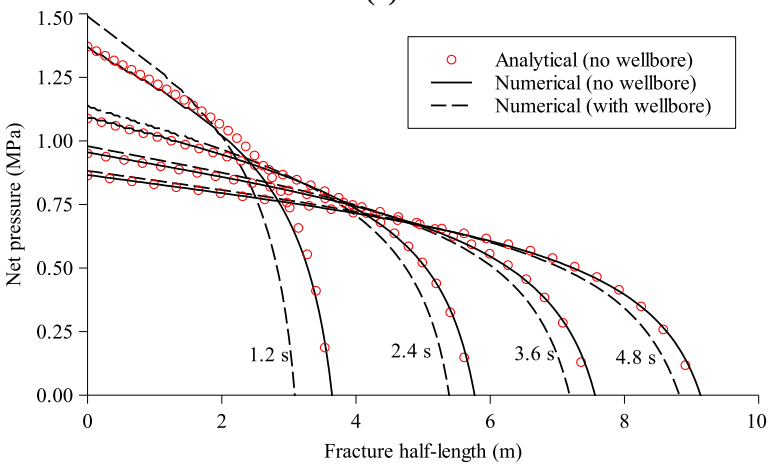

(b)

Figure 5.5 Aperture and net pressure profiles plotted along the fracture length at different time.

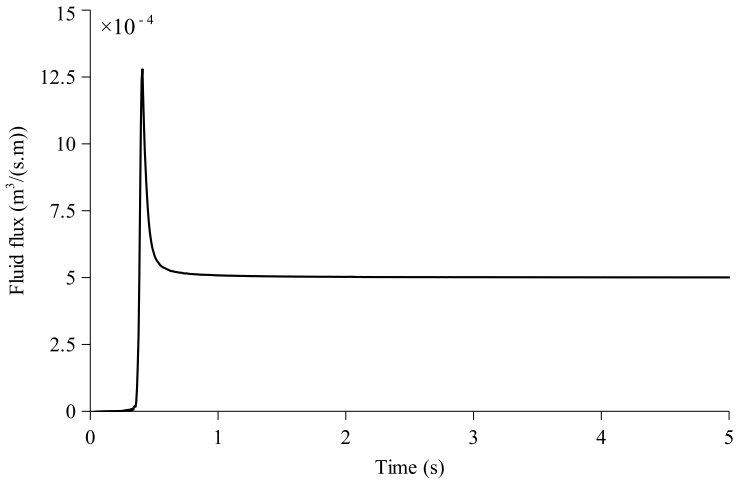

Figure 5.6 Fluid flux entering the hydraulic fracture from the wellbore as a function of time.

5.5.2 Thermo-poroelastic consolidation

Thermo-poroelastic consolidation is a typical fully coupled problem, which involves solid deformation, fluid flow and heat transfer in saturated porous media. Aboustit et al. (1982) studied a 1D thermoelastic consolidation problem using a coupled finite element model without considering convection effect. Based on the results from Aboustit, Noorishad et al. (1984), Lewis et al. (1986), Gatmiri and Delage (1997) and Gao and Ghassemi (2016) performed code-to-code verification. Analytical solutions for the 1D thermoelastic consolidation are provided in Bai (2005). The geometry of the problem is shown in Figure 5.7. Table 5.2 gives the input data. A surface traction of 1 N is applied on the top surface, with a surface temperature of 50 °C and a pore pressure of 0 Pa. The initial temperature of the saturated soil is 0 °C. The soil column is insulated and sealed everywhere, except at the top surface. 3D 8-node hexahedron elements are utilized in our simulation.

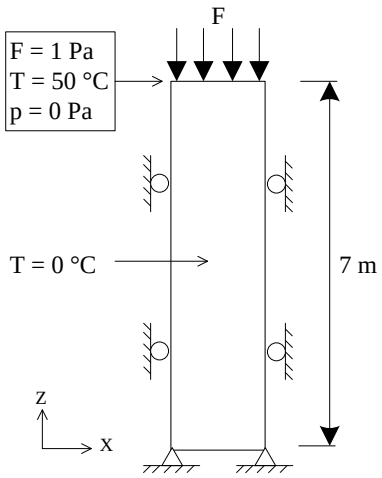

Figure 5.7 Geometry and boundary conditions of the 1D thermo-poroelastic consolidation problem.

Table 5.2 Basic input parameters for thermoelastic consolidation.

Porosity, ϕ	0.20
Young's modulus, E	6000.0 Pa
Poisson's ratio, v	0.40
Volumetric thermal expansion coefficient, α_m	9.0×10^{-7}
Matrix heat capacity, ρC	167.20×10^{3} J/m^3 °C
Thermal conductivity, k^T	0.836 kJ/m s °C
Permeability, k/μ	4.0×10^{-6} m/s
Biot's coefficient, α	1.0
Initial temperature, T_{ini}	0 °C
Surface temperature, T_0	50.0 °C
Surface load	1.0 Pa

Numerical results from our FEM model are compared with those obtained from analytical solutions. The settlements at different locations are plotted as a function of time in Figure 5.8. The model first experiences continuous settlement (contraction). Initially, the settlement caused by drainage of fluid (effective stress increase) and compression of the solid matrix is larger than the expansion due to increase of temperature in the region close to surface on which a higher temperature is applied. As the temperature diffuses further into the domain, it gradually rebounds (expansion) and reaches a final status. Figure 5.9 and Figure 5.10 shows separately the pore pressure and temperature at different locations. As illustrated, they all have a good match with analytical solutions.

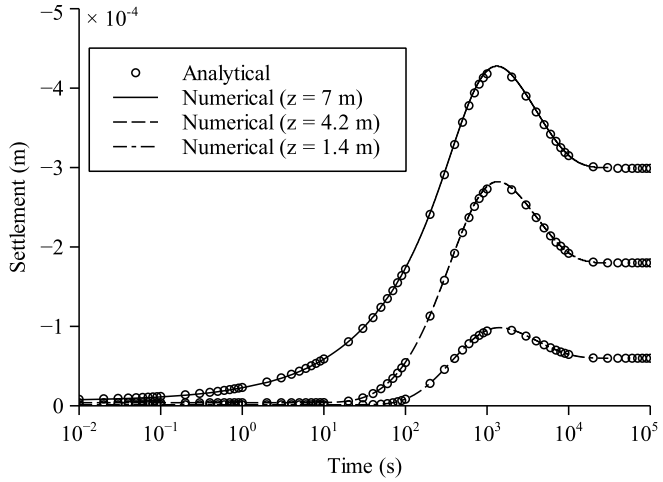

Figure 5.8 Settlement at different locations plotted as a function of time.

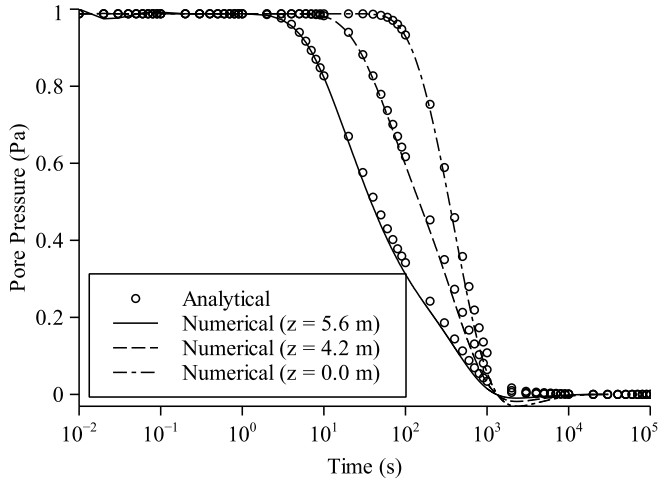

Figure 5.9 Pore pressure at different locations plotted as function of time.

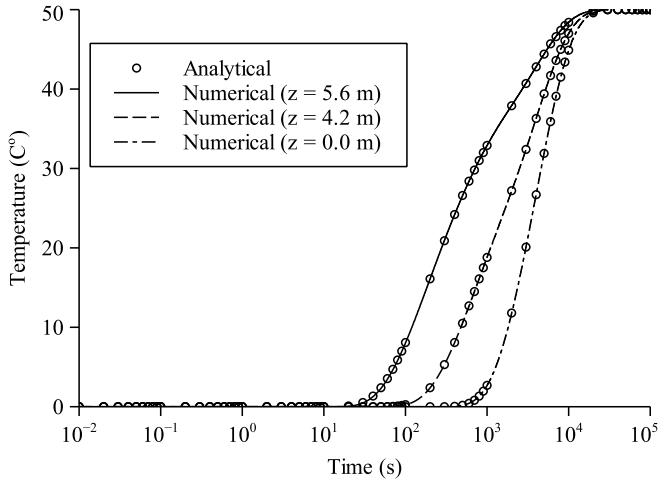

Figure 5.10 Temperature at different locations plotted as function of time.

5.5.3 Stabilization of convection-dominated flow

A simple example is adopted to illustrate the SUPG stabilization technique in convection-dominated flow. The 1D heat transfer problem (Figure 5.11) is governed by the following equation:

$$\begin{aligned} &T_{,t} + uT_{,x} - \kappa T_{,xx} = 0 \\ &T(0,t) = 1\ ^\circ C \\ &T(x,0) = 0\ ^\circ C \end{aligned} \quad . \tag{5.65}$$

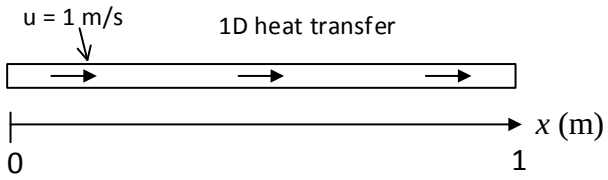

Figure 5.11 Illustration of the 1D heat transfer problem.

The analytical solution for this 1D problem is given as (Carslaw and Jaeger 1959):

$$T(x,t) = \frac{1}{2}\left[erfc\frac{x-ut}{2(\kappa t)^{1/2}} + e^{ux/\kappa} erfc\frac{x+ut}{2(\kappa t)^{1/2}} \right]. \tag{5.66}$$

100 equal-size linear elements (3D 8-node hexahedron) are used in spatial discretization from $x = 0$ to $x = 1$ m. The Crank-Nicolson method ($\theta = 0.5$) is performed in time integration. κ = 0.0001 W/m·°C and u = 1 m/s are assumed.

Figure 5.12 gives the temperature profiles at time = 0.6 s for the convection-dominated heat flow problem. As illustrated, the SUPG stabilization technique reduces the numerical oscillations a lot though it does not completely eliminate the oscillations at the fluid front (as is the case in other studies).

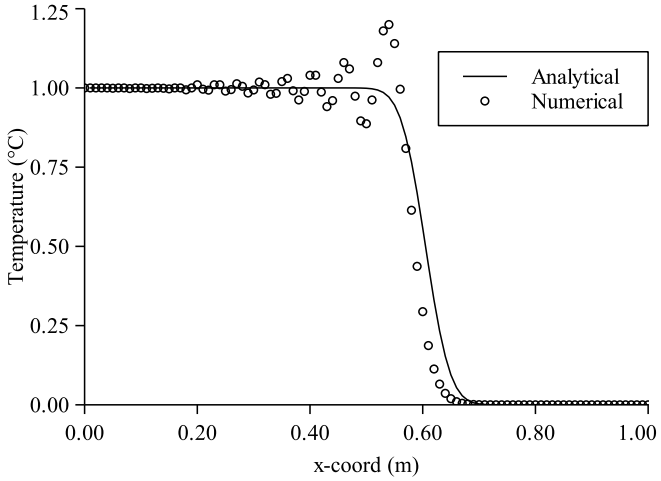

(a)

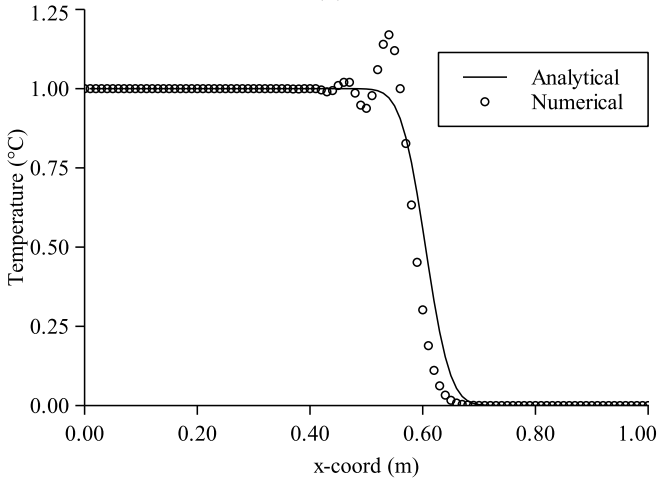

(b)

Figure 5.12 Temperature profiles of the convection-dominated heat flow at time = 0.6 s: (a) without the use of SUPG stabilization; (b) with the use of SUPG stabilization. The analytical solution is for κ = 0.001 since κ = 0.0001 is too small to yield results from analytical solutions.

5.5.4 Heat transport in fractured porous rock

To simulate fractures (newly created or pre-existing) in a porous rock, several ways are usually adopted, as illustrated in Figure 5.13. The first method is to discretize the fractures using 1D or 2D element types and then superimpose them onto the standard continuum element edges (boundary edge of 2D element) or surfaces (boundary surface of 3D element) (Segura and Carol 2004), respectively. Since the elements representing the fracture are superimposed on to the continuum element, the top and bottom surfaces of the fracture are not explicitly simulated. It is difficult to model the mechanical behaviors (opening or sliding) of a fracture when this method

is utilized. The second way to model a fracture is to use standard continuum elements which are the same as those used for the porous matrix but with different properties for the "solid", fluid flow and heat transfer (Gao and Ghassemi 2016). Usually some equivalent approaches should be adopted to obtain those properties. For example, an equivalent permeability should be generated for elements representing fractures. The third way is to explicitly model the fractures through zero-thickness elements (Segura and Carol 2004; Gao and Ghassemi 2018). Through zero-thickness element, the mechanical behavior of the discontinuity can be well described. There are also other methods to account fractures in continuum elements. Interested readers are referred to Wang and Ghassemi (2012), Huang and Ghassemi (2015) and Cheng et al. (2019) for further reading. In this section, we focus on the second and third approaches, and analyze the differences between them based on simulations of heat transport in a fracture.

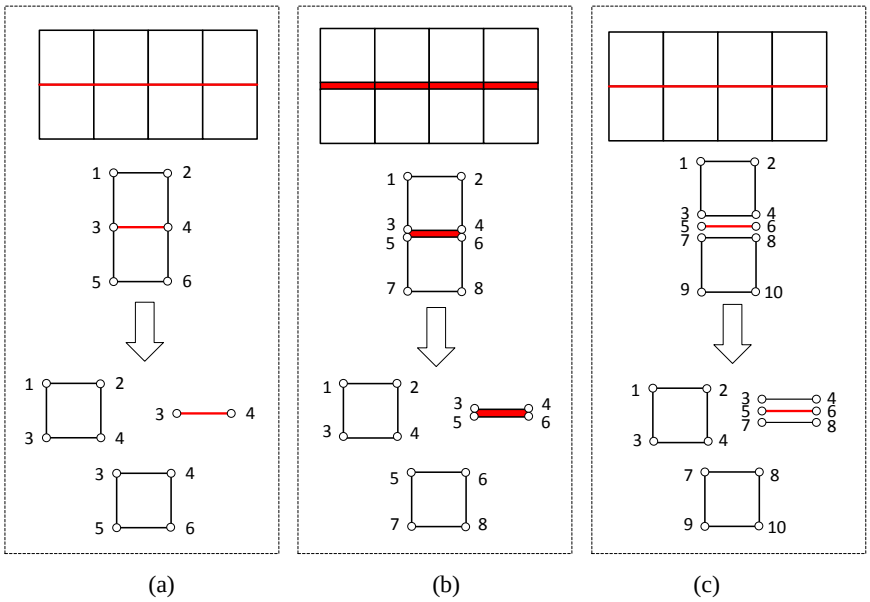

Figure 5.13 Three different ways to simulate fractures in a porous medium: (a) elements representing fractures are superimposed onto the boundary of continuum elements; (b) continuum element which is the same as that used for porous media but with different properties; (c) zero thickness element. Red color indicates the fracture.

(1) Usage of continuum element in simulating fracture

A classical 2D heat transfer problem in a fractured porous rock has been presented in Gringarten et al. (1975) and Cheng et al. (2001). A vertical plane representing the fracture penetrates the entire height of a reservoir that has constant height and infinite horizontal extent. The reservoir is insulated at the top and bottom. The heat conduction in the surrounding rock is simplified to be one dimensional. Based on these assumptions, the problem is formed as a coupling of 1D convection-diffusion heat transport along the fracture and 1D heat conduction in the direction perpendicular to the fracture (Figure 5.14). To obtain an analytical solution of this problem, it is further assumed that the facture aperture is constant; the rock matrix is impermeable; all the mechanical, fluid and thermal properties are constant. Lauwerier (1955) derived analytical solutions for heat transfer between two reservoir formations. If one of the formations is treated as a fracture (by modifying formation parameters), the analytical solutions could also be used in the fractured porous medium as shown in Figure 5.14.

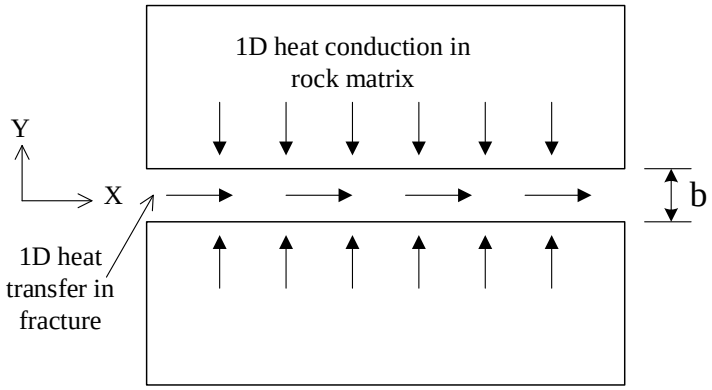

Figure 5.14 Illustration of heat transport in a fractured porous medium.

On the fracture surface, an equilibrium of heat flux between rock matrix and fracture is satisfied in the equation given by Gringarten et al. (1975), Cheng et al. (2001). To obtain an analytical solution, it is also assumed that the temperature is continuous across the fracture surface. In other words, the temperature in fracture equals to the temperature on the surface of rock matrix. As we will illustrate in the following, the continuity of temperature across fracture

surface could be satisfied when we treat the fracture as a "special porous medium" but with different properties; a discontinuity in temperature could exist when a convection boundary condition between fracture and rock matrix is used instead. We first used a standard continuum element (3D 8-node hexahedron element in this study) to model fracture in this fractured porous medium. The 2D problem (Figure 5.14) is simulated through a 3D model that has uniform distributions of parameters in the direction perpendicular to the 2D plane (*xy* plane in Figure 5.14). Table 5.3 gives the input parameters for the thermal related properties and the geometry of the model.

Table 5.3 Geometry and thermal properties for the fractured porous medium.

Geometry of model	$1 \times 1 \times 0.25$ m (length/width/height)
Fracture length	1 m
Fracture half-width, $b/2$	1×10^{-3} m
Thermal conductivity of rock, k^T	1 J/m s °C
Heat capacity of rock, c_r	900 J/kg °C
Density of rock, ρ_r	2650 kg/m^3
Heat capacity of fluid, c_f	4200 J/kg °C
Density of fluid, ρ_f	1000 kg/m^3
Velocity of fluid, v_x	1×10^{-4} m/s
Initial temperature, T_0	0 °C
Temperature of injection fluid, T_{inj}	1 °C

Figure 5.15 gives the temperature distribution along the fracture surface at different injection time. In the numerical simulation, the fracture surface is also the surface of the continuum elements for rock matrix since the 8-node hexahedron element is used to represent the fracture. Through this treatment, both the temperature and the heat flux are continuous at the fracture surfaces. The temperature at several discrete points in rock matrix is plotted as a function of time in Figure 5.16. These points are located along a line that is parallel to the fracture surface and is 0.2 meters away from it. As shown, the temperature in both the fracture

and the rock matrix matches well with analytical solutions as provided in Lauwerier (1955) and Cheng et al. (2001).

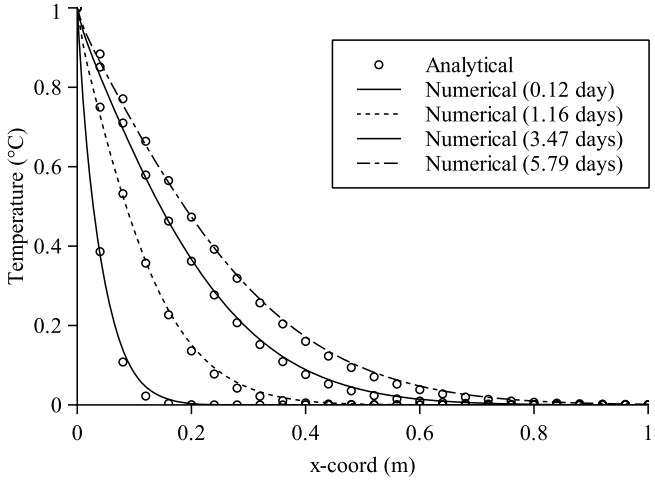

Figure 5.15 Temperature distribution along the fracture surface at different injection time. The fracture surface is also the surface of continuum element since the fracture is simulated using 8-node hexahedron element.

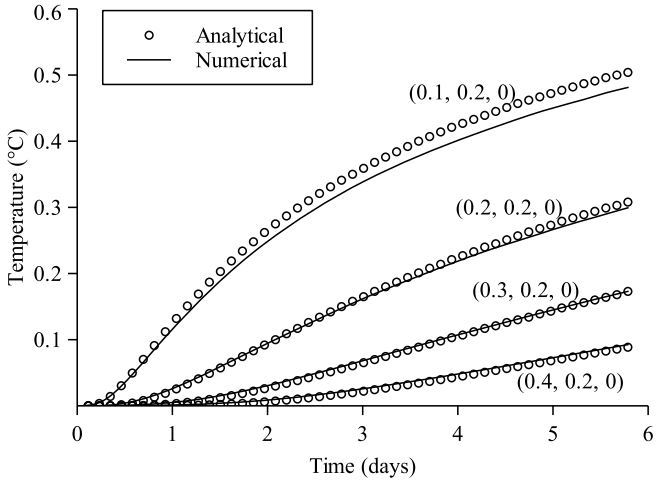

Figure 5.16 Temperature distribution at discrete points plotted as a function of time. The points are located in the rock matrix and are 0.2 meters away from the fracture. Their coordinates are given in the figure.

(2) Using the zero-thickness element for simulating flow and heat transport in a fracture

When continuum elements are used to represent fractures, the degrees of freedom for the temperature in the rock matrix and for the fracture are the same and are shared at nodes connecting the fracture and rock matrix (Figure 5.13 (b)). However, as shown in Figure 5.2 and Figure 5.13 (c), when zero-thickness elements are used, the degrees of freedom for the

temperature in the rock matrix and for it in the fracture are on different nodes; thus they have different degrees of freedom for temperature (the degrees of freedom for fluid pressure are treated in the same way and are also different). The treatment of adopting different nodes for the rock matrix and for the fracture allows discontinuity in temperature and pressure across the fracture surface. The condition that the heat flux (and fluid flux) is in equilibrium between the fracture and the rock matrix can be satisfied when the zero-thickness elements are utilized to represent the fracture. However, the temperature would be discontinuous across the interface elements since the temperature continuity and heat flux equilibrium cannot coexist at the same time at the interface. If fractures are treated as the interior boundary, this means a boundary condition of the first kind (Dirichlet boundary) and a boundary condition of the third kind (mixed boundary) (Bergman et al. 2011) cannot be satisfied simultaneously at the interface; only the "convective surface boundary condition" (mixed boundary) should be used to maintain the equilibrium of heat flux at the interface in numerical models.

In transient heat conduction problems, the convective surface boundary condition exists when convective heat flow is off the surface of rock matrix (Bergman et al. 2011), as shown in Figure 5.17. When fractures are treated as interior boundaries in numerical models, the convection surface condition should also be applicable at the interface that connects fractures with the rock matrix. A simple transient heat conduction example is used to demonstrate the usage of zero-thickness element to simulate the convection surface condition at the interface.

Figure 5.17 illustrates a 1D transient heat conduction problem in a semi-infinite solid, which extends to infinity in all but one direction, and has a single identifiable surface. The convective surface condition exists at the identifiable surface. In the numerical simulation, a 3D model with finite length in x direction (Figure 5.17) is utilized to simulate the semi-infinite

problem. The single identifiable surface for the semi-infinite solid is represented through a zero-thickness element, which is bounded by 8-node hexahedron continuum elements. Half of the model on either side of the zero-thickness element is treated approximately as a semi-infinite solid. The analytical solution for this problem is provided in Bergman et al. (2011). The followings are the boundary conditions (when fractures are treated as interior boundaries) at the interface:

$$T(x,0) = T_i$$
$$-k^T \frac{\partial T}{\partial x}|_{x=0} = h\left(T_f - T|_{x=0}\right) \tag{5.67}$$

In the numerical simulation, convective heat transfer coefficient, h, is 100 W/m^2·°C; heat conduction of rock, k^T, 3 W/m·°C; heat capacity of rock, c_r, 900 J/kg·°C; rock density, ρ, 2650 kg/m^3; initial temperature, T_i, 0 °C; temperature of convective fluid at the interface, T_f, 1 °C. Figure 5.18 illustrates the distribution of temperature along the line perpendicular to the interface (x direction in Figure 5.17) at different time. As shown, numerical results match well with analytical solutions. Temperature discontinuity exists at the interface. As time goes by, the temperature on the surface of rock matrix, $T(x, t)$ at x = 0 m, gradually approaches the temperature of convective fluid (T_f).

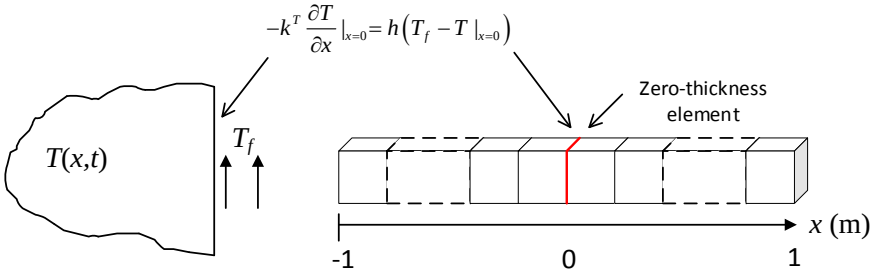

Figure 5.17 Illustration of convection surface condition and the corresponding numerical model to simulate the convection surface condition using a zero-thickness element. 3D hexahedron element is utilized to simulate the solid part of the 1D problem. The red color indicates the zero-thickness element where the convection surface condition is located.

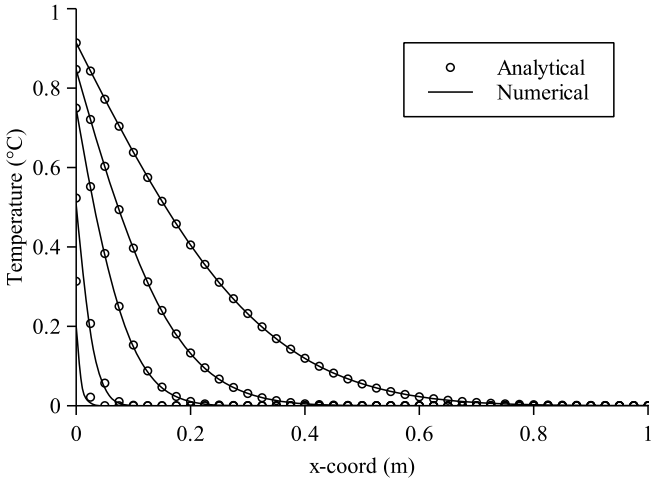

Figure 5.18 Temperature distribution along the line perpendicular to the interface (x direction in Figure 5.17) at different time.

Compared to the aforementioned methods (superposition method and continuum element method) to simulate fractures, the zero-thickness element is much more flexible and effective to handle coupled thermo-hydro-mechanical processes. It can simulate mechanical opening and shearing (Gao and Ghassemi, 2018); it can also be used to describe heat convective boundary conditions which is often encountered in practical applications. When the superposition method or continuum element method is used, the aperture size is usually determined through empirical equations and the discontinuity in temperature or pore pressure across an interface cannot be realized.

Convective heat transfer coefficient, *h*, is a fundamental parameter in numerical analyses related to rock-fracture heat transfer. Though much effort has been spent on measuring it through experiments, it is still a challenging task to obtain typical values for a rock-fracture interaction system (Zhao and Tso 1993). Problems of convective heat transfer are complex because the coefficient depends on fluid properties, as well as the surface geometry and flow conditions on the solid-liquid interface (Bergman et al. 2011). In fractured porous media, many factors could influence the convective heat transfer, for example, fluid flow velocity, fracture geometry, fracture surface roughness, and so on. The same problem as that shown in Figure 5.14 is studied

here to analyze the influence of convective heat transfer coefficient on heat transfer in a fracture in porous rock. The geometry of the model, fluid and thermal related properties are the same as those provided in Table 5.3.

Figure 5.19 illustrates the temperature profile in the fracture for different convective heat transfer coefficients. Carslaw and Jaeger (1959) give the solutions for heat transfer in 1D, which corresponds to $h = 0$, i.e., no heat flux through the interface connecting fracture and rock matrix. The solution provided by Cheng (2001) could be utilized when fractures are treated as a porous medium but with different properties than the surrounding matrix. With such a treatment, both heat flux equilibrium and temperature continuity are satisfied at the interface; since the temperature is continuous at the interface (temperature in the fracture equals to that on the surface of rock matrix), a maximum heat flux through the interface is achieved. As shown in Figure 5.19, when $h = 10000$ W/m^2·°C, results from numerical simulations can approach the solution provided by Cheng et al. (2001); numerical results are not sensitive to h when its value is larger than a certain number, e.g. 100 W/m^2·°C in this case, which yields results very close to the solution derived by Cheng et al. (2001). It should be noticed that the solution derived by Cheng et al. (2001) assumes the temperature is continuous across the interface; in other words, the temperature in fracture is equal to that on the surface of porous medium (fracture surface).

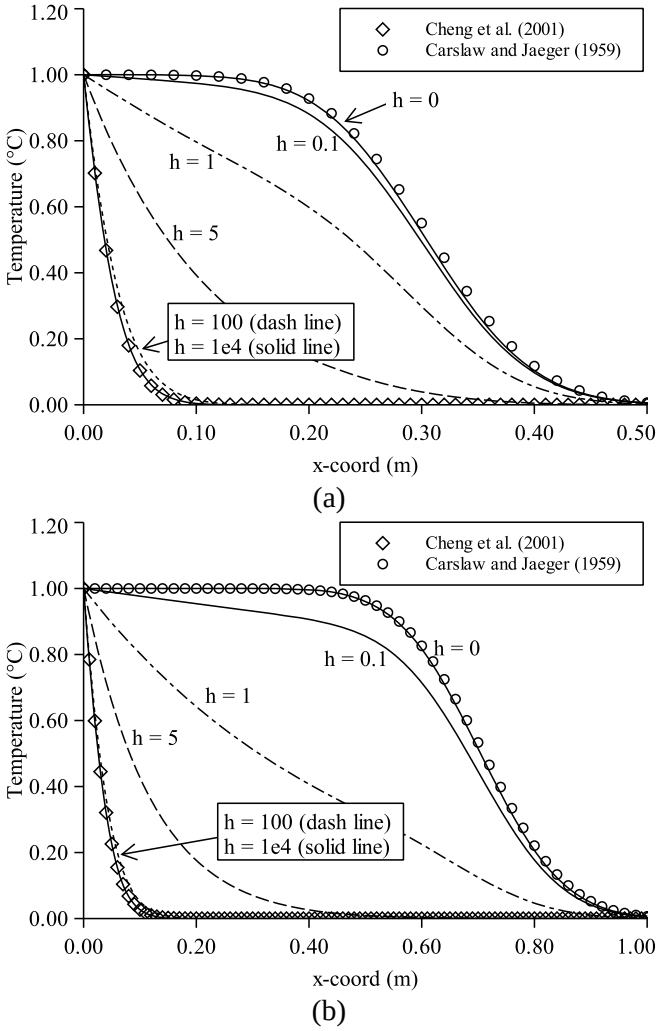

Figure 5.19 Temperature profiles within fracture for different convective heat transfer coefficient (h) at time = 3000 seconds (a) and at time = 7000 seconds (b). The unit for h is W/m^2·°C. Discrete points are from analytical solutions, lines are from numerical simulations.

5.6 Numerical simulations of a lab-scale EGS

Based on the proposed model, a series of numerical simulations of a lab-scale enhanced (or engineered) geothermal system (EGS) are carried out. The main objectives are to gain a better understanding of the hydraulic and thermal related properties of hydraulically induced fractures. Experimental results can be found in detail in Hu et al. (2016); Hu and Ghassemi (2017, 2018b, 2018a). In the following sections, a stepwise pressurization test is performed first. The experiment is designed to obtain information regarding the integrity of the tested block sample and to validate its permeability. Then, the initiation and propagation of hydraulic fracture

in a block sample are modeled. Afterwards, a more complex experiment involving cold water circulation in a hot, hydraulically fractured block sample is simulated and discussed.

5.6.1 Stepwise constant pressure injection

A brief description about the lab-scale EGS system is given here. A 13 inches cubical granite block was drilled with 5 wells, as shown in Figure 5.20. The injection has a depth of 7.5 inches with a diameter of 0.78 inch. The open-hole section at the bottom has a length of 2.0 inches, as indicated by the red color. Four production wells were drilled 3.5 inches away from the injection well with a depth of 9.0 inches and a diameter of 0.4 inch. The open-hole sections of the production wells have a length of 5.0 inches, which is indicated by the blue color in Figure 5.20.

The actual fracturing and circulation experiments were performed on block of Sierra-White granite with an injection well and 4 production well (a five-spot). Before the step-wise pressurization test, the rock block was saturated through 0.002 mol/L NaCl solution. The same solution was used during injection. For each pressurization step, the pressure was kept constant for 3 minutes.

The four production wells were fully open during the pressurization. The laboratory results for the stepped pressurization are given in Table 5.4. The block permeability was measured in the laboratory to be 518 nD. The experimental results indicate the integrity of the rock block and the injection system before hydraulic fracturing. Actually, the rock blocks are carefully chosen to not contain visible cracks so as to study the impact of fracturing.

A trial and error method was used to match the numerical results with the laboratory test ones. The basic mechanical and fluid parameters used in this study are listed in Table 5.5. The properties for Westerly granite are also given for comparison. The viscosity of the injected water

is 0.89 cP, which is the viscosity of water at about 25 °C. Biot's effective stress coefficient and undrained Poisson's ratio are estimated as the same as those for Westerly granite.

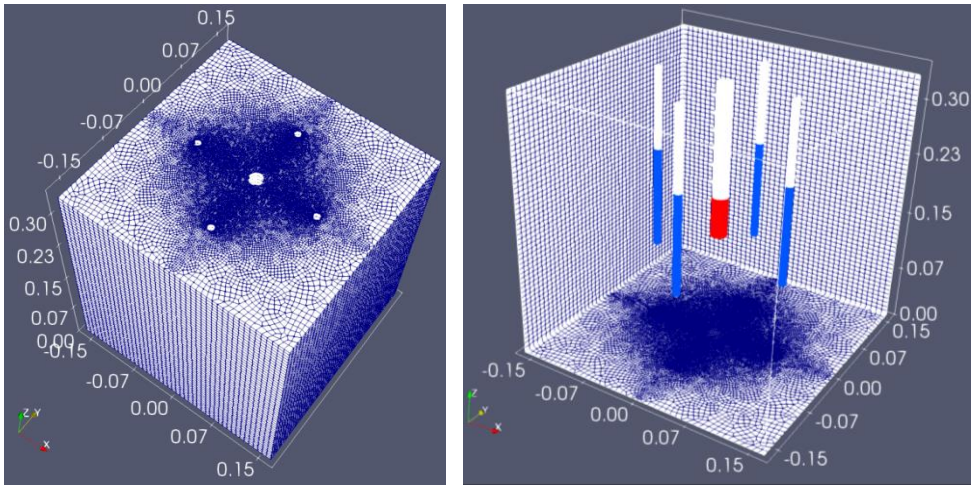

(a) (b)

Figure 5.20 (a) Discretized grid model. 8-node hexahedron element is used; (b) Production and injection wells in the tested block. The red color indicates open-hole section of the one injection well; the blue color indicates open-hole sections of four production wells. Unit: m.

Table 5.4 Experimental results of stepped constant pressure injection. (Hu et al., 2017)

Time slice (mins)	Pressure (psi)	Pressure (Pa)	Flow rate (m^3/s)
0 - 3	50	3.45E+05	6.04E-11
3 - 6	100	6.89E+05	1.55E-10
6 - 9	150	1.03E+06	2.25E-10
9 - 12	200	1.38E+06	2.81E-10
12 - 15	250	1.72E+06	3.36E-10
15 - 18	300	2.07E+06	3.88E-10
18 - 21	350	2.41E+06	4.35E-10
21 - 24	400	2.76E+06	4.81E-10

A series of simulations using different permeability are performed. Results for permeability being 595 nD, 680 nD and 765 nD are shown in Figure 5.21. As illustrated, the injection rate is relatively higher at the beginning of each injection stage due to an abrupt increase of injection pressure; then a stable injection rate is reached. The numerical simulation with a permeability of 680 nD matches well with the laboratory data. This value is close to that measured in laboratory (518 nD). The numerical simulations also indicate that the developed numerical model is correctly set up for the rock block experiments.

Table 5.5 Mechanical and fluid properties for granite in this study and for Westerly granite.

	Granite in this study	Westerly granite
Biot's effective stress coefficient:	0.47 (from Westerly granite)	0.47
Drained Poisson's Ratio, v:	0.25	0.25
Undrained Poisson's Ratio, v_u:	0.34 (from Westerly granite)	0.34
Young's Modulus, E:	6.50×10^{10} Pa (9427452 psi)	3.75×10^{10} Pa
Density, ρ:	2.65 g/m^3	
Tensile strength, T:	8.83×10^6 Pa (1280 psi)	
Porosity, φ:	0.8 %	1%
Permeability, k:	518 nD	4.0×10^{-4} mD
viscosity, μ:	0.89 cP	

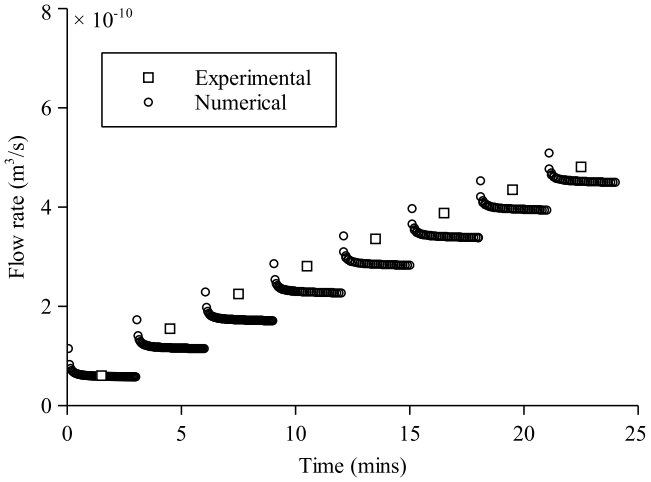

(a)

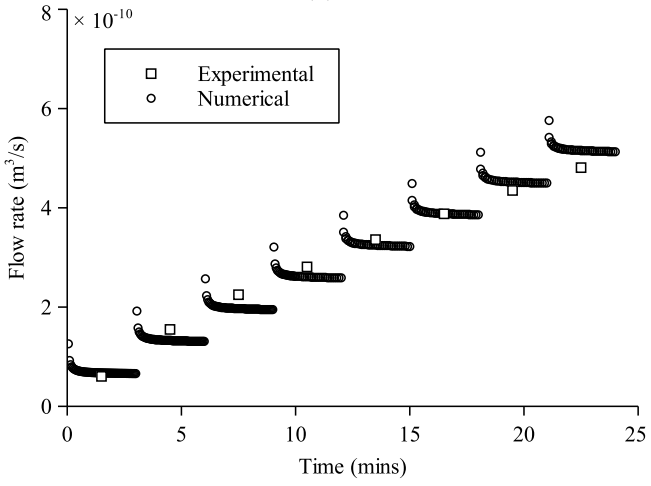

(b)

Figure 5.21 Flow rate plotted as a function of time for the cases with permeability equal to 595 nD (a), 680 nD (b), 765 nD (c). (continued)

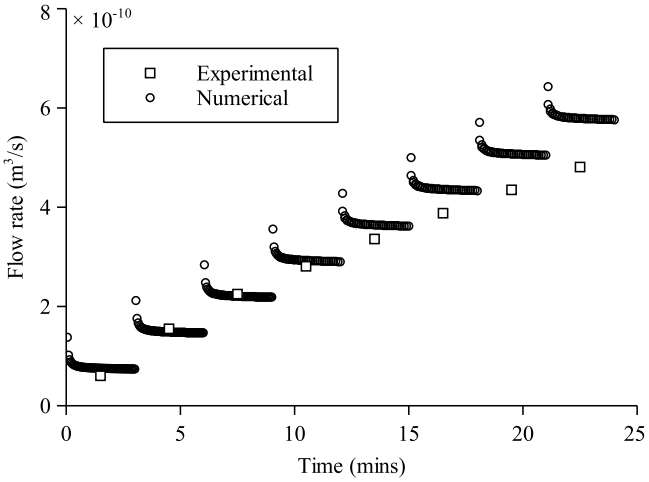

(c)

Figure 5.21 (continued). (Caption shown on previous page.)

5.6.2 Initiation and propagation of hydraulic fracture

To obtain high conductivity flow paths and economical production rate, hydraulic fracturing is usually performed during the development of an EGS system. The lab-scale hydraulic fracturing was performed in laboratory in the previously mentioned block samples. The block samples with the created hydraulic fracture were used in the next step to analyze the extraction of thermal energy. Essentially the main procedures involved in the development of an EGS system in field are realized in laboratory. They are the creation of a geothermal reservoir through hydraulic fracturing and the extraction of the thermal energy from the created fracture.

In this study, we simulate one of the hydraulic fracturing tests. Details about the laboratory setup and the corresponding experimental data can be found in Hu and Ghassemi (2018a). The same geometry as those provided in Figure 5.20 is used. The rock and fluid properties are the same as those given in Table 5.5. The fracture toughness K_{IC} and its corresponding energy release rate G_{IC} are 2.0 MPa.m$^{1/2}$ and 57.7 N/m, respectively. The injection rate is 8.33×10^{-9} m^3/s. The injection well length and diameter are 0.17 m (6.75 inch) and 0.0198 m (0.78 inch), respectively. The length and diameter for each of the four production wells are 0.19 m (7.50 inch) and 0.0099 m (0.39 inch), respectively. The compressibility parameter c of

the wellbore is 9.20×10^{-10} Pa^{-1}, which can be calculated from the experimental records provided in Hu and Ghassemi (2018a).

To prevent the hydraulic fracture from propagating to the block sample surface, the pump was stopped when its pressure drop reached a preset value of 0.28 MPa (40 psi); the initially closed production well were opened when the had rapid increase of pressure (0.07 MPa/s) or the pressure reached a value of 1.38 MPa. In the numerical simulation, the compressibility effects of the production wells are considered through the connection of the nodes of production wells to the 1D wellbore elements using the same scheme shown in Figure 5.3.

Figure 5.22 illustrates the injection pressure plotted as a function of time. The slop of the curve at the pressurization stage is 1.73×10^5 Pa/s. As shown, the results from the numerical simulation match well with those from the laboratory experiment. At t = 182 s, the injection is ceased and the hydraulic fracture touches the production wells. After shut-in, the injection pressure from the numerical simulation drops to a constant value larger than the applied vertical stress. In the laboratory experiment, the pressure at the injection well gradually decreases as time goes by and fluid diffuses into the rock matrix.

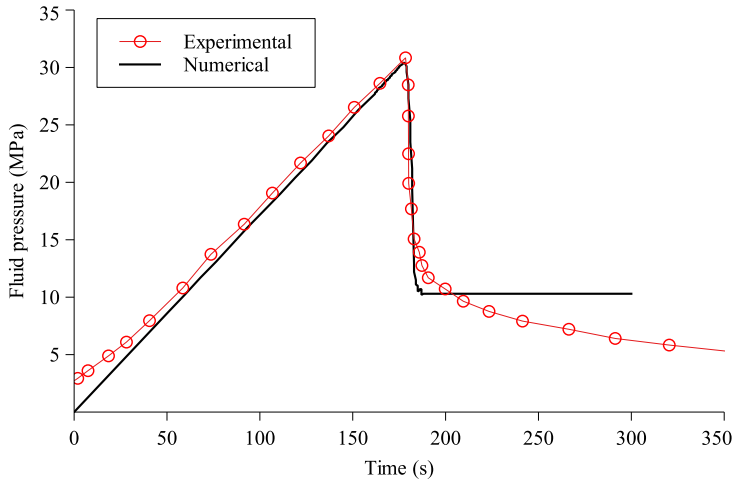

Figure 5.22 Comparison of injection pressure from the numerical simulation to those from the laboratory experiment.

The geometry, loading conditions and input parameters in the numerical simulation are symmetric to the injection point. The created hydraulic fracture is in penny-shape. The fracture radius, aperture and fluid pressure at the node of injection wellbore that connects the wellbore elements to the zero-thickness elements are plotted as a function of time in Figure 5.23. The hydraulic fracture starts propagating at $t \approx 177$ s. Before shut-in, the aperture increases and the injection pressure decreases; the propagation of the hydraulic fracture lasts for about 5 seconds. After shut-in, the hydraulic fracture propagates for an additional 3.5 cm in about 2 seconds; the injection pressure and aperture finally reach constant values.

From both the numerical simulation and laboratory records, it is suggested that the propagation of hydraulic fracture continues for about 7 seconds; the pressurization stage before fracture propagation takes a large portion of the total injection time. The total energy during injection can be calculated using the following equation

$$W_{in} = \int_0^{t_{inj}} pqdt \tag{5.68}$$

where q is the injection rate, p the injection pressure. Through calculations, it is determined that the total input energy before the initiation of hydraulic fracture at $t \approx 177$ s is about 22.4 J. A penny-shaped fracture would consume the surface energy of 22.4 J after propagating 0.35 m in radius, using the energy release rate of 57.7 N/m (corresponding to K_{IC} = 2 MPa.m$^{1/2}$). It should be noted that the edges of the cubic block sample is just 0.33 m. After injection is ceased at t = 182 s, the hydraulic fracture continues to propagate (for about 2 seconds) and the aperture decreases dramatically (Figure 5.23). Figure 5.24 illustrates the fracture extent at t = 182 s and t= 192 s. The red line indicates the fracture front obtained from laboratory by cutting the block sample into slabs and mapping the hydraulic fracture (Hu and Ghassemi 2018a). The numerical simulation produces a penny-shaped hydraulic fracture since the geometry, boundary conditions

and input parameters are symmetric with respect to the injection well. In the laboratory experiment, many factors such as rock heterogeneity, loading and constraining conditions, could make the hydraulic fracture propagate asymmetrically, as indicated by the fracture footprint obtained from laboratory.

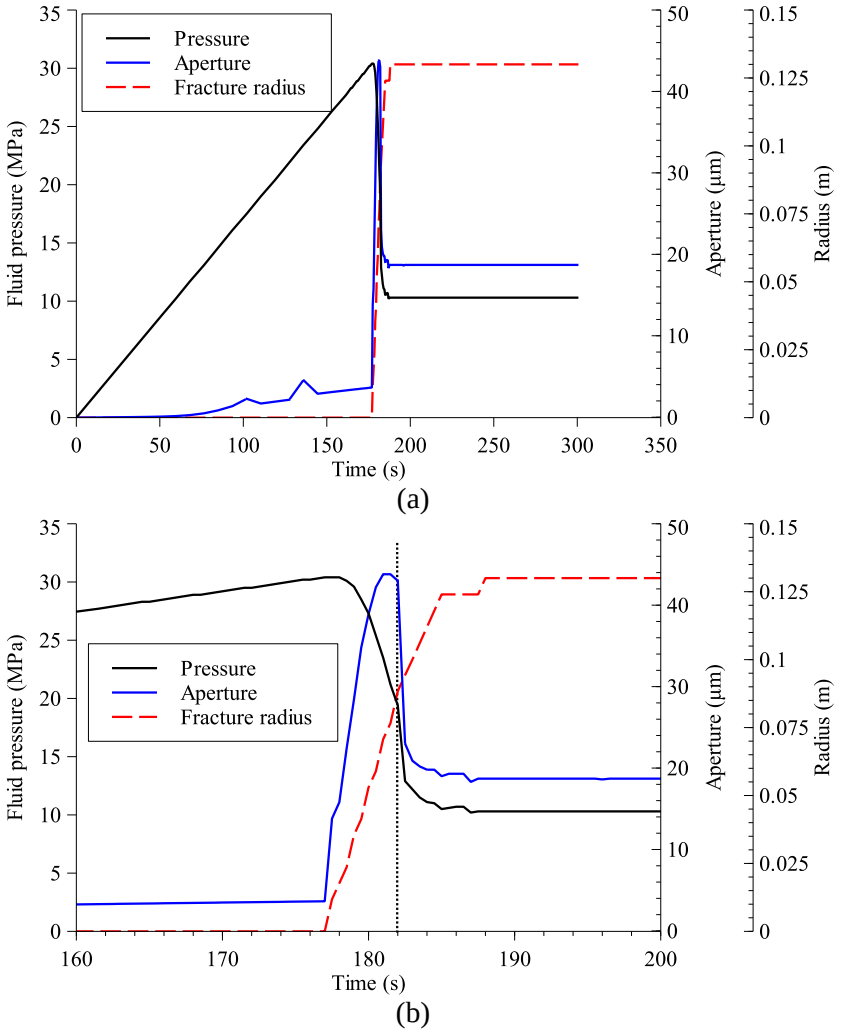

Figure 5.23 Fracture radius, aperture and fluid pressure at the injection well node connecting the zero-thickness element to the wellbore element plotted as a function of time. (a) distribution of variables in the complete numerical simulation duration; (b) simulation time from 160 second to 200 second, during which break down occurs and the hydraulic fracture touches the production wells. The vertical dot line in (b) indicates the time (t = 182 s) at which the injection is ceased.

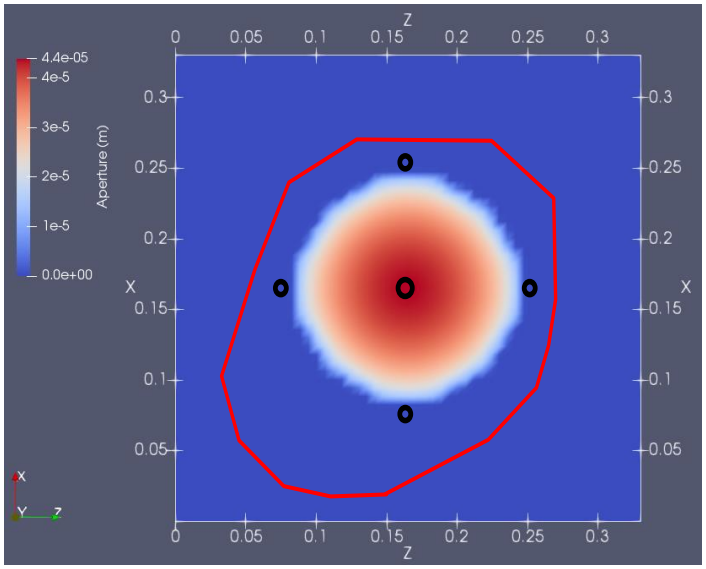

(a)

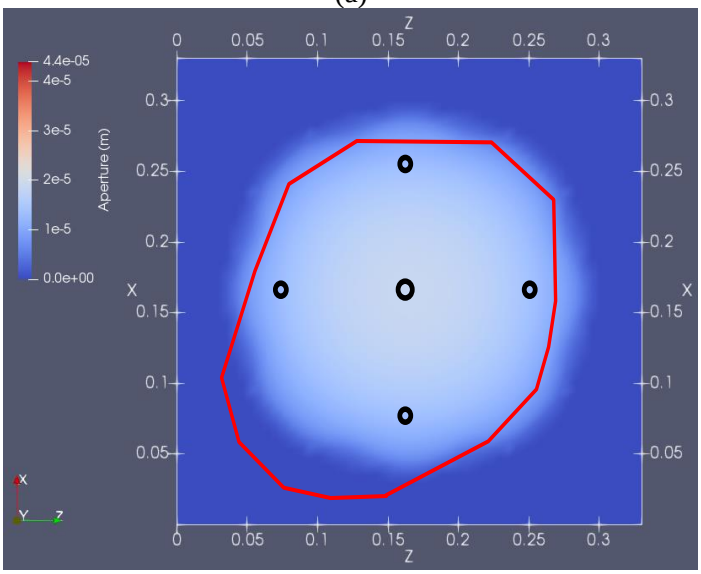

(b)

Figure 5.24 Fracture footprint indicated through the aperture size atdifferent time from the numerical simulation. (a) fracture footprint at *t* = 182 s when the injection is just ceased and the hydraulic fracture touches the four production wells; (b) fracture footprint at *t* = 192 s when the injection pressure is stable after shutin. The redline gives the fracture geometry obtained from the laboratory experiment.

5.6.3 Thermal circulation

Characteristics of mechanical, hydraulic and thermal properties of fractures are essential for evaluating and predicting the performance of an EGS system. Lab-scale experiments were designed and conducted to study the thermal-hydro-mechanical properties of hydraulically induced fractures. Related data were recorded in detail during the experiments. For example, the

injection rate, injection pressure and temperature were recorded at the injection well; the fluid temperature and accumulated fluid volume were also obtained at each production well. Detailed records regarding the experiments can be found in Hu and Ghassemi (2018b). To investigate the mechanisms behind observed phenomena related to fluid flow and heat transfer in a hydraulically created fracture, numerical simulations are performed.

The size of the granite block and the well configurations are the same as those provided in Figure 5.20. A hydraulic fracture was created first at the room temperature. Then the rock block was heated to a nearly uniform temperature of 69 °C. After that cold water was injected into the created fracture through the open-hole section of the injection well; the heated water was produced through the production wells. The injection well, hydraulically created fracture, production wells and block rock are assembled together as a circulation system. We focus on the thermal circulation part of the experiments.

The geometry of the hydraulically created fracture is shown in Figure 5.25, as indicated by the red color. The fracture geometry is somewhat planar and was reconstructed by cutting the block and also by analyzing the AE record (Hu and Ghassemi 2018b). The fracture intersects the open-hole section of the left and bottom production wells. From laboratory records, the recovery rate of the injected fluid is more than 97.5%. The produced fluid from the left and bottom production well is 14.8% and 82.8%, respectively. The fluid produced from the other two production wells is less than 1.0% due to the lack of connectivity with the hydraulic fracture. Since the recovery rate is 97.5%, it is considered that the leak-off effect during water circulation is negligible. Based on this consideration, the rock block is simulated through thermo-mechanical elements (rather than thermo-poromechanical) which have degrees of freedom for displacements and temperature but not for pore pressure. This is justified in view of the small

pore pressure variation due to thermal perturbations in granitic rocks (Ghassemi and Zhang, 2004; Tao and Ghassemi, 2011). The hydraulic fracture is simulated using the proposed thermo-hydro-mechanical interface elements as shown in Figure 5.2. The basic input parameters are the same as those provided in Table 5.5.

The temperature of water at the injection location was recorded in laboratory experiments (Figure 5.26) and is given as boundary conditions for the numerical simulations. In the laboratory, through pre-cooling of the injection water and by placing a long section of the injection tubing into an ice water tank, the temperature of the injection water was maintained at zero Celsius before entering the rock block. The injection water was heated up when flowing from the inlet to the open-hole section at the bottom of the injection well. Since the temperature was recorded in the open-hole section of the wells, the recorded temperature in the injection well is larger than that at the inlet (close to zero Celsius). Initially the flow rate was relatively slow (≈ 4 ml/min), the injection water was heated up to the temperature of rock block (69 °C) till it reached the bottom. Later on the injection rate was increased; the injection water was heated up to relatively lower temperatures. As illustrated in Figure 5.26, the temperature at the injection location (open-hole section at the bottom) gradually decreases from near 70 °C to an approximate constant value of 19 °C as time goes by. The recorded temperature at the open-hole section in the injection well is used as the temperature boundary condition at the intersection location between the created hydraulic fracture and the injection well. The process of heating up the injected water before reaching the intersection location is not simulated in this study. The injection rate at the intersection location is given in Figure 5.27.

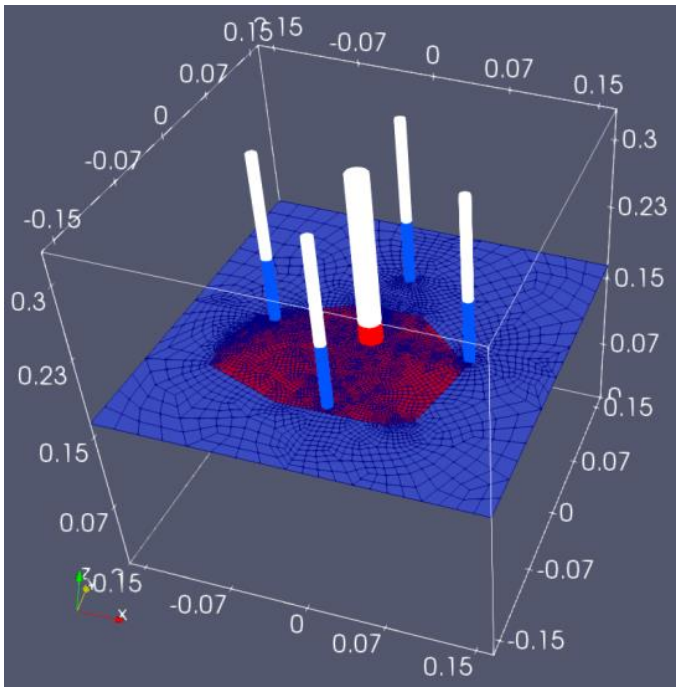

(a)

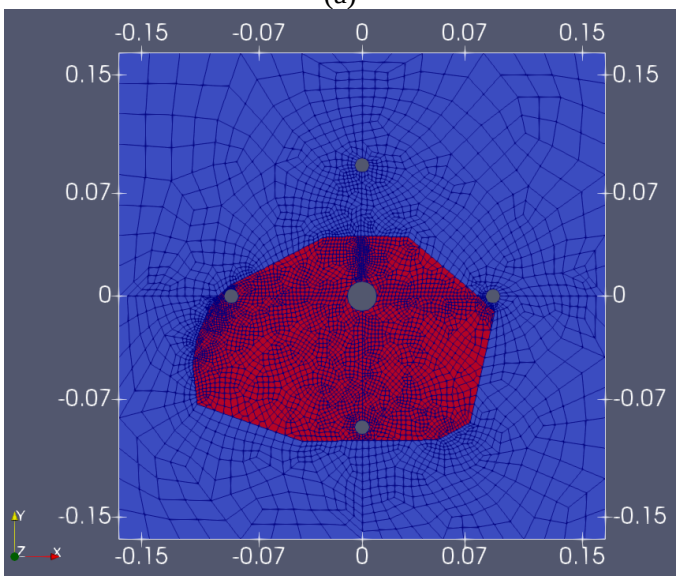

(b)

Figure 5.25 (a) The distritribution of the created hydraulic fracture in the rock block; (b) Geometry of the hydraulically created fracture. The red color on the plane indicates the created hydraulic fracture, which intersects the open-hole section of the left and bottom production wells. (The geometry is reconstructed based on Figure 4 in Hu and Ghassemi (2018b).)

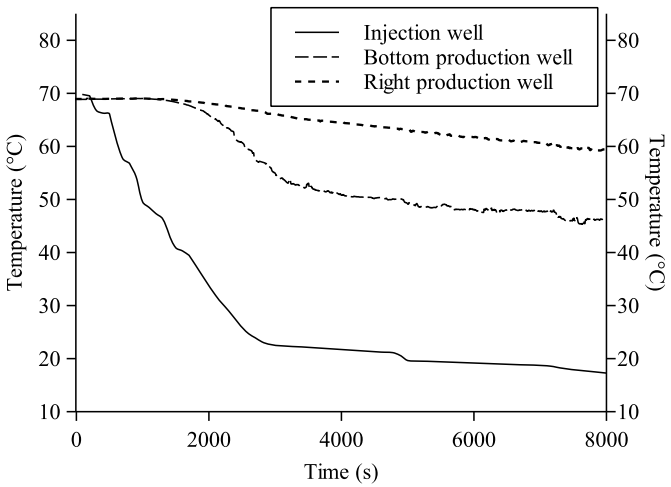

Figure 5.26 Laboratory recorded temperature plotted as a function of time for the injection well and production wells. The total circulation time is around 8000 s; the temperature drop in the injection well is 52.6 °C, in bottom and right production well is 23.8 °C and 10.0 °C, respectively.

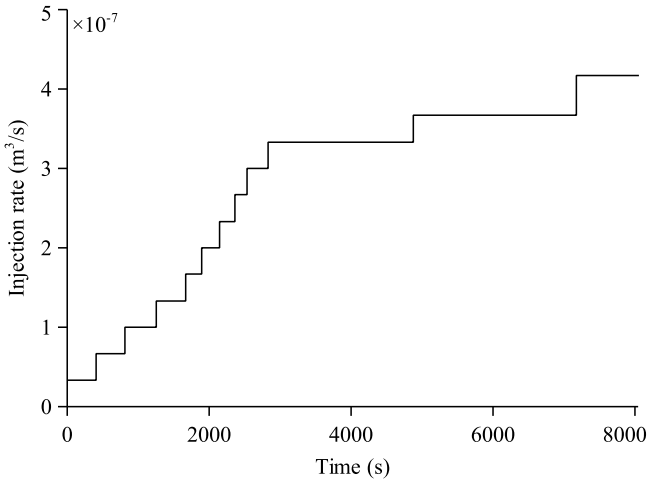

Figure 5.27 Injection rate plotted as a function of time.

The convective heat transfer coefficient is also an input parameter for the interface elements for these simulations. Its value depends on many factors. Usually a range of the values could be obtained if special experiments are designed to evaluate the coefficient (Zhao and Tso 1993). In this study, a trial and error method is used to match the experimental data with respect to fluid pressure at the injection well, and the temperature in the production wells. Two different convective heat transfer coefficients (100 W/(m^2.K) and 500 W/(m^2.K)) are adopted. The value of convective heat transfer coefficient determines the amount of heat flux exchanged between the hydraulic fracture and the rock surrounding the fracture.

Figure 5.28 illustrates the aperture size of the hydraulic fracture from numerical simulations at the location intersecting the injection well. The simulation generates a larger aperture size when using smaller convective heat transfer coefficient (100 W/(m^2.K)). The smaller the coefficient, the weaker the heat flux exchange and thus the lower the contraction of the surrounding rock. The aperture initially increases with time; it then reaches an almost constant value after the temperature in the hydraulic fracture is stable. The injection pressure from numerical simulations is plotted as a function of time in Figure 5.29. The pressure curves corresponding to different convective heat transfer coefficients have the same trends but with different values. For each injection step, the pressure reaches a maximum value in the beginning; it then gradually decreases. The overall trends of the pressure curves are observed as that the injection pressure initially increases until it reaches a maximum value and then gradually decreases to an almost constant value. The decrease of pressure is caused by the effect of cooling on the rock surrounding the hydraulic fracture since continuously circulating of cold water makes surrounding rock contract and thus generates larger aperture size. From Figure 5.28 and Figure 5.29, it is also demonstrated that the response of the fluid pressure is very sensitive to the mechanical and thermal properties of the rock. Less than 5 μm difference in aperture size causes a fluid pressure change of nearly 5 MPa at the injection well.

The temperature in the left and lower production wells is shown in Figure 5.30 and Figure 5.31, respectively. The simulation using convective heat transfer coefficient of 500 W/(m^2.K) yielded results close to the experimental data.

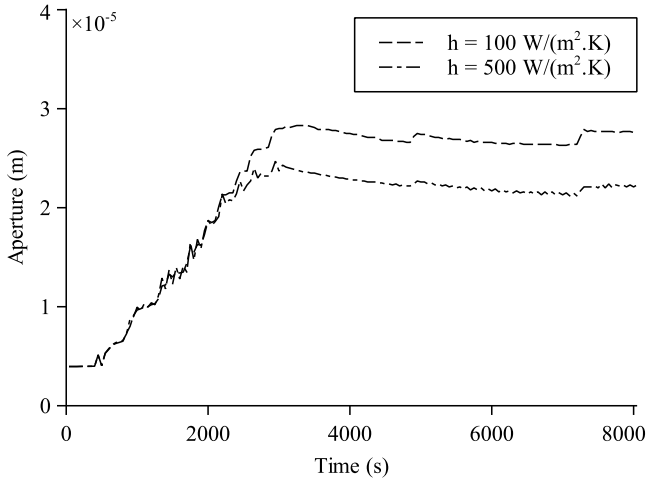

Figure 5.28 Aperture at the injection well plotted as a function of time using convective heat transfer coefficient, *h*, equal to 100 W/(m^2.K) (a) and 500 W/(m^2.K) (b), respectively.

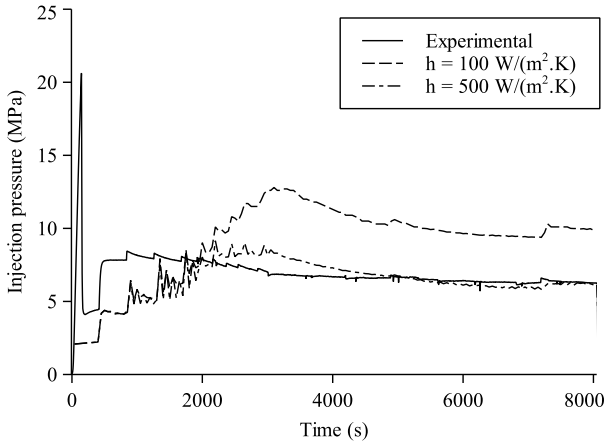

Figure 5.29 Injection pressure plotted as a function of time using convective heat transfer coefficient, *h*, equal to 100 W/(m^2.K) (a) and 500 W/(m^2.K) (b), respectively.

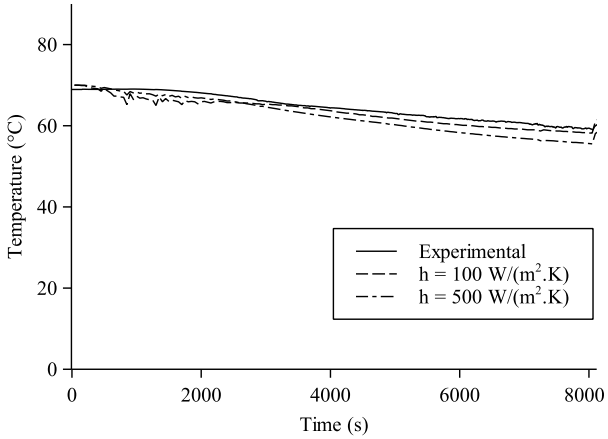

Figure 5.30 Temperature of fluid from the left production well plotted as a function of time using convective heat transfer coefficient, *h*, equal to 100 W/(m^2.K) (a) and 500 W/(m^2.K) (b), respectively.

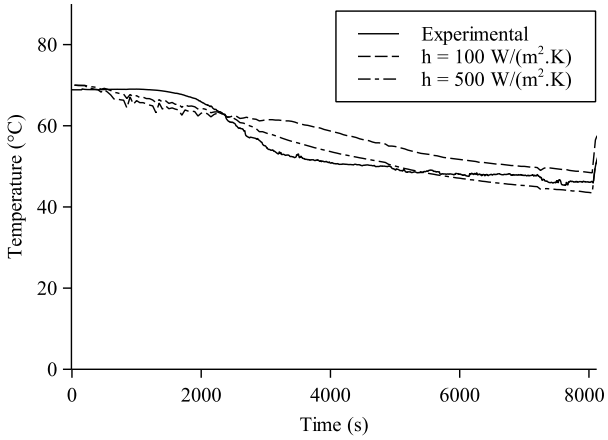

Figure 5.31 Temperature of fluid from the bottom production well plotted as a function of time using convective heat transfer coefficient, *h*, equal to 100 W/(m^2.K) (a) and 500 W/(m^2.K) (b), respectively.

Although the numerical results do not exactly match the experimental data, good agreement has been achieved. The differences in pressure is mostly caused by the near wellbore tortuosity and the complex fracture morphology and roughness which are very difficult to reproduce numerically or even to describe in empirical equations (Zhao and Tso, 1993). Although a range of input parameters might yield similar results, reliable and physically plausible input parameters are confined within a more limited range. For example, the convective heat transfer coefficient could be around 500 W/(m^2.K); however, it could not be close to 10 W/(m^2.K) or 1000 W/(m^2.K) since using these parameters would produce numerical results that vary greatly with the experimental data for reasonable values of other input parameters.

5.7 Conclusions

To simulate the coupled thermo-hydro-mechanical processes in fractured porous media, the governing equations for porous media and discontinuities are given. The mechanical constitutive law of discontinuities is built based on CZM, which can be used to simulate both shear and tensile failures. Fluid flow in discontinuities is governed by the commonly used "cubic law". For heat transport in fractured porous media, the convective heat transfer coefficient, *h*, is introduced; temperature drop is allowed across the interface between fracture and porous

medium. The compressibility effects of the wellbore are also considered by introducing the fluid flow in wellbore. Through temporal and spatial discretization based on finite element method, a 3D fully coupled thermal-hydro-mechanical model for fractured porous media is developed. A special zero-thickness interface element is proposed to simulate the behaviors related to discontinuities. It has degrees of freedom of displacement, fluid pressure and temperature, and can be used to simulate either pre-existing fractures or newly developing fractures. The nonlinear system equations are solved by Newton-Raphson method. Numerical examples are presented to verify and illustrate the application of this model. The initiation and propagation of a KGD hydraulic fracture in 3D domain are studied. The compressibility effects of wellbore are taken into account. Excellent agreements have been achieved through the comparison of numerical results with analytical solutions for the 1D thermo-poroelastic consolidation. The heat transfer between fracture and porous medium is analyzed in detail. It is demonstrated that the convective heat transfer coefficient equal to zero, $h = 0$, corresponds to insulated heat transport in fractures; when it larger than a certain value, the temperature tends to be continuous across the interface between fracture and porous medium. Three lab-scale EGS experiments are studied using the proposed model. The first one investigates the permeability of the tested block sample. Numerical results match well with the experimental data when the permeability used in the simulation is close to that measured in laboratory. The second one investigates the initiation and propagation of the hydraulic fracture in a granite rock block. To model the linear pressurization stage before hydraulic fracture propagation, the wellbore is simulated explicitly through 1D elements. The last one studies the cold water flow through the newly created fracture in a block sample, which is heated to 70 °C. It is found that the responses of the fractured rock sample are very sensitive to mechanical, hydraulic and thermal properties. Two scenarios with h = 100

W/(m^2.K) and h = 500 W/(m^2.K) are considered separately. Numerical results demonstrate that the difference in aperture size at the injection point is less than 5 μm; however, the difference in injection pressure is larger than 5 MPa between the two scenarios.

References

Aboustit, B., Advani, S., Lee, J. et al. 1982. Finite element evaluations of thermo-elastic consolidation. In *The 23rd US Symposium on Rock Mechanics (USRMS)*.

Bai, B. 2005. One-dimensional thermal consolidation characteristics of geotechnical media under non-isothermal condition. *Engineering Mechanics* **22** (5): 186-191.

Barenblatt, G. I. 1962. The Mathematical Theory of Equilibrium Cracks in Brittle Fracture. In *Advances in applied mechanics*, ed. Th von Kármán G. Kuerti F. H. van den Dungen H.L. Dryden and L. Howarth, 55-129. Elsevier.

Beer, G. 1985. An isoparametric joint/interface element for finite element analysis. *International Journal for Numerical Methods in Engineering* **21** (4): 585-600. http://dx.doi.org/10.1002/nme.1620210402.

Bergman, T. L., Lavine, A. S., Incropera, F. P. et al. 2011. *Fundamentals of heat and mass transfer*, seventh edition: John Wiley & Sons.

Biot, M. A. 1941. General theory of three- dimensional consolidation. *Journal of Applied Physics* **12** (2): 155-164.

Booker, J. R. and Savvidou, C. 1984. Consolidation around a spherical heat source. *International Journal of Solids and Structures* **20** (11–12): 1079-1090. http://dx.doi.org/10.1016/0020-7683(84)90091-X.

Booker, J. R. and Savvidou, C. 1985. Consolidation around a point heat source. *International Journal for Numerical and Analytical Methods in Geomechanics* **9** (2): 173-184. http://dx.doi.org/10.1002/nag.1610090206.

Bourgoyne, A. T., Millheim, K. K., Chenevert, M. E. et al. 1991. Applied drilling engineering. Richardson, TX: Society of Petroleum Engineers.

Brooks, A. N. and Hughes, T. J. R. 1982. Streamline upwind/Petrov-Galerkin formulations for convection dominated flows with particular emphasis on the incompressible Navier-Stokes equations. *Computer methods in applied mechanics and engineering* **32** (1–3): 199-259. http://dx.doi.org/10.1016/0045-7825(82)90071-8.

Carslaw, H. S. and Jaeger, J. C. 1959. *Conduction of heat in solids*. Oxford: Clarendon Press, 1959, 2nd ed.

Cerfontaine, B., Dieudonné, A. C., Radu, J. P. et al. 2015. 3D zero-thickness coupled interface finite element: Formulation and application. *Computers and Geotechnics* **69**: 124-140. http://dx.doi.org/10.1016/j.compgeo.2015.04.016.

Cheng, A. H.-D. 2016. *Poroelasticity*. Switzerland: Springer International Publishing.

Cheng, A. H. D., Ghassemi, A. and Detournay, E. 2001. Integral equation solution of heat extraction from a fracture in hot dry rock. *International Journal for Numerical and Analytical Methods in Geomechanics* **25** (13): 1327-1338. http://dx.doi.org/10.1002/nag.182.

Cheng, Q., Wang, X. and Ghassemi, A. 2019. Numerical simulation of reservoir stimulation with reference to the Newberry EGS. *Geothermics* 77: 327-343. https://doi.org/10.1016/j.geothermics.2018.09.011.

Cleary, M. P. 1977. Fundamental solutions for a fluid-saturated porous solid. *International Journal of Solids and Structures* **13** (9): 785-806. http://dx.doi.org/10.1016/0020-7683(77)90065-8.

Codina, R. 1998. Comparison of some finite element methods for solving the diffusion-convection-reaction equation. *Computer methods in applied mechanics and engineering* **156** (1–4): 185-210. http://dx.doi.org/10.1016/S0045-7825(97)00206-5.

Detournay, E. 2004. Propagation Regimes of Fluid-Driven Fractures in Impermeable Rocks. International Journal of Geomechanics 4 (1): 35-45. https://doi.org/10.1061/(ASCE)1532-3641(2004)4:1(35).

Donea, J. and Huerta, A. 2003. *Finite element methods for flow problems*. Chichester: John Wiley & Sons.

Dugdale, D. S. 1960. Yielding of steel sheets containing slits. *Journal of the Mechanics and Physics of Solids* **8** (2): 100-104. http://dx.doi.org/10.1016/0022-5096(60)90013-2.

Gao, Q. and Ghassemi, A. 2016. 3D Thermo-poromechanical Analysis of Reservoir Stimulation Using Damage Mechanics with Application to the Fenton Hill HDR Experiment. Paper presented at the 50th US Rock Mechanics / Geomechanics Symposium, Houston, Texas, USA.

Gao, Q. and Ghassemi, A. 2018. Parallel Finite Element Simulations of 3D Hydraulic Fracture Propagation Using a Coupled Hydro-mechanical Interface Element. Paper presented at the 52nd US Rock Mechanics / Geomechanics Symposium, Seattle, Washington, USA.

Gatmiri, B. and Delage, P. 1997. A formulation of fully coupled thermal–hydraulic–mechanical behaviour of saturated porous media—numerical approach. *International Journal for Numerical and Analytical Methods in Geomechanics* **21** (3): 199-225. http://dx.doi.org/10.1002/(sici)1096-9853(199703)21:3<199::aid-nag865>3.0.co;2-m.

Ge, J. and Ghassemi, A. 2008. Analysis of failure potential around a hydraulic fracture in jointed rock. Paper presented at the The 42nd US Rock Mechanics Symposium (USRMS), San Francisco, California.

Gens, A., Carol, I. and Alonso, E. E. 1990. A constitutive model for rock joints formulation and numerical implementation. *Computers and Geotechnics* **9** (1): 3-20. https://doi.org/10.1016/0266-352X(90)90026-R.

Ghassemi, A. and Zhang, Q. 2004. A transient fictitious stress boundary element method for porothermoelastic media. Engineering Analysis with Boundary Elements 28 (11): 1363-1373. https://doi.org/10.1016/j.enganabound.2004.05.003.

Ghassemi, A. and Zhang, Q. 2006. Porothermoelastic Analysis of the Response of a Stationary Crack Using the Displacement Discontinuity Method. *Journal of Engineering Mechanics* **132** (1): 26-33. http://dx.doi.org/10.1061/(asce)0733-9399(2006)132:1(26).

Ghassemi, A. and Zhou, X. 2011. A three-dimensional thermo-poroelastic model for fracture response to injection/extraction in enhanced geothermal systems. *Geothermics* **40** (1): 39-49. http://dx.doi.org/10.1016/j.geothermics.2010.12.001.

Ghassemi, A., Zhou, X. X. and Rawal, C. 2013. A three-dimensional poroelastic analysis of rock failure around a hydraulic fracture. *Journal of Petroleum Science and Engineering* **108**: 118-127. http://dx.doi.org/10.1016/j.petrol.2013.06.005.

Goodman, R. E., Taylor, R. L. and Brekke, T. L. 1968. A model for the mechanics of jointed rock. *Journal of Soil Mechanics & Foundations Div*.

Gringarten, A. C., Witherspoon, P. A. and Ohnishi, Y. 1975. Theory of heat extraction from fractured hot dry rock. *Journal of Geophysical Research* **80** (8): 1120-1124. http://dx.doi.org/10.1029/JB080i008p01120.

Hillerborg, A., Modéer, M. and Petersson, P.-E. 1976. Analysis of crack formation and crack growth in concrete by means of fracture mechanics and finite elements. *Cement and concrete research* **6** (6): 773-781.

Hu, L. and Ghassemi, A. 2017. Experimental Investigation of Hydraulically Induced Fracture Properties in Enhanced Geothermal Reservoir Stimulation. Paper presented at the 42nd Workshop on Geothermal Reservoir Engineering, Stanford, California, 13-15 February 2017.

Hu, L. and Ghassemi, A. 2018a. Heat and fluid flow characterization of hydraulically induced fracture in Lab-scale. Paper presented at the 52nd US Rock Mechanics / Geomechanics Symposium, Seattle, Washington, USA, 17 20 June 2018.

Hu, L. and Ghassemi, A. 2018b. Lab-scale Investigation of a Multi Well Enhanced Geothermal Reservoir. Paper presented at the 43rd Workshop on Geothermal Reservoir Engineering, Stanford, California, February 12-14, 2018.

Hu, L., Ghassemi, A., Pritchett, J. et al. 2016. Laboratory Scale Investigation of Enhanced Geothermal Reservoir Stimulation. Paper presented at the 50th US Rock Mechanics / Geomechanics Symposium, Houston, Texas, USA, 26-29 June 2016.

Huang, J. and Ghassemi, A. 2015. A poroelastic model for evolution of fractured reservoirs during gas production. *Journal of Petroleum Science and Engineering* 135: 626-644. http://dx.doi.org/10.1016/j.petrol.2015.10.007.

Irwin, G. R. 1957. Analysis of stresses and strains near the end of crack traversing a plate. Journal of applied mechanics 24: 361-364.

Kumar, D. and Ghassemi, A. 2016. A three-dimensional analysis of simultaneous and sequential fracturing of horizontal wells. *Journal of Petroleum Science and Engineering* **146** (Supplement C): 1006-1025. https://doi.org/10.1016/j.petrol.2016.07.001.

Kumar, D. and Ghassemi, A. 2018. Three-Dimensional Poroelastic Modeling of Multiple Hydraulic Fracture Propagation from Horizontal Wells. *International Journal of Rock Mechanics and Mining Sciences* **105**: 192-209. https://doi.org/10.1016/j.ijrmms.2018.01.010.

Kurashige, M. 1989. A thermoelastic theory of fluid-filled porous materials. *International Journal of Solids and Structures* **25** (9): 1039-1052. http://dx.doi.org/10.1016/0020-7683(89)90020-6.

Lauwerier, H. A. 1955. The transport of heat in an oil layer caused by the injection of hot fluid. *Applied Scientific Research, Section A* **5** (2): 145-150. http://dx.doi.org/10.1007/bf03184614.

Lecampion, B. and Desroches, J. 2015. Simultaneous initiation and growth of multiple radial hydraulic fractures from a horizontal wellbore. Journal of the Mechanics and Physics of Solids 82: 235-258. http://dx.doi.org/10.1016/j.jmps.2015.05.010.

Lewis, R. W., Majorana, C. E. and Schrefler, B. A. 1986. A coupled finite element model for the consolidation of nonisothermal elastoplastic porous media. *Transport in Porous Media* **1** (2): 155-178. http://dx.doi.org/10.1007/bf00714690.

Lotfi Hamid, R. and Shing, P. B. 1994. Interface Model Applied to Fracture of Masonry Structures. *Journal of Structural Engineering* **120** (1): 63-80. http://dx.doi.org/10.1061/(asce)0733-9445(1994)120:1(63).

McTigue, D. 1986. Thermoelastic response of fluid- saturated porous rock. *Journal of Geophysical Research: Solid Earth (1978–2012)* **91** (B9): 9533-9542.

McTigue, D. 1990. Flow to a heated borehole in porous, thermoelastic rock: Analysis. *Water Resources Research* **26** (8): 1763-1774.

Moody, L. F. 1944. Friction factors for pipe flow. Trans. ASME 66 (8): 671-684.

Noorishad, J., Ayatollahi, M. S. and Witherspoon, P. A. 1982. A finite-element method for coupled stress and fluid flow analysis in fractured rock masses. *International Journal of*

Rock Mechanics and Mining Sciences & Geomechanics Abstracts **19** (4): 185-193. http://dx.doi.org/10.1016/0148-9062(82)90888-9.

Noorishad, J., Tsang, C. F. and Witherspoon, P. A. 1984. Coupled thermal-hydraulic-mechanical phenomena in saturated fractured porous rocks: Numerical approach. *Journal of Geophysical Research: Solid Earth* **89** (B12): 10365-10373. http://dx.doi.org/10.1029/JB089iB12p10365.

Park, K. and Paulino, G. H. 2012. Computational implementation of the PPR potential-based cohesive model in ABAQUS: Educational perspective. *Engineering Fracture Mechanics* **93** (0): 239-262. http://dx.doi.org/10.1016/j.engfracmech.2012.02.007.

Potts, D. M. and Zdravkovic, L. 1999. *Finite element analysis in geotechnical engineering: theory*, Vol. 1: Thomas Telford.

Rawal, C. and Ghassemi, A. 2014. A reactive thermo-poroelastic analysis of water injection into an enhanced geothermal reservoir. *Geothermics* **50**: 10-23. https://doi.org/10.1016/j.geothermics.2013.05.007.

Rice, J. R. and Cleary, M. P. 1976. Some basic stress diffusion solutions for fluid- saturated elastic porous media with compressible constituents. *Reviews of Geophysics* **14** (2): 227-241.

Rutqvist, J., Wu, Y. S., Tsang, C. F. et al. 2002. A modeling approach for analysis of coupled multiphase fluid flow, heat transfer, and deformation in fractured porous rock. *International Journal of Rock Mechanics and Mining Sciences* **39** (4): 429-442. http://dx.doi.org/10.1016/S1365-1609(02)00022-9.

Safari, R. and Ghassemi, A. 2015. 3D thermo-poroelastic analysis of fracture network deformation and induced micro-seismicity in enhanced geothermal systems. *Geothermics* **58**: 1-14. http://dx.doi.org/10.1016/j.geothermics.2015.06.010.

Schiffman, R. L. 1971. A thermoelastic theory of consolidation. *Environmental and Geophysical Heat Transfer* **4**: 78-84.

Segura, J. M. and Carol, I. 2004. On zero-thickness interface elements for diffusion problems. *International Journal for Numerical and Analytical Methods in Geomechanics* **28** (9): 947-962. http://dx.doi.org/10.1002/nag.358.

Segura, J. M. and Carol, I. 2008. Coupled HM analysis using zero-thickness interface elements with double nodes. Part I: Theoretical model. *International Journal for Numerical and Analytical Methods in Geomechanics* **32** (18): 2083-2101. http://dx.doi.org/10.1002/nag.735.

Sesetty, V. and Ghassemi, A. 2015. A numerical study of sequential and simultaneous hydraulic fracturing in single and multi-lateral horizontal wells. *Journal of Petroleum Science and Engineering* **132**: 65-76. https://dx.doi.org/10.1016/j.petrol.2015.04.020.

Spring, D. W. and Paulino, G. H. 2014. A growing library of three-dimensional cohesive elements for use in ABAQUS. *Engineering Fracture Mechanics* **126** (0): 190-216. http://dx.doi.org/10.1016/j.engfracmech.2014.04.004.

Tao, Q., Ghassemi, A. and Ehlig-Economides, C. A. 2011. A fully coupled method to model fracture permeability change in naturally fractured reservoirs. International Journal of Rock Mechanics and Mining Sciences 48 (2): 259-268. http://dx.doi.org/10.1016/j.ijrmms.2010.11.012.

Vandamme, L. and Curran, J. H. 1989. A three-dimensional hydraulic fracturing simulator. *International Journal for Numerical Methods in Engineering* **28** (4): 909-927. http://dx.doi.org/10.1002/nme.1620280413.

Wang, X. and Ghassemi, A. 2012. A 3D Thermal-Poroelastic Model For Naturally Fractured Geothermal Reservoir Stimulation. Paper ARMA 2012-333 presented at the 46th U.S. Rock Mechanics/Geomechanics Symposium, Chicago, Illinois, 24-27 June.

Wu, R., Bunger, A. P., Jeffrey, R. G. et al. 2008. A comparison of numerical and experimental results of hydraulic fracture growth into a zone of lower confining stress. Paper presented at the The 42nd U.S. Rock Mechanics Symposium (USRMS), San Francisco, California, 29 June - 2 July.

Zhao, J. and Tso, C. P. 1993. Heat transfer by water flow in rock fractures and the application to hot dry rock geothermal systems. *International Journal of Rock Mechanics and Mining Sciences & Geomechanics Abstracts* **30** (6): 633-641. https://doi.org/10.1016/0148-9062(93)91223-6.

Zhao, Z., Jing, L. and Neretnieks, I. 2010. Evaluation of hydrodynamic dispersion parameters in fractured rocks. *Journal of Rock Mechanics and Geotechnical Engineering* **2** (3): 243-254. https://doi.org/10.3724/SP.J.1235.2010.00243.

6 Pore pressure and stress distribution around a hydraulic fracture in heterogeneous rock

Abstract

One of the most significant characteristics of unconventional petroleum bearing formations is their heterogeneity, which affects the stress distribution, hydraulic fracture propagation and also fluid flow. This study focuses on the stress and pore pressure redistributions during hydraulic stimulation in a heterogeneous poroelastic rock. Lognormal random distributions of Young's modulus and permeability are generated to simulate the heterogeneous distributions of material properties. A 3D fully coupled poroelastic model based on the finite element method is presented utilizing a displacement-pressure formulation. In order to verify the model, numerical results are compared with analytical solutions showing excellent agreements. The effects of heterogeneities on stress and pore pressure distributions around a penny-shaped fracture in poroelastic rock are then analyzed. Results indicate that the stress- and pore pressure distributions are more complex in a heterogeneous reservoir than in a homogeneous one. The spatial extent of stress reorientation during hydraulic stimulations is a function of time and is continuously changing due to the diffusion of pore pressure in the heterogeneous system. In contrast to the stress distributions in homogeneous media, irregular distributions of stresses and pore pressure are observed. Due to the change of material properties, shear stresses and nonuniform deformations are generated. The induced shear stresses in heterogeneous rock cause the initial horizontal principal stresses to rotate out of horizontal planes.

6.1 Introduction

Hydraulic fracturing is an essential technology to achieve economic production in unconventional hydrocarbon reservoirs; these include tight gas sands, shale gas and coalbed methane. One of the most significant characteristics of shale source rock is the heterogeneity of reservoir properties, which affect the stress distribution, hydraulic fracture propagation and also fluid flow. However, to our knowledge the impact of heterogeneities on stress and pore pressure distribution around a hydraulic fracture has not been studied. In contrast, the induced stresses around pressurized fractures in an elastic or poroelastic homogeneous medium are well described in the literature (Kumar and Ghassemi 2015; Rawal and Ghassemi 2011; Sesetty and Ghassemi 2015; Warpinski and Branagan 1989).

Vandamme et al. (1989) and Ghassemi and Roegiers (1996) studied 2D and 3D poroelastic effects on hydraulic fracturing. Gordeyev (1993) derived analytical expression for the width of a 3D fracture in homogeneous poroelastic media. Zhou and Ghassemi (2011) used a fully coupled poroelastic displacement discontinuity (DD) method to study the response of a natural fracture in poroelastic media while Ghassemi and Zhou (2011) investigated the impact of thermo-poroelastic effects on fracture width and injection pressure. The transient response of a uniformly pressurized fracture has been quantified by considering a pressurized Griffith crack in poroelastic and thermo-poroelastic media (Detournay and Cheng 1991; Ghassemi and Zhang 2006). Ge and Ghassemi (2008) calculated the injection-induced stress using a thermo-poroelastic model. The potential failure regions around the pressurized fracture were evaluated.

Although extensive work, both theoretical and experimental, has been carried out on fluid flow in heterogeneous porous media (Durlofsky 1991; Guerillot et al. 1990; Warren and Price 1961), analysis of stress and pore pressure distributions in a heterogeneous poroelastic rock is

rarely available. Hydraulic fracturing inevitably alters the stress distribution and fluid flow paths. Investigation of stress redistribution and fluid migration during hydraulic fracturing under heterogeneous reservoir conditions with natural fractures (Safari and Ghassemi 2015; Wang and Ghassemi 2012) will improve our understanding and will help technology development to optimize stimulation design.

The purpose of this study is to provide insight into the influence of heterogeneities in reservoir rock properties on the stress and pore pressure distributions during hydraulic fracturing. The spatial extent of stress-reorientation (horizontal principal stresses rotate a certain degree but less than 90°) and stress-reversal (horizontal principal stresses rotate 90°) are analyzed to illustrate the alteration of in-situ stresses. Sensitivity analyses are performed through variations of material properties which are used to characterize a poroelastic rock, e.g. Biot's effective stress coefficient, Young's modulus, drained- and undrained Poisson's ratios. The drained- and undrained material properties reflect two limiting behaviors of poroelastic rocks. The situation where the applied loads and deformations are slow relative to the time scale of fluid diffusion is called a drained response. The undrained response occurs when the fluid diffusion time scale is too short to allow alterations in the fluid mass content (Rice and Cleary 1976). The drained- and undrained Poisson's ratios are evaluated under drained- and undrained experimental conditions, respectively.

A 3D numerical model based on the finite element method (FEM) is developed and utilized. Numerical solutions are compared with analytical ones developed by Sneddon and Elliot (1946) for a penny shape crack in an infinite, 3D elastic medium. The stress- and pore pressure distributions are illustrated for both homogenous and heterogeneous scenarios.

6.2 Problem description and methodology

6.2.1 Problem description

Usually the information about subsurface rock properties is incomplete. One of the most important problems associated with reservoir characterization is that of determining the nature of heterogeneities that inevitably occur in formations. Theoretical and experimental investigations have provided reasonable descriptions of the physical processes that are involved in hydraulic fracturing. However, the uncertainty about the distributions of natural fractures, in-situ stresses and formation properties such as Young's modulus and permeability, leads to uncertainty in estimating or predicting the stress redistribution and the fluid flow during hydraulic fracturing. In this paper, we investigate the influence of heterogeneous distributions of Young's modulus and permeability on the reservoir rock during hydraulic fracturing. Intact rocks have higher Young's moduli than the rock masses consisting of the same intact materials but with discontinuities such as natural fractures. Also, the permeability of intact rocks is generally much smaller than that of rock masses. Young's modulus and permeability are both affected by the presence of discontinuities and one could establish correlations between the two parameters, however, we consider them as independent.

A challenging aspect of dealing with reservoir heterogeneity is that it is possible to compute behaviors based on specific reservoir heterogeneity and physical models, but it is not possible to specify the in-situ distribution of reservoir heterogeneity (Warren and Price 1961). A simple way to investigate the behavior of hydraulic fracturing in heterogeneous reservoirs is to perform stochastic (Monte Carlo) simulations (Fenton and Griffiths 2008). In this work, we first discuss the generation of random fields of Young's modulus and permeability. Then, the response of each geostatistical realization is simulated using a coupled fluid flow and geomechanical

model. A realization of a random variable is the value generated from a stochastic simulation. Synthetic examples are studied to analyze the linkage between the degree of heterogeneity and the corresponding rock responses in terms of pore pressure and stress distributions.

6.2.2 Generation of random fields

The normal (or Gaussian) distribution is a widely used continuous probability distribution. Its probability density function can be characterized by a mean value μ and a variance σ^2. When the normal distribution is utilized to represent material properties, negative values may be generated (Fenton and Griffiths 2008), which do not have physical meaning. A simple way, commonly adopted in practice, is to use the lognormal distribution.

In our current study, only the Young's modulus and permeability are considered to be spatially random properties and are assumed to follow a log-normal distribution. An exponential semivariogram function $\gamma(L)$ is used to specify the spatial correlation in observations measured at sample locations (Deutsch and Journel 1992),

$$\gamma(L) = C_0\left[1-\exp\left(\frac{-3L}{a}\right)\right] \tag{6.1}$$

where L = lag distance, a = effective range of the variogram, C_0 = sill value. Also, several methods for generating a Gaussian random field, which is completely characterized by the mean and covariance values, can be found in Fenton and Griffiths (2008). To simplify the problem, the heterogeneous fields are assumed to be isotropic, that is, the correlation structure in both the horizontal and vertical directions is assumed to be the same. The assumption of isotropy admittedly has its limitations. Reservoirs often exhibit anisotropic characteristics, but in this study we focus on heterogeneous distributions of material properties. The role of anisotropy in stimulation has been considered by (Sesetty and Ghassemi 2016).

The unconditional Gaussian random field is commonly referred to as spatially correlated random field. A random field that preserves certain known data at specific points is called a conditional random field (Fenton and Griffiths 2008). For unconditional simulations, the mean values of Young's modulus and permeability are constant. The standard deviations are varied to evaluate the effects of input variability on the physical responses of a reservoir. The parameters of the transformed log normal Gaussian random filed are obtained from the following equation (Fenton and Griffiths 2008):

$$\sigma_{\ln}^2 = \ln\left(1+\left(\frac{\sigma}{\mu}\right)^2\right) \tag{6.2}$$

$$\mu_{\ln} = \ln(\mu) - \frac{1}{2}\sigma^2 \tag{6.3}$$

where σ and μ are variance and mean of the normal distribution, σ_{ln} and μ_{ln} are variance and mean for the lognormal distribution.

The actual values are transformed by scaling with respect to the unit-variance Gaussian random field $G(x)$ according to

$$f(x) = \exp(\mu_{\ln} + \sigma_{\ln} G_i) \tag{6.4}$$

where G_i is the value at the ith element of a zero-mean, unit-variance Gaussian random field $G(x)$.

6.2.3 Poroelastic model

The coupled deformation/diffusion processes are characterized by the theory of poroelasticity introduced by Biot (1941). Rice and Cleary (1976) have recast Biot's theory in terms of physical concepts. The equations governing the responses of fluid-infiltrated porous solids are expressed as:

$$2G\varepsilon_{ij} = \sigma_{ij} - \frac{\nu}{1+\nu}\sigma_{kk}\delta_{ij} + \frac{\alpha(1-2\nu)}{1+\nu}p\delta_{ij}$$
$$2G\zeta = \frac{\alpha(1-2\nu)}{1+\nu}\left(\sigma_{kk} + \frac{3}{B}p\right) \tag{6.5}$$

where the indices take the values 1, 2 and 3, and repeated indices imply summation. The constitutive equations are expressed in terms of the total stress σ_{ij}, the pore pressure p, and their respective conjugate quantities, the solid strain ε_{ij} and variation of fluid volume per unit reference pore volume ζ. The basic material constants are: the shear modulus G, the drained- and undrained Poisson's ratios ν and ν_u, and the Biot's effective stress coefficient α. B is the Skempton coefficient:

$$B = \frac{3(\nu_u - \nu)}{\alpha(1-2\nu)(1+\nu_u)} \tag{6.6}$$

Linear poroelastic processes are described by the constitutive equations, Darcy's law, the equilibrium equations and the continuity equations. A set of five material constants, G, ν, ν_u, α and κ are needed to fully characterize a linear isotropic poroelastic system. These equations are combined into field equations in terms of u_i and p which consist of an elasticity equation with a fluid coupling term,

$$G\nabla^2 u_i + \frac{G}{1-2\nu}u_{k,ki} - \alpha p_{,i} = -F_i \tag{6.7}$$

and a diffusion equation with a solid coupling term,

$$\frac{\partial p}{\partial t} - \kappa M\nabla^2 p = -\alpha M\frac{\partial \varepsilon_{kk}}{\partial t} + M\left(\varphi - \kappa f_{i,i}\right) \tag{6.8}$$

where κ is the permeability coefficient, which is equal to k/μ, k is the intrinsic permeability, and μ is the fluid dynamic viscosity, φ is the source density (the rate of injected fluid volume per unit

volume of the porous solid), $f_i = \rho_f g_i$ is the body force per unit volume of fluid, F_i is the body force per unit volume of the bulk material, and M is Biot's Modulus:

$$M = \frac{2G(\nu_u - \nu)}{\alpha^2 (1-2\nu_u)(1-2\nu)} \tag{6.9}$$

The diffusion of pore pressure is coupled with the rate of change of the volumetric strain.

The response of a pressurized fracture can be obtained by superposition of two transient solutions corresponding to two non-zero boundary conditions on the fracture surface (Carter and Booker 1982). These two fundamental loading modes are

Mode 1

$$\begin{aligned} &\sigma_n(x, y, z, t) = -H(t), \\ &p(x, y, z, t) = 0; \end{aligned} \tag{6.10}$$

Mode 2

$$\begin{aligned} &\sigma_n(x, y, z, t) = 0, \\ &p(x, y, z, t) = H(t). \end{aligned} \tag{6.11}$$

where *x, y, z* correspond to the coordinates of the surface of the pressurized fracture, *H(t)* denotes the Heaviside step function. The initial conditions for both modes are stress free and zero pore pressure everywhere. Figure 6.1 illustrates the decomposed boundary conditions.

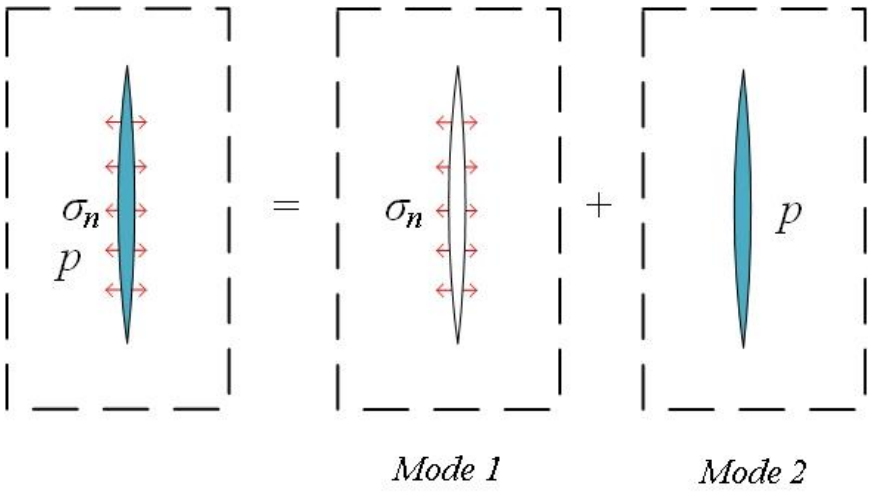

Figure 6.1 Load decomposition for a pressurized fracture in a poroelastic rock: mode 1 (stress loading) is represented by a unit normal stress, σ_n , applied on the fracture surface; mode 2 (pore pressure loading) is represented by a unit pore pressure, p, (equal to σ_n) applied on the fracture surface.

The responses of the model such as stress distribution, pore pressure distribution and aperture opening can be obtained in terms of response functions F_1 and F_2 for modes 1 and 2, respectively (Carter and Booker 1982; Detournay and Cheng 1991). Considering the existence of far-field stress S_0 normal to the fracture surface and pore pressure p_0 (Figure 6.2), the response due to applied constant hydraulic pressure p_f can be found by superposition of the responses of mode 1 and mode 2:

$$F = \left(p_f - S_0\right)F_1 + \left(p_f - p_0\right)F_2 \tag{6.12}$$

Following the Galerkin procedure and neglecting the existence of body forces, Eqs. (6.7) and (6.8) lead to the pair of equilibrium and continuity equations:

$$\begin{aligned} \left[\mathbf{k}_{\mathrm{m}}\right]\{\mathbf{u}\} + \left[\mathbf{c}\right]\{\mathbf{p}_{\mathrm{w}}\} &= \{\mathbf{f}\} \\ \left[\mathbf{c}\right]^{\mathrm{T}}\left\{\frac{\partial \mathbf{u}}{\partial \mathrm{t}}\right\} - \left[\mathbf{k}_{\mathrm{c}}\right]\{\mathbf{p}_{\mathrm{w}}\} - \left[\mathbf{s}\right]\left\{\frac{\partial \mathbf{p}_{\mathrm{w}}}{\partial \mathbf{t}}\right\} &= \mathrm{Q} \end{aligned} \tag{6.13}$$

Linear interpolation in time using the Crank-Nicolson approximation yields:

$$\begin{bmatrix} \mathbf{k}_{\mathrm{m}} & \mathbf{c} \\ \mathbf{c}^{\mathrm{T}} & -\left(\mathbf{s}+\theta\Delta \mathrm{t}\mathbf{k}_{\mathrm{c}}\right) \end{bmatrix} \begin{Bmatrix} \Delta\mathbf{u} \\ \Delta\mathbf{p} \end{Bmatrix} = \begin{Bmatrix} \Delta\mathbf{f} \\ \Delta \mathrm{Q}+\Delta \mathrm{t}\mathbf{k}_{\mathbf{c}}\mathbf{p}_{\mathrm{t_{n-1}}} \end{Bmatrix} \tag{6.14}$$

In which **u** and **p** are the vectors of the nodal displacements and nodal pore pressure. θ is the Crank-Nicolson approximation parameter, which is set to be 1 in this study so that the discretized equations are unconditional stable and numerical oscillations can be smoothed out (Smith and Griffiths 2004). Δt is the time step. $\Delta\mathbf{f}$ is the applied external force on nodes. ΔQ is the source/sink term. $\mathbf{p}_{\mathrm{tn-1}}$ is the nodal pore pressure component from the previous time step. Other matrices are presented as follows:

$$\begin{aligned} \mathbf{k}_{\mathrm{m}} &= \int B^{T} DB dV \\ \mathbf{c} &= \int B^{T} \alpha m N_{p} dV \\ \mathbf{s} &= \int {N_{p}}^{T} \frac{1}{M} N_{p} dV \\ \mathbf{k}_{\mathrm{c}} &= \int \left(\nabla N_{p}\right)^{T} \kappa \left(\nabla N_{p}\right) dV \end{aligned} \tag{6.15}$$

where [D] is the material elastic matrix, [B] is the strain-displacement matrix, and $m = [1,1,1,0,0,0]^{\mathrm{T}}$, $[\mathrm{N_p}]$ is the shape function for pore pressure.

6.3 Model verification

A penny-shaped fracture under uniform pressurization in 3D domain is considered (Figure 6.2). With appropriate change of the minor to major axis ratio, an elliptic fracture or Griffith crack can be modeled. A uniform compressive stress and pore pressure field is initially assumed in the entire poroelastic domain. The initial minimum horizontal stress S_{hmin} is normal to the fracture surface. The initial pore pressure is p_0. At time $t = 0$, a constant pressure p_f is applied on the surface of fracture with a magnitude larger than S_{hmin}. The pressurized boundary of the fracture wall is decomposed into two non-zero boundary conditions as mentioned before.

To verify the poroelastic model, a fully loaded mode 1 penny shaped fracture is modeled. The short- and long-term asymptotic profiles of the fracture aperture can be obtained according to the elastic solution (Sneddon 1946):

$$w(r) = \frac{2p_{net}(1-\nu)R}{\pi G}\sqrt{1-\left(\frac{r}{R}\right)^2} \tag{6.16}$$

where p_{net} is the net pressure, which is defined as the treatment pressure minus the in-situ minimum principal stress, equal to p_f - S_{hmin}, R the radius of the fracture, ν Poisson's ratio, G shear modulus, $w(r)$ fracture half width, and r radial coordinate. Substituting undrained and drained Poisson's ratio into the above equation, the short- and long-term aperture profiles can be found. The short- and long-term responses give the bounding limits of the transient responses of the pressurized fracture (Rice and Cleary 1976). For the short-term ($t \approx 0$) response, a poroelastic medium behaviors as an elastic material with the same shear modulus G and undrained Poisson's ratio ν_u. The long-term ($t = \infty$) response is represented by an elastic response with the drained Poisson's ratio ν.

Figure 6.3 shows the mode 1 (stress loading) transient fracture opening profiles. Dimensionless time $t^* = ct/R^2$ is used for transient evolution of the fracture profile. For comparison, an elastic FEM simulation using a drained Poisson's ratio is also included. As illustrated in the figure, the FEM poroelastic results approach these asymptotic limits (short- and long-term responses). The long-term poroelastic results overlap with the elastic solution using drained Poisson's ratio. A single curve is formed when each of the fracture profiles is normalized by their maximum values (Figure 6.4). The transient poroelastic responses of the pressurized fracture agree well with the asymptotic solutions calculated based on Eq. (6.16), which verifies the applicability of the presented poroelastic model and its corresponding FEM implementation.

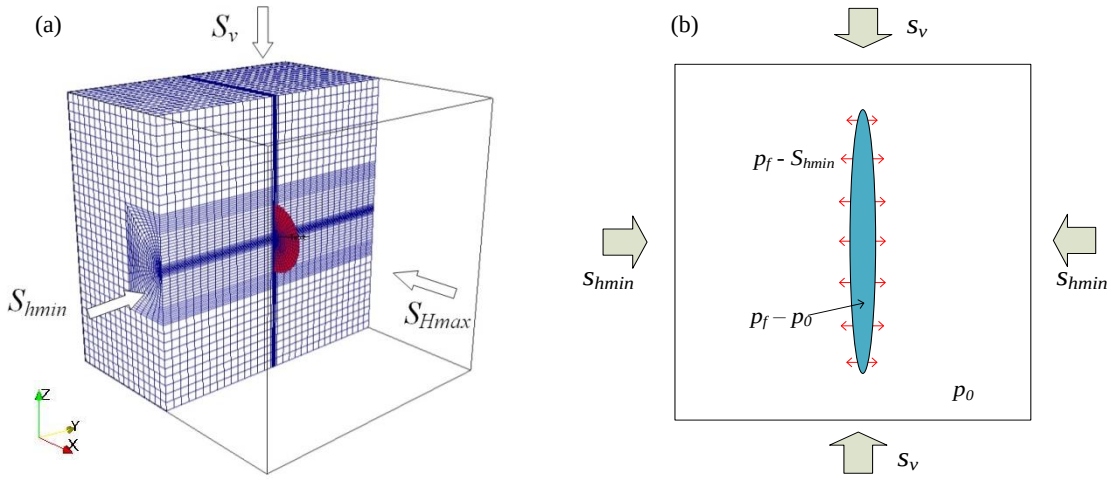

Figure 6.2 A 3D mesh for the numerical simulation domain: (a) Side view of the domain interior showing the circular fracture in red; (b) boundary conditions for the pressurized fracture in (a) showing a vertical section in the YZ-plane.

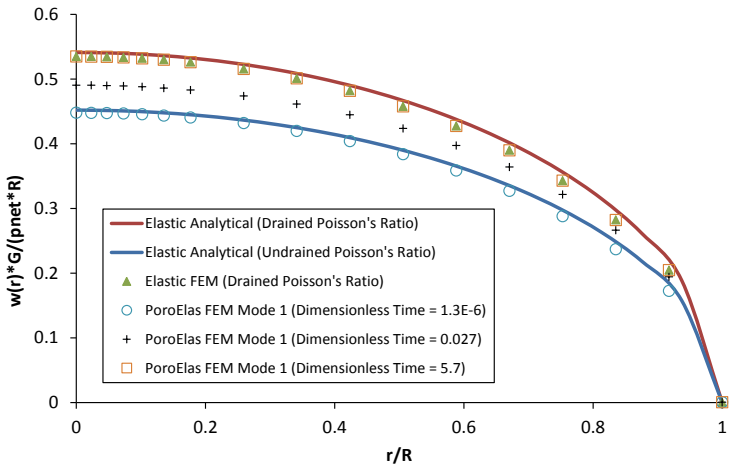

Figure 6.3 Fracture width vs. radial distance for a penny-shaped fracture under mode 1 (or stress) loading. Comparison of numerical and analytical results for elastic and poroelastic cases. The very short time poroelastic results correspond to undrained rock response. The long term poroelastic results correspond to drained response which equal that of a purely elastic rock.

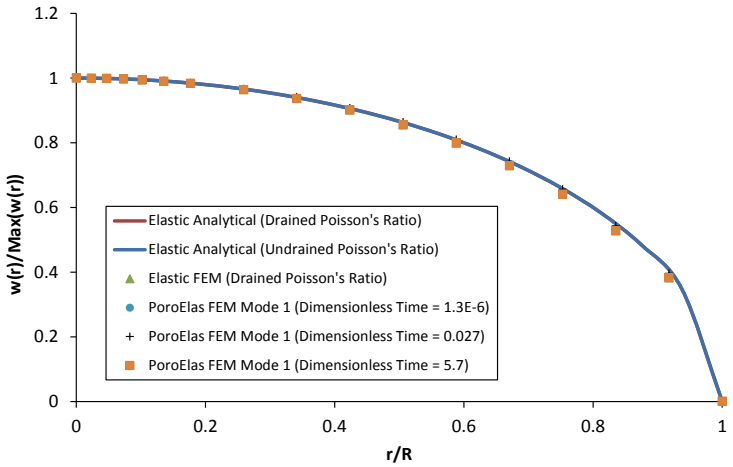

Figure 6.4 Normalized mode 1 fracture width vs. radial distance for a penny-shaped fracture. The profile of the normalized fracture aperture is independent of time and material properties.

6.4 Numerical simulations

In the following sections, the total response of the poroelastic model is found by a linear combination of the responses of mode 1 (stress loading) and mode 2 (pore pressure loading) according to Eq. (6.12). Homogeneous elastic properties are first considered. Then the analysis is extended to more general heterogeneous scenarios.

6.4.1 Homogeneous case

The opening of the fracture and the poroelastic effects during hydraulic stimulation induce stresses around the stimulated region (Ghassemi et al. 2013; Rawal and Ghassemi 2011; Safari and Ghassemi 2015). Consider that a penny-shaped fracture in a rock with mechanical properties of Weber sandstone (Rice and Cleary 1976) is uniformly pressurized. The radius of the fracture is 80 m and the basic input parameters for the homogeneous case are listed in Table 6.1. We assume the stress gradients are 1.0 psi/ft for S_v, 0.8 psi/ft for S_{Hmax}, 0.7 psi/ft for S_{hmin}, and the fluid pressure gradient is 0.433 psi/ft, yielding the values listed in Table 6.1 for a depth of 6000 ft.

Figure 6.5 illustrates the induced total stress and pore pressure distributions along a line (OA) perpendicular to the fracture surface passing through the center of the fracture. On the

fracture surface, the fluid pressure (P_f) is kept at 36 MPa; the induced fluid pressure ($\Delta P = P_f - P_0$) is 18 MPa, based on the assumption that $P_f = P_{net} + S_{hmin}$ on the fracture surface; The induced minimum horizontal stress (ΔS_{yy}) is maintained at 7 MPa, which is equal to the applied net pressure. At the beginning of pressurization (t = 0.02 s and t = 7 mins), the induced pore pressure (ΔP) is larger than the induced horizontal and vertical stresses (ΔS_{xx}, ΔS_{yy}, and ΔS_{zz}) on the fracture surface; the induced pore pressure (ΔP) is less than the induced minimum horizontal stress (ΔS_{yy}) from where L/R > 0.4. As time goes by, the pore pressure gradually diffuses further into the formation. When t = 24 hours, the induced pore pressure is larger than the induced horizontal and vertical stresses (ΔS_{xx}, ΔS_{yy}, and ΔS_{zz}) in the entire numerical domain.

Table 6.1 Basic input parameters for the homogeneous case.

Geometry of models	640×800×640 m (length/width/height)
Poisson's ratio, v	0.15
Undrained Poisson's ratio, v_u	0.29
Biot's effective stress coefficient, α	0.7
Young's modulus, E (Homogeneous Case)	2.76×10^{10}Pa
Permeability (Homogeneous Case), k	5.0 md
Fluid dynamic viscosity, μ	2.0×10^{-4} Pa.s
Initial stress state:	
Vertical stress, S_v	41MPa
Max. Hori. Stress, S_{Hmax}	33MPa
Min. Hori. Stress, S_{hmin}	29MPa
Initial pore pressure, P_0	18MPa
Net pressure, P_f - S_{hmin}	7MPa

The shear stresses are shown in Figure 6.6, and are close to zero in the homogeneous poroelastic rock during the entire process of pressurization. The oscillations in Figure 6.6(b) and Figure 6.6(c) are of the magnitude of 10^{-13} MPa, and can be considered as numerical error.

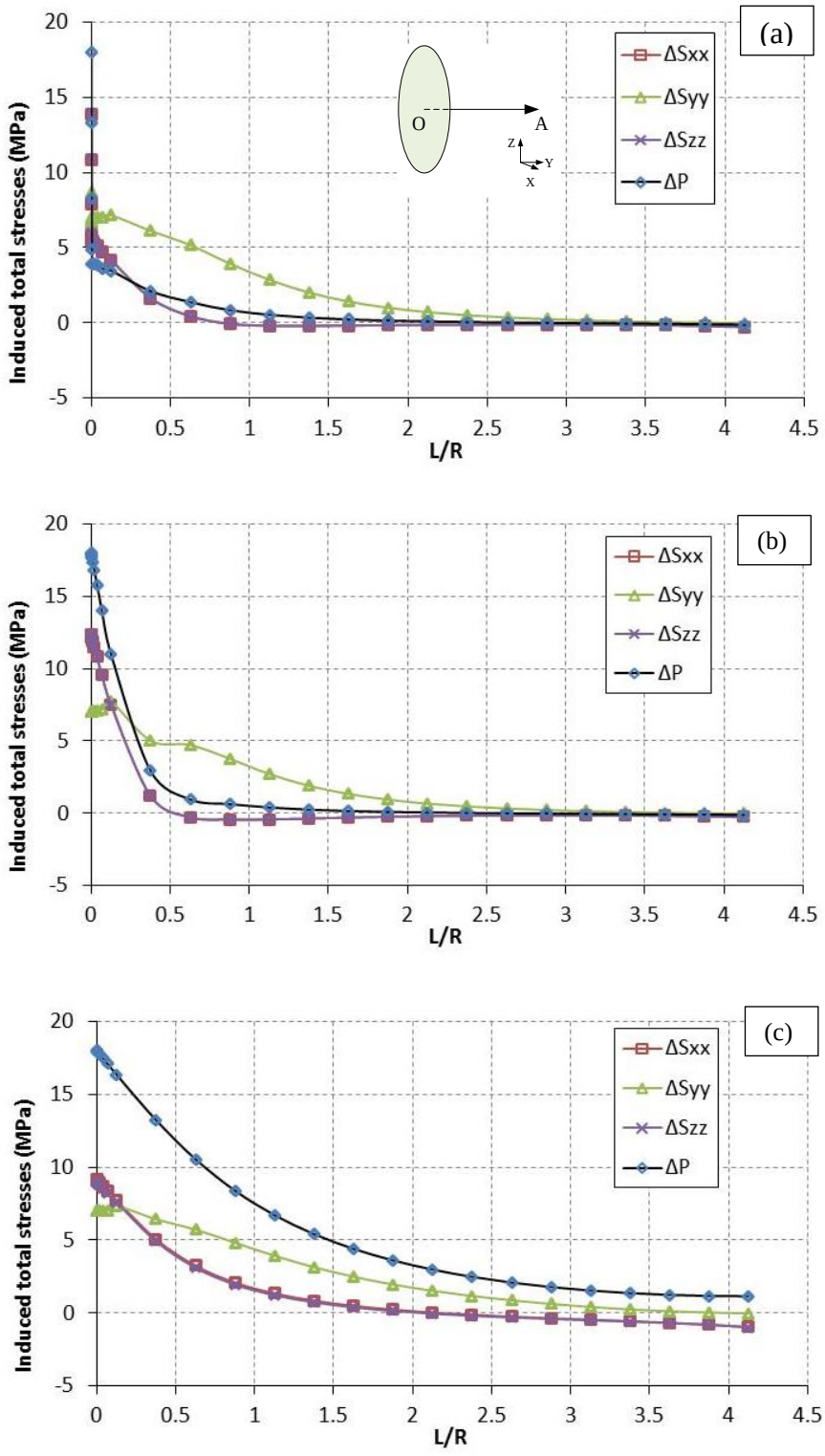

Figure 6.5 Induced total (sum of mode 1 and mode 2) stresses and pore pressure along a line (OA) (top figure) perpendicular to the fracture surface, passing through the center of the fracture: (a) *t* = 0.02s; (b) *t* = 7 mins; (c) *t* = 24 hrs.

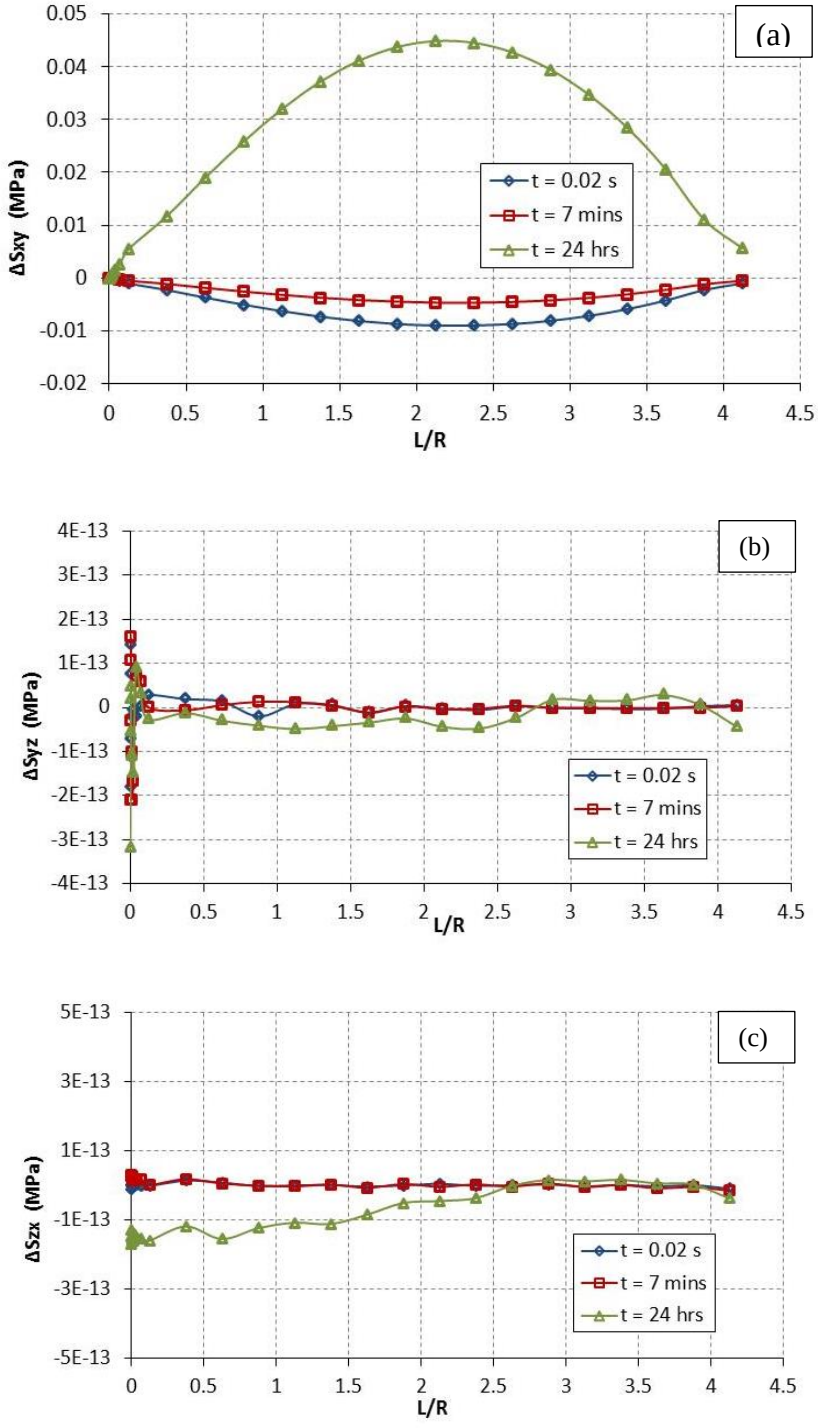

Figure 6.6 Induced (total) shear stresses along the line OA (see the top of Figure 6.5) perpendicular to the fracture surface passing through the center of the fracture: (a) ΔS_{xy}; (b) ΔS_{yz}; (c) ΔS_{zx}.

Figure 6.7 illustrates the orientations of the minimum principal stresses at t = 7 mins and t = 24 hours. Black lines indicate the directions of the minimum principal stress at points within the domain. The color contour represents the rotation angle of the minimum principal stresses from their original orientations and is symmetric to the pressurized fracture (due to the symmetric boundary conditions adopted here). As can be seen, stress-reversal regions, where the minimum principal stresses rotate 90°, exist at t = 7 mins in the areas extended away from the fracture surface. This phenomenon is consistent with Figure 6.5b, and will be analyzed in the Discussion section. After 24 hours of pressurization, no stress-reversal regions exist. The maximum rotation angle is around 30°. The regions with relatively a large rotation angle are close to the fracture tips where the stress singularity exists.

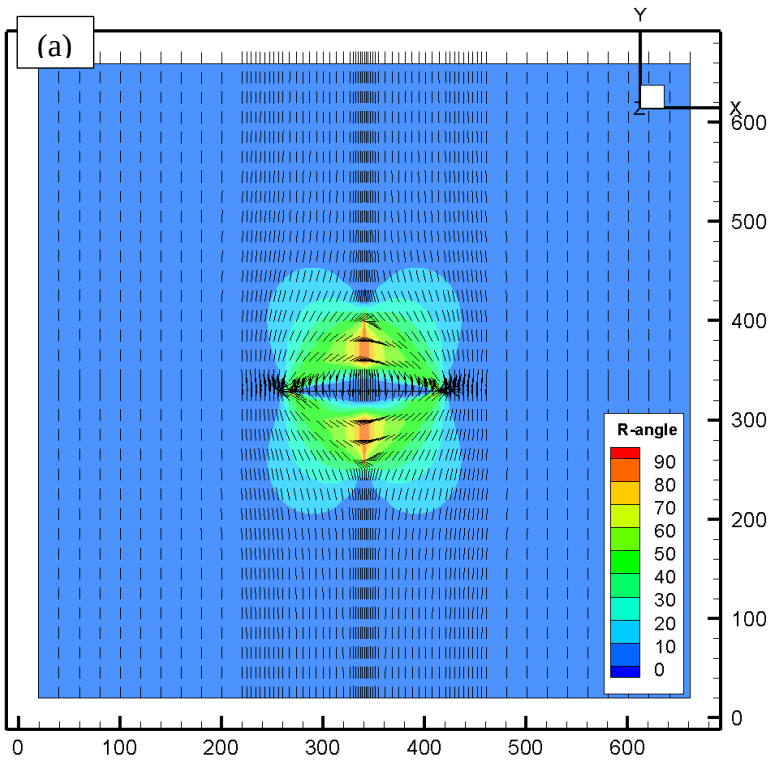

Figure 6.7 Symmetrical distributions of reorientation angle (R-angle) of the minimum principal stress in a plane cut through the center of the fracture (the central plane parallel to the XY plane in Figure 6.2): (a) t = 7 mins; (b) t = 24 hours. The small dashes indicate the orientation of the minimum principal stress at those locations. (continued)

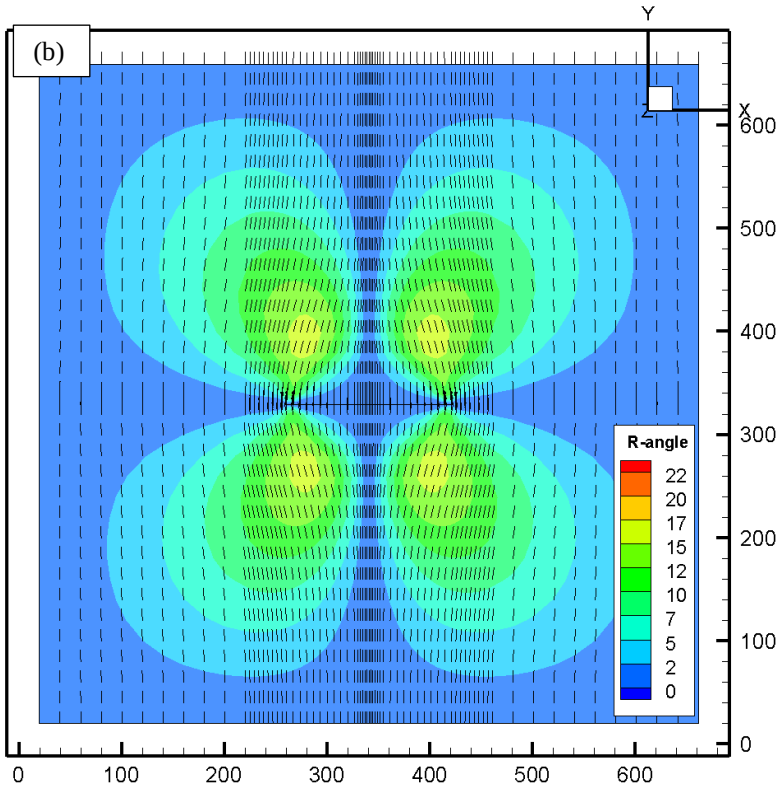

Figure 6.7 (continued). (Caption shown on previous page.)

As can be seen from Figure 6.5, the induced stress component in the *y*-direction (direction of the initial minimum horizontal stress) is always larger than the component in the *x*-direction (direction of the initial maximum horizontal stress) and the extent of the region of stress-reorientation and stress-reversal (stress-reversal indicates that the principal stresses rotate 90°) largely depends on the initial in-situ stress contrast and the applied net pressure. When the initial in-situ stress contrast ($S_{xx} - S_{yy}$) is larger than the generated stress contrast ($\Delta S_{yy} - \Delta S_{xx}$), which is a function of net pressure, the minimum principal stress is still in the *y*-direction and there is no stress-reversal in the vicinity of the fracture surfaces. However, a reoriented-stress region exists around the fracture tips. The generated stress contrast ($\Delta S_{yy} - \Delta S_{xx}$) is shown in Figure 6.8. The red dashed line in Fig. 8 indicates the initial in-situ stress contrast ($S_{xx} - S_{yy}$). At t = 0.02 s and 7 mins, we have ($\Delta S_{yy} - \Delta S_{xx}$) > ($S_{xx} - S_{yy}$), so stress-reversal regions exist in areas

extending away from the fracture surface (Figure 6.7a). At t = 24 hours, there are no stress-reversal regions (($\Delta S_{yy} - \Delta S_{xx}$) < ($S_{xx} - S_{yy}$)) as pore pressure diffuses further into the formation. The stress-reversal phenomenon is discussed further in the Discussion section.

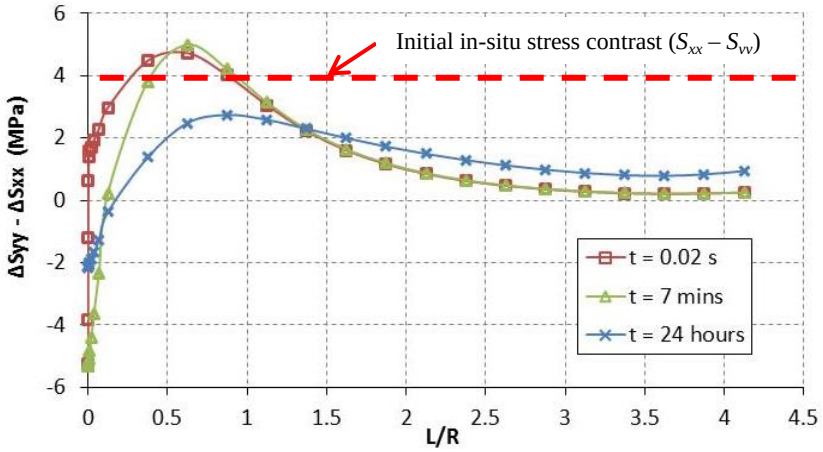

Figure 6.8 Generated stress contrast ($\Delta S_{yy} - \Delta S_{xx}$) at different pressurization time along the line OA (see the top of Figure 6.5) through the center of the fracture and perpendicular to it (homogeneous rock scenario).

6.4.2 Heterogeneous case

As mentioned before, five material constants are needed to fully characterize a linear isotropic poroelastic system. In this work, we use E, v, v_u, α and κ for this purpose. Each of these parameters and their combinations can be considered as randomly distributed variables in the poroelastic model. As we know, flooding a porous rock will cause it to expand. When the expansion is constrained, a confining pressure is generated as a function of α and v (Cheng et al. 1993; Engelder and Fischer 1994). Thus, nonuniform distributions of α and v can generate heterogeneous stress fields. Also, the variation of Young's modulus alters the stiffness matrix in stress-strain relationship so the calculated stresses also experience alterations. The long-time response ($t = \infty$) of a poroelastic rock is similar to the response of an elastic material with drained Young's modulus and Poisson's ratio. The undrained moduli control the rock behavior during short times ($t \approx 0$).

To illustrate the influence of heterogeneity, example simulations using Young's modulus and permeability as random variables are presented and discussed in detail. The same procedure could be used with other parameters treated as random variables. Log normal distribution is adopted here. Statistical values for the assumed random variables are presented in Table 6.2. Figure 6.9 and Figure 6.10 show the 3D random distributions of the Young's modulus and permeability, respectively.

Table 6.2 Statistical values for the assumed random variables.

	Young's modulus (Pa)	Permeability (md)
Input Data		
Mean value	2.76E+10	5.00
Variation value	5.52E+09	1.00
Output Data		
Arithmetic average	2.74E+10	4.95
Geometric average	2.71E+10	4.90
Harmonic average	2.67E+10	4.84
Max. value	4.87E+10	8.83
Min. value	1.42E+10	2.57

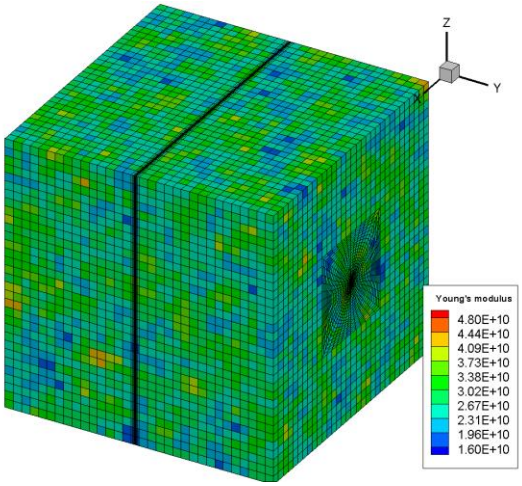

Figure 6.9 Random distribution of Young's modulus (Pa).

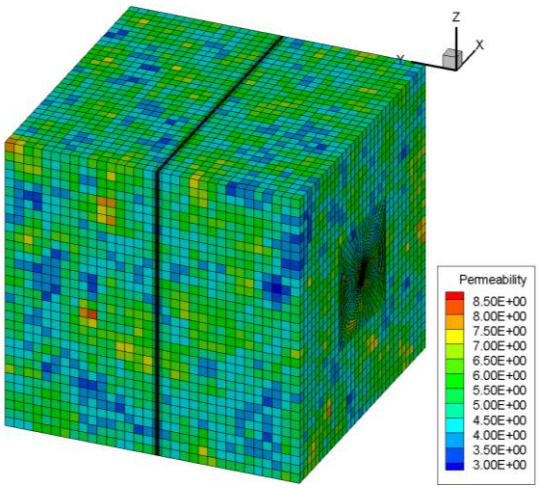

Figure 6.10 Random distribution of permeability (md).

Figure 6.11 illustrates the induced total stresses and pore pressure along a line perpendicular to the fracture surface, passing through the center of the fracture. Comparison with Figure 6.5 shows that the normal stresses in heterogeneous rock (Young's modulus and permeability heterogeneity) have almost the same distributions as those in homogeneous rock. The shear stresses are given in Figure 6.12. As can be seen, they are one order of magnitude larger than those in the homogeneous case. When the shear stress components (S_{xy}, S_{yz}, S_{zx}) are negligible compared to normal stresses components (S_{xx}, S_{yy}, S_{zz}), the normal stresses are also principal stresses. In the heterogeneous case, the induced shear stresses cause the directions of local principal stresses to become heterogeneous (see the reorientation of the minimum principal stress (Figure 6.13)). In the homogeneous case, the deformation of the model is uniform so no shear stresses (or very small shear stresses) are generated. The shear stresses are generated primarily where different materials come into contact (material interfaces). The higher the contrast of material properties along the interface, the larger the generated shear stresses. We will discuss these phenomena in the following section. In addition, the fluctuation of shear stresses is a function of time and is thus related to the diffusion of pore pressure. This is shown in Figure 6.12 for shear stresses at t = 0.02 s, t = 7 min and t = 24 hours, respectively.

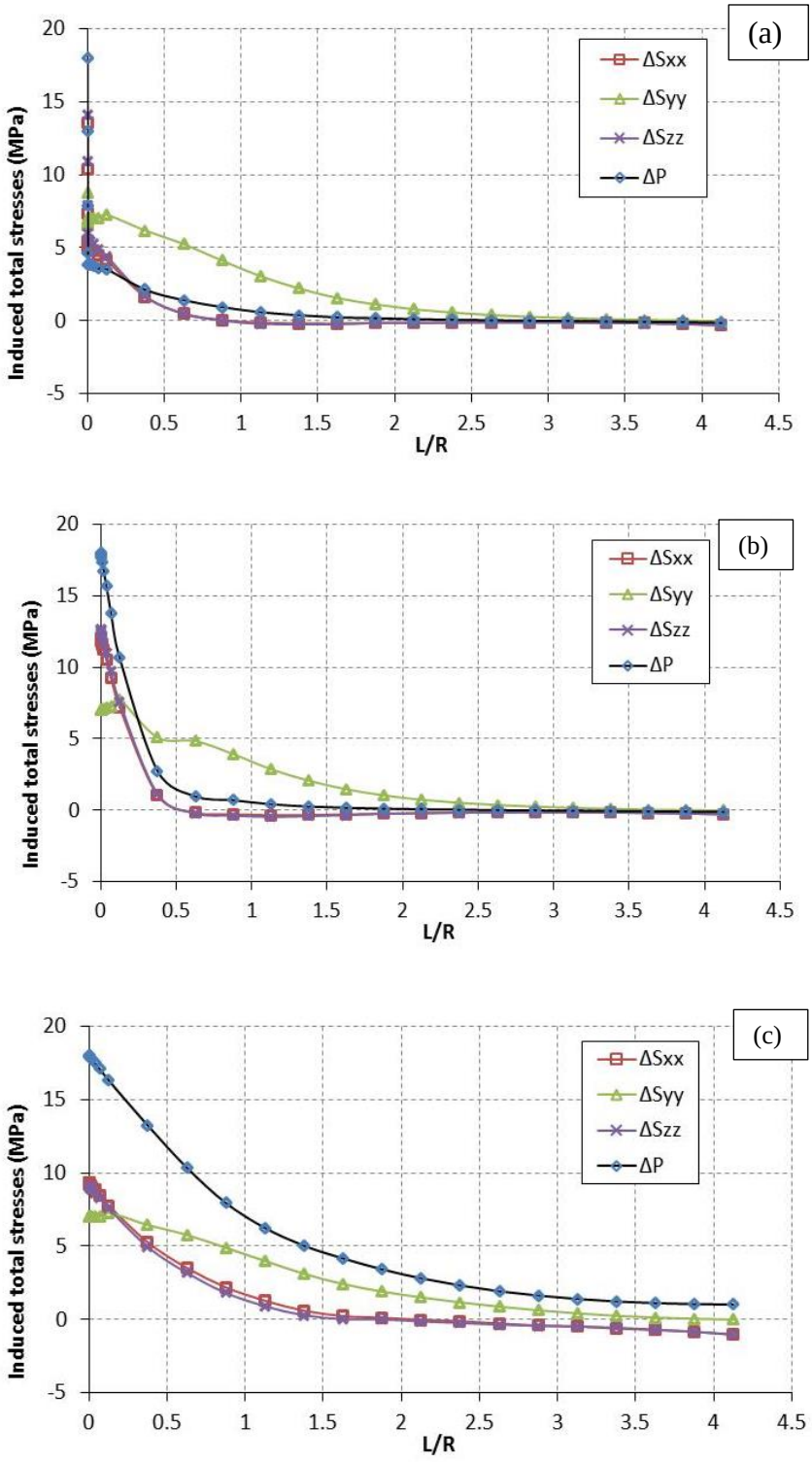

Figure 6.11 Induced total stresses and pore pressure along the line OA (see the top of Figure 5) perpendicular to the fracture surface, passing through the center of the fracture, for the heterogeneous case: (a) *t* = 0.02s; (b) *t* = 7 mins; (c) *t* = 24 hrs.

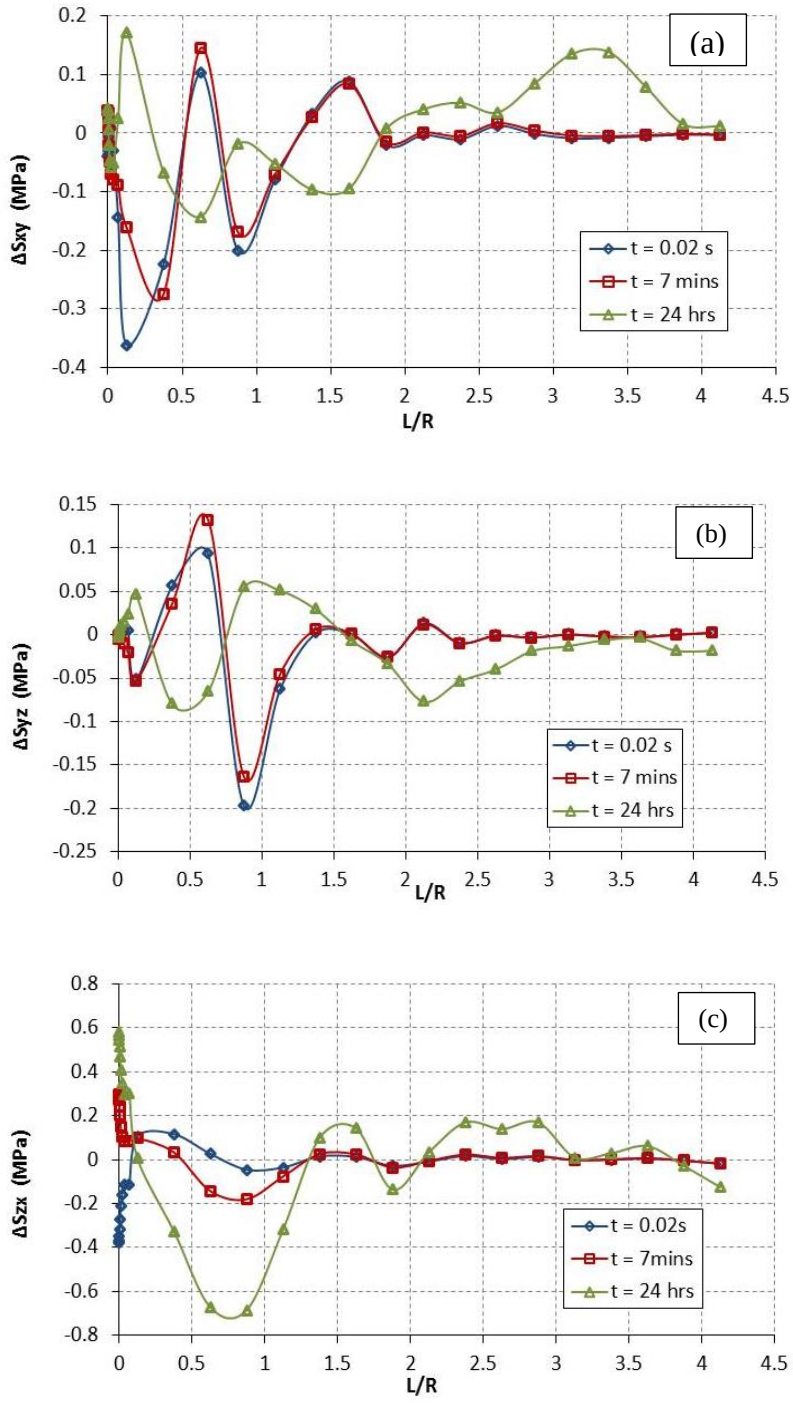

Figure 6.12 Variation of induced shear stresses along the line OA (see the top of Figure 6.5) perpendicular to the fracture surface, passing through the center of the fracture, for the heterogeneous case: (a) S_{xy}; (b) S_{yz}; (c) S_{zx}.

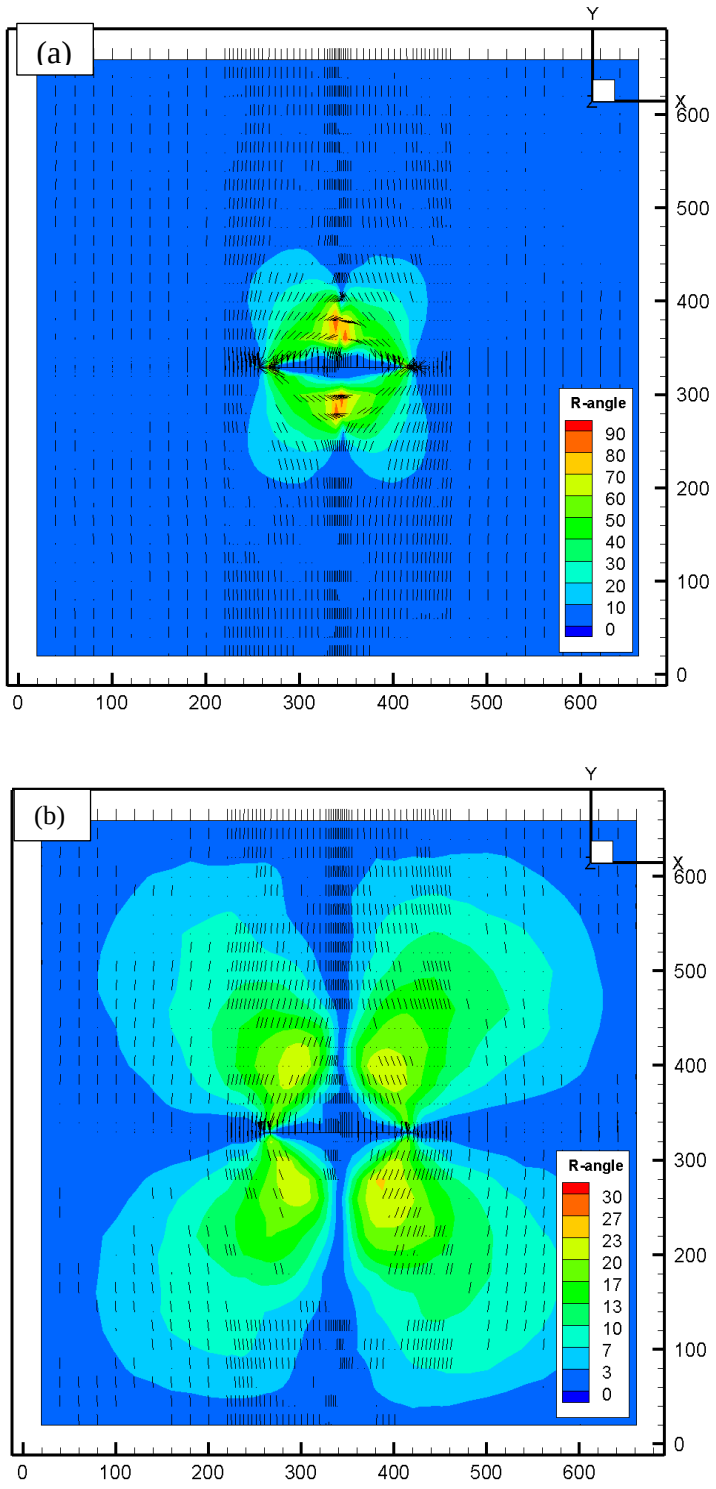

Figure 6.13 Unsymmetrical distributions of reorientation angle (R-angle) of the minimum principal stress for the heterogeneous medium from a top view slice cutting through the center of the fracture: (a) *t* = 7 mins; (b) *t* = 24 hours.

Initially, the minimum principal stress is the horizontal stress (S_{yy}). The black lines in Figure 6.13 show the directions of the minimum principal stresses located in a horizontal plane. After applying hydraulic pressure to the fracture surfaces, we can observe that some regions of the horizontal plane do not have black lines. This indicates that in certain areas the minimum principal stresses are no longer horizontal. In the homogeneous case, the minimum principal stresses remain in the horizontal direction everywhere, although they rotate by a certain angle depending on the position with respect to the pressurized fracture (Figure 6.7). The contours in Figure 6.13 illustrate the rotation angle of minimum principal stresses in the horizontal plane. The value of the rotation angle has a complex distribution and is not symmetric with respect to the pressurized fracture. The rotation angle gradually decreases as time elapses, due to the diffusion of pore pressure into the formation, which causes the induced stress-contrast ($\Delta S_{yy} - \Delta S_{xx}$) to gradually decrease as shown in Figure 6.8.

6.5 Discussion

The importance of understanding stress redistributions during hydraulic stimulation lies in the fact that stresses predominantly control the fracture propagation. Much effort has been devoted to the analyses of stress redistribution around a hydraulic fracture based on the assumption of homogeneous rock properties, ignoring the inherently heterogeneous nature of unconventional reservoirs. As has been demonstrated in previous sections, stress redistributions (magnitude and direction) in heterogeneous poroelastic rocks are much different from those in homogeneous systems. Although the normal stress components in the two different cases are nearly the same, the shear stresses are larger and are non-uniformly distributed in the heterogeneous case (Figure 6.12). The reasons for the observed trends can be explained using a relatively simple simulation as described below.

6.5.1 *Influence of Young's modulus*

Consider a 1.2m x 1.2m x 1.2m cube of rock as shown in Figure 6.14. An interior cubical sub-region of size 0.6 m × 0.4 m × 0.6 m (interior zone) is considered to have poroelastic properties different from the rest of the larger cube (exterior zone). Then, the left side of the cube is subjected to a fluid pressure of 36 MPa with the traction acting in the y-direction (Figure 6.14b). The solid and fluid displacements are set to zero on all other boundaries. The whole simulation domain is divided into cubic elements of size 0.1 m (Figure 6.14). The material properties used for the exterior elements are the same as those used in the homogeneous case (Table 6.1) while the properties of the interior zone are varied and the resulting stress and pore pressure distributions are simulated. To evaluate the influence of Young's modulus on the resulting stresses, we lower the elastic properties of the interior cubical sub-region during different simulation runs such that the Young's modulus ranges from an initial base case value of 2.76×10^{10} Pa, to 90%, 70%, 50%, 30% and 10% of the base case value. For the elements in the exterior zone, the Young's modulus is kept at the initial value.

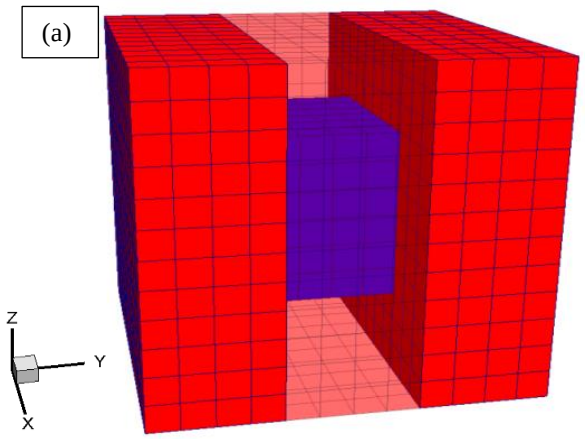

Figure 6.14 (a) A 3D model of a simple heterogeneous system showing a cube of rock with an interior zone having different properties than the rest of the body. Elements with different Young's moduli are shown in purple (interior zone). Red color indicates the exterior zone; (b) A section of the 3D model showing the central section parallel to the yz-plane and the boundary conditions. (continued)

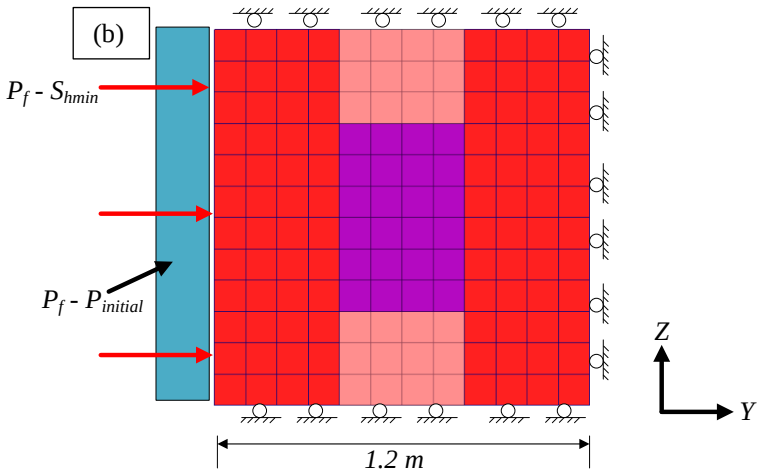

Figure 6.14 (continued). (Caption shown on previous page.)

The following results are obtained at t = 7 min (the small model reaches steady state after 7 minutes of pressurization with a uniform pore pressure of 36 MPa). Figure 6.15 shows the displacements in the *x*- and *y*-direction on the central horizontal plane. In the case shown, the Young's modulus of the elements in the central part (marked by the red dashed lines) is 50% of that for the surrounding elements providing for a larger mode 2 response (dilation) in the interior zone. As expected, the displacement field (and strain) is not uniform. The elements with a lower Young's modulus tend to contract more in the x-direction (due to the system dilation in the y-direction in response to the pore pressure increase). The same phenomenon exists for displacement in the *xz*-plane because the material properties are symmetrically distributed (with respect to the *y*-axis).

Figure 6.16 shows the distribution of induced shear stresses ΔS_{xy} on two orthogonal planes. Induced shear stresses, ΔS_{xy}, are observed at the interface separating zones with different Young's modulus.

A sensitivity analyses on the effects of Young's modulus is presented next. Six different scenarios are considered. In the base case the same Young's modulus values are assigned to the exterior and interior zones. In the other five scenarios, the interior zone has a Young's modulus

equal to 10%, 30%, 50%, 70% and 90% of the base case. The induced total normal- and shear stresses along the line yy' (illustrated in Figure 6.16) are presented in Figure 6.17 and Figure 6.18, respectively.

The elements with smaller Young's modulus are located from 0.4 m to 0.8 m along the line yy'. The induced stress components ΔS_{xx}, ΔS_{yy} and ΔS_{zz} show variations between y = 0.4 m and 0.8 m. The maximum variations for ΔS_{xx}, ΔS_{yy} and ΔS_{zz} are 0.7 MPa, 0.6MPa and 1 MPa, respectively. Because of the change of Young's modulus at these locations, the deformation is nonuniform (Figure 6.15 and Figure 6.19**)**. The magnitudes of the variations are usually less than 1 MPa, even for the extreme scenario ($E_{weak}/E_{original}$ = 0.1), which are rather small when compared with their values in the base case.

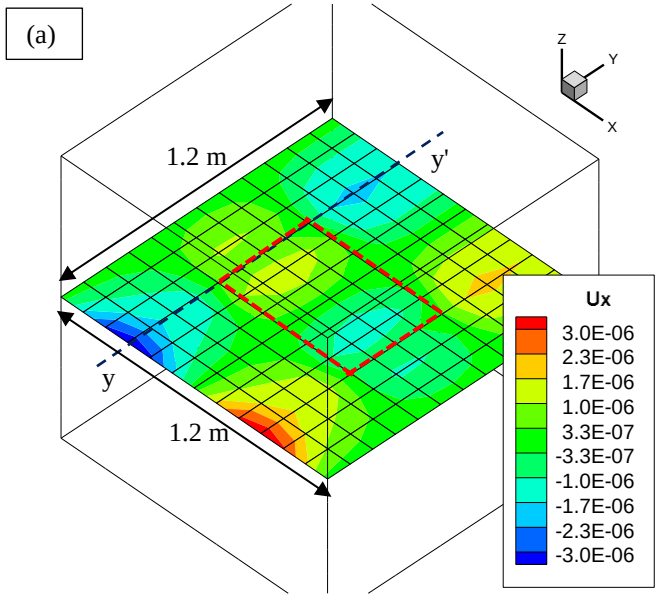

Figure 6.15 Displacements in *x*- and *y*-direction on a central horizontal plane: (a) displacement in *x*-direction; (b) displacement in *y*-direction. (Area encircled by red dash lines has 50% of initial Young's module.) (Unit: m). (continued)

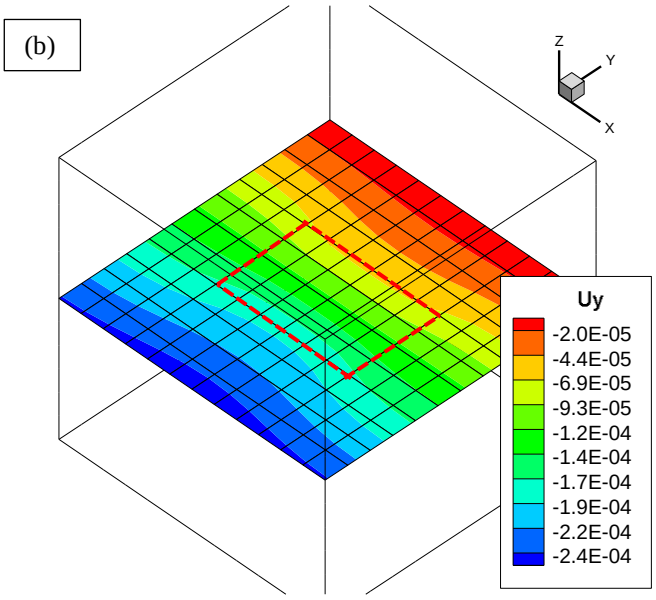

Figure 6.15 (continued). (Caption shown on previous page.)

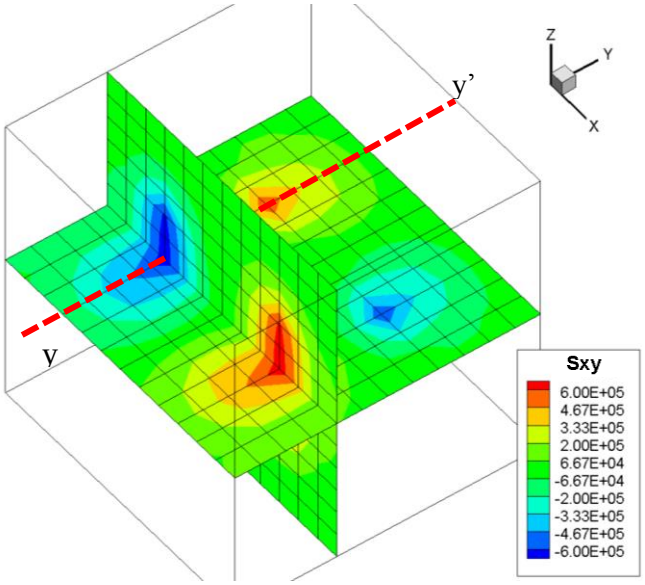

Figure 6.16 Distribution of ΔS_{xy} on two orthogonal slices. (Unit: Pa).

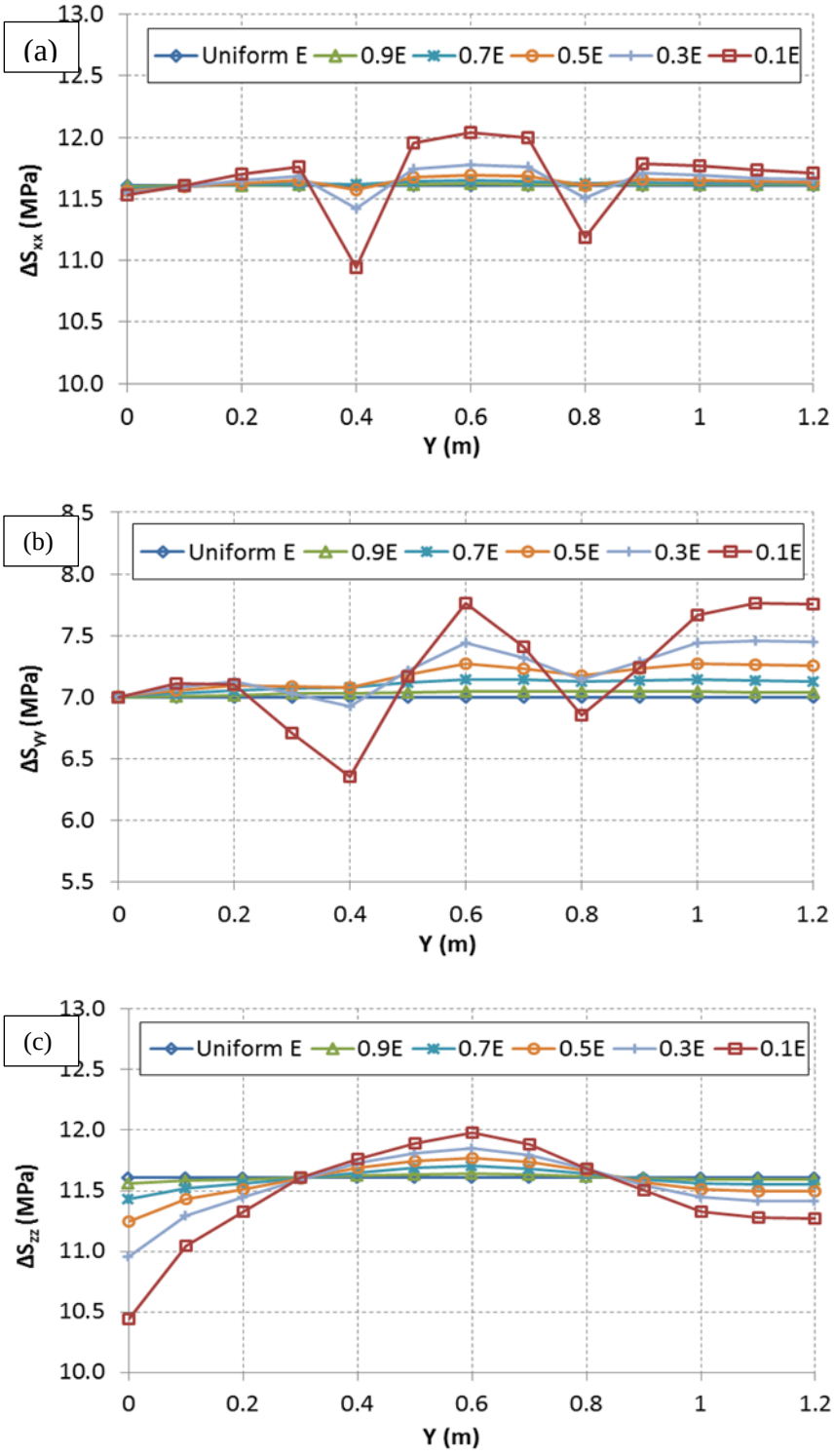

Figure 6.17 Induced normal stresses along the line yy' for cases with different Young's modulus between y = 0.4 m and y = 0.8 m: (a) ΔS_{xx}; (b) ΔS_{yy}; (c) ΔS_{zz}.

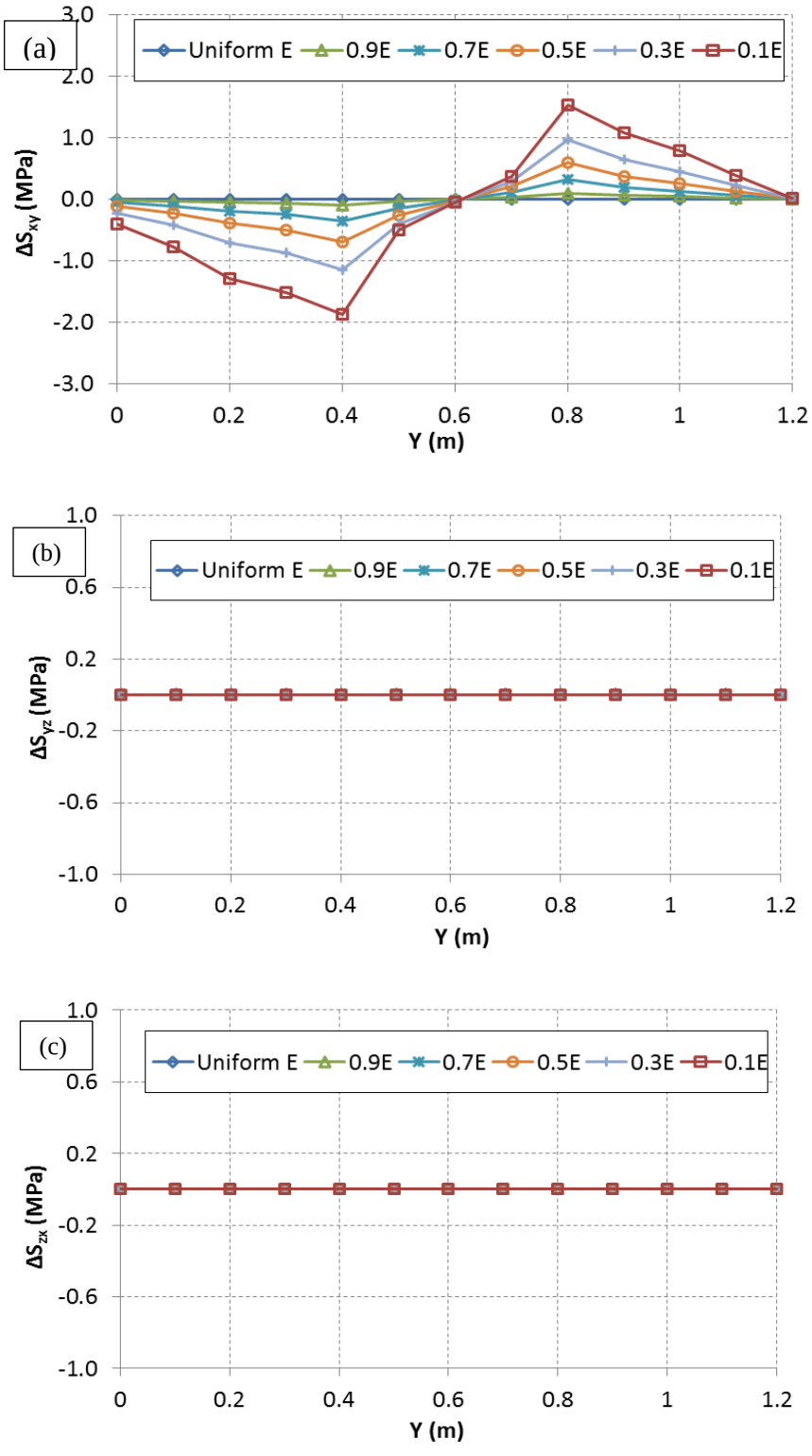

Figure 6.18 Induced shear stresses along the line yy' for cases with different Young's modulus between y = 0.4 m and y = 0.8 m: (a) ΔS_{xy}; (b) ΔS_{yz}; (c) ΔS_{zx}.

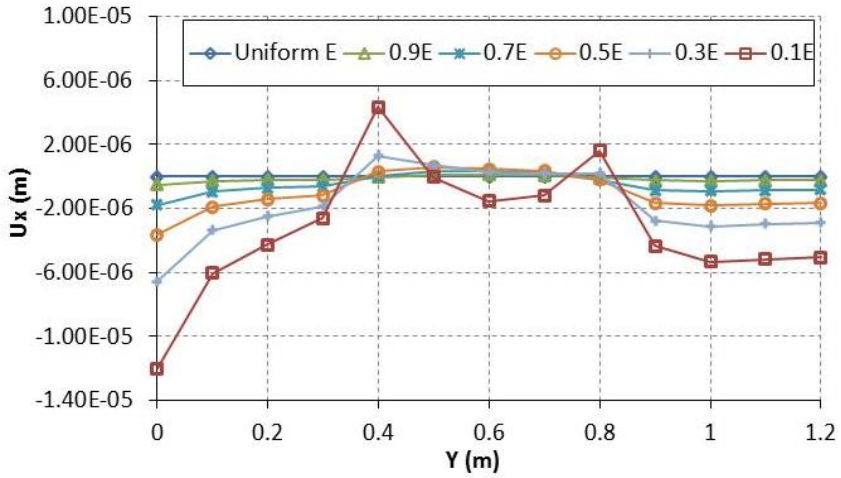

Figure 6.19 Displacement in *x* direction along the line yy'.

The magnitude of the induced shear stress, ΔS_{xy}, varies in the range of 0.5 ~ 2 MPa between y = 0.4 m and y = 0.8 m. For S_{yz} and S_{zx}, the variations are close to zero. Due to the symmetric distribution of material properties with respect to the y- axis, the stress distributions along lines parallel to the y-direction exhibit the same patterns.

From Figure 6.19, it is observed that displacements in the x-direction along the line yy' are negative except at y = 0.4 m and y = 0.8 m, where the two corners of the weak zone (Figure 6.15) are located. However, as can be seen from Figure 6.15a, the x-displacements in the weak zone are in the positive x-direction beyond the line yy' and the weak zone is contracting during pressurization. The net response (mode 1 plus mode 2) is a contraction because of the relatively larger dilation in the y-direction towards the loaded surface due to pore pressure increase.

The distributions of the induced total stress ΔS_{yy} on a central horizontal plane are presented in Figure 6.20 for Mode 1, Mode 2 and Mode 1+2. The interior weak zone encircled by the red dashed lines has a Young's modulus equal to 50% of the surrounding elements. For the homogeneous distribution of Young's modulus, the induced stresses are distributed uniformly in the entire domain, as illustrated in Figure 6.17, Figure 6.18 and Figure 6.19 for the case with uniform E. In the heterogeneous case, Mode 1 loading generates smaller induced total

stress component ΔS_{yy} in the weak zone compared with the induced stresses in exterior elements; Mode 2 has larger ΔS_{yy} in the weak zone. Combining Mode 1 and Mode 2, we observe from Figure 6.20 (c) that the interior weak zone has a larger ΔS_{yy}. We notice from Figure 6.15 that the weak zone is under contraction in the *x*-direction during pressurization. These behaviors are different from those of an elastic (in contract to poroelastic) medium, which only act like mode 1 loading.

Because of the spatial variation of Young's modulus, non-uniform deformations and shear stresses are generated at material interfaces. In addition to the change of mechanical properties, such as Young's modulus, discontinuities (e.g., natural fractures) can also induce heterogeneous stress redistributions when their mechanical properties are different from their surrounding materials. This simple example illustrates some underlying physical processes that lead to the complex stress response observed in the stress field around a pressurized crack considered in the previous section.

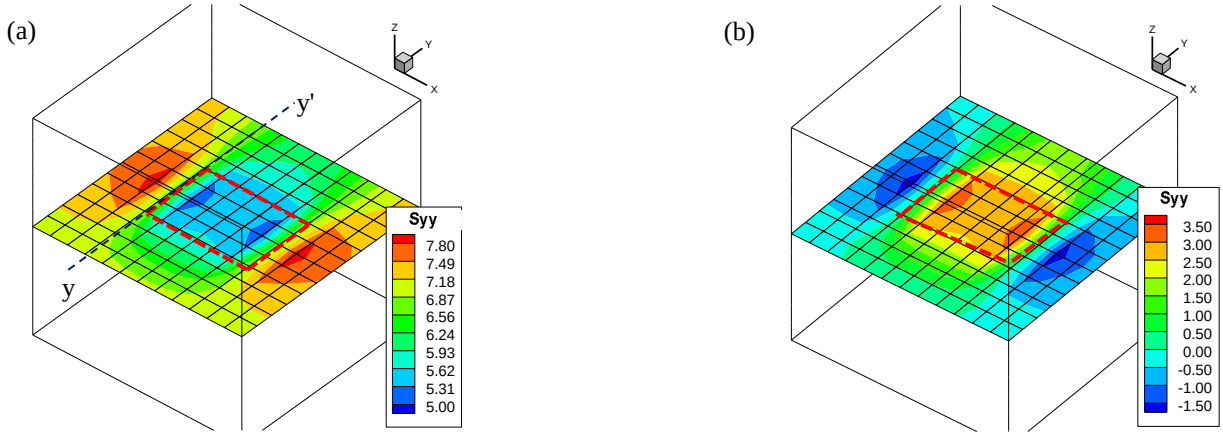

Figure 6.20 Induced total stress ΔS_{yy} (compression positive) on a central horizontal plane: (a) Mode 1; (b) Mode 2; (c) Mode 1+2. (Unit: MPa). (continued)

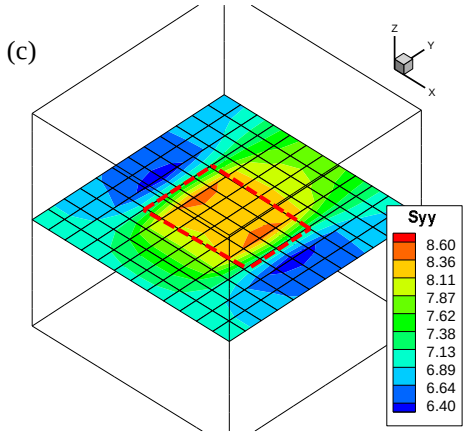

Figure 6.20 (continued). (Caption shown on previous page.)

6.5.2 Influence of Biot's effective stress coefficient

Instead of altering the Young's modulus, consider gradually changing Biot's effective stress coefficient, α, from 0.1 to 0.9 for the elements in the central region while keeping that of the surrounding elements equal to 0.5. Figure 6.21 illustrates the total normal stresses along the line yy'. The value in the legend indicates α for the elements in the central zone. As can be seen, the normal stresses are increased for larger α, and decreased for smaller α. The variations of ΔS_{xx}, ΔS_{yy}, and ΔS_{zz} are in the range of 1.5 MPa ~ 3 MPa, 0.5 MPa ~ 0.8 MPa, and 1 MPa ~ 2 MPa, respectively. Injection into a porous medium causes it to dilate (Cheng et al. 1993). When the expansion is constrained, confining stresses will be generated as a function of Biot's effective stress coefficient:

$$\Delta S_{xx} + \Delta S_{yy} + \Delta S_{zz} = -\frac{2\alpha(1-2\nu)}{1-\nu}\Delta p \tag{6.17}$$

The induced stresses vary in different zones when α changes form one zone to another.

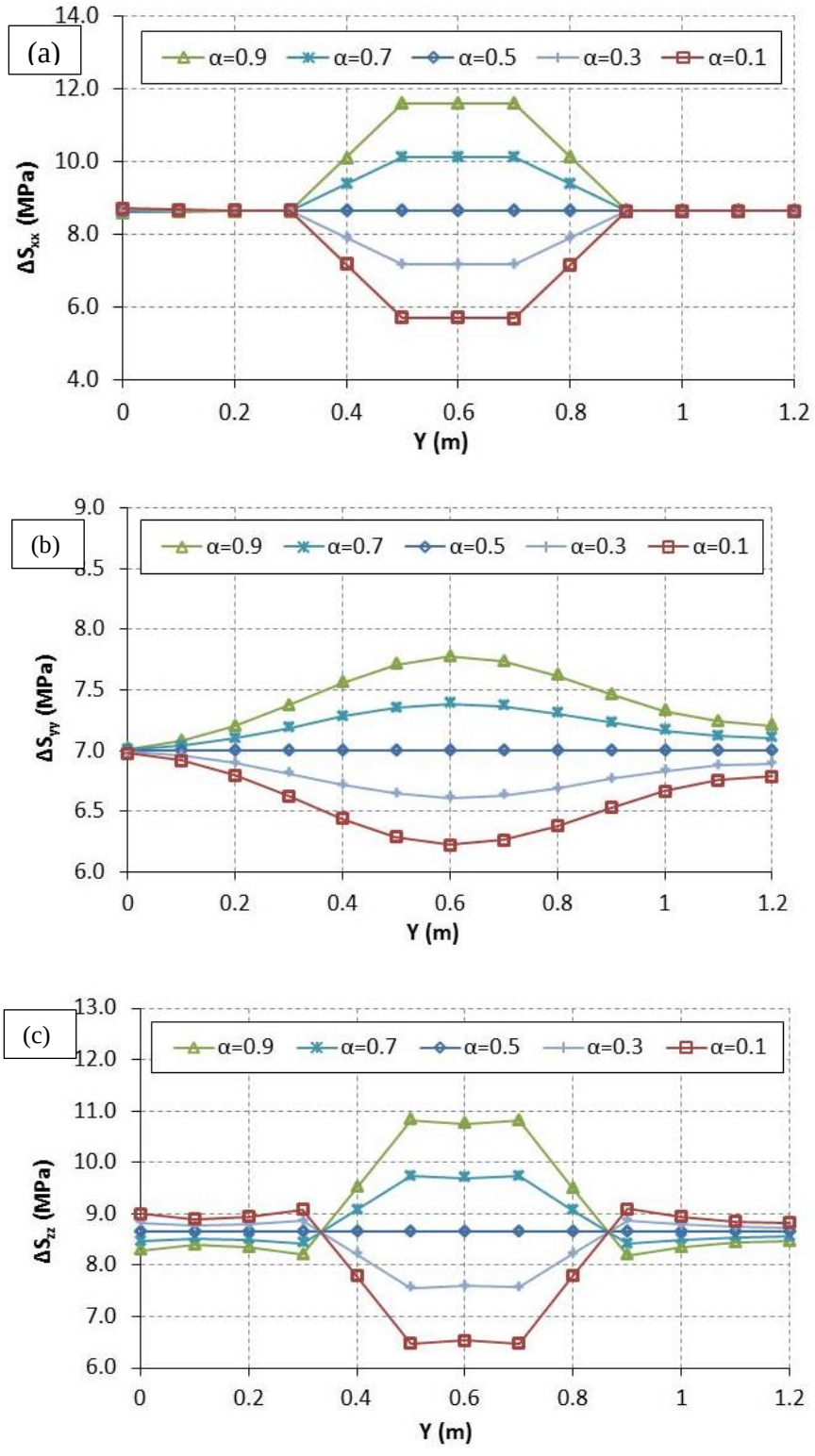

Figure 6.21 Induced normal stresses along the line yy' (see Figure 20) due to the change of the Biot effective stress coefficient α between y = 0.4 m and y = 0.8 m: (a) ΔS_{xx}; (b) ΔS_{yy}; (c) ΔS_{zz}.

In addition to the induced stress variations, the induced displacements also vary in different zones and at the interfaces of the materials with different α. The displacement component in the *x*-direction along the line yy' is plotted in Figure 6.22; it can be seen that it has a uniform distribution when $\alpha = 0.5$. When $\alpha > 0.5$ for elements in the central zone, it tends to expand; when $\alpha < 0.5$, it tends to contract. These are consistent with the changes of normal stresses. Figure 6.23 shows the shear stress distributions along the line yy'. Shear stresses in the range of 1 MPa ~ 2 MPa develop along the interfaces of materials with different α.

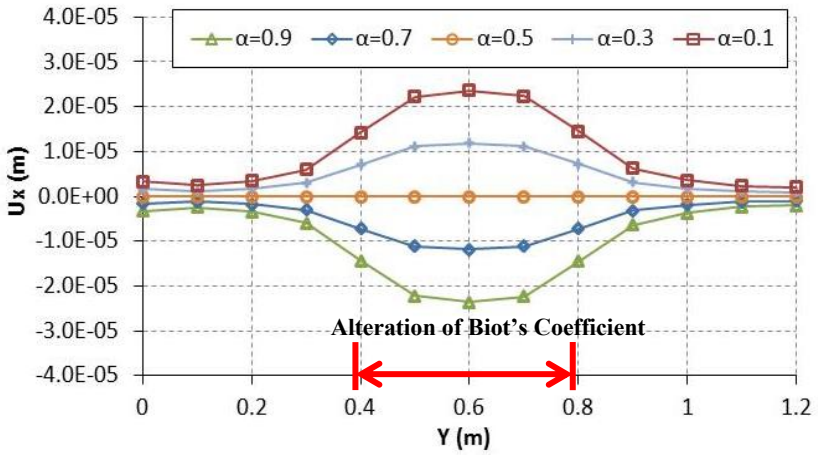

Figure 6.22 Displacement in the *x*-direction along the line yy' (see Figure 6.20) for different Biot's effective stress coefficients in the central zone.

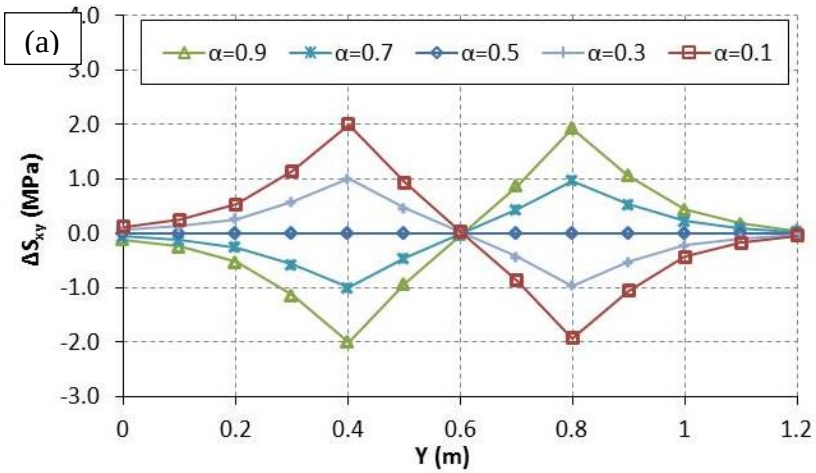

Figure 6.23 Induced shear stresses along the line yy' (see Figure 20) for cases using different Biot effective stress coefficient between y = 0.4 m and y = 0.8 m: (a) ΔS_{xy}; (b) ΔS_{yz}; (c) ΔS_{zx}. (continued)

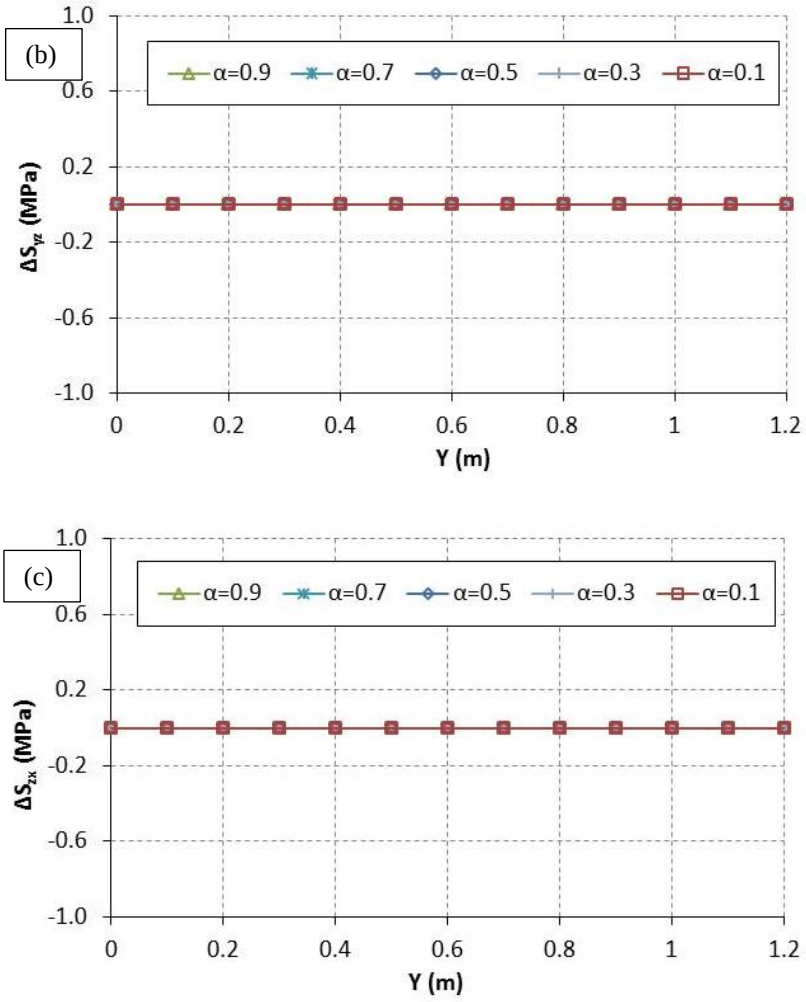

Figure 6.23 (continued). (Caption shown on previous page.)

6.5.3 Influence of drained and undrained Poisson's ratio

According to Eq. (6.17), the induced normal stresses are also a function of drained Poisson's ratio, v. The range for v is $0 \leq v \leq v_u$. If we assume $v = 0.25$ for the elements in the central part of the model and $v = 0.15$ for the surrounding elements, the maximum variations of normal and shear stresses are 0.3 MPa and 0.2 MPa, respectively. When the diffusion of fluid pressure reaches a steady state in a poroelastic rock, the rock's mechanical respons is the same as that of an elastic material with the same drained Poisson's ratio. The undrained Poisson's ratio influences the poroelastic behavior in transient states. The range of undrained Poisson's ratio

values is relatively small. Assuming v_u = 0.4 for the elements in the central zone of the model and v_u = 0.29 for the surrounding elements, the maximum perturbations of normal and shear stresses at t = 0.02s are 0.6 MPa and 0.2 MPa, respectively, so that the difference in the induced stresses at material interfaces are small.

An interesting phenomenon is illustrated in Figure 6.8. The induced stress contrast ($\Delta S_{yy} - \Delta S_{xx}$) due to pressurization of the fracture is less than the original in-situ horizontal stress difference in a region close to the fracture surface (in this case L/R < 0.3). This indicates that the maximum horizontal stress, S_{xx}, will always be larger than the minimum horizontal stress, S_{yy}; there will be no stress reversal in regions close to the fracture surface. This is in contrast to predictions that are based on an elastic formulation without consideration of the pore pressure diffusion effects on rock deformation (and stresses). In an elastic solution to the problem, ΔS_{xx} is always less than ΔS_{yy}; so that ($\Delta S_{yy} - \Delta S_{xx}$) > 0 causing the principal stresses to rotate by 90° provided that the induced stress contrast is larger than the background in-situ stress contrast, $S_{xx} - S_{yy}$.

The induced stress contrast, $\Delta S_{yy} - \Delta S_{xx}$, on fracture surface in a poroelastic rock can also be estimated from the solution to the 1-D problem (Figure 6.24) of fluid pressure loading of an infinite half-space (Cheng 2016). The pressure loading condition can also be decomposed into modes 1 and 2. Using the analytical solution for the 1-D fluid pressure loading with the same parameters as in Table 6.1, the induced stresses are obtained and plotted in Figure 6.25. As can be seen, the induced stress contrast, $\Delta S_{yy} - \Delta S_{xx}$, on the pressure loading surface is -5 MPa, which is almost the same as our numerical results for pressurized penny-shape fracture when t = 0.02 s and t = 7 mins.

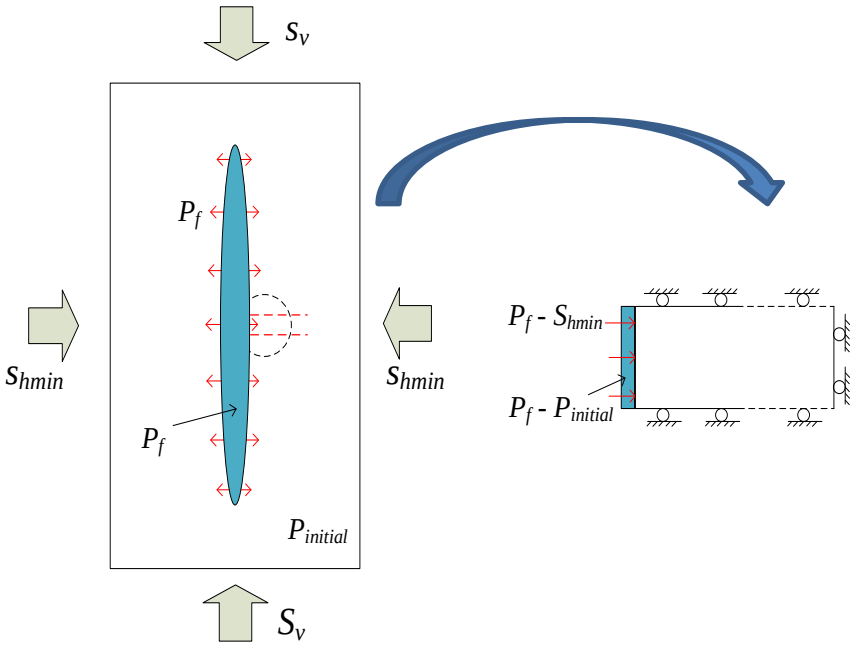

Figure 6.24 1-D fluid pressure loading condition on pressurized fracture surface.

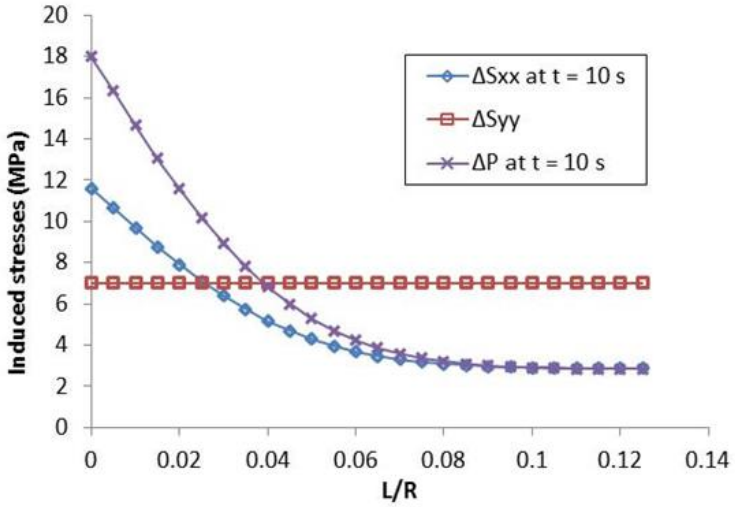

Figure 6.25 Induced stresses and pore pressure for 1-D fluid pressure loading. ΔS_{yy} equals to the applied net pressure during the process of fluid pressure diffusion.

Rocks generally exhibit heterogeneous and anisotropic characteristics. Both of these characteristics could influence the stress- and pore pressure distributions during hydraulic fracturing. Our current model can be used to generate heterogeneous-isotropic parameters. The role of anisotropic rock properties on hydraulic fracturing has been considered in Sesetty and Ghassemi (2016). More effort is needed to improve the model of this paper to consider rock

anisotropy and is left for future work. In real situations, material properties, such as Young's modulus and permeability, could vary by a factor of two and more, especially when discontinuities (e.g. joints, natural fractures) exist. These sudden changes in material properties could be explicitly incorporated into the generated random fields.

Complex processes are involved in hydraulic stimulations, especially when the heterogeneous characteristics of geological formations are considered. For the sake of simplicity, some simplifying assumptions have been made, which may need to be improved when dealing with a real system, and are left for future research.

6.6 Conclusions

A fully coupled 3D poroelastic model based on FEM has been developed to analyze the stress- and pore pressure distributions around a pressurized fracture in heterogeneous porous media. The heterogeneous distributions of Young's modulus and permeability are generated based on lognormal random distribution. Good agreement has been achieved between the analytical solutions and numerical results. Comparison of the pressurized fracture simulation results for a heterogeneous medium with those in a homogeneous one indicates that the normal stress component are almost the same in the two cases, but shear stresses in the heterogeneous media are significantly larger and vary as a function of time, and thus are related with the diffusion of pore pressure. Our analyses show that shear stresses develop along the interfaces of materials with different properties (e.g., Young's modulus). Although normal stresses experience variations along the interfaces, their magnitudes are smaller than the generated shear stresses and much smaller than their initial values. Due to the spatial variation in material properties, shear stresses and nonuniform deformations are generated in a poroelastic rock surrounding a pressurized crack. The induced shear stresses in heterogeneous rock cause the initially horizontal

principal stresses to rotate out of horizontal planes, which may potentially influence the propagation direction of subsequent fractures. As the pore pressure diffuses into formation, the stress reversal regions gradually disappear and the rotation angles of principal stresses decrease. The induced horizontal stress differential caused by the pressurization of the fracture is less than the original in-situ horizontal stress differential in a region close to the fracture surface. As a result, the maximum horizontal stress remains larger than the minimum horizontal stress, and there will be no stress reversal in regions close to the fracture surface. This is in contrast to predictions based on an elastic formulation without consideration of the pore pressure diffusion effects on rock deformation.

References

Biot, M. A. 1941. General theory of three-dimensional consolidation. *Journal of Applied Physics* **12** (2): 155-164.

Carter, J. and Booker, J. 1982. Elastic consolidation around a deep circular tunnel. *International Journal of Solids and Structures* **18** (12): 1059-1074.

Cheng, A. H.-D. 2016. *Poroelasticity*. Switzerland: Springer International Publishing.

Cheng, A. H. D., Abousleiman, Y. and Roegiers, J. C. 1993. Review of Some Poroelastic Effects in Rock Mechanics. *International Journal of Rock Mechanics and Mining Sciences & Geomechanics Abstracts* **30** (7): 1119-1126. http://dx.doi.org/10.1016/0148-9062(93)90081-N.

Detournay, E. and Cheng, A. H.-D. 1991. Plane strain analysis of a stationary hydraulic fracture in a poroelastic medium. *International Journal of Solids and Structures* **27** (13): 1645-1662.

Deutsch, C. V. and Journel, A. G. 1992. *GSLIB, Geostatistical software library and user's guide*. New York: Oxford University Press.

Durlofsky, L. J. 1991. Numerical calculation of equivalent grid block permeability tensors for heterogeneous porous media. *Water Resources Research* **27** (5): 699-708.

Fenton, G. A. and Griffiths, D. V. 2008. *Risk assessment in geotechnical engineering*: John Wiley & Sons Incorporated.

Ge, J. and Ghassemi, A. 2008. Analysis of failure potential around a hydraulic fracture in jointed rock. Paper presented at the The 42nd US Rock Mechanics Symposium (USRMS), San Francisco, California.

Ghassemi, A. and Roegiers, J. C. 1996. A three-dimensional poroelastic hydraulic fracture simulator using the displacement discontinuity method. Paper presented at the Proc. 2nd North American Rock Mechanics Symposium, Rotterdam.

Ghassemi, A. and Zhang, Q. 2006. Porothermoelastic Analysis of the Response of a Stationary Crack Using the Displacement Discontinuity Method. *Journal of Engineering Mechanics* **132** (1): 26-33. http://dx.doi.org/10.1061/(asce)0733-9399(2006)132:1(26).

Ghassemi, A. and Zhou, X. 2011. A three-dimensional thermo-poroelastic model for fracture response to injection/extraction in enhanced geothermal systems. *Geothermics* **40** (1): 39-49. http://dx.doi.org/10.1016/j.geothermics.2010.12.001.

Ghassemi, A., Zhou, X. X. and Rawal, C. 2013. A three-dimensional poroelastic analysis of rock failure around a hydraulic fracture. *Journal of Petroleum Science and Engineering* **108**: 118-127. http://dx.doi.org/10.1016/j.petrol.2013.06.005.

Gordeyev, Y. N. 1993. Growth of a crack produced by hydraulic fracture in a poroelastic medium. *International Journal of Rock Mechanics and Mining Sciences & Geomechanics Abstracts* **30** (3): 233-238. http://dx.doi.org/10.1016/0148-9062(93)92726-7.

Guerillot, D. R., Lemouzy, P., Ravenne, C. et al. 1990. 3D Fluid Flow Behavior in Heterogeneous Porous Media Characterized by Geostatistical Method. Paper 00021081 presented at the SPE Latin America Petroleum Engineering Conference, Rio de Janeiro, Brazil, 14-19 October 1990. http://dx.doi.org/10.2118/21081-ms.

Kumar, D. and Ghassemi, A. 2015. Simulation of mixed-mode poroelastic fracture propagation for reservoir stimulation. *GRC Transactions* **39**.

Rawal, C. and Ghassemi, A. 2011. Poroelastic Rock Failure Analysis Around Multiple Hydraulic Fractures Using a BEM/FEM Model. Paper presented at the 45th US Rock Mechanics/Geomechanics Symposium, San Francisco, CA, 26-29 June 2011.

Rice, J. R. and Cleary, M. P. 1976. Some basic stress diffusion solutions for fluid-saturated elastic porous media with compressible constituents. *Reviews of Geophysics* **14** (2): 227-241.

Safari, R. and Ghassemi, A. 2015. 3D thermo-poroelastic analysis of fracture network deformation and induced micro-seismicity in enhanced geothermal systems. *Geothermics* **58**: 1-14. http://dx.doi.org/10.1016/j.geothermics.2015.06.010.

Sesetty, V. and Ghassemi, A. 2015. A numerical study of sequential and simultaneous hydraulic fracturing in single and multi-lateral horizontal wells. *Journal of Petroleum Science and Engineering* **132**: 65-76. http://dx.doi.org/10.1016/j.petrol.2015.04.020.

Sesetty, V. and Ghassemi, A. 2016. Numerical Modeling of Hydraulic Fracture Propagation from Horizontal Wells in Anisotropic Shale. Paper presented at the 50th US Rock Mechanics/Geomechanics Symposium, Houston, Texas, USA, 26-29 June.

Smith, I. M. and Griffiths, D. V. 2004. *Programming the Finite Element Method*, Fourth edition. West Sussex, UK: John Wiley & Sons Ltd.

Sneddon, I. N. 1946. The Distribution of Stress in the Neighbourhood of a Crack in an Elastic Solid. *Proceedings of the Royal Society of London Series a-Mathematical and Physical Sciences* **187** (1009): 229-260. http://dx.doi.org/10.1098/rspa.1946.0077.

Vandamme, L., Detournay, E. and Cheng, A. H. D. 1989. A two-dimensional poroelastic displacement discontinuity method for hydraulic fracture simulation. *International Journal for Numerical and Analytical Methods in Geomechanics* **13** (2): 215-224. http://dx.doi.org/10.1002/nag.1610130209.

Wang, X. and Ghassemi, A. 2012. A 3D Thermal-Poroelastic Model For Naturally Fractured Geothermal Reservoir Stimulation. Paper presented at the 46th U.S. Rock Mechanics/Geomechanics Symposium, Chicago, Illinois, 24-27 June.

Warpinski, N. R. and Branagan, P. T. 1989. Altered-Stress Fracturing. *Journal of Petroleum Technology* **41** (9): 990-997. http://dx.doi.org/10.2118/17533-pa.

Warren, J. E. and Price, H. S. 1961. Flow in Heterogeneous Porous Media. *Society of Petroleum Engineers Journal* **1** (03): 153-169. http://dx.doi.org/10.2118/1579-g.

Zhou, X. and Ghassemi, A. 2011. Three-dimensional poroelastic analysis of a pressurized natural fracture. *International Journal of Rock Mechanics and Mining Sciences* **48** (4): 527-534. http://dx.doi.org/10.1016/j.ijrmms.2011.02.002.

7 3D Thermo-poromechanical simulation of Fenton Hill HDR experiment

Abstract

Hydraulic stimulation using in geothermal reservoirs involve strong coupling among pressurization and motion of pore pressure, transport of heat, change of in-situ stresses and rock deformation. In this work, a fully coupled thermal-hydro-mechanical model is built to study EGS stimulation. Excellent agreements have been achieved through the comparison of numerical results with both analytical solutions and results from published work. Damage mechanics is utilized to simulate joint opening and material failures. Joint aperture is a key parameter, which controls the injection volume and flow-back volume during injection and venting operations. Semi-analytical equations are utilized to capture the main characteristics of it. A pressurization test at the Phase I Fenton Hill geothermal reservoir is studied. The results from numerical simulations match well with field records. The influence of mesh size on simulation results is also analyzed. The maximum difference is 2 MPa for bottom-hole pressures from models with different mesh size. Four scenarios are proposed to analyze the mechanisms involved in repeated injection-venting experiments. It is found that the stiffness of joint, a key parameter used in aperture calculation, controls the flow-back volume and trapped fluid pressure during venting operations. Considering the size dependent characteristic of joint stiffness and hysteresis behaviors observed during injection and venting, a parameter related to stiffness is gradually changed after each injection-venting treatment in the 3rd scenario. Based on the results from numerical simulations, it is concluded that the 3rd scenario best fits the field observations.

7.1 Introduction

The coupled thermo-hydro-mechanical (THM) processes in porous and fractured media are associated with a wide range of applications. These include solute transport of nuclear waste

repository through rock mass, geothermal energy extraction, fluid injection induced earthquake, injection stimulation of petroleum reservoirs with water colder than in-situ fluids, and so on. All of these problems involves strong coupling among pressurization and motion of pore pressure, transport of heat, change of in-situ stresses and deformation of the porous media.

Since Biot (1941) proposed the theory of poroelasticity in a fluid-saturated isothermal porous media, extensive and excellent efforts have been spent to extend the theory to investigate a wide variety of mechanical phenomena. Rice and Cleary (1976) have recast Biot's theory in terms with straightforward physical concepts. A substantial literature exists to extend the well-known isothermal theory to include the thermal effects (Schiffman, 1971; Booker and Savvidou, 1984, 1985; Kurashige, 1989; McTigue, 1990). The governing equations derived in these papers are different only in detail (McTigue, 1986). Both analytic and numerical methods are developed to demonstrate solutions for coupled heat transfer, changes of fluid pressure, deformation and alteration of in-situ stresses in a linearly elastic, non-isothermal porous medium.

Analytical solutions have the advantages of being stable, accurate and efficient. They are commonly used in parametric studies and verification of numerical models. However, when complex geometries and material non-linearity, or sophisticated coupled processes are involved, numerical solutions are needed. In this work we present a coupled thero-poromechanical finite element method (FEM) with continuum damage mechanics for studying reservoir stimulation considering the presence of natural fractures.

The standard Galerkin finite element method is used to discretize governing equations. A continuum damage approach is described to analyze the joint reactivation (or failure) processes. Numerical examples are provided in the last part to verify the model. Finally, the field case from Phase I Fenton Hill geothermal reservoir is studied.

7.2 Methodology

By extending Rice and Cleary (1976) or Cleary (1977) theory, McTigue (1986) and Kurashige (1989) developed a thermoelastic theory for fluid-saturated porous media. The quasi-linear and quasi-static theory assumes constant material properties and neglects the inelastic terms. The thermo-poroelastic governing equations used here can be found in Chapter 4.

7.2.1 Finite Element Implementation

The finite element method (FEM) is perhaps the most widely used numerical method in science and engineering fields. This is largely due to its flexibility to treat material heterogeneity, non-linear deformability (eg. plasticity), complex boundary conditions, and so on (Jing and Hudson 2002). In this work, approximation of the displacement, pressure and temperature fields within each element through spatial interpolation functions (shape functions), and the discretized thermo-poroelastic formulae are based on standard Galerkin method.

Using the matrix and vector notation, the approximated fields can be expressed as

$$\begin{aligned} \mathbf{u} &= \mathbf{N}_u \bar{\mathbf{u}} \\ p &= \mathbf{N}_p \bar{\mathbf{p}} \\ T &= \mathbf{N}_T \bar{\mathbf{T}} \end{aligned} \tag{7.1}$$

where $\mathbf{u} = [u_x, u_y, u_z]^{\mathrm{T}}$, p, and T are displacement, pore pressure and temperatures variables.

In this study, the Crank-Nicolson type of approximation is used to discretize the temporal domain. After discretization and the Galerkin process are completed, the following equations are obtained (Lee and Ghassemi 2009; Wang and Ghassemi 2012):

$$\begin{bmatrix} K_u & C_{up} & C_{uT} \\ C_{pu} & C_{pp}+\theta K_p \Delta t_k & C_{pT} \\ 0 & 0 & C_{TT}+\theta\left(K_{cdT}+K_{cvT}\right)\Delta t_k \end{bmatrix} \begin{Bmatrix} \Delta u \\ \Delta p \\ \Delta T \end{Bmatrix} = \begin{Bmatrix} F_u \\ -K_p \bar{p}_{t_k} \Delta t_k + F_q \Delta t_k \\ -\left(K_{cdT}+K_{cvT}\right)\bar{T}_{t_k}\Delta t_k + F_h \Delta t_k \end{Bmatrix} \tag{7.2}$$

where θ is a scalar parameter which can vary between 0.5 and 1.0. The explicit expressions of the above matrices are provided in the following:

$$\begin{aligned} K_u &= \int_\Omega B_u^T D B_u d\Omega & C_{up} &= -\int_\Omega B_u^T \alpha I N_p d\Omega \\ C_{uT} &= -\int_\Omega B_u^T \alpha_m^T K I N_T d\Omega & F_u &= -\int_{\Gamma^\sigma} N_u^T \bar{T} d\Gamma \\ K_p &= -\int_\Omega B_p^T \kappa B_p d\Omega & C_{pu} &= -\int_\Omega N_p^T \alpha I^T B_u d\Omega = C_{up}^T \\ C_{pT} &= \int_\Omega N_p^T \left(\alpha \alpha_m^T + \phi_0\left(\alpha_f^T - \alpha_m^T\right)\right) N_T d\Omega \\ C_{pp} &= -\int_\Omega N_p^T \frac{1}{M} N_p d\Omega & F_q &= -\int_{\Gamma^q} N_p^T \bar{q} d\Gamma \\ K_{cdT} &= \int_\Omega B_T^T k^T B_T d\Omega & K_{cvT} &= \int_\Omega N_T^T c_f q_i B_T d\Omega \\ C_{TT} &= \int_\Omega N_T^T \rho_t c_t N_T d\Omega & F_h &= \int_{\Gamma^h} N_T^T h^T d\Gamma \end{aligned} \tag{7.3}$$

7.2.2 Damage mechanics

The well-known ‘Goodman joint element’ has been widely implemented in FEM codes to represent rock fractures. However, numerical ill-conditioning may arise due to large aspect ratios of joint elements and the continuum assumptions (Jing and Hudson 2002). The treatment of fractures and fracture growth remains the most important limiting factor in the application of FEM in geomechanics. Special algorithms have been proposed to overcome this disadvantage. The developments of damage mechanics provide an alternative way to simulate discontinuities or fracture growth. Kachanov (1958) first introduced the concept of damage as a ‘load-bearing area reduction’. Based on the theory of damage mechanics, the stress-strain response and failure evolution can be derived for a material with a given set of elastic properties and defect

population (Ashby and Sammis 1990). In this study, we will concentrate on the simplest, "scalar damage" (Lee and Ghassemi 2009).

Within the framework of damage mechanics, we have the stress-strain equation in the form

$$\sigma_{ij} = (1-\omega) D_{ijkl} \varepsilon_{kl} \tag{7.4}$$

where σ_{ij} is the stress tensor, ε_{kl} is the strain tensor, D_{ijkl} is the forth-order elastic stiffness tensor, and ω is the scalar damage variable, which grows from 0 for the intact material to 1 for the fully damaged material during damage evolution.

The loading/unloading conditions are defined according to the Kuhn-Tucker relations (Simo and Ju 1987) in terms of the damage loading function *f* and the rate of the history variable, $\dot{\kappa}$

$$f \le 0, \quad \dot{\kappa} \ge 0, \quad f\dot{\kappa} = 0 \tag{7.5}$$

The damage loading function is defined as

$$f(\tilde{\varepsilon}, \kappa) = \tilde{\varepsilon} - \kappa \tag{7.6}$$

Different definitions of equivalent strain, $\tilde{\varepsilon}$, are proposed by researchers. For quasi-brittle materials like concrete, rock and ceramics, a popular choice is that suggested by Mazars (1986), which is based on the norm of the positive part of the strain tensor:

$$\tilde{\varepsilon} = \sqrt{\sum_{i=1}^{3} \left(\langle \varepsilon_i \rangle \right)^2} \tag{7.7}$$

where ε_i is the principal strain, $\langle \cdot \rangle$ is the MacAulay brackets defined such that $\langle \varepsilon_i \rangle = \varepsilon_i$ if $\varepsilon_i > 0$ and $\langle \varepsilon_i \rangle = 0$ otherwise.

For quasi-brittle materials, which have a relatively high ratio of compressive to tensile strength, Mazars (1986) introduced two damage parameters, ω_t and ω_c, that are calculated based

on two different damage evolution functions, g_t and g_c, using a same equivalent strain, $\tilde{\varepsilon}$. Under uniaxial conditions, $\omega = \omega_t$ for traction and $\omega = \omega_c$ for compression. For multiaxial case, the damage, ω, is computed based on a combination of ω_t and ω_c:

$$\begin{aligned} \omega &= \alpha_t^{\beta}\omega_t + \left(1-\alpha_t\right)^{\beta}\omega_c \\ \alpha_t &= \sum_{i=1}^{3}\frac{\varepsilon_{ti}\left\langle\varepsilon_i\right\rangle}{\tilde{\varepsilon}^2} \end{aligned} \tag{7.8}$$

where ε_i are the principal strains, ε_{ti} are the principal strains calculated from positive principal stresses, β is the shear parameter.

The damage evolution functions are proposed in the form (Mazars 1986):

$$\begin{aligned} g_t\left(\kappa\right) &= 1-\frac{\varepsilon_0\left(1-A_t\right)}{\tilde{\varepsilon}}-\frac{A_t}{\exp\left[B_t\left(\tilde{\varepsilon}-\varepsilon_0\right)\right]} \\ g_c\left(\kappa\right) &= 1-\frac{\varepsilon_0\left(1-A_c\right)}{\tilde{\varepsilon}}-\frac{A_c}{\exp\left[B_c\left(\tilde{\varepsilon}-\varepsilon_0\right)\right]} \end{aligned} \tag{7.9}$$

where ε_0 is the initial damage threshold and A_t, B_t, A_c, and B_c are characteristic parameters of the material, which are identified from uniaxial tensile and compressive tests, respectively.

Figure 7.1 illustrates a typical stress-strain curve of the damage model during a numerical 1D tension-compression experiment. The idealized specimen is first under tension up to the initial elastic threshold (path O-A); continuous loading leads to damage, along path A-B; reverse loading is then applied, making the curve return to point O along B-O; subsequent compressive loading would reach the elastic threshold C; peak strength is arrived at the point D; along D-E, progressive damage is produced, and ultimate failure is occurred at point E. It could be observed that the isotropic elastic damage model could reproduce the strain softening behavior under tension, and could also capture the hardening and softening behaviors under compression. The path B-O-C indicates the stiffness recovery during the transition from tensile loading to

compressive loading. The stiffness recovery is due to the closure of tensile microcracks under compression.

Figure 7.2 shows the damage evolution corresponding to the uniaxial tension-compression test. No damage occurs during elastic deformation (path O-A); progressive tensile damage is induced along path A-B; during unloading path B-O', damage does not change; path O''-C indicates compressive damage due to the previous tensile failure; progressive compressive damage is generated along path C-D-E; path F-G has strain larger than the ultimate failure point E, and thus has damage value equal to 1, which implies complete failure.

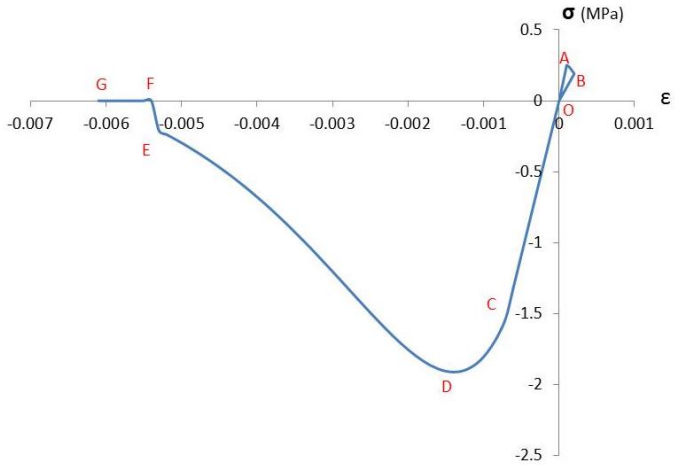

Figure 7.1 Stress-strain curve for a 1D tension-compression test.

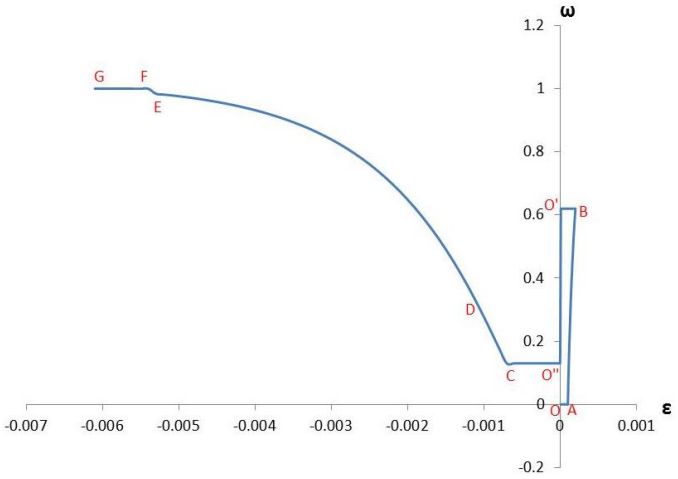

Figure 7.2 Damage evolution curve for an uniaxial tension-compression test.

The performance of the damage model for compressive tests under different confining pressure is also demonstrated in Figure 7.3. Though the damage evolution functions are derived based on uniaxial tensile and compressive tests, the main characteristics of the hardening and softening behaviors of quasibrittle materials are captured.

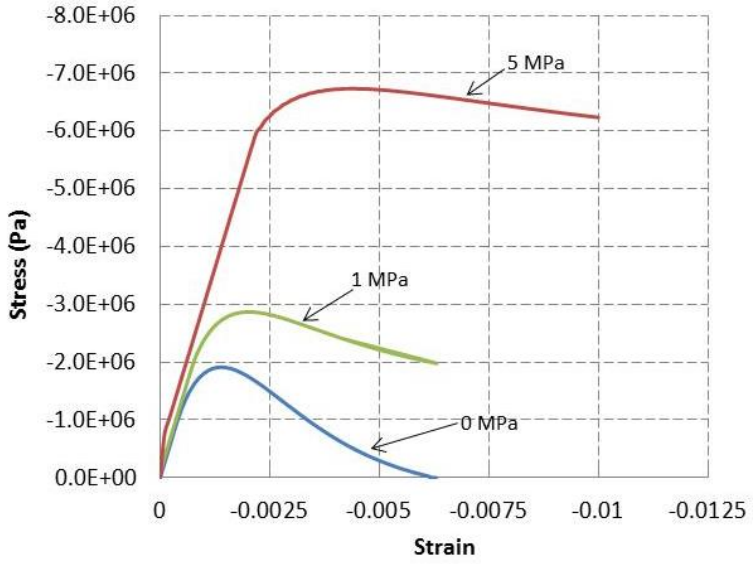

Figure 7.3 Stress-strain curves of compressive tests under different confining pressure.

According to Mazars' damage model (Mazars 1986), it is considered that the tensile failure is caused by microcracks that are created directly by extensions in the same direction as stresses; for compressive failure, the extensions are transmitted by the Poisson's effect and are in the directions perpendicular to stresses.

Progressive damage due to the generation of defects has to be treated as strain softening, which is a typical behavior observed in many brittle heterogeneous materials, such as rocks, concretes, etc (Pijaudier-Cabot and Bazant 1987). Strain softening induces localization of dissipative processes into narrow bands, which makes finite element solutions exhibit strong spurious mesh sensitivity and become unobjective with regard to the mesh size. Objectivity could be restored by various treatments (Jirásek and Bauer 2012).

7.3 Code verification

Several numerical examples are presented to verify the model and to illustrate some typical thermo-poromechanical phenomena. Terzaghi's poroealstic consolidation, Mandel problem and thermoelastic consolidation problem are used to verify the coupled model.

7.3.1 Terzaghi's consolidation

Consider a fluid-filled poroelastic layer of thickness h, resting on a rigid impermeable base. A constant normal traction of magnitude P is suddenly applied on the upper surface of the layer under drained conditions. Initially, an excess pore pressure is induced as a result of the Skempton's effect and the poroelastic layer deforms as an elastic one with undrained moduli. As time goes by, the pore fluid drains out at the upper surface. Eventually, the poroelastic layer acts as a medium with drained moduli.

The boundary conditions are listed as following:

$$\begin{aligned} \sigma_{xx} &= -H(t)P \quad x = 0 \\ p &= 0 \quad x = 0 \quad \forall\, t \\ \frac{\partial p}{\partial x} &= 0 \quad x = h \quad \forall\, t \\ u_x &= 0 \quad x = h \quad \forall\, t \end{aligned} \tag{7.10}$$

The detailed solution of the Terzaghi's one-dimensional consolidation problem can be found in Jaeger et al. (2009), here we list the final solutions:

$$p(x,t) = \frac{B(1+\nu_u)}{3(1-\nu_u)}(-P)\sum_{m\ odd}\frac{4}{m\pi}\left(sin\frac{m\pi}{2h}x\right)e^{-c\left(\frac{m\pi}{2h}\right)^2 t}$$

or

$$\frac{p(x,t)}{p_0} = 1 - \sum_{n=0}^{\infty}(-1)^n\left\{erfc\left[\frac{2nh+z}{(4kt/\mu S)^{1/2}}\right] + erfc\left[\frac{2(n+1)h-z}{(4kt/\mu S)^{1/2}}\right]\right\} \tag{7.11}$$

$$w(z,t) = \frac{P}{(\lambda + 2G)}\left[(z-h) + \frac{\alpha^2 Mh}{(\lambda + 2G + \alpha^2 M)} \sum_{n=1,3,\ldots}^{\infty} \frac{8}{n^2\pi^2} cos\left(\frac{n\pi z}{2h}\right) \times exp\left(\frac{-n^2\pi^2 kt}{4\mu Sh^2}\right)\right] \quad (7.12)$$

In the finite element solution, the one-dimensional consolidation problem is solved using a three-dimensional model. A single column of elements are used in simulation. The problem domain is discretized using 10×10×10 (in the x, y and z directions) 8-node isoparametric hexahedron elements. The four lateral boundaries are impermeable and have no lateral displacement but can have vertical displacements; the bottom surface is frictionless and impermeable; the top surface is frictionless and exposed to drained condition (zero pore pressure in this study). Table 7.1 lists the basic input parameters for this problem.

Table 7.1 Basic input parameters for Terzaghi 1-D consolidation.

Geometry of the model	10×10×10 m (length/width/height)
Number of elements	10×10×10 (length/width/height)
Shear modulus, G	1.2×10^{10} Pa
Poisson's Ratio, v	0.15
Undrained Poisson's Ratio, v_u	0.29
Biot's effective stress coefficient, α	1.0
Permeability, k	0.5 md
Fluid viscosity, μ	3.0×10^{-4} Pa.s
Load	1.0×10^{6} Pa

Figure 7.4 shows the comparison between the analytical solution and the numerical solution for the distribution of pore pressure. The displacement history at different depth is plotted in Figure 7.5. It could be observed that good agreements have been achieved.

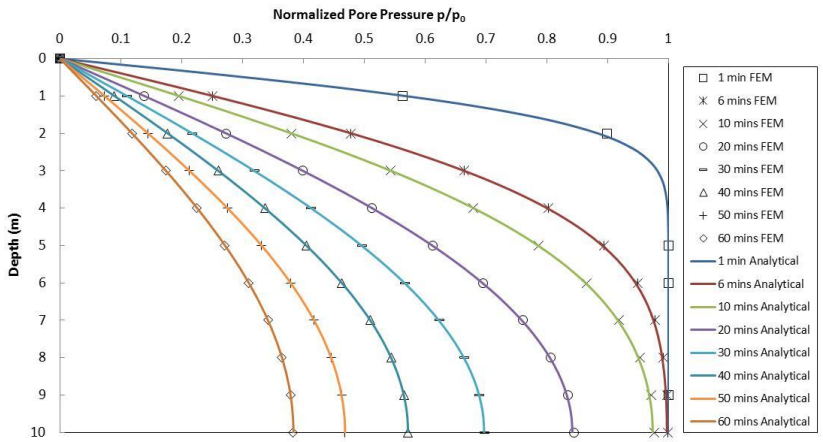

Figure 7.4 Terzaghi's problem: comparison of analytical and numerical solution for the pore pressure distribution.

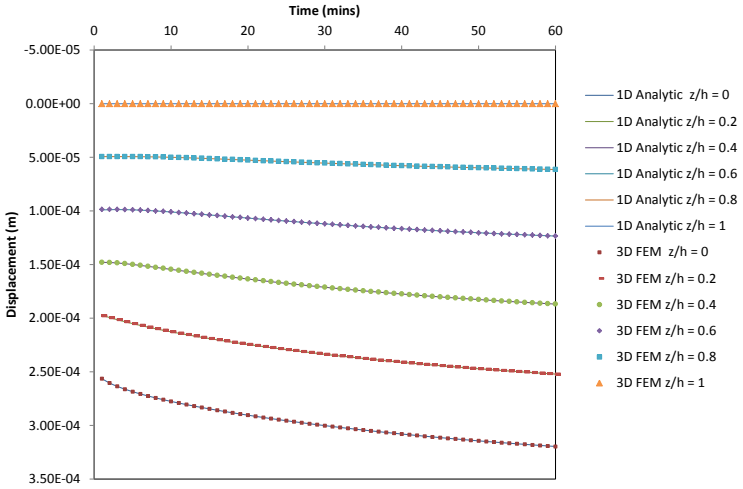

Figure 7.5 Terzaghi's problem: history of displacement for analytical and numerical solutions.

7.3.2 Mandel's problem

As mentioned before, the coupled theory produces essential differences compared with the uncoupled one. Among them is the classical work of Mandel and Cryer which demonstrated that the inhomogeneous diffusion equation for the pore pressure based on theory of poroelasticity could be responsible for a non-monotonic pressure response for a saturated porous specimen under constant boundary conditions.

Mandel's problem involves an infinitely long rectangular specimen sandwiched between two rigid, frictionless, impermeable plates (Figure 7.6). A constant vertical force of 2F is applied

to the rigid plates. The lateral surfaces are traction free and exposed to zero pore pressure. The analytical solution could be found in Cheng and Detournay (1988), here we list the solutions for pore pressure and displacement:

$$p(x,t) = \frac{2FB(1+\nu_u)}{3a}\sum_{i=1}^{\infty}\frac{sin\alpha_i}{\alpha_i - sin\alpha_i cos\alpha_i}\left(cos\frac{\alpha_i x}{a} - cos\alpha_i\right)\exp(-\alpha_i{}^2 ct/a^2) \qquad (7.13)$$

$$u_x(x,t) = \left[\frac{F\nu}{2Ga} - \frac{F\nu_u}{Ga}\sum_{i=1}^{\infty}\frac{sin\alpha_i cos\alpha_i}{\alpha_i - sin\alpha_i cos\alpha_i}\exp(-\alpha_i{}^2 ct/a^2)\right]x + \frac{F}{G}\sum_{i=1}^{\infty}\frac{cos\alpha_i}{\alpha_i - sin\alpha_i cos\alpha_i}sin\frac{\alpha_i x}{a}\exp(-\alpha_i{}^2 ct/a^2) \qquad (7.14)$$

where $tan\alpha_i = \frac{1-\nu}{\nu_u-\nu}\alpha_i$.

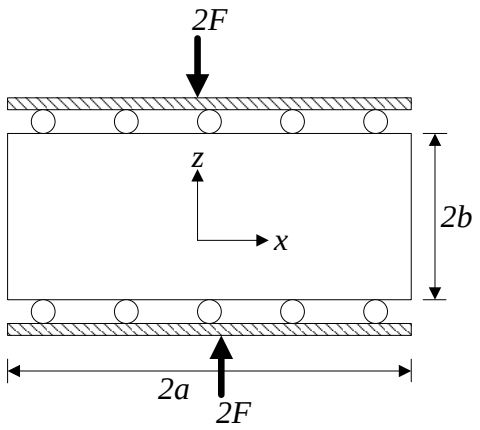

Figure 7.6 Mandel's problem.

Referring to Figure 7.6, the axis of material symmetry is the *z*-axis. Plane strain conditions are assumed in the *y*-direction (perpendicular to the paper). A three dimensional domain is used to simulate the two-dimensional problem with proper boundary conditions to ensure the plane strain condition in *y*-direction. We take the advantage of quarter symmetry about the *x* and *z* axes to build the FEM model. A cubic of 1×1×1 m (length/width/height) is discretized using 10×2×5 (in the *x*, *y* and *z* directions) 8-node isoparametric brick elements. The basic input parameters are provided in Table 7.2.

Table 7.2 Basic input parameters for Mandel's problem.

Geometry of models	1×1×1 m (length/width/height)
Number of elements	10×2×5 (length/width/height)
Shear modulus	1.2×10^{10} Pa
Poisson's Ratio	0.15
Undrained Poisson's Ratio	0.29
Biot's coefficient	1
Permeability	0.005 md
Fluid viscosity	3.0×10^{-4} Pa.s
Load (F)	1.0×10^{6} Pa m

The distribution of pore pressure in the horizontal direction (x-direction) is illustrated in Figure 7.7. As can be seen from it, excellent agreements have been achieved between the analytical and numerical solutions. The distribution of u_x in the horizontal direction (x-direction) is plotted in Figure 7.8. Again, the analytical solution agrees well with the numerical results.

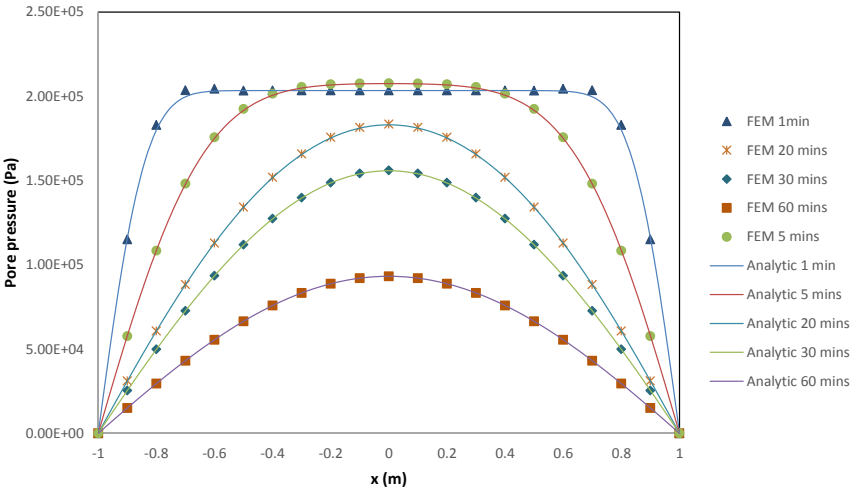

Figure 7.7 Mandel's problem: comparison of analytical and numerical solution for the pore pressure distribution.

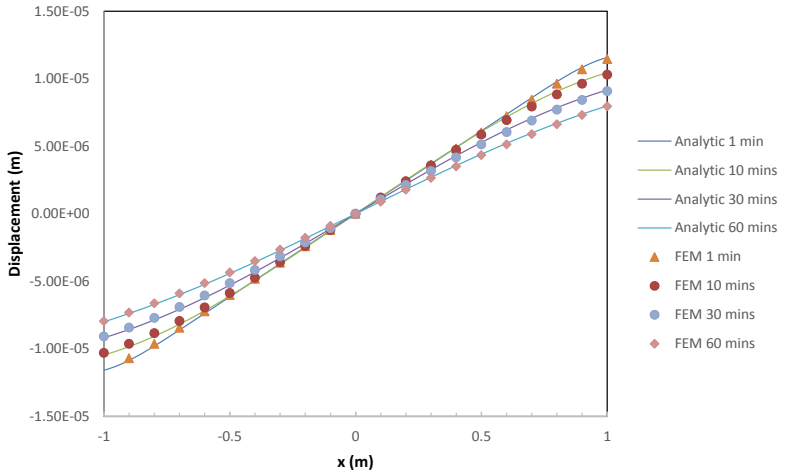

Figure 7.8 Mandel's problem: comparison of analytical and numerical solution for the displacement distribution.

7.3.3 Thermoelastic consolidation

Few analytical solutions are available for fully coupled thermal-poro-elastic problems. The code-to-code comparison, however, provides a way to verify our model. Aboustit et al. (1982) studied a 1-D thermoelastic consolidation problem using a coupled finite element model without considering convection effect. Based on the results from Aboustit, Noorishad et al. (1984), Lewis et al. (1986), and Gatmiri and Delage (1997) performed code-to-code verification. Table 7.3 gives the input data used in this problem. Again, 3-D 8-node hexahedron elements are utilized in our simulation. A surface traction of unity is applied on the top surface, with a surface temperature of 50 °C. The initial temperature of the saturated soil is 0 °C. The soil column is insulated and sealed everywhere, except at the top surface.

Figure 7.9 gives the results from Aboustit et al. (1982) and Noorishad et al. (1984) along with our solution of the same problem. A nearly perfect agreement is achieved between Noorishad's and ours. Noorishad suggested that the slight discrepancy between Aboustit's and their solutions was due to their solution scheme, under which the temperature solution lags one step behind the hydro-mechanical calculation. However, our fully coupled solution, based on Newton Raphson iteration, indicates that one step lag may not be the reason.

Table 7.3 Basic input parameters for thermoelastic consolidation.

Porosity, ϕ	0.20
Young's modulus, E	6000.0 Pa
Poisson's ratio, v	0.40
Volumetric thermal expansion coefficient, α_m	9.0×10^{-7}
Matrix heat capacity, ρC	167.20×10^{3} J/m^3 °C
Thermal conductivity, k^T	836.0 J/m s °C
Permeability, k/μ	4.0×10^{-6} m/s
Biot's coefficient, α	1.0
Initial temperature, T_{ini}	0 °C
Surface temperature, T_0	50.0 °C
Surface load	1.0 Pa

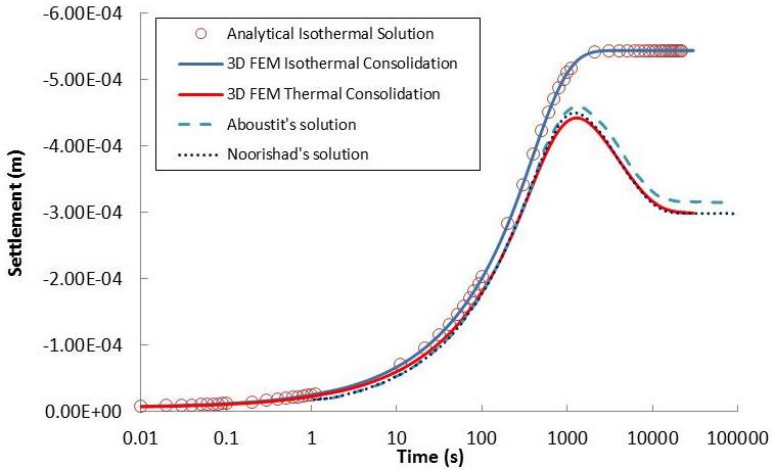

Figure 7.9 Surface settlement plotted as a function of time for thermoelastic consolidation.

7.4 Fluid injection at Phase 1 Fenton Hill geothermal reservoir

As an application of the fully coupled thermo-poromechanical model, the Hot Dry Rock (HDR) geothermal system at Fenton Hill, New Mexico, is studied. In 1974, the world's first HDR geothermal reservoir was under construction, which is referred to as the Phase I reservoir. From 1978 to 1980, major flow tests were performed, including a 9-month continuous circulation test. Then, a deeper and hotter geothermal reservoir was constructed at the same site, which is referred to as the Phase II reservoir (Brown et al., 2012). In this study, attention is focused on the Phase I reservoir.

The principal objective of the Phase I reservoir was to assess the technical feasibility of the enhanced geothermal system concept in hot dry rock (Brown et al., 2012). Multiple

pressurization and venting experiments were performed over a fresh open-hole interval (Zone 7) from 6499 to 6702 ft (1980 m to 2042 m) at the bottom of GT-2 borehole after stage 2 drilling. Field observations indicated that the opening pressure for the stimulated joints was as high as 2500 psi (17 MPa). After some calculation, the inclined angle of the two joints was estimated as 70°. Based on pressure records, it was considered that the applied hydraulic pressure was opening two pre-existing joints, intersecting the borehole, rather than fracturing intact rock (Brown et al., 2012). Table 7.4 gives the input parameters used in this study for Phase I Fenton Hill geothermal reservoir.

After several years of exploration, it was suggested that all Fenton Hill "fractures" were actually pre-existing but resealed joints that were being reopened during hydraulic stimulations (Brown et al., 2012). Pressure testing of the open-hole interval (Zone 7) at GT-2 borehole found no evidence of hydraulic fracturing. During a very brief test, the injection pressure experienced a sharp rise and then an abrupt leveling off at about 2500 psi (17 MPa) before shut-in. The data has been interpreted to indicate joints were opened at or below a pressure around 2500 psi (17 MPa).

Four injection-venting experiments were also performed in the open-hole interval (Zone 7) at GT-2 borehole. The first three experiments injected 11,000, 20,000 and 36,000 gal. of water (corresponding to 41.64, 75.71 and 136.27 m^3), at a maximum injection pressure of 2500 psi (17 MPa) and a maximum and a maximum flow rate of 4BPM (10.6 L/s). Observation indicated that much less than half of the injected fluid was recovered in each of the three subsequent tests. In the fourth injection, treated fluid using cross-linked polymer mixed with sand was adopted. 4500 gal. (17.03 m^3) of treated fluid was pumped at a rate of 9 BPM (23.9 L/s). The pumping pressure was as high as 2950 psi (20.34 MPa) during the treatment. In less than an hour, over 90% of the

injected fluid was recovered. Another 8% was recovered from continued venting (Brown et al., 2012). These observations provoked a great deal of discussion.

Table 7.4 Model parameters for Phase I Fenton Hill geothermal reservoir.

Rock Properties	
Young's modulus, E	6.0×10^{10} Pa
Poisson's ratio, ν	0.25
Undrained Poisson's ratio, ν_u	0.33
Biot's effective stress coefficient, α	0.5
Rock density, ρ_{rock}	2.7×10^{3} kg/m^3
Tensile strength of intact rock	6.0×10^{6} Pa
Hydraulic Properties	
Porosity, φ	0.0001
Permeability, k	0.15 md
Viscosity, μ	3.0×10^{-4} kg/(m s)
Density of fluid, ρ_f	1.0×10^{3} kg/m^3
Thermal Properties	
Volumetric thermal expansion coefficient of matrix, α_m	2.4×10^{-5} 1/°C
Volumetric thermal expansion coefficient of fluid, α_f	2.1×10^{-4} 1/°C
Thermal conductivity of rock, κ^T_r	3.0 J/(m s °C)
Thermal conductivity of fluid, κ^T_r	0.6 J/(m s °C)
Heat capacity of rock, C_r	900 J/(kg °C)
Heat capacity of fluid, C_f	4200 J/(kg °C)
Stress and Temperature States	
Vertical stress, S_v	53 MPa
Max. horizontal stress, S_{Hmax}	44 MPa
Min. Horizontal stress, S_{hmin}	34 MPa
Initial pore pressure, P_{ini}	19.6 MPa
Reservoir temperature, T_{ini}	146 °C
Injection fluid temperature, T_{inj}	66 °C

In this study, we use our coupled model to simulate this pressure behavior and analyze the mechanisms involved. The method utilized to update joint permeability during reactivation is first presented. Two field examples are then adopted as examples to illustrate the performance of the model. The first is a pressure-stimulation test, during which some 105 gal. of fluid was injected in the open-hole interval (Zone 7) at GT-2 borehole for about 1 minute (p. 72, Brown et al., 2012). We then demonstrate the model responses during four injection-venting operations and try to analyze the mechanisms involved in these treatments.

7.4.1 Permeability of natural fracture (joint)

The opening of joints during fluid injection is simulated using the previously proposed damage model. Initially, the joint is assumed to be in sealed conditions with a same permeability of intact rock. The tensile strength of the sealed joint is set at a low value (600 Pa), which is assumed to be the tensile strength of the joint-filling material. Whenever the joint is opened by injected fluid, the aperture of joint would be altered as a function of effective normal stress (Willis-Richards et al., 1996)

$$a = \frac{a_0}{1+\beta\sigma'/\sigma_{nref}} + a_s + a_{res} \tag{7.15}$$

where σ' is the effective normal stress acting on joint surface, a_0 is the aperture of joint under zero effective stress, σ_{nref} is the effective normal stress applied to make aperture to be $a_0/(1+\beta)$, a_{res} is residual aperture at high effective stress, a_s is the aperture change caused by shear dilation, $a_s = U \tan(\phi_{dil})$, U is shear displacement of joint, ϕ_{dil} is shear dilation angle. Aperture, a, is plotted as a function of β and σ' in Figure 7.10.

For fully open fractures, the effective normal stress is zero and the fracture asperities are no longer in contact. Under such circumstance, the value of joint aperture is chosen as the maximum one between the initial aperture a_0 and the aperture change calculated from element deformation. Finally, the joint permeability is calculated based on the well-known “cubic law” (Willis-Richards et al., 1996)

$$k = \frac{a^2}{12} \tag{7.16}$$

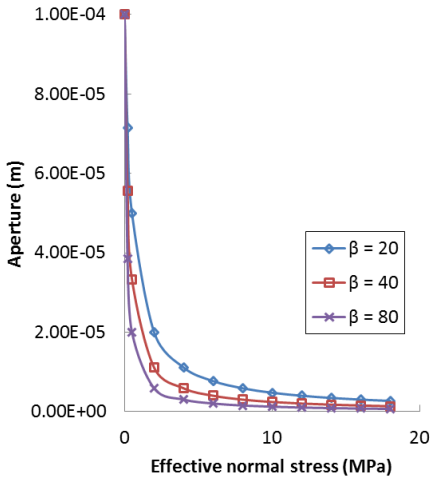

Figure 7.10 Aperture plotted as a function of β and σ'. (a_0 = 100 × 10^{-6} m, σ_{nref} = 1.0 × 10^7 Pa, a_{res} = 0.1 × 10^{-6} m)

Evolution of joint aperture and permeability under pressurization is a complex process. Joint aperture is a key parameter that controls the injection volume and flow-back volume during injection and venting operations. Semi-analytical equations are utilized to capture the main characteristics of it. As mentioned before, different assumptions are proposed regarding the mechanisms involved in repeated pumping and venting operations. In this study, three scenarios are considered based on different assumptions.

7.4.2 A pressure-stimulation test

The simulation domain size is 200 m by 300 m by 300 m in x, y, and z directions, respectively (Figure 7.11). The x direction is aligned with the direction of minimum horizontal principal stress. In order to analyze the influence of mesh size on the simulations, two different grid models are built. They are meshed using different element sizes in the y-z cross-section. The joints, found in Zone 7 of GT-2 borehole at depth around 2000 m, are explicitly represented by elements in our model (Figure 7.11a). The elements containing the joint, we call them joint elements, have a thickness of 0.1 m (joint aperture is much smaller than the element thickness.). Though smaller thickness of joint elements could be adopted, it is not computationally economic to do so. As shown in Figure 7.11, the joint plane has a dip angle of 70 degree, and strikes

parallel to the y direction. One model has 60 by 60 elements on the joint plane, and another has 30 by 30 elements. The joint parameters used in the first pressure-stimulation test are a_0 = 100 × 10^{-6} m, σ_{nref} = 1.0 × 10^7 Pa, ϕ_{dil} = 3°, a_{res} = 0, β = 200.

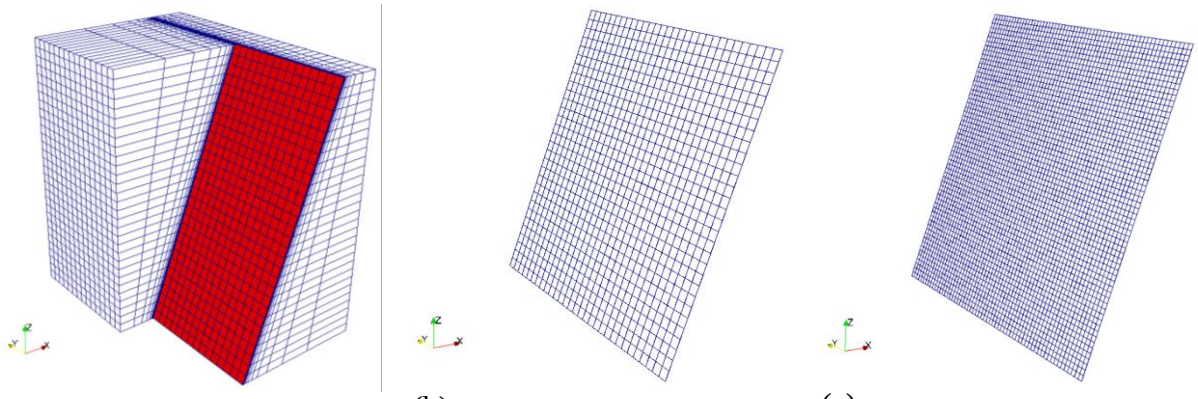

(a) (b) (c)

Figure 7.11 Grid model and discretized joint plane with different element mesh size. (a) grid model (200 m×300 m×300 m), red color indicates joint elements; (b) coarse mesh for joint plane, element size is 10 m; (c) finer mesh for joint plane, element size is 5 m.

Figure 7.12 illustrates the bottom-hole pressure (BHP) plotted as a function of time using a coarse mesh with 31×30×30 elements in x, y and z directions, respectively. As can been seen, there is an initial sharp rise in pressure during the first 15 seconds of injection. And then a leveling off of BHP is observed at about 37 MPa during the injection treatment. Then the BHP gradually decreases to the initial bottom-hole pressure (19.6 MPa) after shut-in. For the finer mesh with 31×60×60 elements in x, y and z directions, a similar profile of BHP vs. time is observed (Figure 7.13). The pressure plateau is at about 38 MPa during the injection stage. This pressure behavior, a sharp rise followed by an abrupt "flattening out", matches the field observation very well, which indicates the appropriateness of the proposed model. The red dash lines in Figure 7.12 and Figure 7.13 are from field records. Through comparison, it is considered that a reasonable match is achieved. The maximum difference of bottom-hole pressure caused by mesh size is around 2 MPa, and should be acceptable in practical application.

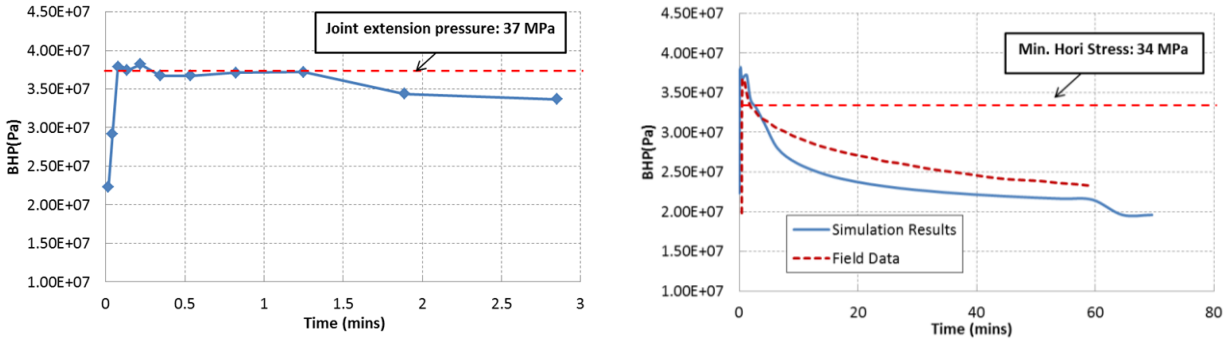

(a) (b)

Figure 7.12 Bottom-hole pressure plotted as a function of time using a coarse mesh, 31×30×30 elements are respectively used in x, y, and z directions. (a) pressure profile during first 2 mins; (b) pressure profile over 70 mins.

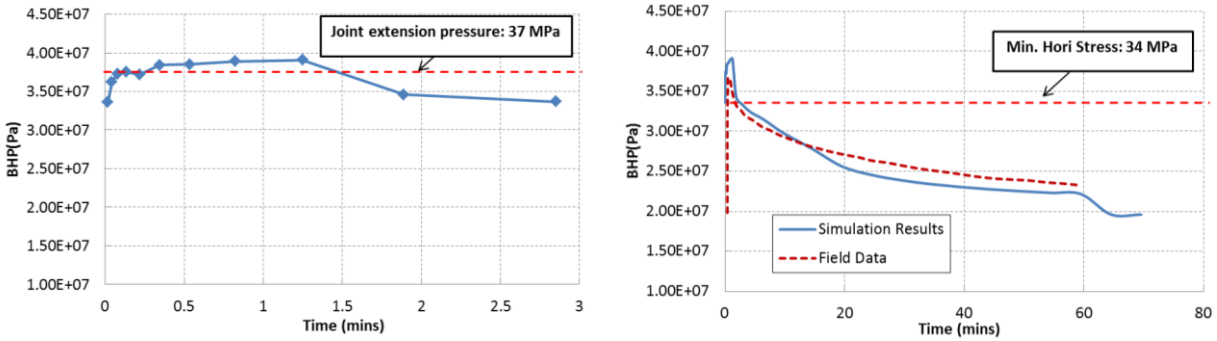

(a) (b)

Figure 7.13 Bottom-hole pressure plotted as a function of time using a finer mesh, 31×60×60 elements are respectively used in x, y, and z directions. (a) pressure profile during first 2 mins; (b) pressure profile over 70 mins.

7.4.3 Injection-venting experiments

After the first pressure test, four injection-venting experiments were performed at the same site. Three scenarios are proposed in order to match the field records.

(1) Scenario #1

The joint parameters used are a_0 = 100 × 10^{-6} m, σ_{nref} = 1.0 × 10^7 Pa, ϕ_{dil} = 3°, a_{res} = 0.1 × 10^{-6} m, β = 80. The size of simulation domain is 200 m by 500 m by 500 m with 31×50×50 elements in x, y, and z directions, respectively. Four injection-venting operations are simulated. A shut-in period of 60 mins exists after each of the injections (41.64, 75.71, 136.27 and 17.03 m^3) of water. After shut-in, one hour venting operation is performed, and the corresponding

flow-back volumes are calculated for each injection. The injection rate for the first three operations is 7.9 L/s. The last injection has a rate of 23.9 L/s.

We assume the natural fracture is initially sealed, and its initial permeability is the same as the matrix permeability. After reactivation, the fracture aperture increases due to shearing and opening. Its permeability is then determined by Eqs. (7.15) and (7.16). During venting stages, the flow-back volumes largely depend on the size of aperture or the equivalent permeability. We first consider the case with $a_{res} = 0.1 \times 10^{-6}$ m during injection, shut-in, and venting operations (case 1). We then change the residual aperture, a_{res}, into 5×10^{-6} m (case 2) and 1×10^{-5} m (case 3) in the last venting treatment in order to evaluate the sensitivity of recovery ratio to aperture size. Figure 7.14 illustrates aperture, a, plotted as a function of effective normal stress for the three cases.

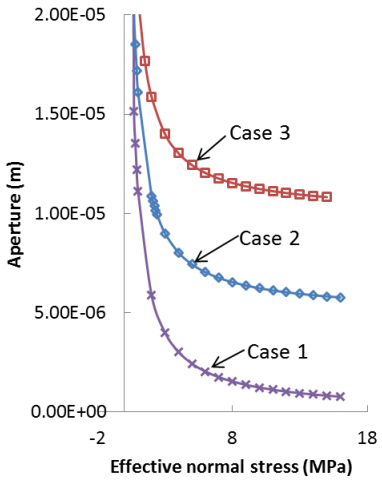

Figure 7.14 Aperture plotted as a function of effective normal stress for three cases in scenario #1.

Bottom-hole pressure (BHP) is plotted as a function of time in Figure 7.15. Four sequential injection-shut-in-venting treatments are separated by red dash lines. Pressure perturbation happens during injection operations. The 1st and 4th treatments have larger pressure drop than the 2nd and 3rd treatments during shut-in operations. This could be due to the smaller injected volume during the 1st and 4th injection treatments.

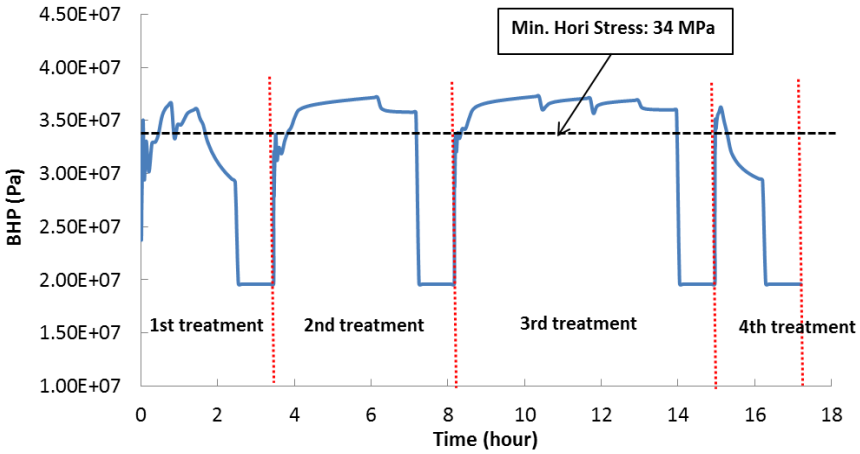

Figure 7.15 Bottom-hole pressure plotted as a function of time for the four injection-venting treatments (β = 80).

Table 7.5 gives the flow-back volumes at the end of each venting operation. The smallest aperture size and its corresponding equivalent permeability are also given. 7.7×10^{-7} m is the calculated smallest aperture size, which is also the aperture size for the joint element containing wellbore.

Table 7.5 Flow-back volume and permeability at the end of each venting for scenario #1.

Treatment	1st	2nd	3rd	4th
Flow-back ratio	7%	22%	40%	23%
Perm (md)	50	50	46	50
Aperture (m)	7.8×10^{-7}	7.7×10^{-7}	7.7×10^{-7}	7.7×10^{-7}

If we set the residual aperture as 5.0×10^{-6} m (case 2), which is 1/6 of the maximum aperture during the 4th injection, the flow-back ratio is calculated as 137%. When 1×10^{-5} m is used (case 3), the flow-back ratio is 171%. In the last treatment, the flow-back volume is larger than the injection volume. This indicates that fluid in the 3rd treatment flows back during the venting in the 4th treatment.

(2) Scenario #2

Instead of changing the residual aperture in the last venting treatment, we try to match field observations by making the joint "softer". In scenario #2 β is decreased from 80 to 20 and all the other parameters are kept as those used previously. The aperture size is plotted as a

function of β in Figure 7.10. The larger of β, the stiffer of the joint. The joint parameters used are $a_0 = 100 \times 10^{-6}$ m, $\sigma_{nref} = 1.0 \times 10^7$ Pa, $\phi_{dil} = 3°$, $a_{res} = 0.1 \times 10^{-6}$ m, $\beta = 20$.

The recovery ratio of injected fluid and the smallest aperture size at the end of each venting are listed in Table 7.6. The recovery ratio increases compared with the cases with $\beta = 80$ in scenario #1. In the last venting operation, the recovery ratio is 84%, which is close to the field observation of 90%.

Table 7.6 Flow-back volume and permeability at the end of each venting for scenario #2, $\beta = 20$.

Treatment	1st	2nd	3rd	4th
Flow-back ratio	31%	35%	45%	84%
Perm (md)	768	763	754	756
Aperture (m)	3.0×10^{-6}	3.0×10^{-6}	3.0×10^{-6}	3.0×10^{-6}

Figure 7.16 illustrates the aperture distribution along a line passing through an injection point and parallel to the direction of maximum horizontal stress, at the end of each injection. The 3rd injection cycle generates the largest aperture. The largest aperture in the end of 4th injection is 5.5×10^{-5} m. The fluid pressure distribution along the line at the end of each venting is shown in Figure 7.17. As can been see from it, high fluid pressure is trapped in the joint in the end of venting.

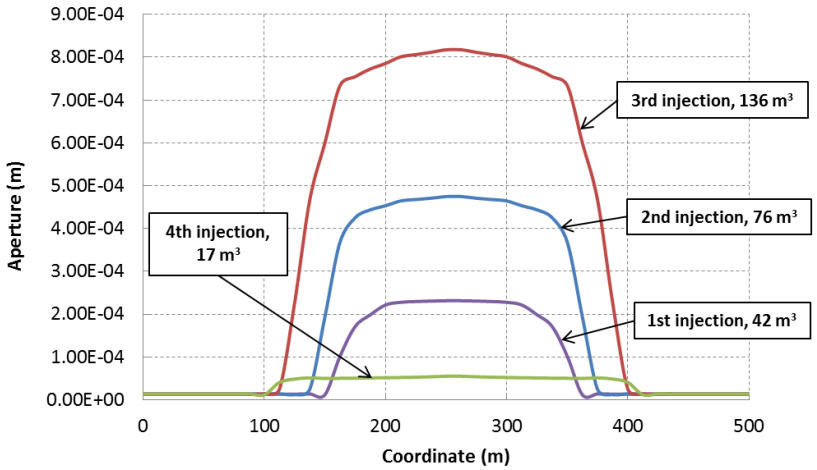

Figure 7.16 Aperture distribution along a line passing through an injection point and parallel to the direction of maximum horizontal stress ($\beta = 20$).

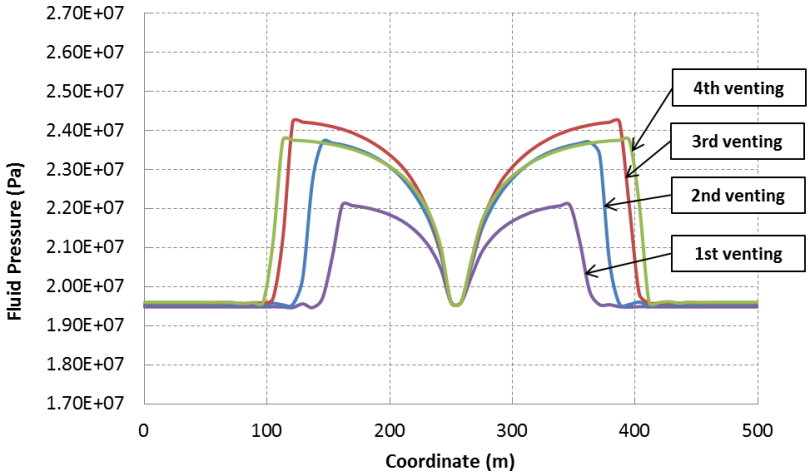

Figure 7.17 Fluid pressure distribution at the end of each venting treatment along a line passing through an injection point and parallel to the direction of maximum horizontal stress (β = 20).

(3) Scenario #3

From published field experiments, it is found that natural fractures underground tends to be softer during injection-venting treatments (Jung 1989). In our model, the stiffer or softer behavior of a joint is related to β. If we assume the joint becomes softer during each injection-venting operation, β should decrease from a higher value in the first treatment to smaller values in subsequent treatments. Also, we should remember the stiffness of joint is size dependent, the larger of a joint, the softer of its stiffness.

In scenario #3, β decreases from 80 to 20: β = 80 for the 1st injection-venting treatment; β = 60 for the 2nd injection-venting treatment; β = 40 for the 3rd injection-venting treatment; β = 20 for the 4th injection-venting treatment. All the other parameters are kept as those used before.

The fluid pressure trapped in the joint at the end of each venting is presented in Figure 7.18. The 1st treatment has the largest trapped pressure. The 2nd treatment also has a larger trapped pressure than the 3rd treatment. In contrast, the 3rd treatment has the largest trapped pressure in scenario #2 with β = 20; the 1st treatment has the lowest trapped pressure. Also, all the trapped pressures for the first three venting operations in scenario #3 are larger than those in scenario #2.

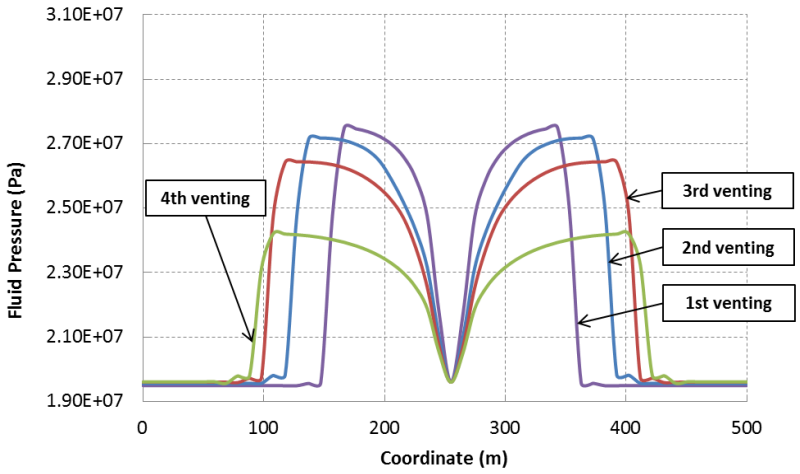

Figure 7.18 Fluid pressure distribution at the end of each venting treatment along a line passing through an injection point and parallel to the direction of maximum horizontal stress.

Table 7.7 summaries the recovery ratio, the smallest aperture size and its corresponding equivalent permeability for each treatment. As can be seen from it, the recovery ratio is very close to field observations.

Table 7.7 Flow-back volume and permeability at the end of each venting for scenario #3.

Treatment	1st	2nd	3rd	4th
Flow-back ratio	7%	26%	45%	91%
Perm (md)	51	88	195	759
Aperture (m)	7.9×10^{-7}	1.0×10^{-6}	1.5×10^{-6}	3.0×10^{-6}

(4) Scenario #4

It is well known that joint stiffness depends on the size of the joint. The following simple linear equation is used to represent joint stiffness as a function of the size:

$$\beta = \frac{\beta_1 - \beta_0}{R_1 - R_0}(x - R_1) + \beta_1 \tag{7.17}$$

where β_0, β_1, R_0, R_1 are input parameters, x is the radius of reactivation zone.

Based on previous simulations, we find that the radius of reactivation zone ranges from 100 m to 200 m. In this scenario, R_0 and R_1 are chose as 100 and 200, respectively. β_0 and β_1 are chose as 400, and 20. Table 7.8 summaries the recovery ratio, the smallest aperture size and its

corresponding equivalent permeability for each treatment. As can be seen from it, the recovery ratio increases after each treatment. We do not have perfect matches with the field observations. It is reasonable because the factors that influence the flow-back volume are not completely considered in the simulations.

Table 7.8 Flow-back volume and permeability at the end of each venting for scenario #4.

Treatment	1^{st}	2^{nd}	3^{rd}	4^{th}
Flow-back ratio	3%	30%	54%	72%
Perm (md)	5.9	31	327	327
Aperture (m)	2.7×10^{-7}	6.2×10^{-7}	2.0×10^{-6}	2.0×10^{-6}

7.5 Conclusions

A fully coupled thermal-hydro-mechanical model is developed. Numerical examples are presented to verify and illustrate the application of this model. Excellent agreements have been achieved through the comparison of numerical results with both analytical solutions and results from published work. The reopening of joints is simulated based on damage mechanics. Evolution of joint aperture and permeability controls the injection volume and flow-back volume during injection and venting operations. Semi-analytical equations are utilized to capture the main characteristics of it. A pressurization test at Phase I Fenton Hill geothermal reservoir is used to evaluate our model. Numerical results from our model match well with field records according to the pressure profile characteristics. The influence of mesh size on simulation results is also analyzed. The maximum differences of bottom-hole pressure caused by mesh size is around 2 MPa. Three scenarios are proposed to evaluate the mechanisms involved in the repeated injection-venting experiments. It is found that the stiffness of joint, a key parameter used in aperture calculation, controls the flow-back volume and trapped fluid pressure during venting operations. Considering the size dependent characteristic of joint stiffness and hysteresis behaviors observed during injection and venting, a parameter related to stiffness is gradually

changed after each injection-venting treatment in the 3rd scenario. Based on the results from numerical simulations, it is concluded that the 3rd scenario best fits the field observations.

References

Aboustit, B., Advani, S., Lee, J. et al. 1982. Finite element evaluations of thermo-elastic consolidation. In The 23rd US Symposium on Rock Mechanics (USRMS).

Ashby, M. F. and Sammis, C. G. 1990. The damage mechanics of brittle solids in compression. *Pure and Applied Geophysics* 133 (3): 489-521. http://dx.doi.org/10.1007/bf00878002.

Biot, M. A. 1941. General theory of three- dimensional consolidation. *Journal of Applied Physics* 12 (2): 155-164.

Booker, J. R. and Savvidou, C. 1984. Consolidation around a spherical heat source. International *Journal of Solids and Structures* 20 (11–12): 1079-1090. http://dx.doi.org/10.1016/0020-7683(84)90091-X.

Booker, J. R. and Savvidou, C. 1985. Consolidation around a point heat source. *International Journal for Numerical and Analytical Methods in Geomechanics* 9 (2): 173-184. http://dx.doi.org/10.1002/nag.1610090206.

Brown, D. W., Duchane, D. V., Heiken, G. et al. 2012. Mining the earth's heat: hot dry rock geothermal energy. Heidelberg: Springer Science & Business Media.

Cheng, A. H. D. and Detournay, E. 1988. A direct boundary element method for plane strain poroelasticity. *International Journal for Numerical and Analytical Methods in Geomechanics* 12 (5): 551-572.

Cleary, M. P. 1977. Fundamental solutions for a fluid-saturated porous solid. *International Journal of Solids and Structures* 13 (9): 785-806. http://dx.doi.org/10.1016/0020-7683(77)90065-8.

de Borst, R. 2002. Fracture in quasi-brittle materials: a review of continuum damage-based approaches. *Engineering Fracture Mechanics* 69 (2): 95-112. http://dx.doi.org/10.1016/S0013-7944(01)00082-0.

Gatmiri, B. and Delage, P. 1997. A formulation of fully coupled thermal–hydraulic–mechanical behaviour of saturated porous media—numerical approach. *International Journal for Numerical and Analytical Methods in Geomechanics* 21 (3): 199-225. http://dx.doi.org/10.1002/(sici)1096-9853(199703)21:3<199::aid-nag865>3.0.co;2-m.

Jaeger, J. C., Cook, N. G. W., and Zimmerman, R. (2007). Fundamentals of Rock Mechanics (Fourth ed.). Malden, MA: Wiley-Blackwell Publishing.

Jing, L. and Hudson, J. A. 2002. Numerical methods in rock mechanics. International *Journal of Rock Mechanics and Mining Sciences* 39 (4): 409-427. http://dx.doi.org/10.1016/S1365-1609(02)00065-5.

Jirásek, M. and Bauer, M. 2012. Numerical aspects of the crack band approach. *Computers & Structures* **110–111**: 60-78. http://dx.doi.org/10.1016/j.compstruc.2012.06.006.

Jung, R. 1989. Hydraulic in situ investigations of an artificial fracture in the Falkenberg granite. *International Journal of Rock Mechanics and Mining Sciences & Geomechanics Abstracts* 26 (3): 301-308. http://dx.doi.org/10.1016/0148-9062(89)91978-5.

Kachanov, L. 1958. Time of the rupture process under creep conditions. Isv. Akad. Nauk. SSR. Otd Tekh. Nauk 8: 26-31.

Kurashige, M. 1989. A thermoelastic theory of fluid-filled porous materials. *International Journal of Solids and Structures* 25 (9): 1039-1052. http://dx.doi.org/10.1016/0020-7683(89)90020-6.

Lee, S. H. and Ghassemi, A. 2009. Thermo-poroelastic Finite Element Analysis of Rock Deformation And Damage. Paper ARMA-09-121 presented at the The 43rd US Rock Mechanics Symposium and 4th U.S.-Canada Rock Mechanics Symposium, Asheville, NC, 28 June-1 July 2009.

Lewis, R. W., Majorana, C. E. and Schrefler, B. A. 1986. A coupled finite element model for the consolidation of nonisothermal elastoplastic porous media. *Transport in Porous Media* 1 (2): 155-178. http://dx.doi.org/10.1007/bf00714690.

Mazars, J. 1986. A description of micro- and macroscale damage of concrete structures. *Engineering Fracture Mechanics* 25 (5): 729-737. http://dx.doi.org/10.1016/0013-7944(86)90036-6.

McTigue, D. 1986. Thermoelastic response of fluid- saturated porous rock. *Journal of Geophysical Research: Solid Earth* (1978–2012) 91 (B9): 9533-9542.

McTigue, D. 1990. Flow to a heated borehole in porous, thermoelastic rock: Analysis. *Water Resources Research* 26 (8): 1763-1774.

Noorishad, J., Tsang, C. F. and Witherspoon, P. A. 1984. Coupled thermal-hydraulic-mechanical phenomena in saturated fractured porous rocks: Numerical approach. *Journal of Geophysical Research: Solid Earth* 89 (B12): 10365-10373. http://dx.doi.org/10.1029/JB089iB12p10365.

Pijaudier-Cabot, G. and Bazant, Z. P. 1987. Nonlocal damage theory. *Journal of Engineering Mechanics* **113** (10): 1512-1533.

Rice, J. R. and Cleary, M. P. 1976. Some basic stress diffusion solutions for fluid saturated elastic porous media with compressible constituents. *Reviews of Geophysics* 14 (2): 227-241.

Schiffman, R. L. 1971. A thermoelastic theory of consolidation. *Environmental and Geophysical Heat Transfer* 4: 78-84.

Simo, J. C. and Ju, J. W. 1987. Strain- and stress-based continuum damage models—I. Formulation. *International Journal of Solids and Structures* 23 (7): 821-840. http://dx.doi.org/10.1016/0020-7683(87)90083-7.

Willis-Richards, J., Watanabe, K. and Takahashi, H. 1996. Progress toward a stochastic rock mechanics model of engineered geothermal systems. *Journal of Geophysical Research: Solid Earth* 101 (B8): 17481-17496. http://dx.doi.org/10.1029/96jb00882.

8 Summary and future work

8.1 Summary

In this dissertation, the coupled processes of fluid flow, heat transport and geomechanics are studied based on the theories of thermo-poromechanics, fracture mechanics and fluid mechanics. The governing equations for fractured porous rock, fluid flow and heat transport in fractures, and fluid flow in wellbores are discretized through the finite element method (FEM). Special hydro-mechanical and thermo-hydro-mechanical zero-thickness interface elements are developed to model the fully coupled processes in discontinuities, such as newly created hydraulic fractures, pre-existing fractures and joints. Typical finite element types suitable to model the coupled phenomena are implemented into a parallel computation framework. Numerical examples are utilized to verify the proposed models and to illustrate the physical mechanisms that are important in multi-physics and multi-scale analyses. Several laboratory experiments are also used to validate the proposed numerical model. Multiple applications are investigated and discussed.

8.2 Future work

There are still many aspects that could be extended based on the current studies in this dissertation.

Simulations of hydraulic fracturing in 3D based on finite element method need a large number of elements to discretize the rock matrix surrounding the hydraulic fractures. Adaptive mesh or remeshing techniques could be used to decrease the number of elements tremendously since relatively smaller elements are needed only near fracture tips and elements with larger size could be used in the regions away from the fracture tips. When remeshing or adaptive mesh techniques are implemented, hydraulic fractures propagating in nonplanar manner could be

realized. Investigation of multiple fracture propagation and the interaction between them could be possible.

As discussed in Chapter 2, when hydraulic fractures propagate close to the formation interface, the slippage along the interfaces could act as an efficient way to stop fracture height growth. The shear failure (or mixed failure mode) should be considered in CZM in order to model the slippage of interfaces. With this improvement, more complex problems could be simulated. The interaction between hydraulic fracture and natural fracture shares the same physical mechanisms as those involved in slippage and/or opening of formation interfaces.

The model provided in Chapter 2 could be improved to consider the fracture propagation in a poroelastic medium. Poroelastic model can effectively handle the pore pressure and stress evolutions during both fluid injection and production. A better understanding of the change of pore pressure and stresses benefits the optimization of drilling, production and re-fracturing.

Appendix A: Publications

Several subjects related to thermo-hydro-mechanical analyses are studied in this dissertation. Papers on these subjects have been published, or will be published in journals or conferences:

JOURNAL PAPERS

Gao, Q., Ghassemi, A. 2019. Finite Element Simulations of 3D Planar Hydraulic Fracture Propagation Using a Coupled Hydro-mechanical Interface Element. submitted.

Gao, Q., Ghassemi, A. 2019. Three Dimensional Finite Element Simulations of Hydraulic Fracture Height Growth in Layered Formations Using a Coupled Hydro-mechanical Model. submitted.

Gao, Q., Ghassemi, A. 2019. 3D Thermo-Poromechanical Analysis of Flow, Heat Transport and Deformation in Fractured Rock with Applications to a Lab-scale Geothermal System. submitted.

Gao, Q., Ghassemi, A. 2017. Pore Pressure and Stress Distributions Around a Hydraulic Fracture in Heterogeneous, Rock. Rock Mechanics and Rock Engineering 50: 3157–3173. https://doi.org/10.1007/s00603-017-1280-5.

CONFERENCE

Gao, Q., Ghassemi, A. 2019. Height Growth in Layered Unconventional Reservoirs: The Impact of Formation Moduli, Interfaces and In-situ Stress. Paper to be presented at the Unconventional Resources Technology Conference, Denver, CO, USA, 22-24 July.

Gao, Q., Ghassemi, A. 2018. Parallel Finite Element Simulations of 3D Hydraulic Fracture Propagation Using a Coupled Hydro-mechanical Interface Element. 52th US Rock Mechanics/Geomechanics Symposium, Seattle, Washington, USA, 17-20 June. ARMA-2018-872.

Gao, Q., Ghassemi, A. 2016. 3D Thermo-poromechanical Analysis of Reservoir Stimulation Using Damage Mechanics with Application to the Fenton Hill HDR Experiment. 50th US

Rock Mechanics/Geomechanics Symposium, Houston, TX, USA, 27-29 June. ARMA-2016-152.